



HAL
open science

Structures of electrostatic complexes between a polyelectrolyte of variable rigidity and nanoparticles of controlled size

Li Shi

► **To cite this version:**

Li Shi. Structures of electrostatic complexes between a polyelectrolyte of variable rigidity and nanoparticles of controlled size. *Soft Condensed Matter [cond-mat.soft]*. Université Denis Diderot-PARIS VII École Doctorale: Matière condensée et interfaces, 2013. English. NNT: . tel-02668618

HAL Id: tel-02668618

<https://theses.hal.science/tel-02668618>

Submitted on 31 May 2020

HAL is a multi-disciplinary open access archive for the deposit and dissemination of scientific research documents, whether they are published or not. The documents may come from teaching and research institutions in France or abroad, or from public or private research centers.

L'archive ouverte pluridisciplinaire **HAL**, est destinée au dépôt et à la diffusion de documents scientifiques de niveau recherche, publiés ou non, émanant des établissements d'enseignement et de recherche français ou étrangers, des laboratoires publics ou privés.

UNIVERSITÉ DENIS DIDEROT- PARIS VII

ÉCOLE DOCTORALE : MATIÈRE CONDENSÉE ET INTERFACES

THÈSE DE DOCTORAT

Li SHI

**STRUCTURES DE COMPLEXES ÉLECTROSTATIQUES
ENTRE UN POLYÉLECTROLYTE DE RIGIDITÉ VARIABLE
ET DES NANOPARTICULES DE TAILLE CONTRÔLÉE**

Thèse dirigée par : Eric Buhler et François Boué

Soutenue le 05 Avril 2013

JURY

M. Michel Rawiso	Rapporteur
M. Patrick Guenoun	Rapporteur
M. Bernard Cabane	Membre invité
M. Florent Carn	Membre invité
M. Eric Buhler	Directeur de thèse
M. François Boué	Co-directeur de thèse

Remerciements

Mon travail de thèse a été effectué au sein du laboratoire Matière et Systèmes Complexes (MSC) UMR- CNRS-Université Paris Diderot et du laboratoire Léon Brillouin (LLB-UMR CNRS-CEA). Je tiens d'abord à remercier Jean-Marc di Meglio et Loïc Auvray successivement directeurs du MSC, ainsi que Philippe Mangin et Christiane Alba-Simionesco successivement directeurs du LLB, qui ont soutenu l'attribution et le financement de ma thèse, m'ont accueillie dans ces deux laboratoires.

Monsieur Patrick Guenoun, Directeur de Recherche au CEA, et Monsieur Michel Rawiso, Directeur de Recherche au CNRS à Strasbourg, ont bien voulu juger ce travail et écrire leur rapport dans un délai très court en formulant des remarques judicieuses. Je les en remercie vivement. Je suis très honorée que Bernard Cabane, Directeur de Recherche au CNRS à l'ESPCI, ait manifesté de l'intérêt pour ce travail et soulevé des problèmes pertinents grâce à son expertise.

J'adresse mes remerciements les plus sincères et les plus chaleureux à mes directeurs de thèse pour m'avoir accordé leur soutien et leur confiance pendant ces trois années. Tout d'abord, Eric Buhler, Professeur à l'Université Paris Diderot (Paris 7), qui m'a appris très pédagogiquement les techniques de diffusion du rayonnement et m'a initiée au domaine de la matière molle. Sa rigueur et son expérience en diffusion du rayonnement a permis une critique constructive pour l'analyse des résultats obtenus pendant ces trois années. Son suivi attentif en référence à l'orientation du sujet et des expériences, à la rédaction du manuscrit et à de premières publications a été un élément déterminant de ce travail. Je tiens à le remercier d'avoir dirigé cette thèse, et de m'avoir donné la possibilité de réaliser ce travail dans d'excellentes conditions. Ensuite, je voudrais exprimer mes vifs remerciements à François Boué, Directeur de Recherche au CNRS, pour sa disponibilité exponentiellement croissante au cours de ma thèse : pour son intérêt et ses conseils pour la synthèse des particules, pour son soutien sur tous les grands instruments utilisés (surtout pendant les WE et jours fériés), pour les nombreuses discussions, en particulier pendant la rédaction du manuscrit. Ça me fait toujours grand plaisir de travailler avec lui.

Je tiens également à remercier Florent Carn, Maître de Conférences à l'Université Paris Diderot, pour sa disponibilité pendant toute ma thèse. Grâce à lui je me suis vite intégrée dans le laboratoire, j'ai pu initier et définir le mode de synthèse des nanoparticules d'or et ai eu

accès à plusieurs laboratoires extérieurs. Je le remercie également pour sa participation aux mesures sur les grands instruments et à la rédaction de la thèse. Mon travail en commun avec Florent, François et Eric s'est effectué dans une ambiance harmonieuse

Je voudrais également remercier les membres des deux laboratoires. Au LLB, beaucoup des membres du groupe « Petits Angles » m'ont aidée sans que j'ai toujours pu les en remercier. Didier Lairez nous a beaucoup guidés dans la maîtrise du pilotage du spectromètre PACE, sur lequel nous avons bénéficié de la disponibilité et de la gentillesse d'Arnaud Helary. Merci aussi à Arsen Gukassov et Florence Porcher pour leur aide indispensable sur l'interprétation du signal des cristaux mixtes. Aurore Verdier, Anne Touze, Catherine Doira, Claude Rouse m'ont beaucoup aidée dans la résolution de nombreux problèmes administratifs.

Au sein de l'équipe « Structure et Dynamique des Milieux Complexes » du MSC, j'ai bénéficié de nombreux soutiens de tous les membres, mais tout particulièrement de Marie-Alice Guedeau-Boudeville : Booboo, merci ! Merci à Nicolas Jouault, pour les expériences de diffusion des RX réalisées à l'ESRF et pour l'aide au dépouillement ! Carole Barache, Nadine Beyer, Danielle Champeau, Lucie Bouchu m'ont également aidée de façon indispensable dans la jungle administrative.

J'ai effectué les expériences de microscopie électronique au sein du laboratoire de Chimie de la Matière Condensée du Collège de France avec Gervaise Mosser. C'est elle qui m'a initiée à la technique de la cryo-TEM. Qu'elle trouve ici toute ma reconnaissance. Je voudrais également remercier les personnes qui m'ont aidée à réaliser mes expériences sur les Grands Instruments. Il s'agit d'Isabelle Grillo au réacteur de l'Institut Laue Langevin de Grenoble (sur D11), de Jérémie Gummel au synchrotron de Grenoble (sur la ligne ID2 de l'ESRF), où nous avons pu préciser la structure de type bâton, de Sergio Funari qui nous a accueillis avec chaleur à Hambourg (DESY), ce qui nous a mis sur la piste des cristaux, mais également de Florian Meneau (SOLEIL) que nous avons beaucoup sollicité jusqu'à des heures trop tardives sur SWING, et qui nous a ainsi permis l'accès à des données conclusives.

Enfin, mes pensées vont à mes amies de tous les jours : Camille Gambini, Cécilia Galindo-Gonzalez, Malak Safi, Jelena Kolosnjaj, Amanda Brun, Anne-Florence Bitbol, Delphine Fayol, Nawel Ould-Moussa, Laurie Karim et Chiho Watanabe. Nous avons partagé la plupart des jours heureux, et les jours malheureux ont été moins durs à vos côtés. Recevez ici toute mon affection!

Table des Matières

Introduction Générale.....	5
I. Rappels Théoriques et Bibliographiques.....	13
I.1 Généralités sur les Polyélectrolytes ^[1-5]	13
I.1.1 Longueurs caractéristiques.....	13
I.1.2 Conformation des chaînes électrostatiques :	14
I.1.3 Longueurs de persistance intrinsèque et électrostatique	19
I.2 La Complexation Electrostatique.....	23
I.2.1 Les complexes polyélectrolytes-macroions	23
I.2.2 Paramètres Physiques des Systèmes	29
I.3 Vers notre choix des systèmes étudiés.....	33
II. Méthodes Expérimentales Physiques: Diffusion du Rayonnement	37
II.1 Le vecteur d'onde de transfert	37
II.2 Facteur de forme $P(q)$ et facteur de structure $S(q)$	39
II.3 La diffusion de la lumière.....	41
II.3.1 La diffusion statique de la lumière	41
II.3.2 La diffusion dynamique de la lumière	45
II.4 La diffusion des neutrons aux petits angles (DNPA ou SANS)	51
II.4.1 L'interaction neutron-matière.....	52
II.4.2 Le contraste.....	53
II.4.3 La méthode de « matching ».....	55
II.4.4 Spectromètre de DNPA	55
II.4.5 Traitement des données	56
II.5 La diffusion des rayons X aux petits angles (DXPA ou SAXS)	57
II.5.1 L'interaction rayon-x matière.....	57
II.5.2 Principe de mesure.....	58
II.5.3 Le contraste.....	59

II.6 Appendice :.....	60
III. Electrostatic Complexation Between a Polyelectrolyte and Large Nanoparticles (10-20nm): Effect of the Polyelectrolyte Persistence Length and of the Sign of Charge	63
III.1 General Introduction	63
III.2 Interaction between a Semiflexible Polycation and Oppositely Charged Nanoparticles: Case of Chitosan/Silica Nanoparticles	65
III.2.1 Introduction	65
III.2.2 Single Solute Solutions Characterization	66
III.2.3 Sequence of phase behaviors.....	72
III.2.4 Nanorods SAXS characterization.....	77
III.2.5 Combined SAS and cryo-TEM measurements of the different shapes.....	81
III.2.6 Conclusion.....	84
III.3 Effect of the Polyelectrolyte Persistence Length:	87
III.3.1 Complexation of 10 nm Radius Silica Nanoparticles with Flexible Poly-L-lysine	87
III.3.2 Phase diagram of the PLL-SiNP system	87
III.3.3 Structure of the PLL-SiNP complexes: SANS characterization	90
III.4 Swapping the Sign of Charges: Interaction between Semi-flexible Polyanion Hyaluronan and Positively Charged Silica Nanoparticles	98
III.4.1 Introduction	98
III.4.2 Sequence of Phase Behaviors.....	100
III.4.3 Structure of the Hyaluronan/SiNP complexes: similarities with the inversed charges case.....	104
III.4.4 General summary: some common trends to all systems	114
III.5 Appendix 1 of Chapter III: Silica particles and Poly-L-lysine.....	118
III.6 Appendix 2 of Chapter III: Positively charged SiNP and Hyaluronan	121
III.6.1 Positively charged SiNP (Ludox CL).....	121
III.6.2 Hyaluronan	125

III.7 Appendix 3 of Chapter III: SAXS pattern of system HA-SiNP, using Bonse- Hart configuration	129
III.8 Appendix 4 of chapter IV: The double layer model and the estimate of the particle charge	131
IV. Synthesis of gold nanoparticles (AuNP).....	135
IV.1 Introduction.....	135
IV.2 Wet chemical synthesis of water dispersible cationic AuNPs	136
IV.2.1 Turkevich method	137
IV.2.2 Brust Method.....	147
IV.3 Characterization of AuNPs obtained by the Brust's method	152
IV.3.1 Size and shape of gold nanoparticle.....	152
IV.3.2 Determination of AuNP mother solution concentration	159
IV.3.3 Surface charge of AuNP	160
IV.4 Conclusion	162
V. Complexation of polyelectrolyte (PEL) and nanoparticles (NPs) of small size (2~5nm)	165
V.1 General introduction.....	165
V.2 Complexation of sodium polystyrene sulfonate (PSSNa) and gold nanoparticles (AuNPs).....	165
V.2.1 Materials.....	165
V.2.2 Complexation PSSNa-AuNPs without salt	167
V.2.3 Complexation PSSNa-AuNPs in screened conditions (0.1M NaCl).....	174
V.3 Complexation of Hyaluronan (HA) and gold nanoparticles (AuNPs)	181
V.3.1 Introduction	181
V.3.2 Materials.....	181
V.3.3 Complexation Hyaluronan-AuNPs without salt.....	181
V.3.4 Complexation Hyaluronan-AuNPs with 0.1M NaCl	188
V.3.5 Discussion on crystals	199

V.4 Conclusion.....	208
General Conclusion	215
Bibliography	221

Introduction Générale

Les complexes formés de polyélectrolytes, c'est-à-dire de polymères chargés, et de particules de charges opposées (par exemple des protéines ou des nanoparticules de tailles et formes diverses) par interaction électrostatique sont très fréquents. Beaucoup de complexes de ce type se trouve dans la nature et présente des applications diverses et variées. Un des intérêts majeurs de ces complexes d'origine naturelle est qu'ils sont solubles en milieux aqueux, une propriété permettant de travailler dans des conditions peu onéreuses et de moduler/contrôler l'ensemble des paramètres physico-chimiques. Les objets ainsi formés, sont à priori, peu coûteux, biocompatibles et dans certains cas stimulables. Ils font partie de ce qui est communément appelé les « complexes électrostatiques ».

La très grande variété des « complexes électrostatiques » a amené les scientifiques et les industriels à effectuer deux catégories principales d'études, selon leur type d'applicabilité. Pour une première catégorie, les applications peuvent ainsi être industrielles et très orientées. Ces études, assez développées, sont souvent spécifiques à un système donné dans des conditions très particulières. En particulier, dans le cas des polyélectrolytes, ceux-ci peuvent être amphiphiles, linéaires ou branchés, des homopolymères ou des copolymères, naturels ou synthétiques. Il est donc très difficile d'isoler l'effet de l'interaction électrostatique, et de comprendre son rôle dans la formation des objets et son implication dans les propriétés finales.

La deuxième catégorie d'études sur la complexation électrostatique (CE) est plus théorique et fondamentale liées à générale entre deux espèces colloïdales de charges opposées. Au-delà de la physique et de la chimie, elle concerne également les systèmes biologiques, où sont impliqués des polyélectrolytes particuliers, que ce soit le Hyaluronane, qui pourrait être impliqué dans des interactions électrostatiques avec des protéines au sein de la matrice extracellulaire ou du liquide synovial (articulations), ou dans une tout autre direction, l'ADN –également un polyanion- enroulé de façon spécifique autour des histones (cationiques) au sein de la chromatine dans les chromosomes. La CE semble jouer aussi un rôle primordial dans les problèmes de transfection de brins d'ADN à l'intérieur de la cellule. Malgré la large gamme de phénomènes où elle peut donc être impliquée, la complexation entre espèces colloïdales de charges opposées n'est pas encore totalement comprise d'un point de vue fondamental. Dans ce travail de thèse, on étudiera la complexation entre des objets simples, modèles, les nanoparticules de taille variable et des polyélectrolytes de charges opposées

d'origine naturelle ou synthétique les plus simples également. Les théories de la complexation mettent en avant le rôle déterminant de la rigidité des chaînes sur l'état complexé. La rigidité des chaînes de polyélectrolytes, c'est-à-dire la longueur de persistance, L_p , peut être décrite comme la somme de la longueur de persistance intrinsèque, L_0 (qui représente la rigidité naturelle de la chaîne et qui peut être dans certains cas liée à des structures de type hélice ou double hélice, cf ADN), et de la longueur de persistance électrostatique, L_e , qui dépend des interactions électrostatiques entre les segments au sein du milieu solvant. Trois types de polymères à longueur de persistance sont distingués : les polyélectrolytes flexibles (pour lesquels $L_e > L_0$), comme le poly(styrène sulfonate de sodium), les polyélectrolytes semi-rigides (avec $L_e \sim L_0$) comme ceux de la famille des polysaccharides, et enfin les chaînes rigides comme l'ADN ($L_0 \sim 500 \text{Å} > L_e$). Des études antérieures sur la formation des complexes ont par ailleurs montré que le rôle des autres caractéristiques du polyélectrolyte (la densité de charge le long de la chaîne, la longueur de contour, etc.), et des paramètres physico-chimiques (le rapport des taux de charges entre les deux espèces, le pH, la force ionique de la solution, etc) pouvait être primordial. Des simulations théoriques ont essayé de prédire une structure à l'échelle des composants individuels mais elles ne concernent qu'un nombre limité d'objets-limité par le temps de calcul - et donc très loin des situations réelles. Pour ce qui est des études expérimentales publiées, malgré leur nombre important, très peu d'entre elles parviennent à comparer différents systèmes en contrôlant systématiquement les variables mentionnées ci-dessus. Cela rend une généralisation des résultats très difficile. Une des difficultés est de trouver des particules modèles chargées. La plupart des études expérimentales concernent des protéines ou des nanoparticules commerciales polydisperses et dont le taux de charge est souvent mal connu. Certes, les protéines sont monodisperses, mais leur taille, c'est-à-dire leur rayon, ne peut être varié indépendamment de leurs autres propriétés. L'influence de ce paramètre sur la formation et le comportement des complexes reste donc mal comprise. De plus, les protéines présentent des groupements hydrophobes à l'origine d'une distribution de charges de surface non homogène : il peut ainsi y avoir attraction même si les charges globales des deux espèces sont de même signe. Une autre difficulté majeure concerne le domaine de concentration extrêmement dilué dans lequel les complexes isolés de polyélectrolytes/nanoparticules, attendus avant agrégation/précipitation en objets plus gros sont observés. Ces complexes individuels (communément appelés « single complexes », par exemple composés d'une chaîne et de plusieurs nanoparticules ou protéines) sont donc très difficiles à étudier par les techniques habituelles.

Mon travail de thèse a comme premier but de comprendre le rôle du paramètre L_p/R , représentant le rapport entre la longueur de persistance du polyélectrolyte et de rayon de nanoparticules modèles, sur la formation et le contrôle de la géométrie de complexes électrostatiques. Les nanoparticules utilisées sont modèles, c'est-à-dire caractérisées par un taux de charge, une taille et une forme contrôlés. Afin de clarifier le rôle joué par la rigidité du polyélectrolyte, plusieurs types de polyélectrolytes modèles de rigidité différente ont été utilisés (d'origine naturelle ou synthétique). L'éventail de polyélectrolytes et de nanoparticules choisis nous a permis de varier le paramètre L_p/R entre 0.1 et 1.25 et de réaliser une étude pionnière dans ce domaine. Les composants choisis sont déjà connus et d'ailleurs beaucoup utilisés industriellement.

- les polysaccharides Chitosane ($L_p=9$ nm, polycation), et Hyaluronane ($L_p=5$ nm, polyanion) sont des polyélectrolytes naturels semirigides
- tandis que la polylysine ($L_p=1$ nm, polycation) et le polystyrène sulfonate de sodium ($L_p=0.94$ nm, un polyanion bien connu) sont des polyélectrolytes flexibles.
- les « grosses » nanoparticules, sont faites de silice (SiNP) et caractérisées par deux tailles différentes (celles chargées négativement dont le rayon est de 9.2 nm, et celles chargées positivement dont le rayon est de 17 nm).
- enfin les « petites » particules sont difficiles, voire impossibles, à trouver dans le commerce en version chargées positivement (sachant que les polyélectrolytes modèles les plus courants sont chargés négativement). Nous avons **synthétisé nous-même des petites nanoparticules d'or (AuNP)** relativement monodisperses, sphériques ($R=4$ nm) et fonctionnalisées par des ligands thiols chargés positivement.

Le tableau suivant permet de visualiser l'ensemble des systèmes étudiés dans ce travail. ce choix des polyélectrolytes et des nanoparticules nous a permis non seulement de faire varier le rapport L_p/R mais également le rapport de signe de charges.

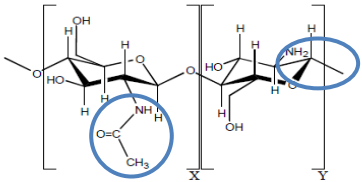

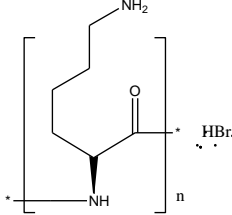

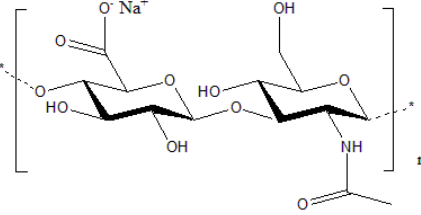

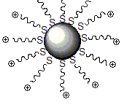
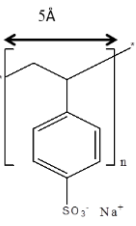
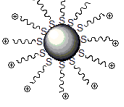
Chapitre	PEL	L_p (nm)	NP	R (nm)	L_p/R	Signe de charges
III	 Chitosane	9	 SiNP	9.2	≈ 1	+/-
III	 Polylysine	1	 SiNP	9.2	0,1	+/-
III	 Hyaluronan	5	 SiNP	17	0,3	-/+
V			 AuNP	4	1,25	-/+
V	 PSSNa	0.94	 AuNP	4	0.23	-/+

Tableau 1 : Systèmes étudiés : longueur de persistance du polyélectrolyte, rayon des nanoparticules et signe de charge des composants individuels. La première colonne indique le chapitre correspond à l'étude du système

Pour chaque système, la détermination du diagramme de phase, issue d'une observation visuelle, a été obtenue en fonction des concentrations respectives des deux composants, de la force ionique de la solution et suivant les cas de la longueur de la chaîne. En présence d'un excès de nanoparticules ou de polyélectrolytes, le système reste monophasique. Pour les

rapports de concentrations intermédiaires, une séparation de phase de type coacervation (liquide-liquide ou liquide-solide) est observée systématiquement. Les structures des complexes dans les domaines monophasiques en présence d'un excès de nanoparticules ou de polyélectrolytes ainsi que dans les coacervats et les phases surnageantes (domaines diphasiques) ont été déterminées à partir d'expériences conjointes de diffusion des neutrons (DNPA), des RX aux petits angles (DXPA) et de la lumière afin de mettre en évidence le rôle primordial joué par le rapport L_p/R . Des mesures de microscopie (lumière ou électrons) ont été effectuées dans quelque cas. Nous nous sommes également intéressés, dans les limites des possibilités techniques à notre disposition, à l'observation de la séparation de phases, de sa cinétique et des types de phase formées.

Les cinq chapitres constituant ce mémoire se décomposent de la manière suivante. Le chapitre I est consacré à un rappel théorique sur les solutions de polyélectrolytes, sur le principe de l'interaction électrostatique ainsi que sur les effets des paramètres mis en jeu lors de complexation. Un rappel bibliographique sur la complexation entre espèces colloïdales de charges opposées est également présenté. Dans le chapitre II sont décrites les différentes techniques expérimentales ainsi que les méthodes d'analyse et de traitements utilisées. Les principales techniques étant les techniques de diffusion du rayonnement.

Les chapitres III et V regroupent les principaux résultats concernant les phénomènes de complexation électrostatique et les propriétés structurales des objets complexes obtenus.

Le chapitre III concerne la complexation électrostatique entre des nanoparticules de silice de grande taille ($R \sim 10-20$ nm) et des polyélectrolytes de rigidité variable caractérisée par une longueur de persistance comprise entre 9 et 1 nm. L'effet du signe de charge, de la force ionique et de la longueur des chaînes a été étudié. Pour cela, trois systèmes ont été sélectionnés : pour les systèmes chitosane/SiNPs et polylysine/SiNPs, nous utilisons les mêmes nanoparticules mais faisons varier la flexibilité du polyélectrolyte, tout en gardant la même concentration du sel rajouté de la solution (force ionique élevée). Pour les systèmes Chitosane/SiNPs et Hyaluronane/SiNPs, les deux polyélectrolytes sont semiflexibles, mais le signe de charges est inversé. Un des résultats majeurs concerne la formation de bâtons de nanoparticules monodisperses en section en présence d'un polyélectrolyte semi-rigide à force ionique élevée. Les évidences d'un enroulement de la chaîne semiflexible sur la surface des « grosses » nanoparticules sont discutées.

Le chapitre IV porte sur la synthèse des nanoparticules d'or sphériques (AuNPs) de petite taille chargée positivement. Ce chapitre présente également un bref rappel des principales voies de synthèse, ainsi que la justification de notre méthode. La caractérisation de ces AuNPs bien définies en taille et en charges de surface réalisée à partir d'expériences conjointes de diffusion des neutrons et des RX et diffusion quasi-élastique de la lumière constitue la deuxième partie de ce chapitre.

Enfin, le dernier chapitre (chapitre V) est dédié à l'étude physique et physico-chimique des complexes formés à partir de nanoparticules d'or « AuNPs » de petite taille et des polyélectrolytes flexibles (polystyrène sulfonate de sodium, PSSNa) ou semirigides (Hyaluronan) de longueur variable. L'effet de la force ionique n'est pas oublié. Le type d'objets obtenus peut être sensiblement différent. Un résultat central et surprenant est l'apparition de cristaux obtenus lors de la complexation des AuNPs avec les polyélectrolytes en présence de 0.1M NaCl. La discussion sur la structure, la composition, la taille et la formation de ces cristaux fait l'objet de la deuxième partie de ce chapitre.

La conclusion générale résume les points communs aussi bien que les particularités observées sur les cinq systèmes choisis et représentatifs. Une tentative de compréhension et de prédiction de la structure des complexes à partir de paramètres moléculaires universels est ainsi proposée, à notre avis pour la première fois sur un éventail expérimental aussi large.

CHAPITRE I

RAPPELS THEORIQUES ET BIBLIOGRAPHIQUES

I. Rappels Théoriques et Bibliographiques

I.1 Généralités sur les Polyélectrolytes^[1-5]

Le terme polyélectrolyte désigne une solution –généralement aqueuse- d'un polymère portant des charges électrostatiques (positives ou négatives) et par extension ce polymère lui-même dans les mêmes conditions, c'est-à-dire quand les charges sont dissociées par solvation. Les charges d'un signe donné sont fixées le long de la chaîne qui devient un polyion, tandis que les charges opposées, les contre-ions, sont susceptibles de se mouvoir dans la solution.

L'existence de charges le long de la chaîne induit des interactions électrostatiques à longue, où à moyenne portée à cause de l'écrantage par les contre-ions libres ou les autres ions présents (co-ions), qui s'ajoutent aux interactions à courte portée (de type volume exclu). Il existe donc des paramètres électrostatiques et des longueurs additionnels qui vont intervenir dans les équations. Pour cette raison, les systèmes polyélectrolytes sont généralement plus complexes que les systèmes de type polymères neutres.

I.1.1 Longueurs caractéristiques

En tant que polymères, les polyélectrolytes sont déterminés par les grandeurs caractéristiques suivantes^[6, 7] :

Localement sur une chaîne, pour toute masse de chaîne :

- la taille du monomère : a ,
- La longueur de persistance intrinsèque de la chaîne, L_{p0} (ou L_0) qui caractérise la longueur sur laquelle la chaîne est intrinsèquement rigide

Globalement sur une chaîne, selon la masse : la longueur de contour $L = N \times a$ (N nombre d'unités monomériques),

- La distance moyenne bout à bout $\langle R \rangle$,
- Le rayon de giration R_G des chaînes,

Entre plusieurs chaînes, en régime semidilué:

La longueur de corrélation interchaînes ξ caractérisant le régime semidilué, c'est-à-dire la taille du blob représentant la portée des interactions de type volume exclu.

Les polyélectrolytes, puisque des charges sont présentes, font intervenir de nouveaux paramètres électrostatiques :

Intrinsèques à la solution :

- La longueur de Bjerrum l_B , telle que $e^2 / 4\pi\epsilon l_B = kT$ (e correspond à une charge élémentaire, ϵ est la permittivité du milieu, k la constante de Boltzmann et T la

température absolue). Deux ions monovalents séparés de $r=l_B$ ressentent une attraction ou une répulsion égale à kT . Dans l'eau à 25°C, cette longueur est égale à $l_B=7.13\text{Å}$. La longueur de Bjerrum correspond à la distance au-delà de laquelle l'interaction électrostatique entre deux charges élémentaires devient inférieure à l'énergie thermique kT .

- La force ionique I , qui dépend de l'ensemble des ions libres de la solution, donc de la concentration en contre-ions dissociés $f_{eff} \times C$ et en sel ajouté C_s . La longueur d'écran κ^{-1} , qui est l'échelle sur laquelle les interactions électrostatiques sont écrantées. Dans l'ensemble des théories exposées, elle correspond à la longueur de Debye- Hückel κ_{DH}^{-1} et est reliée à la concentration des contre-ions, c'est-à-dire à la force ionique, I :

$$\kappa_{DH}^{-1} = (4\pi l_B I)^{-1/2} \approx I^{-1/2} \quad \text{I-1}$$

κ_{DH}^{-1} est définie à partir du potentiel du même nom $\varphi(r)=(e/4\pi\epsilon)\exp(-r\kappa)$, pour un gaz idéal d'ions, dans la pratique peu dense, et représente l'échelle de distance sur laquelle le potentiel s'atténue.

Au niveau de la chaîne :

- Le taux de charge $f=a/b$ qui représente le rapport entre la taille d'un monomère, a , et la distance entre deux charges successives le long de la chaîne, b
- Le paramètre de charge ζ qui caractérise le rapport de la longueur de Bjerrum, l_B , et de la distance entre deux sites ioniques successifs le long de la chaîne, b . La longueur de persistance électrostatique des chaînes, L_{pe} , qui s'ajoute à la contribution intrinsèque L_{pe} pour caractériser la longueur sur laquelle la chaîne est rigide.

I.1.2 Conformation des chaînes électrostatiques :

Suivant le taux de charges, les polyélectrolytes peuvent être classés en chaînes fortement ou faiblement chargées.

I.1.2.1 Chaînes fortement chargées—condensation de Manning

Lorsque le paramètre de charge ζ est élevé (supérieur à une valeur seuil, ζ_{Manning} , que nous allons définir), une partie des contre-ions restera proche du macroion, et va être totalement liée à celui-ci (bloquée à une distance finie) ; on parle d'effets de condensation.

Cette condensation peut être vue comme une non-dissociation de certains contre-ions de la macromolécule ou comme une quantité de contre-ions piégée dans le voisinage très proche de

la chaîne. Dans ce dernier cas, les contre-ions seraient libres de se mouvoir longitudinalement le long de la chaîne.

Le processus de condensation proposé par Manning^[8,9], après les premiers calculs d'Oosawa par exemple, concerne une chaîne rigide. Sa longueur, L , est beaucoup plus grande que la taille des unités monomériques a . La chaîne porte une fraction de charges monovalentes distantes de b . La chaîne est modélisée par un fil infiniment fin ayant une densité linéique de charges uniforme. Dans ces conditions, le potentiel électrostatique créé par la chaîne à une distance $r \ll L$ s'écrit (on néglige la contribution des contre-ions) :

$$\varphi(r) = \left(\frac{e}{4\pi\epsilon_0\epsilon_r b} \right) \ln(r) = \left(\frac{2kTl_B}{eb} \right) \ln(r) \quad \text{I-2}$$

Si la distribution des contre-ions suit la statistique de Maxwell-Boltzmann, elle s'écrit:

$$n(r) = n_0 \exp(-\varphi(r)) \approx r^{-2l_B/b} \quad \text{I-3}$$

où n_0 est la densité moyenne des contre-ions. Le nombre de contre-ions par unité de longueur situés à une distance inférieure à r est donc :

$$P(r) = \int_0^r 2\pi r' n(r') dr' = 2\pi n_0 \int_0^r r'^{\left(1 - \frac{2l_B}{b}\right)} d(r') \quad \text{I-4}$$

La dernière intégrale ne converge en " 0 " que si la puissance de r est supérieure à -1 , c'est-à-dire si $b > l_B$ (lorsque $\zeta < 1$). Dans ces conditions, on considère qu'il n'y a pas de condensation. En revanche, si $b < l_B$ (lorsque $\zeta > 1$) l'intégrale diverge. Il est donc nécessaire d'admettre que, dans ces conditions, il y a condensation. La condensation des contre-ions sur la chaîne, écrante une partie des charges. Virtuellement, il se créera une nouvelle distance entre les charges qui sera inférieure à la distance réelle de telle façon que la distance entre charges dissociées b_{eff} rétablisse la relation $b_{eff} > l_B$. La longueur de Bjerrum revêt alors un nouveau sens physique : c'est la longueur minimale entre deux charges dissociées le long de la chaîne. Lorsque $\zeta > 1$, la condensation de Manning ramène la distance entre deux sites ioniques à l_B de telle sorte que l'énergie de Coulomb entre ces sites soit inférieure ou égale à kT . Le seuil de Manning s'écrit donc : $\zeta_{Manning} = l_B/b = 1$. Pour des valeurs de ζ supérieures à 1, les propriétés physiques du système deviennent ainsi indépendantes du taux de charge.

I.1.2.2 Notion de blob électrostatique

En admettant le principe d'une condensation, un paramètre de charge ζ inférieur à 1 peut être considéré comme un paramètre de charge faible.

Pour un taux de charge $f = a/b$ suffisamment faible, les corrélations entre les monomères peuvent ne pas être affectées par les répulsions électrostatiques aux courtes distances, c'est-à-dire au-dessous d'une taille de blob électrostatique ξ_e , telle que l'énergie électrostatique soit égale à l'énergie thermique kT . On obtient alors :

$$\xi_e = \frac{(gfe)^2}{4\pi\epsilon_0\epsilon kT} = (gf)^2 l_B \quad \text{I-5}$$

g étant le nombre de monomères par blob électrostatique. La taille du blob électrostatique est ainsi une longueur qui correspond à la valeur au dessous de laquelle les chaînes ne sont pas sensibles aux interactions électrostatiques et sont donc gaussiennes, à volume exclu ou encore « collapsées » suivant l'écart au point thêta.

Dans le régime de bon solvant, à l'intérieur du blob électrostatique, la chaîne sera ainsi sensible aux effets de volume exclu, en tout cas au delà de la taille ξ_T du blob thermique. La taille ξ_T du blob thermique représente la valeur en dessous de laquelle la chaîne est toujours gaussienne, et ceci quelque soit la qualité du solvant.

Si $\xi_T > \xi_e$, la chaîne est gaussienne jusqu'à ξ_e et :

$$\xi_e^2 = ga^2 \quad \text{I-6}$$

et donc :

$$\xi_e = a \left(\frac{l_B}{a}\right)^{-1/3} f^{-2/3} \quad \text{I-7}$$

Aux plus grandes échelles la chaîne est un alignement de blobs électrostatiques ξ_e .

Si $\xi_T < \xi_e$, la chaîne sera successivement gaussienne, puis gonflée et enfin étirée.

I.1.2.3 Ecrantage des interactions électrostatiques--Loi limite de Debye-Hückel

La présence d'ions libres provoque un écrantage électrostatique. Si les contre-ions sont situés à des distances finies de la chaîne, et plus encore si du sel est ajouté en solution, la chaîne perd son caractère rigide à grande échelle car les interactions électrostatiques le long de cette dernière seront « écrantées ».

Le point de départ du modèle proposé par Debye et Hückel est de placer un ion ponctuel i à l'origine et de calculer le potentiel électrostatique $\psi_i(r)$ tout autour. Si cet ion était seul dans la solution, on aurait :

$$\psi_i(r) = \frac{Z_i e}{4\pi\epsilon_0\epsilon r} \quad \text{I-8}$$

avec Z_i la charge (en unité e) de la particule i et ε la permittivité relative du milieu. ε_0 représente la permittivité du vide. Du fait de la présence des autres ions, le potentiel sera certainement moins intense que ce potentiel direct. En effet, la présence de l'ion central i va modifier l'environnement ionique : les ions de signe opposé à i vont être attirés alors que les ions de même signe vont être repoussés. L'équation de Poisson s'écrit :

$$\Delta\psi_i(r) = -\frac{\rho_e(r)}{\varepsilon_0\varepsilon} = -\frac{e}{\varepsilon_0\varepsilon} \sum_j Z_j n_j(r) \quad \text{I-9}$$

où $\rho_e(r)$ est la densité locale de charge et $n_j(r)$ est la densité locale de l'espèce j . Par définition des fonctions de distribution de paires, $g(r)$, on a $n_j(r) = \rho_j g_{i,j}(r)$. La somme porte sur toutes les espèces ioniques présentes en solution. Debye et Hückel ont alors utilisé l'approximation suivante :

$$g_{i,j}(r) = e^{-\frac{Z_j e \psi_i(r)}{kT}} \quad \text{I-10}$$

avec la condition implicite $\psi_i(\infty) = 0$ (potentiel totalement " écranté " à l'infini). Cette approximation de type " champ moyen " néglige l'effet de l'introduction de la particule j en r sur les ions voisins (pas de corrélation ion-ion dans l'environnement ionique de i). Les équations conduisent ainsi à l'équation de Poisson-Boltzmann :

$$\Delta\psi_i(r) = -4\pi d_B \sum_j \rho_j Z_j e^{-Z_j \varphi_i} \quad \text{où} \quad \varphi_i = \frac{e\psi_i}{kT} \quad \text{I-11}$$

avec φ_i le potentiel sans dimension (en unité $kT/e \approx 25\text{mV}$).

L'étape d'après consiste à linéariser les facteurs exponentiels, ce qui conduit à l'équation de Poisson-Boltzmann linéarisée ou Debye-Hückel :

$$\Delta\varphi_i(r) = \kappa^2 \varphi_i(r) \quad \text{I-12}$$

où la constante κ est définie par

$$\kappa = \sqrt{4\pi d_B \sum_j \rho_j Z_j^2} \quad \text{I-13}$$

Le terme constant dans l'équation de Debye-Hückel a disparu grâce à la condition d'électroneutralité :

$$\sum_j \rho_j Z_j = 0 \quad \text{I-14}$$

La solution à l'équation de Debye-Hückel est finalement :

$$\varphi_i(r) = \frac{Z_i l_B}{r} e^{-\kappa r} \quad \text{I-15}$$

A grande distance, le potentiel coulombien direct dû à l'ion central est donc fortement affaibli par la présence de l'environnement ionique. Le potentiel décroît comme $e^{-\kappa r}/r$ au lieu de $1/r$.

Ce phénomène propre aux systèmes chargés s'appelle l'écrantage électrostatique. κ est appelé constante d'écrantage. $\kappa^{-1} = \lambda_0$, appelée longueur de Debye, ou longueur d'écran, représente l'échelle de distance sur laquelle le potentiel s'atténue c'est-à-dire l'échelle sur laquelle les interactions électrostatiques sont écrantées.



Figure I-1: Représentation de la gaine d'écrantage autour de la chaîne due à la longueur d'écran κ^{-1}

Dans l'ensemble des théories, elle correspond à la longueur de Debye-Hückel et est reliée à la concentration des contre-ions c'est-à-dire à la force ionique, I .

$$\kappa^{-1} = (4\pi l_B I)^{-1/2} \quad \text{I-16}$$

Chaque ion contribue à la force ionique comme le carré de sa valence. Pour un électrolyte +1/-1 (NaCl par exemple), I s'identifie à la concentration en ions C_f .

$$I = \frac{1}{2} \sum_j \rho_j Z_j^2 \quad \text{I-17}$$

Dans le cas des solutions diluées, on peut simplifier la relation (I-13) et écrire :

$$\kappa^2 = 4\pi l_B C_f \quad \text{I-18}$$

avec C_f la concentration des ions monovalents libres $C_f = C_{ci} + 2C_s$ avec C_s la concentration en sel ajouté (coions) et C_{ci} la concentration en contre-ions libres, égale à la concentration en monomères C dans le cas où le paramètre de charge ζ est inférieur à 1 et à C/ζ si ζ est supérieur à 1.

I.1.2.4 Interactions attractives

Il est intéressant de signaler que des interactions attractives entre chaînes sont prédites à très courte distance. Cela peut avoir lieu lorsque deux chaînes sont suffisamment proches et que les contre-ions voisins de la chaîne (condensés par exemple le long de celle-ci) peuvent se mouvoir longitudinalement, créant des fluctuations de charges à l'origine des interactions

attractives. La portée des forces attractives serait beaucoup plus faible que la longueur d'écran. Quant à leur intensité, elle serait du second ordre par rapport aux répulsions électrostatiques. Leur rôle est cependant évoqué pour expliquer les agrégations d'origine électrostatique (en l'absence de sel) menant à des hétérogénéités de concentration très visibles par diffusion de rayonnement.

I.1.3 Longueurs de persistance intrinsèque et électrostatique

La conformation des chaînes peut être dictée par les blobs thermiques et électrostatiques ζ_e décrits ci-dessus mais aussi par la longueur de persistance L_p (qui, au-delà de la rigidité intrinsèque traduit également les répulsions électrostatiques entre les charges le long de la chaîne). Le point de départ des théories est une description analytique en régime dilué, initié par la théorie d'Odijk, que nous décrivons ci-dessous.

En 1977, Odijk^[10], et parallèlement Skolnick^[11] et Fixman^[12], ont les premiers proposé un calcul de la longueur de persistance (théorie OSF) d'une chaîne **quasi-rigide**, c'est-à-dire de très grande longueur de persistance. Dans leur modèle, la chaîne est unique et faiblement chargée. L'influence des contre-ions n'est pas prise en compte (ils sont supposés infiniment éloignés).

Le principe du calcul d'Odijk consiste à considérer l'énergie libre de la chaîne comme étant une somme de son énergie de courbure, et de l'énergie électrostatique des charges le long de la chaîne: $\Delta F = \Delta F_{elast} + \Delta U_{el}$

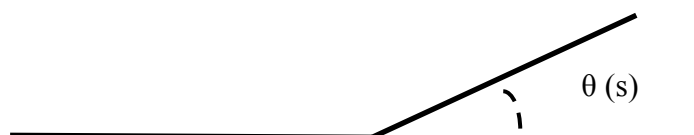
L'énergie de courbure est donnée sous sa forme intégrale, et l'énergie électrostatique est donnée par le potentiel de Debye-Hückel:

$$\Delta U_{el} = \sum_{i,j} \frac{e^{-\kappa r_{i,j}}}{r_{i,j}} \quad \text{I-19}$$

où i et j notent la position des charges le long de la macromolécule, et κ^{-1} est la longueur d'écran de Debye.

Puisque la chaîne est très quasi-rigide, sa conformation ne peut pas s'écarter sensiblement de celle d'un bâtonnet légèrement courbé. Cela va avoir deux implications:

- 1) Dans un référentiel curviligne d'abscisse s , l'expression de l'angle de courbure de la chaîne $\theta(s)$, va pouvoir être linéarisée et discrétisée puisque celui-ci est petit. Le calcul pourra donc se faire exactement.



- 2) L'énergie électrostatique va être considérée, en première approximation, comme une perturbation par rapport à l'énergie de courbure.

La longueur de persistance totale de la chaîne L_T sera alors une somme d'une longueur de persistance "nue" L_0 , c'est-à-dire intrinsèque, (qui est celle qu'aurait la chaîne si elle ne portait pas de charges), et de L_e , la longueur de persistance électrostatique, parfois appelée longueur d'Odijk^[10]. Elle s'écrit:

$$L_T = L_0 + L_e \quad \text{I-20}$$

La chaîne doit être proche d'un bâton, le critère étant : $L < L_T/2$. On obtient alors pour L_e une fonction analytique de κL (L est la longueur étirée de la chaîne). A condition que κL soit très grand (L très grand devant κ^{-1}), on a:

$$L_e = l_B / 4\kappa^2 A^2 \quad \text{I-21}$$

Les deux conditions sur L ($L < L_T/2$ et κL grand) conduisent à $L_T \gg \kappa^{-1}$ comme Odijk le précise plus tard^[13].

Si l'on tient compte de la condensation de Manning, A est égal à l_B et:

$$L_T = L_0 + \frac{1}{4\kappa^2 l_B} \quad \text{si } \zeta \geq 1 \quad \text{I-22}$$

On doit retenir deux résultats importants de ce modèle, qui découlent de l'hypothèse selon laquelle l'énergie électrostatique est une perturbation de l'énergie élastique.

- 1) Ce traitement impose la condition $L_e \ll L_0$
- 2) Il amène au résultat assez inattendu, que L_e est proportionnelle à κ^{-2}/l_B , au lieu de κ^{-1} , comme l'annoncent les lois d'échelle.

En 1978, Odijk et ses collaborateurs^[14] proposent d'étendre le calcul au-delà de la limite du bâtonnet, c'est-à-dire pour des chaînes formées de plusieurs longueurs de persistance ($L/L_0 \gg 1$). Ceci correspond soit à des chaînes beaucoup plus longues soit à une longueur de persistance intrinsèque plus faible, mais il faut conserver la relation suivante: $L_0 > 5\kappa^{-1}$. Ceci sera facilité par le fait que l'on considère le cas d'une concentration en sel ajoutée non nulle. L'écrantage permet également de considérer un ensemble de chaînes, interpénétrées, mais qui seront en fait supposées indépendantes.

En séparant les monomères en séquences de longueur L_0 le long de la chaîne, les auteurs proposent de ne considérer que les interactions au sein de ces régions. Si la chaîne reste suffisamment rigide à plus grande taille, la distance entre deux séquences sera supérieure à κ^{-1} .

Il suffit de considérer que la contribution des configurations pour lesquelles la chaîne, en se courbant, rapproche des charges éloignées sur le squelette, est négligeable.

On retrouve alors les résultats précédents : $L_e = \frac{1}{4\kappa^2 l_B}$, toujours avec les conditions $L_e \ll L_0$,

$L_T \gg \kappa^{-1}$, et donc $L_0 \gg \kappa^{-1}$ et $L_0 > l_B$, qui est la condition pour que le potentiel électrostatique soit une perturbation par rapport à l'énergie de courbure.

En opposition au modèle précédent, Barrat et Joanny^[15] proposent un second modèle pour les chaînes flexibles, soit $L_e > L_0$ (la rigidité électrostatique est dominante) qui limite le modèle d'Odijk, à:

$$A \ll (L_0 l_B)^{1/2} \quad \text{I-23}$$

Toujours à partir d'une énergie de courbure et d'une énergie électrostatique écrantée, ils reprennent numériquement le calcul de la moyenne de $\langle \theta(s)^2 \rangle$ sur toutes les configurations d'une chaîne semi-flexible (s est à nouveau l'abscisse curviligne le long de la chaîne). Lorsque s est petit,

$$\langle \theta(s)^2 \rangle = s / L_0 \quad \text{I-24}$$

comme pour un polymère neutre. L'hypothèse d'Odijk selon laquelle on peut négliger la contribution électrostatique des charges éloignées le long du polyion semi-flexible (second modèle), n'est valable que dans le cas où la courbure des chaînes reste faible : aux petites tailles, $\theta(s)$ est trop grand.

En revanche, si s dépasse une valeur critique s_c , $\langle \theta(s)^2 \rangle$ augmente et on retrouve le résultat de la théorie OSF:

$$\langle \theta(s)^2 \rangle = \frac{s}{L_e + L_0} + Cste \quad \text{I-25}$$

Les distances sont suffisamment grandes pour que la chaîne puisse se rigidifier.

Dans le cas d'un faible écrantage (κ^{-1} grand), le calcul donne pour s_c un résultat qui peut se retrouver qualitativement. Une chaîne de petite section et de longueur $s < \kappa^{-1}$, qui se courbe d'un angle θ , dépense une énergie de courbure : $kTL_0\theta^2/2$, et une énergie électrostatique $kTl_B(s/A)^2\theta^2/2$. Les deux énergies sont comparables à $s \sim s_c$:

$$S_c \sim A \left(\frac{L_0}{l_B} \right) H^{1/2} \quad \text{I-26}$$

La condition de validité du modèle d'Odijk s'écrit donc: $\langle \theta(s_c)^2 \rangle \ll 1$, soit, à partir des Eqs. I-24 & I-26 (faible écrantage):

$$A \ll (L_0 l_B)^{1/2} \quad \text{I-27}$$

Ayant exposé les limites de validité d'une théorie adéquate dans le cas de chaînes rigides, les auteurs proposent un traitement variationnel^[16], dont le but est de minimiser l'énergie libre variationnelle du système. Les auteurs se penchent sur le cas d'un polyion très flexible en l'absence d'effets d'écran ($\kappa=0$). Ils repartent du modèle simple d'une succession linéaire de blobs électrostatiques. La chaîne est considérée comme étant sans interaction à l'intérieur de chaque blob. En revanche, chacun d'entre eux est soumis à une tension $kT\tau$ (τ est l'amplitude de la force de tension). Le volume du blob est donc de l'ordre de $1/\tau$. Pour traiter simultanément le cas où la chaîne peut être gonflée à grande échelle (au delà de L_p), la direction de la tension peut changer (pas son amplitude). Cette orientation restera cependant corrélée sur la taille L_p .

L'énergie libre qui va être calculée dépendra de l'énergie associée à la rigidité intrinsèque locale de la macromolécule, de l'énergie d'une succession linéaire de tous les blobs de taille $1/\tau$ de la chaîne, mais aussi de l'entropie due aux changements de directions de la tension au delà de L_p , ainsi que de l'augmentation de l'énergie électrostatique engendrée par le changement de direction de la tension. Finalement:

$$L_p = \kappa^{-1} \quad \text{I-28}$$

Barrat et Joanny mettent bien en évidence les deux domaines différents, lorsque la chaîne est rigide ($A \ll (L_0 l_B)^{1/2}$), et pour laquelle la théorie d'Odijk s'applique ($L_T=L_0+L_e$ avec $L_e \sim \kappa^{-2}$), et lorsque la chaîne est flexible ($A \gg (L_0 l_B)^{1/2}$), où $L_p \sim \kappa^{-1}$. Cependant ils soulignent que le domaine intermédiaire, lui, n'est pas encore clairement expliqué.

Il faut remarquer que la décomposition de la longueur de persistance totale en une somme constituée par la longueur de rigidité intrinsèque et par celle qui caractérise la rigidité électrostatique ($L_T=L_0+L_e$) n'est judicieuse que lorsque l'on considère des macromolécules semi-rigides. Dans le cas des polyions flexibles cela n'a pas vraiment lieu d'être. C'est la raison pour laquelle en général on définit la longueur de persistance "physique", L_p .

Expérimentalement, E. Buhler et F. Boué^[17] ont étudié pour la première fois à partir d'expériences conjointes de diffusion des neutrons aux petits angles et de la lumière la variation avec la force ionique de la longueur de persistance d'un polyélectrolyte semi-rigide modèle, le Hyaluronane, qui est un homopolysaccharide linéaire bien défini. Ils montrent entre autre que la contribution électrostatique L_e est proportionnelle à κ^{-2} , comme prévue par Odijk pour des polyélectrolytes semi-flexibles (eq.I-21).

I.2 La Complexation Electrostatique

Nous considérerons la mise en présence d'un polyélectrolyte (PE) d'un macroion, autres polyions, protéines ou NP, portant de nombreuses charges dont la somme est de signe opposée. Il peut y avoir formation d'un complexe, qui reste à détecter. En pratique on observe, dans des conditions appropriées, une séparation de phase très visible, plus ou moins complète, jusqu'à l'apparition d'une phase dense composée d'objets concentrés. Ce phénomène montre l'importance des interactions électrostatiques attractives entre les deux espèces.

Deux effets s'opposent à la complexation : l'entropie conformationnelle des polyélectrolytes, et les contraintes stériques ou élastiques. Le premier traitement théorique concernant les phénomènes de complexation entre deux espèces polyélectrolytes flexibles est celui développé par Overbeek et Voorn^[18], qui ont estimé l'énergie libre totale comme la somme de deux termes, l'un d'origine entropique et l'autre d'origine électrostatique dérivant du modèle classique de Debye-Hückel décrit pour les solutions simples de polyélectrolytes. Le premier terme favorise le mélange homogène tandis que le deuxième favorise la formation d'une phase dense de complexes. Il reste à considérer les macroions autres que les PE flexibles (PE semi-flexibles, bâtonnets linéaires, sphériques/globulaires, ou encore résultant de l'auto-association de molécules amphiphiles), qui ont beaucoup moins de degré de liberté et d'entropie conformationnelle. De ce fait, les complexes stœchiométriques de macroions non flexibles ont tendance à être plus denses, mais le degré de neutralisation des charges reste largement déterminé par les possibilités d'arrangement stériques (par exemple en cas d'interaction de PE avec des sphères de signe de charges opposé), ou par un équilibre entre les énergies électrostatique et celle de déformation élastique (par exemple pour le cas des chaînes polyélectrolytes s'enroulant autour des sphères de signe de charges opposé).^[19] Nous retrouverons ce problème dans nos systèmes.

I.2.1 Les complexes polyélectrolytes-macroions

Grâce à leurs charges le long de la chaîne, les polyélectrolytes, même partiellement hydrophobes, sont dans la plupart des cas très solubles dans l'eau et peuvent donc se complexer électrostatiquement avec les macroions de signe de charge opposé, telles que des polyélectrolytes, des tensio-actifs ou des micelles, des protéines ou encore des nanoparticules. Ce phénomène de complexation a été observé dans de nombreux processus naturels et a attiré beaucoup d'intérêts dans différents domaines industriels.

Plusieurs études ont été abordées par les chercheurs pour mieux comprendre le phénomène de complexation entre différentes espèces chargées. Dans ces études, les polyélectrolytes utilisés

peuvent être des sels d'ammonium quaternaires chargés positivement à bas pH, donc des polycations qui se complexent alors avec un macroion caractérisé par une charge globale négative dans ces conditions, c'est-à-dire par un point isoélectrique bas. Le cas inverse de polyélectrolytes chargés négativement en interaction avec des macroions de signe de charge opposé a été beaucoup plus étudié du fait du plus grand nombre de polyanions disponibles dans la nature et commercialement. Vu que les fonctions chimiques telles que les groupes sulfate, sulfonate, carboxylate ou phosphate permettant d'obtenir des charges négatives en solution sont nombreuses et variées, les possibilités pour les polyanions en sont d'autant plus vastes.

Toutefois, le mécanisme de complexation mis en jeu est loin d'être bien compris. Une des difficultés est le manque d'un modèle théorique qui puisse décrire toutes les situations à cause des propriétés uniques des différents systèmes (polyélectrolytes, micelles, nanoparticules...), ces derniers faisant souvent intervenir d'autres types d'interactions : il faut donc traiter les situations au cas par cas car le nombre de paramètres liés aux deux composants est souvent très élevé. De plus, les systèmes mixtes étant plus compliqués que les solutions de polyélectrolytes, dont les phénomènes sont déjà très complexes, les simulations numériques sont encore malheureusement peu efficaces. Enfin, les méthodes expérimentales existantes pour déterminer les propriétés structurales des complexes ainsi que les conformations des chaînes ne sont accessibles que pour des conditions limitées et exigeantes. Dans les paragraphes suivants, nous allons détailler quelques études de référence réalisées dans ce domaine :

Selon la nature des macroions en interaction avec les polyélectrolytes (PE) de signe de charge opposé, on peut classer les différents types de complexes obtenus en différentes catégories : Les principales sont les complexes PE-PE, PE-micelles, PE-protéines, PE-Nanoparticules (NPs). Dans les paragraphes qui suivent nous nous focaliserons uniquement sur les polyélectrolytes linéaires et hydrophiles, les polymères insolubles partiellement chargés, ou encore les polymères amphiphiles ne faisant pas l'objet d'études dans ce travail de thèse. Néanmoins, bien que la force principale de la complexation soit d'origine électrostatique, chaque famille de systèmes présente des propriétés bien particulières.

1) Complexes PE-PE^[20-22] « mélanges polyanions-polycations »

L'effet de forte corrélation de charges dans les polyélectrolytes a été observé il y a centaine d'années. Mélanger des polyélectrolytes synthétiques ou naturels de charges opposées conduit

à la formation de complexes forts car la plupart des polyélectrolytes sont caractérisés par des densités linéaires de charges importantes. Un cas particulier concerne les polyacides ou les polybases faibles qui ont la particularité de présenter un degré de dissociation, et donc un taux de charge, qui dépendant du pH. Ce caractère « pH-stimulable » leur confère des propriétés uniques ainsi que des applications variées dans les domaines des bio et des nanotechnologies. Un exemple est l'auto-assemblage de micelles polymères obtenu à partir de polycations et de polyanions où l'un des deux polymères comporte des blocs chargés et des blocs hydrophiles dont l'état de charge varie avec le pH. Le cœur des micelles résulte ainsi de la complexation des blocs chargés des deux espèces, tandis que la charge de la couronne hydrophile (acide ou basique), initialement neutre, varie en fonction du pH. Un autre exemple est axé sur les capteurs d'ADN^[23] basés sur la complexation de molécules d'ADN ciblées (anioniques) avec des polycations conjugués synthétiques.

Dans le processus de complexation PE-PE, le taux de charges, la longueur de la chaîne et sa flexibilité sont les trois paramètres les plus importants. Le taux de charges détermine le potentiel d'absorption du polyélectrolyte, qui peut être fixé dans le cas des polyélectrolytes sous leur forme « sel », ou être pH-dépendant dans le cas des polyacides ou polybases. En effet, on y retrouve toutes les lois s'appliquant aux solutions de polyélectrolytes simples : condensation du Manning, blob électrostatique, etc. Une particularité est que les charges le long des chaînes peuvent être mobiles. Jusqu'à présent, la majorité des travaux concerne le cas où les deux polyélectrolytes sont caractérisés par les mêmes paramètres physiques mis à part leur signe de charge qui est opposé-un cas encore très loin des situations réelles.

Récemment Mengarelli, Zhegal et Auvray^[24] ont étudié la formation et la structure des complexes stables électrostatiques entre polyélectrolytes de charge opposée, un acide polyméthacrylique longue et une plus courte polyéthylèneimine, à un pH faible, où le polyacide est faiblement chargée. Nous explorons le diagramme de phase en fonction de la charge et le rapport de concentration des constituants. En accord avec la théorie, la turbidité et les mesures de potentiel ζ montrent deux régimes distincts de complexation, faible et forte, qui apparaissent successivement quand on augmente le pH, avec une limite bien définie. Des complexes « faibles » observés par diffusion de neutrons montrent une structure ouverte, non compacte, alors que les complexes « forts » sont condensés. Leur description s'appuie sur un diagramme de phase théorique purement électrostatique de Shklovskii et al, où l'énergie de répulsion entre complexes de même charge est compensée par une énergie attractive due aux corrélations spatiales de charge (Figure I-2).^[25]

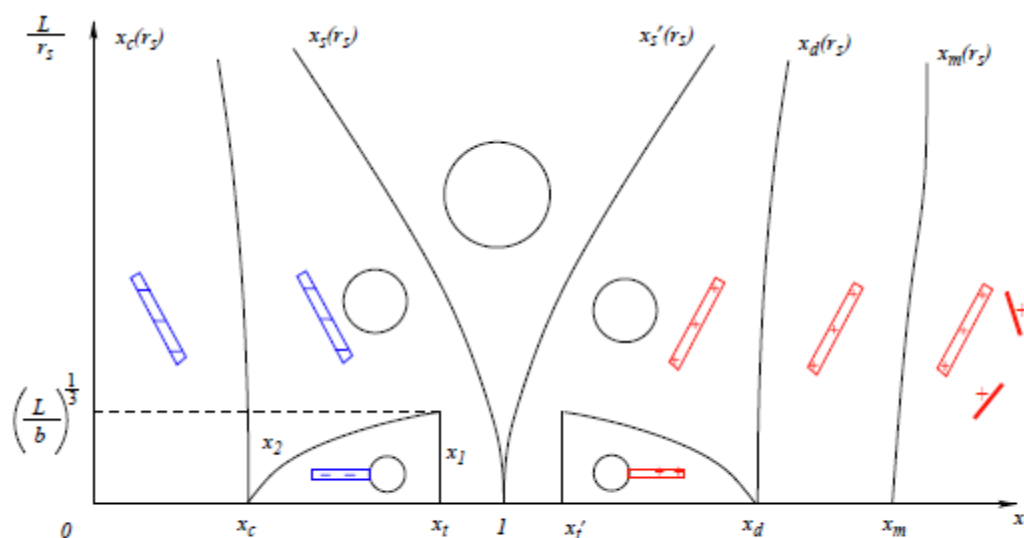


Fig. 2. Typical phase diagram of a solution of PA and PC. The horizontal axis x is the ratio of total charges of PC and PA in the solution. The vertical axis L/r_s is the ratio of the length of a free PA-PCs complex to the Debye-Hückel screening radius r_s . Symbols are explained in Fig. 1.

Figure I-2 : Diagramme de phase entre un polycation et un polyanion, issu de la référence [25]

2) Complexes PE-micelles

Les complexes PE-micelles constituent un domaine très important dans l'industrie cosmétique^[26], alimentaire^[27] et pharmaceutique^[28] où les polyélectrolytes sont utilisés pour leur caractère associatif avec des tensio-actifs et des micelles.

Les micelles composées de tensio-actifs sont considérées comme des macroions. Les tensio-actifs étant des molécules amphiphiles, contenant des groupes hydrophobes et hydrophiles (souvent chargés), s'associent dans l'eau au-delà d'une concentration micellaire critique (CMC) sous forme de micelles exposant à l'eau les groupes chargés. Ces micelles, suivant la nature et la géométrie des tensio-actifs, sont de géométrie variable et caractérisées par un taux de charge de surface.^[29]

De nombreuses publications^[30-32] ont montré qu'à très faible concentration, les tensio-actifs s'adsorbent sur les polyélectrolytes pour former des complexes de type « polyelectrolyte-surfactant complexes » (PSCs) quand une concentration critique d'agrégation (CAC) est atteinte. La valeur de cette CAC est de l'ordre de 1 à 3 fois plus petite que la CMC des tensio-actifs. Le signe de charge des complexes va s'inverser lorsque la concentration en tensio-actifs continue d'augmenter, les polyélectrolytes sont maintenant décorés par des micelles et on parle désormais de « polyelectrolyte-micelle complexes » (PMCs). Quand la concentration en tensio-actifs est au-dessus de la CMC, on trouve les micelles libres qui coexistent avec les

complexes solubles en solution. Certains de ces complexes présentent une structure cristalline, où les deux espèces sont positionnées régulièrement dans un métacristal de grande maille.^[33]

3) Complexes PE-protéines

Les acides aminés constituant les protéines ont la possibilité de porter des charges négatives ou positives suivant la valeur du pH et donnent donc un caractère polyélectrolyte à la macromolécule biologique.

Les premières études sur ce sujet datent d'il y a plus de 50 ans. Elles avaient été menées par Morawetz et Hugues^[34] dans le but de séparer et de purifier les protéines. Les chaînes de polyélectrolytes pouvant facilement interagir avec une protéine de signe de charge opposé, ils s'en servirent pour jouer le rôle de séparateur. Le même Morawetz a ensuite étudié ce type de complexation afin de stabiliser des protéines en milieu potentiellement dénaturant pour des activités enzymatiques^[35]. En effet les protéines incluses dans ces complexes conservent généralement leur état natif comme le montre plusieurs études menées sur des protéines enzymatiques^[36, 37]. Cette propriété a donc permis d'étendre le champ des applications à l'agro-alimentaire ou encore à la pharmacologie où la protection et l'encapsulation des protéines nécessitent qu'elles conservent leurs propriétés.

Dans de nombreux cas, la complexation entre des polyélectrolytes cationiques et des protéines chargées négativement induit des séparations de phase^[38, 39]. Le cas inverse considérant des polyanions en interaction avec des protéines chargées globalement positivement a également montré des résultats analogues^[40, 41]. J. Gummel, F. Cousin et F. Boué ont notamment systématiquement étudié en régime dilué et semi-dilué - correspondants dans tous les cas à des concentrations volumiques en composants assez élevées, la formation des agrégats de complexes, leurs structures dans les différentes phases, ainsi que la libération des contrions à partir d'expériences de diffusion du rayonnement^[40, 42-47].

Dans le groupe de Paul Dubin, Xia^[48] et Park^[49] ont constaté que des polyélectrolytes chargés négativement peuvent former des complexes solubles avec des protéines également chargées négativement près de leur point isoélectrique. Bien que la charge globale reste négative, la présence de « patches » de charges positives à la surface de la protéine permet aux polyélectrolytes d'interagir avec la protéine via un point d'ancrage qui localement est plus fort que les forces de répulsion dues à la charge nette négative de la protéine. Effectivement, cette hétérogénéité de la distribution de charges à la surface complique la compréhension générale de la complexation électrostatique des macroions de charges opposées, bien que les simulations les plus récentes aient tenté de tenir compte de ce paramètre.

4) Complexes PE-Nanoparticules (NPs)

Un domaine de recherche en plein développement concerne les nanoparticules, qui, à l'état auto-assemblé peuvent révéler des propriétés collectives différentes de celles des nanoparticules individuelles et des matériaux de synthèse classiques. L'intérêt actuel de ces assemblages est motivé par la capacité d'exploiter leurs propriétés collectives et la possibilité d'utiliser ces propriétés pour des applications bien ciblées dans des domaines aussi variés que les biotechnologies ou encore l'électronique et l'optique.

Parmi les diverses stratégies pour obtenir des assemblages de nanoparticules, l'approche de type « bottom-up^[50] » simple et peu coûteuse, consiste à placer les nanocomposants définis à proximité l'un de l'autre et de jouer sur les interactions inter-particules afin d'obtenir l'architecture auto-assemblée désirée, ordonnée ou désordonnée, et surtout choisie et contrôlable.

Cette approche fait intervenir les différents types d'interactions interparticules^[51], telles que les interactions de Van der Waals, magnétiques, dipôlares, les liaisons hydrogènes ou encore les interactions électrostatiques. Nous nous focaliserons dans ce travail sur l'interaction électrostatique induite par des polyélectrolytes, souvent appelés « soft templates » dans ce cas car ils peuvent induire, de façon souple, la forme finale des complexes. La complexation électrostatique entre des polyélectrolytes et des nanoparticules de signe de charge opposé ont de nombreux avantages. En effet, cette technique permet de réaliser des auto-assemblages de nanoparticules à température et pression ambiante. Les NPs préfabriquées sont soit métalliques, stabilisées par des ligands de charges opposées à celles du polyion, en solution, soit colloïdales avec des surfaces modifiées chargées également, donnant dans les deux cas une bonne stabilité en solution. On peut par exemple citer les monocouches de groupements thiols, disulfures ou encore dithiolanes sur les nanoparticules d'au^[52], d'Ag^[53], de Cu^[54], de Pt^[55], de Pd^[56] ou de Ni^[57]; de silanes sur les nanoparticules de silice^[58, 59], d'alumine^[60], de dioxyde de titane^[61, 62]; d'acides carboxyliques^[63] ou phosphoriques^[64, 65] sur les nanoparticules d'oxyde de fer, etc. La densité de charges à la surface des nanoparticules peut être régulée soit par l'introduction d'une dose choisie de ligands ou de molécules chargés/non chargés, soit par le contrôle in situ de la fraction chargées (par le pH par exemple). La portée des interactions électrostatiques est également modulable par simple ajout de contre-ions en solution. Le paramètre physique traduisant cet effet et facilement contrôlable est la longueur d'écran de Debye-Hückel définie plus haut (modèle de double couche).

Différentes stratégies permettent d'obtenir une morphologie désirée ou une organisation directionnelle privilégiée pour les assemblages de NPs. L'utilisation de chaînes d'ADN est très répandue, car les structures de ces chaînes linéaires étendues peuvent induire des liaisons électrostatiques avec les nanoparticules stabilisées par des ligands cationiques sur les groupes phosphoriques. Les chaînes d'ADN permettent ainsi d'obtenir une organisation contrôlable des nanoparticules d'au^[66], d'Ag^[67] et de CdSe^[68], etc. Le groupe d'Umetsu^[69] a par exemple utilisé l'ADN comme support pour réaliser un arrangement unidimensionnel de nanoparticules de zircone par simple mélange des deux composants en solution. D. Baigl a ensuite étudié la complexation entre des nanoparticules cationiques de silice et des chaînes d'ADN^[70]. D'autres polyélectrolytes d'origine naturelle ou synthétique, et des biomacromolécules, ont aussi été employés pour complexer des nanoparticules. Pour ce qui est de systèmes bidimensionnels, en se basant sur ces phénomènes de complexation électrostatique, G. Decher^[71] a développé une approche très fréquentée pour obtenir des assemblages de type multi-couches de polyélectrolytes. Par la suite, Kotov et ses collaborateurs^[72] ont adopté cette approche utilisant la complexation pour obtenir des assemblages de nanoparticules. Là aussi cette méthode est particulièrement intéressante pour l'organisation de particules chargées sur des substrats planaires^[73-75]. Les applications des mélanges polyélectrolytes/colloïdes sont extrêmement nombreuses dans des domaines aussi variés que la fabrication papetière, l'agro-alimentaire, la chimie environnementale, la coagulation des colloïdes, le transport de polluants associés à des nanoparticules inorganiques.

I.2.2 Paramètres Physiques des Systèmes

Les paramètres physiques intervenant lors des phénomènes de complexation électrostatique sont nombreux, tels que le rapport des charges^[76], la longueur des chaînes polyélectrolytes^[77], la flexibilité des chaînes^[78], la force ionique^[79], le pH de la solution^[80], etc. Ces paramètres sont souvent liés ce qui complique la compréhension et le contrôle des processus d'auto-association et de séparation de phase. Par exemple, dans le cas des polyacides faibles, une variation de pH induit un changement du taux effectif de charges linéaires sur les chaînes et ainsi l'association de ces dernières avec des colloïdes de signe de charge opposé. D'ailleurs, si certains paramètres ont des effets sur la conformation locale des chaînes ou sur la structure des composants individuels, d'autres influent plutôt sur le comportement global des complexes (apparition d'une séparation de phase par exemple).

I.2.2.1 Effet de la rigidité des polyélectrolytes

Comme nous avons décrit dans la section précédente, suivant leur nature et leur origine, les polyélectrolytes présentent des rigidités variables caractérisées par la longueur de persistance. Par exemple, dans la nature, l'ADN est un polyélectrolyte semi-rigide, voir rigide, caractérisé par une structure en double hélice et une longueur de persistance intrinsèque de l'ordre de 400-500 Å. A l'opposé, la polylysine est très flexible avec une longueur de persistance de l'ordre de la taille du monomère chimique (5-10 Å). L'effet de la flexibilité des polyélectrolytes sur la complexation électrostatique a été étudié par différents groupes de théoriciens. La flexibilité peut bien sûr jouer un rôle sur la conformation des chaînes à la surface des particules de signe de charges opposé, notamment sur la façon dont elles s'enroulent sur une particule de géométrie variable. Cependant ces études font généralement intervenir peu de particules et une seule chaîne ; elles décrivent ainsi uniquement des phénomènes locaux.

Linse^[78] a étudié l'effet de la flexibilité des polyélectrolytes sur les processus de complexation dans des systèmes de type « polyélectrolytes-macroions » par simulation Monte Carlo, en comparant 4 types de polyélectrolytes caractérisés par différents degrés de flexibilité. Les macroions sont des sphères, dont le nombre à l'état complexé est cependant très faible : il varie entre 1 et 4 (ce dernier nombre correspond à la neutralisation, comme illustré dans la Figure I-3). Ses résultats démontrent qu'avec un seul macroion complexé, plus la chaîne est rigide, plus le macroion conserve localement (à l'échelle de son diamètre) sa charge initiale (il reste « sous-chargé »). En cas d'un excès de macroions, tous les macroions complexés sont sous-chargés, quelle que soit la flexibilité de la chaîne. Il en conclut que pour les chaînes flexibles et les complexes pas encore neutralisés, les macroions sont proches et complexés fortement avec le polyélectrolyte, tandis qu'ils sont plus éloignés et arrangés de manière linéaire lorsque la rigidité du polyélectrolyte augmente. Ses résultats sont cohérents avec les autres études théoriques sur les polyélectrolytes flexibles^[81, 82] ou semiflexibles^[83, 84].

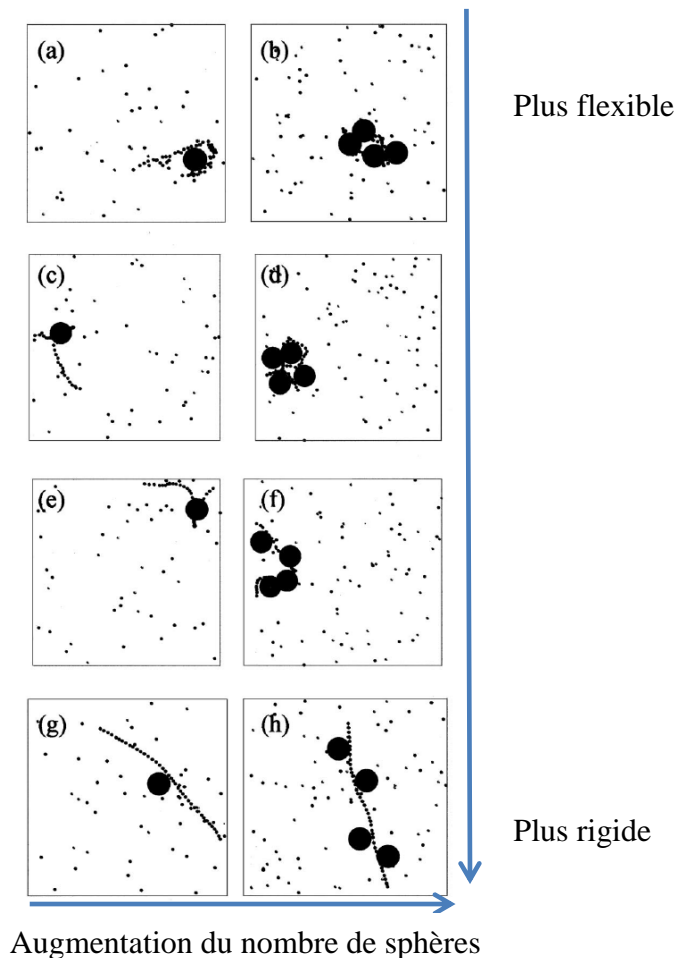


Figure I-3: Résultats des simulations de Linse sur l'effet de la flexibilité sur la complexation électrostatique dans les systèmes « polyélectrolytes-macroions ». 4 polyélectrolytes avec différents degrés de flexibilité (de haut en bas) ont été comparés, ainsi que le nombre de sphères complexées variant de 1 à 4 (de gauche à droite). Figure issue de la référence [78] Plus tard, Skepo et Linse^[85] ont travaillé sur les systèmes plus compliqués impliquant plusieurs polyélectrolytes et plusieurs macroions, notamment en variant la flexibilité des chaînes, le nombre de monomères et la taille des macroions. Ils ont montré que la tendance de séparation de phase est favorisée en présence de macroions de taille petite (charge totale fixée, rapport de charge stœchiométrique) et de chaînes plus longues. Cette séparation de phase (coacervation) est également favorisée pour des longueurs de persistance faibles. La plus fine couche de polyélectrolytes adsorbés à la surface des macroions de signe de charge opposé est obtenue quand cette longueur est comparable au rayon des macroions.

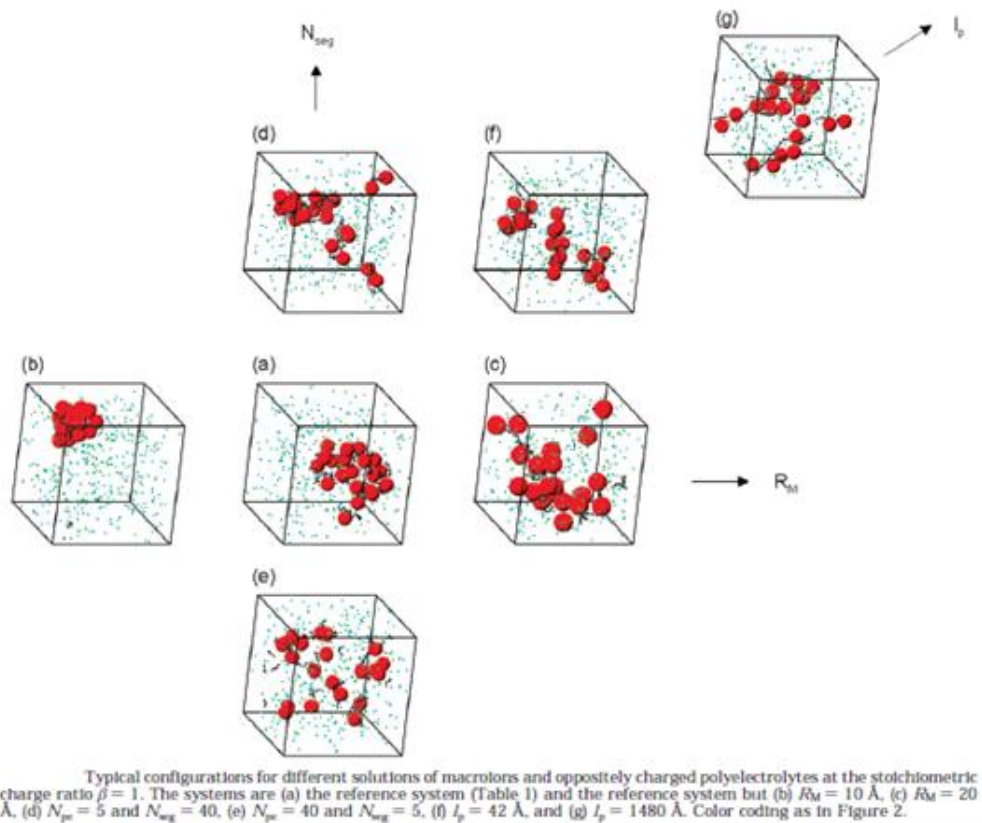


Figure I-4 : Résultats de Linse sur l'effet de la flexibilité, de la longueur des chaînes et de la taille des macroions sur la structure et la stabilité des complexes au rapport stoechiométrique de charges. Figure issue de la référence [81]

I.2.2.2 Effet de la force ionique^[86-89]

Quand deux macroions de charges opposées forment un complexe, leurs doubles couches de contre-ions partiellement condensés (ce concept est détaillé en Appendice du Chapitre III) sont détruites à un certain niveau, et les contre-ions positifs et négatifs sont libérés dans la solution comme lors de la dissolution d'un sel ordinaire. Cela implique des changements enthalpiques et entropiques du système. Ces deux contributions vont varier en fonction de la force ionique de la solution. Le changement en entropie est supposé être positif, puisque la libération des contre-ions qui sont initialement piégés sur une double couche est un terme dominant ici. A faible force ionique, cette contribution est importante puisque la concentration d'ions à l'intérieur du nuage d'écrantage est très importante. Avec l'augmentation de la concentration en excès de sel de la solution, ce gain d'entropie dû à la libération des contre-ions devient moins important.

Une autre contribution au changement de l'entropie est la perte de l'entropie conformationnelle et translationnelle des chaînes polyelectrolytes pendant la formation des complexes. Ce terme s'oppose à la formation des complexes, mais pour les chaînes longues,

il est plutôt petit devant le gain d'entropie des contre-ions libérés. En résumé, la complexation est favorable du point de vue entropique.

Du point de vue enthalpique, la formation des complexes peut être soit endothermique soit exothermique, tout dépend de la concentration en sel. A faible force ionique, la longueur de Debye est grande et les nuages des contre-ions des macroions s'étendent à grande distance de la surface ; les c.i. sont donc assez dilués. Après complexation et relargage de ces c.i., les charges présentes dans les complexes sont concentrés avec un couplage étroit entre les groupes de charges opposées. Par ce couplage, le système abaisse considérablement son énergie électrostatique, et la complexation est exothermique. A force ionique importante, en revanche, les nuages des contre-ions avant complexation sont compacts, et l'augmentation de l'énergie (entropie) due à la libération des ions ne peut pas être compensée par la diminution en énergie issue de la création des paires d'ions entre PE et macroion. Dans ce cas, la complexation est de nature endothermique.

Nous verrons qu'un autre effet de l'écrantage électrostatique est le contrôle de l'interaction entre complexes déjà formés, vers la construction d'assemblages plus grands, ou vers la séparation de phases. Cette situation n'a pas semblé être abordée dans la littérature que nous avons revue dans ce chapitre.

I.3 Vers notre choix des systèmes étudiés

Bien que les simulations soient avantageuses et qu'elles permettent de jouer librement sur les paramètres des composants, la limitation principale de ce genre d'études est le nombre limité de sphères et de chaînes qu'il est possible de prendre en compte du fait des capacités de calcul. Donc, il est très important de trouver les modèles expérimentaux afin de valider les théories. Dans cette thèse, nous avons essayé de jouer au maximum sur les paramètres en choisissant des systèmes modèles. Du côté des polyélectrolytes, quatre polyélectrolytes ont été choisis :

- deux polysaccharides, le chitosane et le hyaluronane qui sont des polyélectrolytes **semi-flexibles** caractérisés par une longueur de persistance intrinsèque de l'ordre de 5 à 9 nm (une détermination précise sera présentée dans les chapitres des résultats), le premier étant chargé positivement et le deuxième négativement.
- la polylysine (polycation) et le polystyrène sulfonate de sodium (polyanion) qui sont des polyélectrolytes **flexibles** caractérisés par une longueur de persistance similaire à la taille de leurs monomères.

Du côté des nanoparticules, notre choix s'est porté dans un premier temps sur les nanoparticules de silice commerciales de 10 nm de rayon qui peuvent être chargées

positivement ou négativement. Des nanoparticules d'or plus petites ont été synthétisées par la suite (Chapitre 4) afin d'étudier l'effet de la taille des nanoparticules sur les phénomènes de complexation. Les autres paramètres physiques, tels que la force ionique, la longueur des chaînes ou encore le rapport de concentration des deux espèces ont bien sûr été étudiés (Chapitres 3, 4 et 5). Parmi l'ensemble couvert par ces situations, très peu ont été étudiées systématiquement jusqu'à présent, tout particulièrement en ce qui concerne la structure précise des complexes par diffusion de rayonnement, ce qui justifie pleinement notre étude.

CHAPITRE II

METHODES EXPERIMENTALES
PHYSIQUES: DIFFUSION DU
RAYONNEMENT

II. Méthodes Expérimentales Physiques: Diffusion du Rayonnement

Dans ce Chapitre nous détaillerons le principe des mesures physiques essentiellement utilisées dans notre travail, qui impliquent la diffusion du rayonnement. Les méthodes chimiques de synthèse concernent seulement les particules d'Or, et le Chapitre IV leur sera consacré. Les autres particules sont utilisées telles qu'achetées. La purification des polymères concerne les polysaccharides ; déjà connue, et assez simple, elle sera résumée aux Chapitres correspondants, Chapitre III et V. Les diverses préparations des échantillons de complexes, assez directes (mélange), seront également décrites dans ces Chapitres.

La microscopie électronique sera très brièvement rappelée pour ce qui de la cryo-TEM en Appendice de ce Chapitre II.

Enfin les principes de la mesure du potentiel zeta et sa relation avec la charge de la particule sont rappelés en Appendice du Chapitre III.

La diffusion du rayonnement ^[90-93] est une technique qui permet d'obtenir des informations sur la structure de la matière. Il s'agit d'un cas spécifique d'interaction rayonnement-matière où les phénomènes d'absorption, d'émission avec changement de fréquence, ou d'un simple changement dans la direction de propagation sont réputés négligeables. Une expérience typique de diffusion de rayonnement consiste à envoyer un faisceau incident monochromatique sur l'échantillon à étudier et à analyser le rayonnement diffusé a priori dans toutes les directions, sans dissipation globale d'énergie et sans changement notable de fréquence. Il existe plusieurs types de rayonnement qui diffèrent avant tout par leur longueur d'onde incidente (de l'ordre du micron pour la lumière visible, du nanomètre ou de l'Angström pour les neutrons et les rayons X). On peut ainsi observer des échantillons à différentes échelles spatiales. Les rayonnements électromagnétiques (lumière, rayons X) sont diffusés par les électrons présents dans la solution alors que les neutrons sont diffusés par les noyaux des différents atomes qui constituent l'échantillon.

II.1 Le vecteur d'onde de transfert

Le mode d'interaction du rayonnement avec la matière dépend de la structure électronique ou nucléaire du matériau et de la nature du rayonnement utilisé. Dans une expérience de diffusion du rayonnement (Figure II-1), un faisceau incident monochromatique de vecteur d'onde incident \vec{k}_i traverse l'échantillon à étudier. Le rayonnement est diffusé par un

ensemble de diffuseurs ponctuels de manière isotrope, ces points matériels étant très petits devant la longueur d'onde incidente λ_i utilisée.

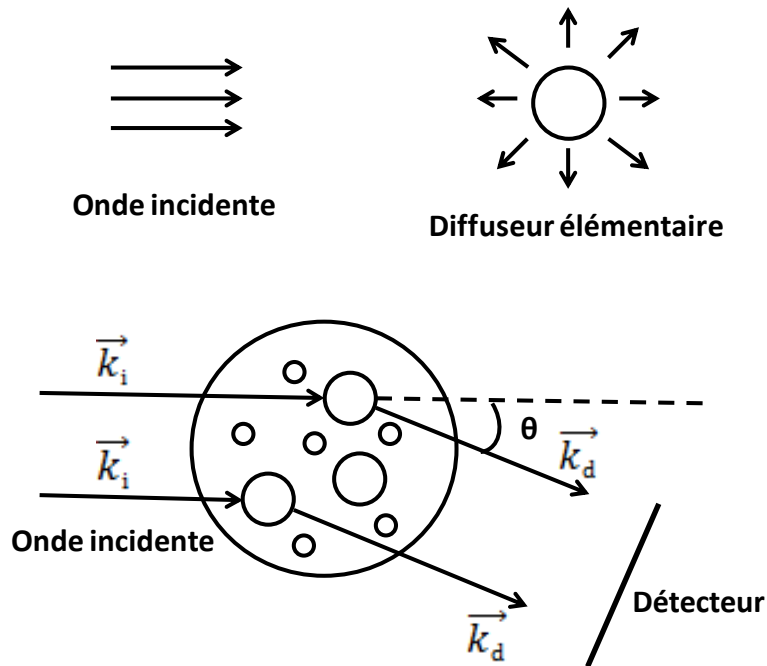


Figure II-1: Diffusion a) par un diffuseur ponctuel ou élémentaire ; b) par un ensemble de particules

Les modules des vecteurs d'onde incident \vec{k}_i et diffusé \vec{k}_d sont définis par les relations suivantes:

$$|\vec{k}_i| = \frac{2\pi n}{\lambda_i} \quad |\vec{k}_d| = \frac{2\pi n}{\lambda_d} \quad \text{II-1}$$

où λ_i et λ_d sont les longueurs d'onde incidente et diffusée dans le vide et n l'indice de réfraction du milieu (1,33 pour l'eau à 20°C).

Le vecteur d'onde de transfert \vec{q} est défini comme étant la différence des vecteurs incident et diffusé :

$$\vec{q} = \vec{k}_i - \vec{k}_d \quad \text{II-2}$$

Dans le cas d'une diffusion élastique (c'est-à-dire sans transfert d'énergie), les modules des vecteurs d'onde incidente et diffusé sont égaux :

$$\|\vec{k}_i\| = \|\vec{k}_d\| \quad \text{II-3}$$

L'inverse du module du vecteur d'onde, q^{-1} , représente l'échelle d'observation du système fixée par l'angle de diffusion θ et la longueur incidente λ_i . Dans le cas de la diffusion de la lumière, l'angle θ varie typiquement entre 15° et 150° . Ainsi, pour une longueur d'onde incidente fixée à 632.8 nm et un indice de réfraction égal à 1,34 (solution aqueuse), q^{-1} varie de 300 Å à 2300 Å. La diffusion de la lumière est donc une technique complémentaire de la diffusion des rayons X et des neutrons aux petits angles où q^{-1} varie typiquement entre 10 et 500 Å.

II.2 Facteur de forme $P(q)$ et facteur de structure $S(q)$

Dans le cas d'une solution de macromolécules, l'intensité peut s'exprimer en fonction du facteur de forme et du facteur de structure de la solution. Dans le cas de particules à symétrie sphérique, à la fois du point de vue " intra " pour le facteur de forme et du point de vue " inter " pour le facteur de structure, on peut écrire :

$$I(q) = A_0^2 f^2 \left\langle \sum_{i=1}^N \sum_{j=1}^N \exp i\vec{q}\vec{r}_{ij}(t) \sum_{k=1}^n \sum_{l=1}^n \exp i\vec{q}\vec{r}_{kl}(t) \right\rangle_T = A_0^2 f^2 NP(q)S(q) \quad \text{II-4}$$

$\langle \rangle_T$ représente une moyenne temporelle sur la durée de l'expérience T, A_0^2 une constante, $P(q)$ le facteur de forme de la macromolécule, $S(q)$ le facteur de structure de la solution, N le nombre de macromolécules (i, j) présentes dans la solution et n le nombre de diffuseurs élémentaires identiques (k, l) constituant une macromolécule c'est-à-dire le nombre de monomères (Figure II-2). Cette diffusion correspond au cas général de la diffusion élastique par un milieu de $N \times n$ diffuseurs et peut être reliée aux corrélations entre paires par l'intermédiaire des vecteurs $\vec{r}_{ij}(t) = \vec{r}_i(t) - \vec{r}_j(t)$ et $\vec{r}_{kl}(t) = \vec{r}_k(t) - \vec{r}_l(t)$. Pour des particules en solution, ces vecteurs sont fonctions du temps car les diffuseurs sont soumis au mouvement brownien. C'est pourquoi dans le cas des liquides pour lesquels la position des diffuseurs varie au cours du temps, l'intensité diffusée mesurée est moyennée sur un temps très grand T par rapport aux temps caractéristiques du système. Dans le cas d'un système ergodique, les diffuseurs explorent la totalité des configurations dans l'espace pendant la durée de l'expérience T. La moyenne temporelle sera ainsi égale à la moyenne spatiale.

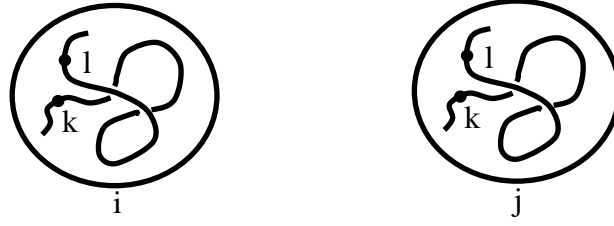


Figure II-2: Représentation des macromolécules (i, j) avec les diffuseurs élémentaire (k, l) (monomères)

Le facteur de Structure permet de caractériser l'état de dispersion des objets dans le milieu. Il peut décrire les attractions (états d'agrégation) et les répulsions, l'intensité des interactions, permettre une mesure du second coefficient du Viriel, de la compressibilité osmotique, etc. Il est par définition égal à 1 aux grands q , soit à l'échelle des objets individuels, puisqu'une organisation n'a de sens qu'à partir d'une échelle supérieure à la taille d'un objet.

Le facteur de structure normé de la solution $S(q)$ s'écrit pour $i \neq j$:

$$S(q) = \frac{1}{N} \sum_{i=1}^N \sum_{j=1}^N \exp i q \vec{r}_{ij}(t) \quad \text{II-5}$$

Il mesure les corrélations spatiales entre les N macromolécules i et j et donne ainsi des informations sur la structure de la solution.

Lorsque $i=j$, on définit le facteur de forme $P(q)$ de l'objet individuel de la manière suivante :

$$P(q) = \sum_{k=1}^n \sum_{l=1}^n \exp i q \vec{r}_{kl}(t) \quad \text{avec} \quad \vec{r}_{kl}(t) = \vec{r}_k(t) - \vec{r}_l(t) \quad \text{II-6}$$

Différents facteurs de forme typiques existent suivant le type d'objet considéré. Par exemple, pour les nanoparticules sphériques monodisperses, homogènes et pleines, de rayon R , le facteur de forme s'écrit :

$$P(q) = \left[\frac{3}{(qR)^3} \times (\sin(qR) - qR \cos(qR)) \right]^2 \quad \text{II-7}$$

Et pour les bâtons rigides de longueur L , (on fera souvent l'approximation suivante par la suite pour le rayon de giration: $R_G^2=L^2/12$), et le $P(q)$ s'écrit :

$$P(X) = \frac{2}{X} \int_0^X \frac{\sin(Z)}{Z} dZ - \left[\frac{2}{X} \sin \frac{X}{S} \right]^2 \quad \text{avec} \quad X = qL \quad \text{II-8}$$

II.3 La diffusion de la lumière

La diffusion de la lumière est une technique très utilisée pour étudier la dynamique et la structure des solutions macromoléculaires et colloïdales.

Deux types d'expériences seront abordés : la diffusion quasi-élastique ou dynamique de la lumière et la diffusion élastique ou statique de la lumière

II.3.1 La diffusion statique de la lumière

La diffusion élastique ou statique de la lumière qui, par mesure de l'intensité diffusée, permet d'accéder aux facteurs de structure et de forme de la solution et donc à la masse, la forme, la taille des particules et aux coefficients du Viriel qui renseignent sur les interactions intermoléculaires. On remonte ainsi aux propriétés d'équilibre et de structure de la solution.

II.3.1.1 L'intensité diffusée

Le champ électrique diffusé par un ensemble de N diffuseurs i s'écrit :

$$\vec{E}_d(q,t) = \sum_{i=1}^N a_i \exp(i\vec{q}\vec{r}_i(t)) \exp(-i\omega t) \quad \text{II-9}$$

avec N le nombre de diffuseurs, a_i l'amplitude du champ électrique diffusé par le $i^{\text{ème}}$ diffuseur et $\vec{r}_i(t)$ sa position à l'instant t . En diffusion de la lumière, a_i est fonction de la polarisabilité de la molécule.

Pour les solutions, les molécules étant soumises au mouvement brownien, l'intensité diffusée fluctue au cours du temps. L'intensité diffusée pendant la durée de l'expérience T est moyennée dans le temps et est donnée par la relation suivante :

$$\begin{aligned} I(q) &= \langle I(q,t) \rangle_T = \left\langle \left| E_d(q,t) \right|^2 \right\rangle_T = \left\langle E_d^*(q,t) E_d(q,t) \right\rangle_T \\ &= \left\langle \sum_{i=1}^N a_i \exp(i\vec{q}\vec{r}_i(t)) \sum_{j=1}^N a_j \exp(i\vec{q}\vec{r}_j(t)) \right\rangle_T \end{aligned} \quad \text{II-10}$$

Pour un système ergodique, les diffuseurs explorent la totalité des configurations dans l'espace de phase pendant la durée de l'expérience T . Il est alors possible de remplacer la moyenne d'ensemble par une moyenne temporelle. Le détecteur mesure une moyenne temporelle sur la durée de l'expérience T , d'où : $\langle \rangle_{\text{espace}} = \langle \rangle_{\text{temporelle}} = \text{moyenne}$

On a ainsi :

$$I(q) = \sum_{i,j=1}^N a_i^2 + \left\langle \sum_{i \neq j}^N a_i a_j \exp i\vec{q} \cdot \vec{r}_{ij}(t) \right\rangle \quad \text{avec} \quad \vec{r}_{ij}(t) = \vec{r}_i(t) - \vec{r}_j(t) \quad \text{II-11}$$

II.3.1.2 Facteur de Rayleigh

Lors d'une expérience de diffusion statique (ou élastique) de la lumière, on mesure l'intensité diffusée de la lumière. Elle permet de remonter aux propriétés d'équilibre et de structure de la solution telles que la masse des particules, leur forme, leur taille, les interactions entre les molécules... Pour cela, l'intensité diffusée de la lumière est généralement exprimée en terme de facteur de Rayleigh R (cm^{-1}), c'est-à-dire en unité absolue :

$$I(\text{cm}^{-1}) = KCM_w P(q)S(q) \quad \text{avec} \quad K = 4\pi^2 n^2 \left(\frac{dn}{dc}\right)^2 / N_A \lambda^4 \quad \text{II-12}$$

où M_w représente la masse molaire moyenne en poids des molécules, N_A le nombre d'Avogadro, C la concentration massique en particules en g/cm^3 , n l'indice de réfraction du milieu, dn/dc l'accroissement de l'indice de réfraction avec la concentration en particules et K la constante de diffusion. Expérimentalement, on obtient la mesure du facteur de Rayleigh de façon indirecte, en comparant l'intensité diffusée par l'échantillon, I , à celle diffusée par un liquide de référence (le toluène dans notre cas), I_{ref} , mesurée dans les mêmes conditions expérimentales, pour lequel le facteur de Rayleigh est connu ($40 \times 10^{-6} \text{cm}^{-1}$ à $\lambda = 623.8 \text{nm}$ pour le toluène). $R(q)$ est ainsi obtenu de la manière suivante :

$$R(\text{cm}^{-1})(q) = \frac{I_{solution} - I_{solvant}}{I_{ref}} \times \left(\frac{n_{solvant}}{n_{ref}} \right)^2 \times R_{ref}(\text{cm}^{-1}) \quad \text{II-13}$$

Notre liquide de référence étant le toluène, à la longueur d'onde utilisée dans nos expériences, le rapport $I_{eau}/I_{toluène}$ est égal à 0,115. On peut donc évaluer l'intensité diffusée normée par les particules ainsi que le facteur de Rayleigh. Dans le Tableau II-1, nous avons récapitulé les valeurs de la constante de diffusion et de l'accroissement de l'indice de réfraction avec la concentration en particules pour les différents systèmes étudiés dans cette thèse. Les indices de réfraction ont été mesurés à différentes concentrations en particules à l'aide d'un réfractomètre Mettler Toledo (« Portable Lab »)

Soluté	Solvant	dn/dc (cm^3/g)
Chitosane	CH_3COOH 0,3 M / CH_3COONa 0,2M	0.195
Poly-L-lysine	KBr 0.2M	0.165
SiNP Ludox AM30	CH_3COOH 0,3 M / CH_3COONa 0,2M	0.0658
SiNP Ludox CL	NaCl 0,1M	0.064
Hyaluronan	NaCl 0,1M	0.14

Tableau II-1: Valeurs de la constante de diffusion et de l'accroissement de l'indice de réfraction avec la concentration en particules, dn/dc , pour les différents systèmes étudiés dans cette thèse

II.3.1.3 Paramètres moléculaires et thermodynamiques obtenus par diffusion élastique de la lumière

La grandeur caractéristique première des particules est leur masse. Pour l'obtenir, il est nécessaire d'extrapoler les résultats expérimentaux à concentration nulle ($S(q)=1$) et à angle nul ($P(q)=1$). Dans le régime de Guinier défini pour $qR_G \ll 1$, le facteur de forme $P(q)$ se met sous la forme suivante :

$$P(q)_{q \rightarrow 0} \approx 1 - \frac{q^2}{3} \langle R_G^2 \rangle \quad \text{II-14}$$

où R_G est le rayon de giration des particules défini de la manière suivante :

$$\langle R_G^2 \rangle = \frac{1}{n^2} \sum_k^n r_k^2 \quad \text{II-15}$$

avec n le nombre de diffuseurs élémentaires k appartenant à la molécule (k monomères composant une macromolécule par exemple).

Pour obtenir la masse molaire moyenne en masse M_w des particules, on mesure l'intensité diffusée à différents angles pour chaque concentration et on extrapole à la fois à concentration nulle et à angle nul. On utilise habituellement le diagramme de Zimm (Figure II-3) qui permet de représenter sur le même graphique le produit $KC/R(q)$ en fonction de q^2 pour chaque concentration. Cette méthode, valable en régime dilué et dans le cas où les macromolécules sont caractérisées par une taille inférieure à 200 nm, permet d'obtenir simultanément la masse, le rayon de giration R_G , et le second coefficient du Viriel A_2 .

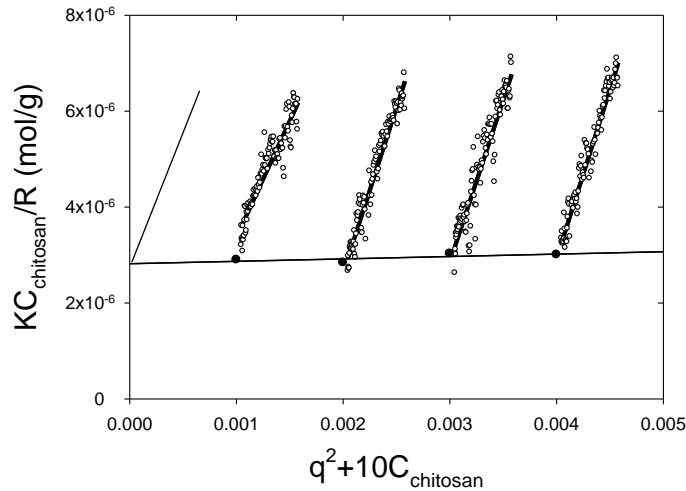


Figure II-3: Diagramme de Zimm obtenu pour des solutions de chitosane à $C=0.1, 0.2, 0.3,$ et 0.4 g/l en présence de 0.3 M CH_3COOH et de 0.2 M CH_3COONa à $T=20^\circ\text{C}$

La courbe obtenue par extrapolation à angle nul ($q^2 \rightarrow 0$) représente $\gg 1/M_w \cdot S(0)$ en fonction de C . L'ordonnée à l'origine de cette courbe donne $1/M_w$ et donc M_w . Les valeurs de $KC/R(q)$ divisées par l'ordonnée à l'origine donnent $S(0)^{-1}$, c'est-à-dire $(\partial C/\partial \Pi)^{-1}/kT$, l'inverse de la compressibilité osmotique (Π étant la pression osmotique). Pour des solutions diluées où C est suffisamment faible, on peut faire un développement limité en fonction de C , dit du Viriel de $S(0)^{-1}$:

$$S(0)_{c \rightarrow 0}^{-1} \approx 1 + 2A_2C + \dots \quad \text{II-16}$$

où A_2 est le second coefficient du viriel qui traduit les interactions entre les macromolécules (Figure II-3). Ce coefficient est positif pour des interactions répulsives entre molécules et négatif pour des interactions attractives. Lorsque A_2 est nul, on est en solvant dit Θ , ces interactions sont donc nulles. Ceci est valable entre segments à l'échelle submacromoléculaire, et on a une chaîne idéale sans interaction c'est-à-dire gaussienne.

Pour une concentration C tendant vers zéro ($S(q)=1$), la courbe $KC/R(q)$ en fonction de q^2 représente $1/M_w P(q)$. L'ordonnée à l'origine ($q=0$) vaut $1/M_w P(0)$, tandis que la pente vaut $\langle R_G^2 \rangle / 3$ (Figure II-3). En effet, pour C tendant vers zéro (régime dilué) et pour q^{-1} très grand par rapport à la taille des particules ($q \rightarrow 0$) nous avons :

$$\frac{C}{I(q)} = \frac{C}{I(0)} \left(1 + \frac{q^2 R_G^2}{3} \right) \quad \text{Avec } qR_G \ll 1 \quad \text{II-17}$$

II.3.2 La diffusion dynamique de la lumière

La diffusion dynamique de la lumière permet d'étudier les propriétés dynamiques et viscoélastiques des solutions et des gels. A partir de la mesure des temps de relaxation coopératifs on peut déterminer, par exemple, les coefficients de diffusion du système. En solution, les diffuseurs sont soumis au mouvement brownien et leur position dépend du temps. De ce fait, on a un déplacement en fréquence $\Delta\omega$ par rapport à la pulsation initiale ω_i de la lumière incidente. Le rapport $\Delta\omega/\omega_i$ est très faible, de l'ordre de 10^{-12} , et centré sur zero. On parlera donc de diffusion quasi-élastique de la lumière.

II.3.2.1 Le mouvement brownien et les fonctions d'autocorrélation temporelles

Si l'on enregistre en fonction du temps l'intensité diffusée par un système physique constitué de particules browniennes dans un milieu continu (solvant), l'intensité mesurée $I(t)$ représente la somme des intensités diffusées par le solvant et les particules browniennes.

$$I(t)_{\text{solution}} = I(t)_{\text{particules}} + I(t)_{\text{solvant}} \quad \text{II-18}$$

Les fluctuations de $I(t)$ autour de sa valeur moyenne $\langle I \rangle$ sont dues à la marche au hasard des particules browniennes dans le volume diffusant défini par la géométrie expérimentale. Une illustration de la variation de $I(t)$ est donnée sur la Figure II-4.

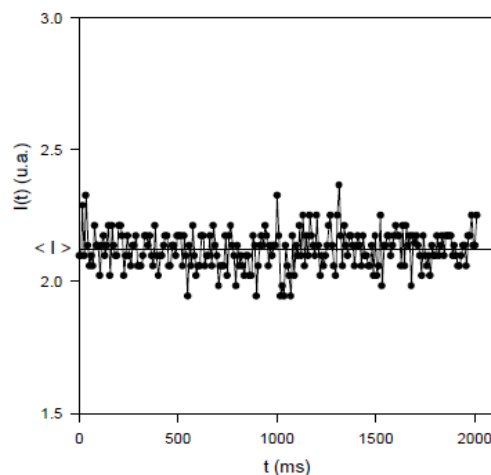


Figure II-4: Fluctuations de l'intensité diffusée au cours du temps autour de sa valeur moyenne $\langle I \rangle$

Une méthode classique pour extraire des informations d'une grandeur fluctuante $f(t)$ consiste à calculer sa fonction d'autocorrélation temporelle $G(t) = \langle f(0) f(t) \rangle$ qui exprime le degré de corrélation entre deux temps voisins séparés de t ou le degré de mémoire d'un événement survenu t plus tôt. $G(t)$ est en général une fonction qui décroît lorsque t augmente. Après un

temps suffisamment long, la corrélation avec l'instant zéro est devenue inexistante, ce phénomène est la conséquence du mouvement brownien et $G(\infty) = \langle f^2 \rangle$. Si le temps est très court, la fonction f à l'instant t est similaire à celle de l'instant zéro et $G(0) = \langle f^2 \rangle$.

II.3.2.2 Fonction d'autocorrélation temporelle du champ électrique diffusé

La première de ces fonctions est la fonction d'autocorrélation de l'amplitude de l'onde diffusée ou du champ électrique diffusé, $G_1(t) = \langle E(0) E(t) \rangle$. At = 0, $G_1(0)$ n'est autre que l'intensité de la lumière diffusée (à un facteur de normalisation près). $G_1(t)$ est proportionnelle au facteur de structure dynamique $S(q, t)$ défini par :

$$S(q, t) = \frac{1}{N} \left\langle \sum_{i,j=1}^N \exp \left[i q (\vec{r}_i(0) - \vec{r}_j(t)) \right] \right\rangle \quad \text{II-19}$$

Nous avons donc $S(q, 0) = S(q)$ et $S(q, \infty) = 0$. $S(q, t)$ est la transformée de Fourier spatiale de la fonction $g(r, t)$, probabilité de trouver une particule en r à l'instant t sachant qu'une particule (éventuellement la même) se trouvait à l'origine à l'instant initial.

Cependant, dans une expérience de diffusion de la lumière on ne détecte pas directement le champ électrique diffusé, mais l'intensité de la lumière diffusée par la solution. On mesure donc ainsi la fonction d'autocorrélation temporelle normée de l'intensité diffusée, notée :

$$g^{(2)}(q, t) = \frac{\langle I(q, 0) I(q, t) \rangle}{\langle I(q, 0) \rangle^2} \quad \text{II-20}$$

Le symbole $\langle \rangle$ représente une moyenne temporelle. Pour un système ergodique, les diffuseurs explorent la totalité des configurations dans l'espace de phase pendant la durée de l'expérience. Il est alors possible de remplacer la moyenne d'ensemble par une moyenne temporelle. Pour la variable I , nous avons $\langle I^2 \rangle = 2 \langle I \rangle^2$.

Si le champ électrique obéit à une distribution gaussienne, on peut relier par la relation de Siegert les fonctions d'autocorrélations temporelles normées du champ électrique diffusé, $g^{(1)}(q, t)$, et de l'intensité diffusée, $g^{(2)}(q, t)$:

$$g^{(2)}(q, t) = 1 + |g^{(1)}(q, t)|^2 \quad \text{II-21}$$

Expérimentalement, on mesure une fonction d'autocorrélation qui tient compte du facteur de cohérence entre les ondes diffusées détectées et du rapport signal sur bruit:

$$g^{(2)}(q,t) = A + \beta |g^{(1)}(q,t)|^2 \quad \text{II-22}$$

où β représente le facteur de cohérence et A l'asymptote ces deux facteurs dépendent de la géométrie de l'expérience) et où :

$$g^{(1)}(q,t) = \frac{\langle E_d^*(q,0)E_d(q,t) \rangle}{\langle |E_d(q,0)|^2 \rangle} \quad \text{II-23}$$

Est la fonction d'autocorrélation temporelle normée du champ électrique diffusé. Elle est également la fonction d'autocorrélation temporelle normée des fluctuations de concentrations, le facteur de structure dynamique $S(q, t)$ étant lié aux fluctuations de concentrations.

$$g^{(1)}(q,t) = \frac{\langle \delta C(q,0)\delta C(q,t) \rangle}{\langle \delta C(q,0)^2 \rangle} \quad \text{II-24}$$

a) Analyse des fonctions d'autocorrélation Méthode d'analyse " Contin "

Une méthode classique pour déterminer les différents temps de relaxation est la méthode " Contin " développée par Provencher^[94, 95], basée sur la transformée de Laplace de $g^{(1)}(q,t)$. Si le profil du spectre de diffusion de la lumière est décrit par une multi-Lorentzienne, alors $g^{(1)}(q,t)$ peut se mettre sous la forme :

$$g^{(1)}(q,t) = \int_0^{\infty} G(\Gamma) \exp -[\Gamma t] d\Gamma \quad \text{II-25}$$

$G(\Gamma)$ représente la distribution des constantes de décroissance normalisées et $\Gamma=1/\tau$ l'amplitude de décroissance.

Cependant, comme de nombreuses méthodes, la méthode " Contin " a ses limites, et il faut prendre des précautions lorsqu'on l'utilise. On rencontre ainsi plusieurs situations:

a) Solution idéale polydispersée (plusieurs populations monodisperses)

Cette méthode est très bien appropriée dans le cas où l'on a plusieurs types de particules de tailles très différentes. La fonction $g^{(1)}(q,t)$ sera donc une somme discrète ou continue d'exponentielles. Le traitement est relativement aisé pour des mélanges de particules bien distinctes (pics bien définis dans la distribution). Dans le cas contraire cette méthode peut donner lieu à des difficultés (recouvrement de pics, épaulements...).

b) Exponentielles étirées

De même, dans le cas où l'une des exponentielles est une exponentielle étirée, le pic de distribution obtenu par cette méthode ne sera pas symétrique. Il faudra donc analyser la fonction avec une autre méthode.

c) Solution composée d'une population polydisperse

La dernière limite est le cas où la solution contient une seule population très polydisperse. Dans ce cas, le pic de distribution obtenu sera très large et l'interprétation sera plus complexe, voire très difficile.

II.3.2.2.1 Méthode d'analyse des cumulants

Une autre méthode, couramment utilisée lorsqu'un seul temps de relaxation caractéristique est présent, consiste à traiter l'écart à une mono-exponentielle en termes de cumulants.^[96] On développe le logarithme de la fonction d'autocorrélation en puissance de t et en s'arrêtant généralement au terme quadratique.

$$\ln g^{(1)}(t)_{t \rightarrow 0} \approx k_0 - k_1 t + k_2 \frac{t^2}{2} + \dots \quad \text{II-26}$$

Les coefficients k_n sont appelés cumulants. Pour une solution idéale monodispersée, le développement s'arrête au terme linéaire et $k_1 = \Gamma$. Pour une solution polydisperse, le premier cumulant $k_1 = \langle \Gamma \rangle$ donne la valeur moyenne tandis que le deuxième cumulant $k_2 = \langle \Gamma^2 \rangle - \langle \Gamma \rangle^2$ donne l'écart type de la distribution $G(\Gamma)$. Le degré de polydispersité est donné par le rapport k_2/k_1^2 .

II.3.2.3 Analyse des temps caractéristiques des modes de relaxation et des amplitudes correspondantes

Lors de nos expériences, nous avons étudié différents systèmes physiques. Plusieurs analyses ont été nécessaires pour extraire les temps de relaxation caractéristiques du système et les amplitudes correspondantes. Les différents cas que nous avons rencontrés et les méthodes d'analyse que nous avons utilisées sont décrits dans les paragraphes qui suivent.

a) Simple mono-exponentielle : solution idéale monodispersée

Une illustration typique d'une fonction d'autocorrélation temporelle des fluctuations de concentration $g^{(1)}(q,t)$ caractérisée par une simple exponentielle est représentée en échelle logarithmique sur la Figure II-5. Cette fonction a été obtenue à partir d'une solution diluée de nanoparticules de silice. Nous observons clairement pour cette concentration diluée une

relaxation unique. La fenêtre montre la fonction de distribution temporelle $A(t)$ des relaxations obtenue à partir de la méthode d'analyse "Contin". Cette méthode montre que le pic correspondant à la relaxation est symétrique et qu'il caractérise donc un simple processus de relaxation exponentielle. L'ajustement de la fonction d'autocorrélation avec l'expression d'une simple exponentielle est représenté sur la Figure II-5. Dans ce cas, nous avons également utilisé la méthode classique des cumulants, et des résultats similaires ont été obtenus. La méthode des cumulants a donc été utilisée par commodité dans notre travail pour analyser les solutions diluées des nanoparticules ou de polymères caractérisées par un facteur de structure dynamique monoexponentiel.

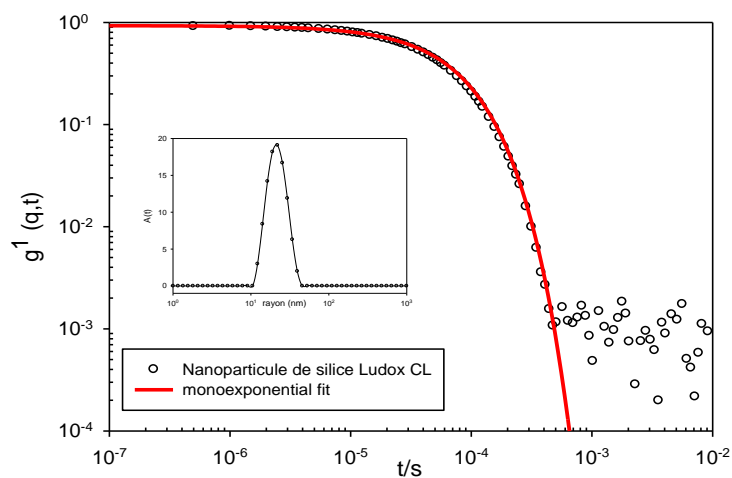


Figure II-5: Représentation en coordonnées logarithmiques de $g^1(q,t)$ pour une solution diluée de nanoparticules de silice Ludox CL à la concentration de $1 \times 10^{-4} \text{M}$ et à $\theta=90^\circ$. La ligne rouge représente l'ajustement de $g^1(q,t)$ obtenu en utilisant l'équation II-26. Dans la fenêtre est représenté le pic (symétrique) obtenu par la méthode "Contin"

De plus, l'analyse de $g^{(1)}(q,t)$ nous a permis de conclure que ce mode unique exponentiel est un mode coopératif avec un temps caractéristique τ proportionnel à q^{-2} . Dans ce cas, le facteur de structure dynamique est défini de la manière suivante :

$$g^{(1)}(q,t) = A \exp(-Dq^2t) \quad \text{II-27}$$

Il est ainsi possible de déterminer le coefficient de diffusion apparent égal à $D=1/\tau q^2$ (loi de Fick) lorsque $q^2=0$ à une concentration donnée en polymère ou en nanoparticules. L'équation d'Einstein relie le coefficient D au facteur de frottement hydrodynamique ζ_0 de la particule : $D=kT/\zeta_0$ (k étant la constante de Boltzmann et T la température absolue). Pour une sphère, Stokes a montré que $\zeta_0=6\pi\eta_s R_H$ où η_s représente la viscosité du solvant et R_H le rayon hydrodynamique de la particule. On obtient ainsi la formule de Stokes-Einstein.

$$D = \frac{kT}{6\pi\eta_s R_H} \quad \text{II-28}$$

Le coefficient de diffusion apparent, D , que l'on mesure à concentration fixe s'exprime à l'aide des coefficients d'interaction et du coefficient de diffusion réel obtenu à concentration nulle, D_0 :

$$D(\Phi) = D_0(1 + K_D\Phi + \alpha\Phi^2) \quad \text{II-29}$$

L'expression ci-dessus représente le développement de Viriel de D en fonction de la fraction volumique Φ . K_D est le deuxième coefficient du Viriel dynamique (il est relié au deuxième coefficient du Viriel statique par l'intermédiaire d'un terme hydrodynamique) et α le troisième coefficient du Viriel. Pour une suspension de sphères dures dans laquelle les interactions sont seulement dues aux effets de volume exclu, $K_D = 1,56$; les interactions sont légèrement répulsives.

Le coefficient de diffusion réel D_0 est donc obtenu par extrapolation à angle nul et à concentration nulle. C'est à partir de ce dernier que l'on peut calculer le rayon hydrodynamique réel des nanoparticules et des chaînes en régime dilué.

II.3.2.3.1 Facteur de structure dynamique bimodal

Dans certains cas, le facteur de structure dynamique $g^{(1)}(q,t)$ est bimodal, c'est-à-dire qu'il est caractérisé par la somme de deux relaxations séparées distinctement dans le temps et qu'il peut être exprimé de la manière suivante :

$$g^{(1)}(q,t) = A_{fast}(q) \exp\left(\frac{-t}{\tau_{fast}}\right) + A_{slow}(q) \exp\left(\frac{-t}{\tau_{slow}}\right) \quad \text{II-30}$$

avec $A_{fast}(q) + A_{slow}(q) = 1$. $\tau_{fast}(q)$ et $\tau_{slow}(q)$ représentent respectivement les temps caractéristiques associés à la relaxation rapide et lente. A_{fast} et A_{slow} sont les amplitudes correspondantes.

La Figure II-6 représente un facteur de structure dynamique typique obtenu pour une solution semi-diluée de hyaluronane de faible masse (45K). Sur cette figure, on peut observer que l'ajustement de $g^{(1)}(q,t)$ obtenu avec l'équation (II-30) est très satisfaisant (ligne rouge continue). De plus, les deux relaxations étant très bien séparées dans le temps (au moins une décade), la méthode " Contin " est également très satisfaisante car elle permet d'obtenir deux pics de relaxation très fins et très bien séparés. De plus, ces deux relaxations étant

exponentielles, les deux pics obtenus sont symétriques. Les résultats obtenus avec la méthode " Contin " sont également illustrés sur la Figure II-6. Par commodité, la méthode " Contin " sera ainsi utilisée pour les solutions semi-diluées de hyaluronan de faibles masses. De plus, les relaxations lente et rapide sont d'origine diffusive avec des temps de relaxation proportionnels à q^{-2} .

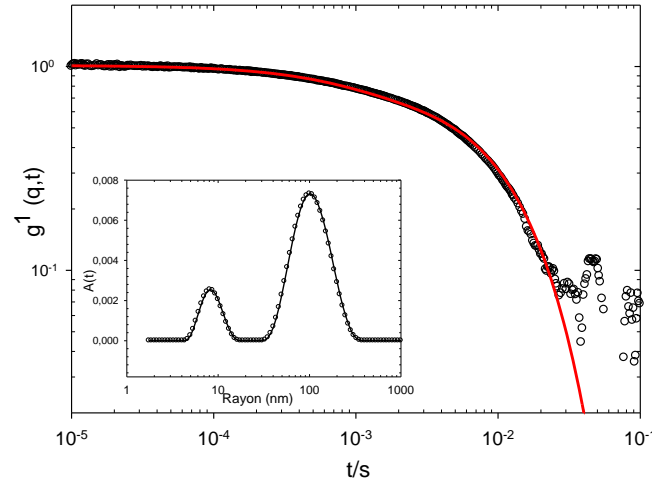


Figure II-6: Représentation du facteur de structure dynamique $g^1(q,t)$ en échelle logarithmique obtenu sur une solution semi-diluée de hyaluronan de masse 45K à une concentration de $2.5 \times 10^{-4} \text{ g/cm}^3$ et pour un angle de diffusion $\theta=90^\circ$. La ligne continue rouge représente l'ajustement de $g^1(q,t)$ obtenu en utilisant l'équation II-30. Les pics obtenus à partir de la méthode " Contin " sont présentés dans la fenêtre

II.4 La diffusion des neutrons aux petits angles (DNPA ou SANS)

Le neutron est à la fois une onde et une particule ce qui fait de lui un puissant outil d'investigation. Il possède une longueur d'onde qui suit la relation suivante :

$$\lambda = \frac{h}{mv} \quad \text{II-31}$$

Où h est la constante de Planck, m la masse du neutron égale à $1,675 \times 10^{-27} \text{ kg}$ et v sa vitesse. Mais étant également une particule, son énergie correspond à son énergie cinétique et est donnée par la relation :

$$E = \frac{1}{2}mv^2 = \frac{1}{2} \frac{h^2}{m\lambda^2} \quad \text{II-32}$$

Lorsque les neutrons proviennent d'un réacteur, ils sont généralement produits par une source froide dont la longueur d'onde se situe typiquement entre 3 et 25 Å ce qui correspond à une fenêtre d'énergie comprise située entre 10^{-1} et 10 MeV.

II.4.1 L'interaction neutron-matière

Considérons un faisceau de neutrons monochromatique comme une onde plane. Sa propagation peut s'écrire :

$$\psi = \psi_0 \exp\left[i(\vec{k}\vec{z} - \omega t)\right] \quad \text{II-33}$$

Après interaction avec l'échantillon, celui-ci émet une onde diffusée sphérique.

$$\psi = \frac{\psi_0}{R} \exp\left[i(\vec{k}R - \omega t)\right] \quad \text{II-34}$$

où ψ_0 est l'amplitude de l'onde, caractérise l'énergie véhiculée par le rayonnement, \vec{k} , vecteur d'onde, la direction le long de laquelle le rayonnement se propage, ainsi que la fréquence de l'oscillation spatiale et enfin ω , pulsation, la fréquence de l'oscillation temporelle. R représente la distance entre la singularité ponctuelle et le point d'observation localisé en z , c'est-à-dire $R = \|\vec{z}\|$.

Afin de caractériser la diffusion, on considère une section efficace de diffusion. Ce paramètre est obtenu lorsque l'échantillon reçoit un flux de neutrons $\Phi(\lambda)$ en $\text{cm}^{-2}\text{s}^{-1}$ et qu'il diffuse un nombre de neutrons $I(\Theta)$ en s^{-1} sur une surface S située à une distance r (soit dans un angle solide $\Delta\Omega = S/r^2$). Soit, en vecteur d'onde q :

$$I(q) = \Phi(\lambda) \frac{d\sigma(\theta)}{d\Omega} \Delta\Omega \quad \text{II-35}$$

Cette section efficace est homogène à une surface. Elle est exprimée en barns et est indépendante de la longueur d'onde. Elle est divisée par le volume de l'échantillon et devient donc homogène à des cm^{-1} et peut se réécrire de la manière suivante :

$$\frac{1}{V} \frac{d\sigma}{d\Omega} = \langle A(q)A(-q) \rangle = \sum_{i,j} \langle \rho_i \rho_j \rangle \langle e^{i\vec{q}(\vec{r}_i - \vec{r}_j)} \rangle \quad \text{II-36}$$

où l'amplitude de diffusion $A(q) = \int \rho(r) e^{i\vec{q}\vec{r}} d\vec{r}$ est la transformée de Fourier de la densité de longueur de diffusion $\rho(r) = \frac{1}{V} \sum_i^n b_i \delta(\vec{r} - \vec{r}_i)$, le volume V contenant n noyaux de longueur de diffusion b_i . Les $\langle \rangle$ indiquant une moyenne sur l'ensemble de l'échantillon. On peut finalement écrire :

$$\frac{d\sigma}{d\Omega} = nb_{inc}^2 + b^2 \sum_{i,j}^N \left\langle e^{iq(\vec{r}_i - \vec{r}_j)} \right\rangle \quad \text{avec} \quad b_{inc}^2 = \langle b_i^2 \rangle - \langle b_i \rangle^2 \quad \text{et} \quad b = b_{inco} = \langle b_i \rangle \quad \text{II-37}$$

L'intensité totale diffusée est la somme de deux termes : Le premier terme est le terme de diffusion incohérente lié à l'écart quadratique moyen des longueurs de diffusion b_{inc}^2 et le second le terme de diffusion cohérente qui représente les corrélations spatiales collectives entre les objets diffusants. Le terme incohérent représente les dynamiques individuelles de chaque diffuseur non corrélé avec un autre. Le terme incohérent est dû à des fluctuations de b_i qui sont elles-mêmes dues à deux phénomènes : Le premier correspond au désordre isotopique qui vient du fait que chaque isotope possède sa propre longueur de diffusion b et qui implique donc l'existence d'une moyenne pour un élément donnée. Le second est le spin nucléaire dont la répartition est aléatoire si l'échantillon et le faisceau incident ne sont pas polarisés (ce qui est le cas dans nos expériences de DNPA).

Les mesures de diffusion cohérente sans changement de vitesse du neutron (élastique) servent à déterminer les structures au sein d'un système, la diffusion incohérente élastique est indépendante de q , et est considérée comme un bruit de fond constant, qui sera ensuite retiré du signal total pour obtenir uniquement la diffusion cohérente. Les mesures de diffusion incohérente peuvent servir à déterminer la dynamique au sein d'un système d'un diffuseur donné, tandis que la diffusion cohérente inélastique détermine la dynamique des corrélations entre deux diffuseurs. Nous ne nous intéresserons ici au cas élastique.

II.4.2 Le contraste

Lors d'une expérience de DNPA, l'intensité totale de l'échantillon (en cm^{-1}) correspond au produit du carré du contraste, $\Delta\rho^2$ (en cm^{-4}), du volume de l'objet, V , (« volume « sec »), de la fraction volumique en monomères, ϕ , du facteur de forme, $P(q)$, et enfin du facteur de structure $S(q)$:

$$I = \Delta\rho^2 V \Phi P(q) S(q) \quad \text{II-38}$$

où le contraste se définit par une différence de densité de longueur de diffusion ρ par unité de volume, qui se calcule à partir du volume molaire, V_m , et de la somme des longueurs de diffusion cohérentes des atomes constituant le monomère ou la nanoparticule :

$$\rho = \frac{\sum_i^N b_i N_A}{V_m} \quad \text{II-39}$$

où b_i représente la longueur de diffusion cohérente de l'élément i , et N_A le nombre d'Avogadro.

Le contraste, qui intervient au carré dans l'intensité diffusée, s'écrit :

$$\Delta\rho^2 = (\rho_1 - \rho_2)^2 \quad \text{II-40}$$

où ρ_1 est la densité de longueur de diffusion de l'objet et ρ_2 celle du milieu.

Les valeurs de ρ s'expriment généralement en 10^{-10} cm^{-2} . Nos mesures étant toutes faites en milieu aqueux, nous donnerons ici les valeurs de ρ pour l'eau. L'eau (H_2O) possède une ρ de $-0.56 \times 10^{-10} \text{ cm}^{-2}$ et l'eau lourde (D_2O) $6.63 \times 10^{-10} \text{ cm}^{-2}$. La grande différence entre ces deux valeurs est due aux atomes d'hydrogène qui suivant leur état isotopique (^1H ou ^2H) possèdent une ρ négative ou positive. Ceci est lié au fait que l'interaction neutron-matière peut être attractive ou négative, contrairement à l'interaction RX-matière. Pour un système étudié en solution aqueuse, il sera judicieux de se placer dans un solvant dont la ρ la plus éloignée possible de celle de l'objet sondé afin de maximiser le contraste et donc le signal total mesuré.

Nous avons collecté dans le tableau suivant les valeurs des densités de longueur de diffusion des différents composants étudiés dans ce travail.

Composant	Formule	densité SANS ($\times 10^{10} \text{ cm}^{-2}$)
Eau	H_2O	0,56
Hyaluronane	$\text{C}_{14}\text{H}_{21}\text{NO}_{11}$	2,37
Chitosane	$\text{C}_6\text{H}_{11}\text{NO}_4$	2,45
chitosan80%+chitin20%		2,47
Chitin	$\text{C}_8\text{H}_{13}\text{NO}_5$	2,56
Nanoparticule de silice	SiO_2	3,48
Chitin/xD2O	$\text{C}_8\text{H}_{(13-3x)}\text{NO}_5\text{D}_{3x}$	4,36
chitosan80%+chitin20%/xD2O		5,32
Chitosane/xD2O	$\text{C}_6\text{H}_{(11-4x)}\text{NO}_4\text{D}_{4x}$	5,56
Alumine	Al_2O_3	5,69
Eau lourde	D_2O	6,32
Poly-L-lysine	$\text{C}_6\text{H}_{12}\text{N}_2\text{O}$	1,06
Nanoparticule d'or	Au	4,50
Ligand TMA	$\text{C}_{14}\text{H}_{32}\text{NS}$	-0,23
Polystyrene sulfonate de sodium	$\text{C}_8\text{H}_7\text{SO}_3\text{Na}$	2,55
PSSNa deutéré	$\text{C}_8\text{D}_7\text{SO}_3\text{Na}$	6,24

Tableau II-2: Liste des densités de longueurs de diffusion neutroniques par unité de volume des différents composants étudiés

II.4.3 La méthode de « matching »

Le signal mesuré est directement lié au contraste neutronique entre l'objet soluté et le solvant. Dans le cas d'un mélange de deux composants dans un solvant, il y aura trois valeurs de contrastes différentes, donnant un signal contenant les contributions des deux objets par rapport au solvant et entre eux. Il est possible de réaliser une adaptation de contraste par un simple marquage isotopique. La condition nécessaire pour réaliser ce type d'expérience est que les valeurs des densités de longueur de diffusion des deux composants se situent entre celle de l'eau légère et de l'eau lourde et assez loin l'une de l'autre pour le contraste soit assez élevé. Il suffit ensuite de faire un mélange approprié D_2O/H_2O dans des proportions telles que ce mélange atteigne la densité de longueur de diffusion de l'un des deux composants, celui-ci ayant ainsi un contraste nul avec le solvant, sa contribution dans le signal sera alors nulle.

II.4.4 Spectromètre de DNPA

Un faisceau de neutrons monochromatique est collimaté et envoyé sur l'échantillon. Les neutrons sont ensuite diffusés par l'échantillon dans toutes les directions (Figure II-7). Si l'échantillon est isotrope, nous obtiendrons plusieurs angles solides de diffusion, chacun étant centré sur la direction du faisceau incident. Les neutrons diffusés sont ensuite détectés par une cellule du détecteur. La distance de la cellule par rapport au centre donne l'angle de diffusion, et de là la valeur du vecteur de diffusion q .

Les détecteurs sont soit une grille de fils horizontaux et verticaux (détecteurs XY), soit un ensemble d'anneaux (détecteur centré). Ces détecteurs sont dans une atmosphère de BF_3 , gaz qui capte les neutrons et réémet un rayonnement gamma qui va ioniser le gaz, créer une différence de potentiel entre les fils et donc être détecté. Pour des échantillons isotropes un regroupement est ensuite effectué pour sommer tous les neutrons comptés à une même distance du centre (cette opération n'est nécessaire qu'avec des détecteurs XY). On obtient donc une courbe d'intensité en fonction de q . Pour faire varier les valeurs de q deux choix sont possibles : varier la distance détecteur-échantillon ou la longueur d'onde. Les longueurs d'onde sont typiquement comprises entre 4 et 25 Å et les distances entre 1 m et 7 m à Saclay (jusqu'à 40 m sur la ligne D11 à l'Institut Laue Langevin de Grenoble). Les échelles de q ainsi obtenues sont comprises entre 1×10^{-3} et 1 \AA^{-1} . Dans l'espace réel cela correspond à une fenêtre de mesure de taille d'objets comprise entre 1 et 1000 Å environ. Pour couvrir une gamme importante de vecteurs d'onde, il est ainsi nécessaire de faire les mesures en utilisant plusieurs configurations.

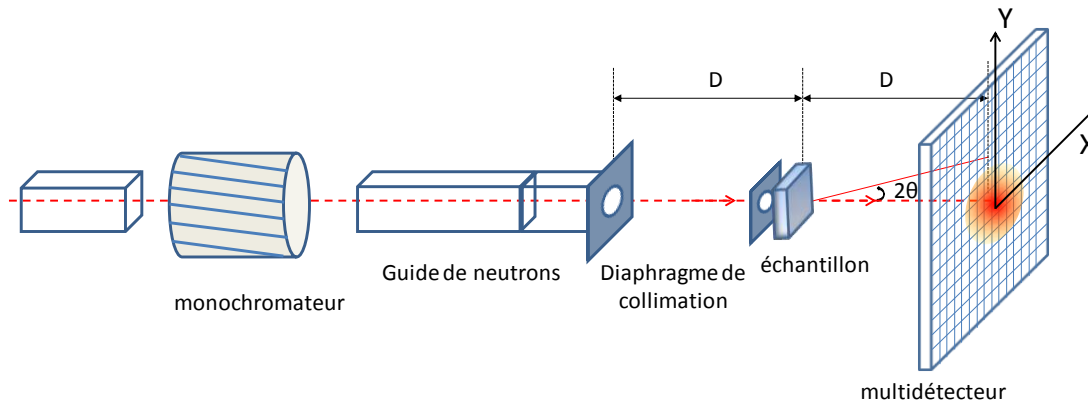


Figure II-7 Schéma typique d'un appareil de diffusion de neutrons aux petits angles (DNPA)

Nous avons utilisé des spectromètres de deux sources différentes : le Laboratoire Léon Brillouin à Saclay et l'Institut Laue Langevin à Grenoble. A Saclay nous avons utilisé les spectromètres PACE, PAXY et PAXE tandis que le spectromètre D11 a été utilisé à l'ILL. PACE et D11 sont les spectromètres à détecteur en anneaux et PAXY et PAXE sont deux spectromètres à détecteurs XY.

II.4.5 Traitement des données

Une fois l'acquisition effectuée, un traitement des données brutes est nécessaire afin d'obtenir l'intensité absolue en cm^{-1} . Il faut tout d'abord soustraire la diffusion due à la cellule utilisée qui est en quartz et dont les joints de grain diffusent notamment aux petits q . Il faut ensuite tenir compte du fait que les détecteurs n'ont pas tous la même efficacité. Pour cela il faut mesurer un témoin incohérent pur (par exemple l'eau légère) qui va diffuser de manière identique dans toutes les directions et possède donc théoriquement un signal plat. Le signal de l'échantillon sera donc ensuite divisé par ce signal incohérent pour faire disparaître les fluctuations dues à l'efficacité du détecteur. Ainsi une mesure normée par rapport à l'eau est obtenue. Il suffit ensuite de mesurer le $d\sigma/d\Omega$ de l'eau et de multiplier le signal par ce facteur pour obtenir des intensités absolues.

$$I_{abs}(\text{cm}^{-1}) = \left(\frac{d\sigma}{d\Omega} \right)_{H_2O} \frac{\frac{I_{ech}}{T_{ech}Me} - \frac{I_{CV}}{T_{CV}Me}}{\frac{I_{H_2O}}{T_{H_2O}Me} - \frac{I_{CV}}{T_{CV}Me}} \quad \text{II-41}$$

Avec T les valeurs de transmissions et e les différentes épaisseurs de cellule.

On peut mesurer la section efficace de l'eau $\left(\frac{d\sigma}{d\Omega}\right)_{H_2O}$ en mesurant l'intensité du faisceau direct décalé atténué (en mesurant l'atténuation sur un diffuseur fort comme le graphite). Mais en pratique, on peut aussi imposer une valeur constante précédemment mesurée, ou plus ou moins « calculée » théoriquement à partir de données précédentes.

Enfin la dernière opération consiste à soustraire la partie incohérente du signal indépendante de q et généralement nommé bruit de fond. Pour cela le solvant est mesuré seul et est soustrait. Le signal incohérent lié aux particules peut avoir une contribution non négligeable aux grands vecteurs d'onde et doit également être évalué et soustrait.

II.5 La diffusion des rayons X aux petits angles (DXPA ou SAXS)

La DXPA est une technique très appropriée pour la caractérisation structurale de nos échantillons à l'échelle locale. Elle permet d'explorer la matière en sondant une gamme de vecteur d'onde similaire à la DNPA. Elle est très sensible à la différence de densité électronique entre les composants, ce qui la rend plus rapide que la DNPA pour obtenir des informations sur les particules métalliques dans nos échantillons. Sur le principe, les méthodes de diffusion des neutrons et des rayons X aux petits angles sont similaires. Le formalisme ondulatoire décrivant la diffusion est d'ailleurs le même. Ces techniques se différencient cependant sur certains points, notamment les gammes d'espace sondées, la durées des expériences ou encore la nature des interactions.

II.5.1 L'interaction rayon-x matière

Les RX sont des rayonnements électromagnétiques dont les longueurs d'onde sont généralement comprises entre 10^{-2} et 2.5 \AA , mais ceux utilisés pour étudier la structure des matériaux ont une gamme de longueurs d'onde plus étroite allant de 0.5 jusqu'à 2.5 \AA . Contrairement aux neutrons, l'énergie des photons issus des synchrotrons est très élevée (de l'ordre de 10^4 eV), et les rayons X résultant possèdent une énergie de l'ordre du keV soit 6 ordres de grandeurs de plus que les neutrons, ce qui peut parfois endommager les échantillons. La résolution en longueur d'onde est excellente (10^4 au RX et 10^3 aux neutrons) et la durée des expériences est beaucoup plus courte.

Dans le cas des RX, l'interaction est directement liée à la densité électronique dans la matière et peut se produire même si le photon passe à une distance relativement grande de l'atome. Ce mécanisme, établi par J.J. Thomson, conduit à l'émission d'un rayonnement de même longueur d'onde que le photon incident. Lorsque l'électron est lié (modèle « masse+ ressort +

amortissement »), la présence d'une force de rappel entraîne une oscillation de l'atome à une fréquence propre qui correspond à un maximum de couplage photon-électron.

Il existe donc des seuils d'absorption. Lors des mesures, il faut donc se situer en dessous ou au-dessus des seuils d'absorption des différents composants. Dans notre cas, le seuil d'absorption de l'or étant de 11,92 keV, nous avons travaillé en dessous de cette valeur à 9keV et 10keV.

II.5.2 Principe de mesure

Le principe d'une mesure DXPA est identique à celle d'une mesure DNPA. L'expérience consiste à envoyer sur l'échantillon un faisceau collimaté de photons monochromatiques grâce à une optique constituée d'un monochromateur et d'un ou plusieurs miroirs focalisants. Les photons sont ensuite diffusés par l'échantillon dans plusieurs directions et sont mesurés par un détecteur en fonction de l'angle de diffusion.

Dans le cas général, un faisceau de RX, de flux initial ϕ_0 , éclaire un échantillon placé à une distance d du détecteur. La section efficace de diffusion différentielle pour un faisceau non polarisé s'écrit de la manière suivante :

$$\frac{d\sigma}{d\omega}(\theta) = r_e^2 \frac{1 + \cos^2 2\theta}{2} \quad \text{II-42}$$

avec $r_e^2 = \frac{e^2}{mc^2}$, m la masse de la particule, e sa charge, c la vitesse de la lumière, 2θ l'angle de diffusion et r_e le rayon classique de l'électron égal à 0.28×10^{-5} nm. L'équation II-42 est valable aussi bien pour des électrons que pour des noyaux. Comme la section efficace de diffusion varie en $1/m^2$, on peut négliger la diffusion des noyaux, leur masse étant très significativement supérieure à celle des électrons. Seuls les électrons diffusent donc dans une expérience de diffusion de RX. La longueur de diffusion d'un électron est donnée par la relation :

$$b_e = r_e [P(\theta)^{1/2}] \quad \text{II-43}$$

avec $P(\theta)$ le facteur de polarisation. La section efficace de diffusion (cohérente) d'un ensemble de n atomes s'écrit est de la forme :

$$\frac{d\sigma}{d\omega}(q) = A_0^2 b_e^2 f(q)^2 \sum_n^{i,j} \left\langle e^{i\vec{q}\cdot\vec{r}_j} e^{-i\vec{q}\cdot\vec{r}_i} \right\rangle \quad \text{II-44}$$

avec $f(q)$ le facteur de diffusion atomique et A_0 l'amplitude du faisceau incident.

L'expression II-44 peut se mettre sous la forme suivante:

$$\frac{d\sigma}{d\omega}(q) = K^2 f(q)^2 S_{aa}(q) \quad \text{II-45}$$

Sous cette forme, l'expression de la section efficace de diffusion en RX est analogue à celle de la section efficace de diffusion pour les neutrons. Les relations établies dans le cas de DNPA peuvent donc être utilisées pour la DXPA.

II.5.3 Le contraste

Le contraste des rayons X est différent de celui des neutrons. L'amplitude diffusée est proportionnelle à la densité électronique (qui pour un atome donné est proportionnelle au numéro atomique Z) et à l'amplitude du faisceau incident. L'amplitude varie ainsi de manière croissante avec Z . La densité de longueur de diffusion électronique d'un atome est en effet :

$$b = r_e Z \quad \text{II-46}$$

On donc obtient le contraste c'est-à-dire la différence entre les valeurs des densités de longueur de diffusion du solvant et du soluté $\Delta\rho$

$$\Delta\rho = \rho - \rho_{Lsm} = \left(\frac{\sum_j Z_j}{V_1} - \frac{\sum_k Z_{k,Lsm}}{V_1} \right) r_e \quad \text{II-47}$$

Ici, on liste les longueurs de diffusion RX des composants utilisés dans notre travail.

Composant	formule	densité SAXS ($\times 10^{10} \text{cm}^{-2}$)
Eau lourde	D ₂ O	9,46
eau	H ₂ O	9,46
hyaluronan	C ₁₄ H ₂₁ NO ₁₁	15,1
chitin	C ₈ H ₁₃ NO ₅	18,0
chitin/xD ₂ O	C ₈ H _(13-3x) NO ₅ D _{3x}	18,0
silice	SiO ₂	18,5
chitosan	C ₆ H ₁₁ NO ₄	18,8
chitosan/xD ₂ O	C ₆ H _(11-4x) NO ₄ D _{4x}	18,8
Alumine	Al ₂ O ₃	32,8
Nanoparticule d'or	Au	130
Ligand TMA	C ₁₄ H ₃₂ NS	8,56
Polystyrene sulfonate de sodium	C ₈ H ₈ SO ₃ Na	15,0

Tableau II-3: Longueurs de diffusion RX pour les différents composants étudiés dans notre travail

Ici, on voit bien que pour certains composants, comme les nanoparticules d'or, le contraste est beaucoup plus important en DXPA qu'en DNPA.

Pour ce travail, les premières mesures ont été réalisées sur la ligne ID02 de l'ESRF-Grenoble avec comme configurations choisies 10keV/1m et 10keV/10m. Nous avons pu également sonder des vecteurs de diffusion plus petits en utilisant une caméra de type Bonse-Hart ($10^{-4} < q < 10^{-2} \text{ \AA}^{-1}$).

Puis nous avons eu la chance de faire une première campagne sur le synchrotron DESY, sur les complexes PEL/AuNP. Par la suite deux campagnes de mesures ont été réalisées sur la ligne SWING à Soleil en utilisant en général comme configuration 9keV/1m, permettant de travailler sur une gamme de q variant de 0.003 \AA^{-1} à 0.5 \AA^{-1} . Pour quelques mesures nécessitant d'aller à très petits q , un cache-faisceau spécial de très petite dimension a été utilisé, permettant ainsi de descendre jusqu'à $q=0.001 \text{ \AA}^{-1}$.

II.6 Appendice :

Microscopie électronique à transmission cryogénique (Cryo-TEM)

Dans notre étude, les expériences de cryo-TEM ont été réalisées sur les complexes vitrifiés préparés à certaines concentrations de chitosan et de nanoparticules caractérisant les différents domaines du diagramme de phase, grâce à Madame Gervaise Mosser, Collège de France..

En bref, une goutte de solution à photographier a été versée sur une grille TEM de carbone recouvert par une membrane de polymère perforée de 100 nm d'épaisseur. La gouttelette est absorbée avec du papier filtre, et la grille est trempée rapidement dans l'éthane liquide afin d'éviter la cristallisation de la phase aqueuse. L'échantillon vitrifié est ensuite stocké sous azote liquide et transféré jusqu'à la colonne sous vide d'un microscope électronique Tecnai fonctionnant à 120kV. L'agrandissement pour les expériences de cryo-TEM a été sélectionné à 40 000 X.

CHAPTER III

**ELECTROSTATIC COMPLEXATION
BETWEEN A POLYELECTROLYTE
AND LARGE NANOPARTICLES
(10-20NM):**

**EFFECT OF THE
POLYELECTROLYTE
PERSISTENCE LENGTH AND OF
THE SIGN OF CHARGE**

III. Electrostatic Complexation Between a Polyelectrolyte and Large Nanoparticles (10-20nm): Effect of the Polyelectrolyte Persistence Length and of the Sign of Charge

III.1 General Introduction

In this chapter we have regrouped all systems containing silica particles, which all have sizes of order 10 nm, which can be considered as large compared to AuNps studied in the next chapters. They can bear negative charges –the usual case, or positive ones, and will be combined with polyelectrolytes (PEL) of opposite charges, and of different flexibility.

In part A, we present an example taken as a reference work: chitosan, a semiflexible polycations complexed with anionic silica particles. We follow here the presentation of the recently submitted manuscript.

In part B we present comparisons with systems involving flexible polycations with similar silica NPs, and finally, we consider the case of positively charged SiNPs, complexed with a semiflexible polyanion, Hyaluronan. All along this part, we will try to extract mainly the similarities, which are numerous, and the differences, which are quite instructive, and try to establish some first evidences of the role of flexibility with respect to the size of the NPS, i.e. the ration L_p/R .

Finally we will summarize the different trends.

Part A (submitted article):

III.2 Interaction between a Semiflexible Polycation and Oppositely Charged Nanoparticles: Case of Chitosan/Silica Nanoparticles

III.2.1 Introduction

Synthetic silica NPs are generally considered as very simple model systems with fixed characteristics (size, shape, surface function), with regular shape and homogeneous surface. Under well-defined conditions a sensible evaluation of the different kinds of interactions (electrostatic, hydrogen bonds, hydrophobic) can be made showing that electrostatic interactions dominate and can be estimated - contrary to proteins, where they are more complex limiting quantitative data analysis.^[41, 42, 44, 46, 97-99] In this context our aim was to study the electrostatic complexation between model silica nanoparticles (SiNPs) with radius~10nm and chitosan, which is a well-known polysaccharide polyelectrolyte bearing positive charges and displaying a semi-flexible backbone characterized by a persistence length of $L_p \sim 7.5$ nm,^[100, 101] and thus to obtain shape-controlled NPs/polymer assemblies. The phase diagram as a function of chitosan and SiNP concentrations at fixed charge density provides useful information on the equilibrium architectures of the NPs assemblies. We have characterized the regions of the whole phase diagram: soluble “single complexes” in excess of SiNPs or chitosan, or coexistence of poor/rich phase (coacervate). We have in particular revealed for $L_p/R \sim 1$ the presence of well-defined single physical complexes displaying a 1D array structure for low chitosan concentrations and displaying an elongated branched structure for low NPs concentrations. Here, we call “single complex” the physical assembly of NPs complexed with a small number of oppositely charged polymer chain. It is expected to be of nanometric size and can be present in the monophasic or diphasic systems. Thanks to the convenient suite of small-angle X-ray and neutron scattering q-range combined with the light scattering one, we have fully characterized the structure of these objects: mass, radius, linear density. Molecular structural parameters like the ratio L_p/R and phase diagram determination allow a quantitative prediction of their structural features: shape, size, NPs organization, number of NPs in an ensemble, formation 1D arrays. This methodology might open the door to a greater degree of control over the way NPs assemble into larger nanostructures. It can be applied to metallic NPs that have been attracting many concerns for their remarkable

industrial potential. This “electrostatic route” is simple, and we show for the first time that it can lead, in particular, to rods made out of nanoparticles.

III.2.2 Single Solute Solutions Characterization

III.2.2.1 Chitosan, a Semiflexible Polycation

Polysaccharide chitosan belongs to a family of linear cationic biopolymers obtained from alkaline N-deacetylation of chitin, which is the second most abundant polymer in nature. The chitosan studied here is a commercial polymer (with polydispersity index around 1.3) from Sigma-Aldrich composed of β 1 \rightarrow 4 D-glucosamine units with a degree of N-acetylation equal to 12.5% (determined by NMR). The mass and the length of the monomer are respectively equal to 5 Å and 166 g/mol. In acid conditions, chitosan is water-soluble due to the presence of protonated amino groups.

The solutions were then investigated in the solvent 0.3 M acetic acid (CH₃COOH) in the presence of 0.2 M sodium acetate (CH₃COONa). We obtain thus a pH=4.5 buffer where all the amino groups bear a positively charged proton. So chitosan exhibits a high polyelectrolyte character with one positive charge every 5 Å, ^[100-103] which would be reduced to one charge per 7 Å after Manning condensation.

Simple Dilute Chitosan Solutions: The data obtained at low q using SLS and corresponding to large spatial scales can be fitted by a Zimm law as:

$$\frac{KC_{chitosan}}{R(q, C_{chitosan})} = \frac{1}{M_W} \left(1 + q^2 \frac{R_G^2}{3} \right) + 2A_2 C_{chitosan} \quad \text{III-1}$$

From the best fits to the data, one obtains $R_G=66\pm 5$ nm and $M_W= 313\pm 20$ kDa, which corresponds to a contour length $L_c=943$ nm. The small positive value obtained for the second Virial coefficient, $A_2=(2.5\pm 0.3)\times 10^{-4}$ cm³g⁻²mol, indicates that the 0.3 M CH₃COOH / 0.2 M CH₃COONa aqueous medium is a good solvent for chitosan.

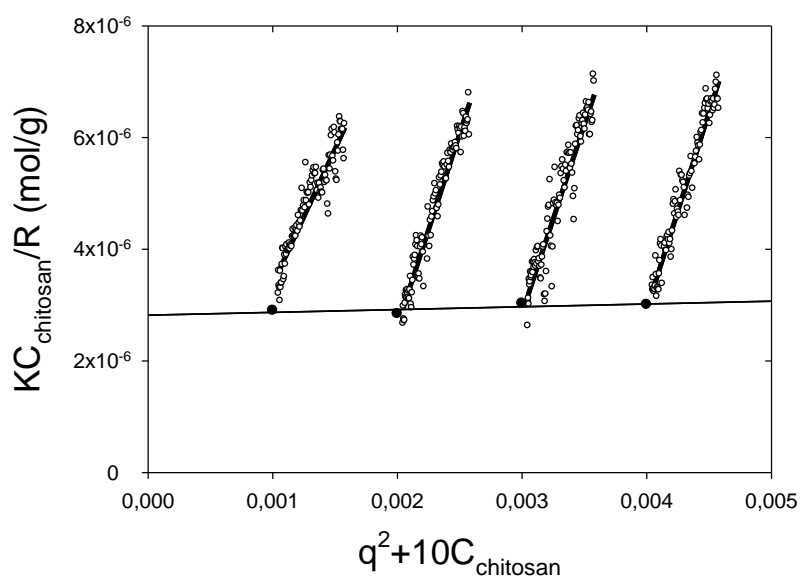


Figure III-1: Zimm plot of chitosan at four different concentrations (0.1, 0.2, 0.3, and 0.4 g/l) with 0.3 M CH_3COOH and 0.2 M CH_3COONa at $T=20^\circ\text{C}$

In the dilute regime the scattered electric field autocorrelation function $g^{(1)}(q,t)$ is clearly monomodal, as illustrated by (Figure III-2). From the relaxation time, which varies as q^{-2} , one obtains the apparent cooperative diffusion coefficient of chitosan chains. Using the Stokes-Einstein relation (eq.II-28), one obtains an apparent hydrodynamic radius of $R_H=44$ nm. The value of the ratio $R_G/R_H\sim 1.5$ is characteristic of the semi-rigid polymer-like conformation of chitosan.^[104] In the inset is also presented the results obtained by applying the Contin procedure to our data. One obtains a relatively narrow single distribution indicating that chitosan chains are well-dispersed in the buffer at $\text{pH}=4.5$. Moreover the polydispersity index has been calculated using the cumulant procedure and one obtains $k_2/k_1^2=0.24$ confirming the trend observed using the Contin method.

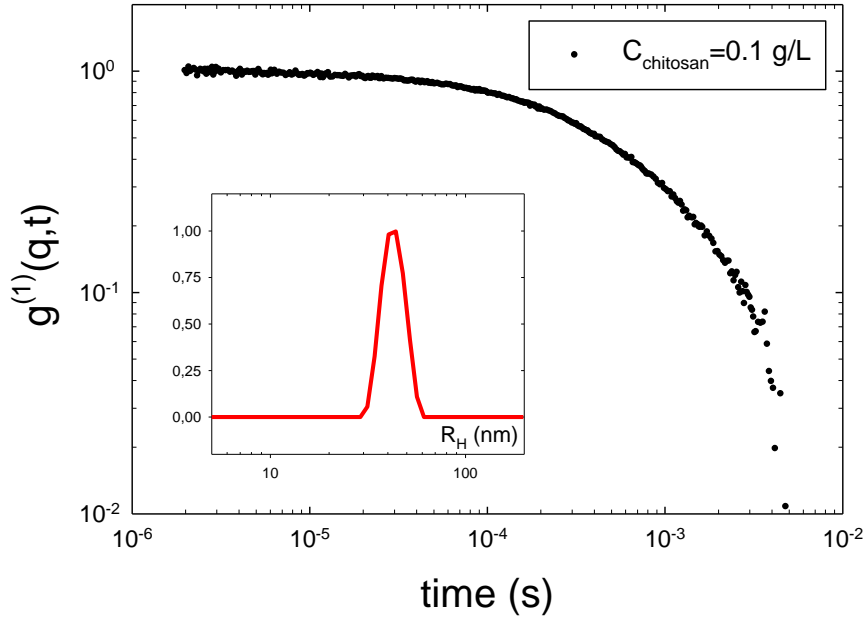


Figure III-2: Scattered electric field autocorrelation function, $g^{(1)}(q,t)$, at $\theta=90^\circ$ for a $C_{\text{Chitosan}}=0.1$ g/l chitosan solution in 0.3 M CH_3COOH and 0.2 M CH_3COONa at $T=20^\circ\text{C}$. The normalized distribution of scattered intensity as a function of the size obtained with the Contin method is presented in the inset

Figure III-3 displays the scattering pattern of a 0.1 g/l chitosan solution obtained by coupling SLS (low- q data, with $6 \times 10^{-4} \leq q \text{ (\AA}^{-1}) \leq 2.5 \times 10^{-3}$) and SANS measurements. SANS experiments were carried out using D11 (Institut Laue Langevin-ILL, Grenoble) spectrometers. We used $D = 8$ m and $\lambda = 5 \pm 0.5 \text{ \AA}$, giving a q -range of $8.4 \times 10^{-3} \leq q \text{ (\AA}^{-1}) \leq 0.104$.

We normalized, for both techniques, the scattered intensity by the corresponding contrast term. Then assuming that 0.1 g/l is a concentration low enough to consider the solution as dilute, the result is $M_w \times P(q)$, where $P(q)$ is the form factor. The gap between the SLS and the SANS data, comprised between 3×10^{-3} and 10^{-2} \AA^{-1} , is relatively important. Nevertheless, these experiments would give us a good direct estimation of the chitosan persistence length that is anyway determined at higher q .

The plot as a function of q exhibits three domains: i) a low- q smooth variation with measurable zero- q limit ($I(q=0)$), analogous to a Guinier regime; ii) an intermediate polymer coil regime in which the q -dependence of the scattered intensity can be described by a power law with exponent close to -2, like in Gaussian coils; and finally iii) a q^{-1} domain at higher q characteristic of rigid rodlike behavior for distances smaller than the persistence length L_p . This suite of variations can be fitted satisfactorily to the form factor of a wormlike chain

model with no excluded volume interactions (this is justified by the small value of the second Virial coefficient A_2 determined above in the presence of a 0.2 M excess of salt). We used an expression^[105] based on the expressions derived by Burchard and Kajiwara for rodlike structures^[106] in which the form factor calculated by Sharp and Bloomfield^[107] for finite wormlike chains of contour length L_c is used at low q :

$$P(q) = \left[\frac{2[\exp(-x) + x - 1]}{x^2} + \left[\frac{4}{15} + \frac{7}{15x} - \left(\frac{11}{15} + \frac{7}{15x} \right) \exp(-x) \right] \frac{2L_p}{L_c} \right] \times \exp \left[- \left(\frac{2qL_p}{\alpha} \right)^\beta \right] + \left[\frac{1}{2L_c L_p q^2} + \frac{\pi}{qL_c} \right] \times \left[1 - \exp \left[- \left(\frac{2qL_p}{\alpha} \right)^\beta \right] \right] \quad \text{III-2}$$

with $x=L_c L_p q^2/3$ and valid for $L_c > 4L_p$. Values of the empirical parameters $\alpha=5.53$ and $\beta=5.33$, which contribute to the balance between the low- q and the large- q terms, have been optimized in ref [105]. Eq.III-2 does not account for excluded volume interactions, which are anyway negligible in the SANS q -range where L_p is determined.^[108, 109]

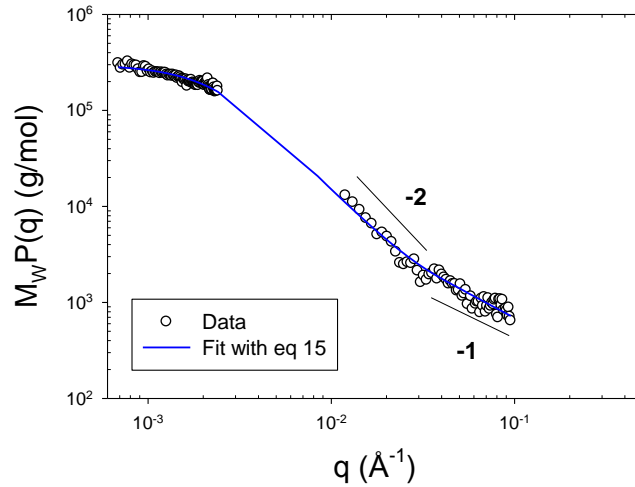


Figure III-3: Combined SLS and SANS spectra for a 0.1 g/l chitosan solution. To superimpose both techniques we plot $M_w P(q)$ as a function of q . The continuous line represents the fit of the data with III-2

The fit of the data (see Figure III-3) yields to $M_w=301K$, in good agreement with the value determined using the Zimm analysis, $L_c=1116$ nm corresponding to the theoretical value of a single strand chitosan chain and $L_p=9$ nm: here L_p is approximately equal to the intrinsic persistence length, the electrostatic additive contribution to the persistence length being negligible in the presence of 0.2 M of salt. This value is close to that previously reported, 7.5

nm, by Buhler et al.^[100] by another method. It is determined here directly by SANS for the first time.

III.2.2.2 Negatively charged silica nanoparticle

Silica dispersions of the desired concentration were obtained by dilution of the required quantity of commercial dispersion ([SiO₂] =30 wt.%) in the 0.3 M CH₃COOH/ 0.2 M CH₃COONa buffer of pH =4.5. In Ludox AM, tetravalent silicon ions have been substituted for part by trivalent aluminum ions ([Al₂O₃] = 0.2 wt.% in our dispersion according to the supplier) on the surface of the particles (see Figure III-4). Therefore, these modified silica particles carry a more pronounced negative surface charge density over a wide pH range giving rise to very good stability against variation of pH. Such stability with time of the SiNPs solutions has been checked using light scattering measurements.

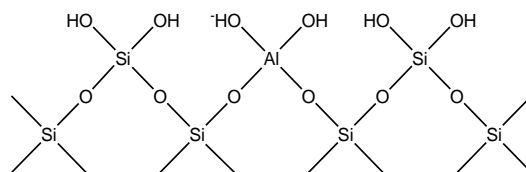


Figure III-4: chemical structure of ludox AM colloidal surface

Electrophoretic mobility μ was measured with a Malvern ZetaSizer apparatus. Measurements are based on the laser Doppler velocimetry principle yielding the velocity of the complexes submitted to an alternating electrical field of 125 V/cm oscillating at a frequency of 20 Hz.

The results shown in Figure III-5 revealed that the iso-electric point (IEP) of SiNPs (Ludox AM) is located around pH~2, which corresponds to literature data.^[110, 111] These particles carry a pronounced negative surface charge over the entire pH range above IEP due to the substitution of tetravalent silicium by trivalent aluminum ions as was also observed in previous studies.^[110, 111] To derive the electrical charge per SiNP, Z_{eff} , we choose the expression of electrophoretic mobility derived from the Hückel model : $Z_{eff} = 6\pi\mu\eta_s R_H = \mu k_B T / D$,^[112] $Z_{eff} = 6\pi\mu\eta R_H = \mu k_B T / D$ where D is the diffusion coefficient of SiNP and η_s the viscosity of the solvent. We obtain $Z_{eff}=25$ elementary charges per SiNP at pH = 5. This value seems however much lower than the one given by chemical titration^[113], which is around 1 e/nm², giving here $Z_{lit} = 1000$ e per particle. One difference lies in the determination of the charge. In the mobility measurement, the charge is defined at the “slipping plane” separating the layer containing counterions moving with the particle from the rest of the solution. Z_{lit} is assumed to correspond to the total titrated charge at the surface

of the particle (see more details in Appendix 4). We will return to this difference when commenting the phase diagram of complexation of the SiNP with chitosan.

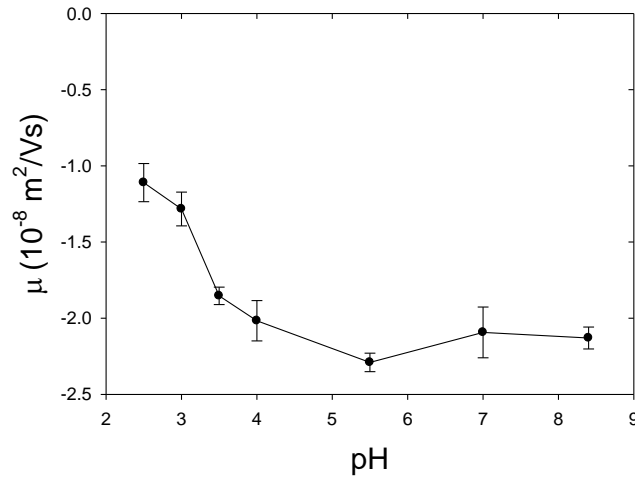


Figure III-5: Electrophoretic mobility μ as a function of the pH for SiNP solutions at $C_{\text{SiNP}}=10$ g/l

The SiNPs were characterized in the dilute regime by DLS and SAXS in the same experimental conditions for a concentration $C_{\text{SiNP}}=3$ g/l. The correlation function $g^{(1)}(q,t)$ depicts a monoexponential cooperative relaxation mode (see Figure III-6), with a relaxation time inversely proportional to q^2 , corresponding to $R_{\text{H,app}}=11.7\pm 1.5$ nm. The narrow size distribution obtained by applying the Contin procedure to our data shows that the SiNPs are monodisperse in size (see inset of Figure III-6). This is corroborated by the value of the polydispersity index, 0.1, obtained using the cumulant method. Also the DLS experiments performed at different aging times during several months show no time evolution of the system. Thus, SiNPs are well dispersed and stable in solution and show no tendency to aggregation with time.

Figure III-7 shows the SAXS spectra obtained for the same solution at large qs . For dilute solutions and/or for large qs , it is generally assumed that the scattering is arising from isolated non-interacting NPs, with a structure factor $S(q) \sim 1$. The data can be fitted satisfactorily by means of the form factor expression derived for hard spheres of radius R (eq.II-7).

The form factor oscillations, damped by the size distribution, are well reproduced with $I(q)$ calculated as indicated above (eq.II-7). The SiNPs solution is well represented by a suspension of hard spheres with $R=9.2$ nm, and $\sigma=0.12$.

The extrapolation of the SAXS scattered intensity to zero- q allows us to determine a weight-average molecular weight for the NPs, one obtains $M_w=(3\pm 0.2)\times 10^6$ g/mol.

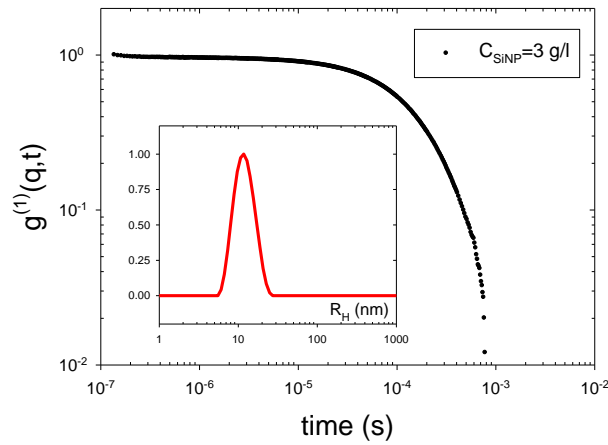


Figure III-6: Scattered electric field autocorrelation function, $g^{(1)}(q,t)$, at $\theta=90^\circ$ for a $C_{\text{SiNP}}=3$ g/l SiNPs solution in 0.3 M CH_3COOH and 0.2 M CH_3COONa at $T=20^\circ\text{C}$. The normalized distribution of scattered intensity as a function of the size obtained with the Contin method is presented in the inset

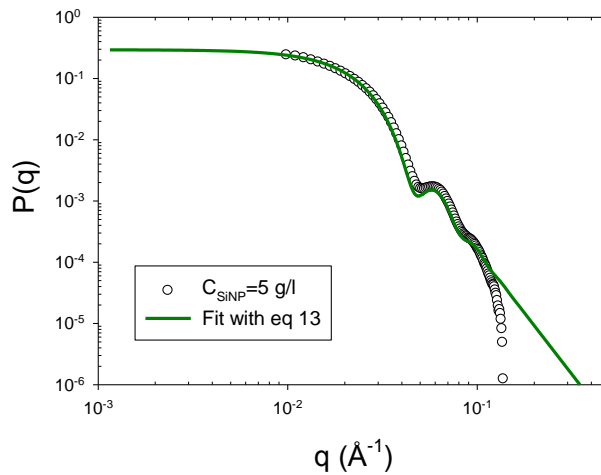


Figure III-7: Variation of the SiNPs form factor, $P(q)$, with q obtained using SAXS measurements for a $C_{\text{SiNP}}=5$ g/l solution at $T=20^\circ\text{C}$. The continuous red line correspond to the best fit of the data using the form factor expression derived for hard spheres of radius $R=9.2$ nm with $\sigma=0.12$

III.2.3 Sequence of phase behaviors

This section deals with the phase behavior and the SANS experiments performed on charged SiNPs in the presence of oppositely charged chitosan semiflexible chains at fixed temperature $T=20^\circ\text{C}$ and $\text{pH}\sim 4.5$. In these conditions, the surface charge density of the SiNPs is equal to 0.02 charges. nm^{-2} (it corresponds to 25 negative charges per SiNP) and the persistence length, L_p , of chitosan is roughly equal to the intrinsic one close to 9 nm. The buffer solution is the aqueous solution consisting of a mixture of 0.3 M CH_3COOH and 0.2 M CH_3COONa . Since SiNPs and chitosan chains are both fully charged in a relatively small pH range, this buffer

was used as a mean of keeping the pH at a constant value of 4.5 in the whole range of mixing ratio. Within these experimental conditions the electrostatic complexation between the two partners takes place readily.

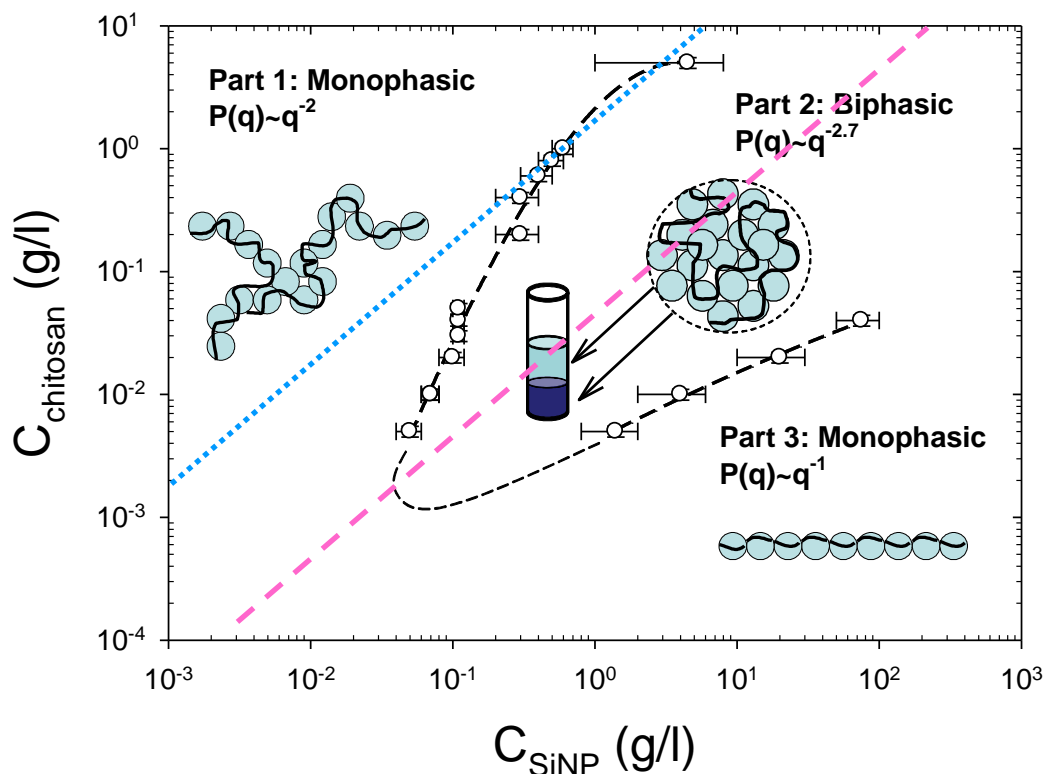


Figure III-8: Sequence of phase behaviors in the chitosan concentration-SiNP concentration plane at $T=20^{\circ}\text{C}$ and fixed $\text{pH}\sim 4.5$. The form factor, $P(q)$, scales as $\sim q^{-2}$, $\sim q^{-2.7}$, and q^{-1} respectively in part 1, 2, and 3 of the phase diagram. The two lines are indicative; they correspond to charge stoichiometry $[+]/[-] = 1$ with surface charge values 25e per particle, as given by mobility and Hückel formula (light blue), and titration value^[113] (pink), corresponding to 1017e per particle

In Figure III-8, we have sketched the phase evolution of the samples with the chitosan concentration (vertical axis) and the SiNPs concentration (horizontal axis). For extremely low chitosan addition, the solutions are monophasic and transparent over the whole range of NPs concentration. When the chitosan concentration is increased, one observes for intermediate NPs concentrations a phase separation: a dilute phase coexists with a more concentrated and viscous phase (see Part 2), while, at lower (Part 1) and higher (Part 3) NPs concentrations, the samples remain clear monophasic solutions.

The shape of the phase diagram reported in Figure III-8 is reminiscent of “complex coacervation”^[41, 98] due to electrostatic attraction between polyelectrolytes and oppositely charged NPs or proteins.^[43, 44, 78, 97, 99, 114-116] The two kinds of objects can first associate in

primary complexes, which then are neutral. Above a certain concentration they precipitate in rich and poor liquid phases, or form fractal aggregates by controlled (diffusion limited or better reaction limited) aggregation, or solid clusters (this depends on the form of the attraction potential).^[42] Another aspect is the release of the counterions of both species, which has an entropic contribution on the free energy, as predicted and experimentally observed.^[46] We have plotted two indicative lines corresponding to charge stoichiometry $[+]/[-] = 1$ with surface charge values 25 per particle, as given by mobility and Hückel formula and titration value^[113], as formerly discussed above. The titration value gives a stoichiometric line in the center part of the biphasic region, which agrees with an electrostatic origin for complexation. This suggests that all counterions are released so that the net charge of the SiNP is relevant. Note that we have also assumed a net charge (all c.i. released and thus ignoring Manning condensation) for chitosan.

In practice for our system, SANS results indicate that the concentrated lower phase contains the major part of the NPs and of the chitosan, while the upper fluid phase is a very dilute solution of both NPs and chitosan. It is noteworthy that the phase separation is observed for minute quantities of chitosan.

To gain insight into the arrangement of the SiNPs and the local structure of the complexes, SANS experiments were performed on solutions characterizing the different parts of the phase diagram: Part 1 (excess of chitosan chains-monophasic domain), Part 2 (Biphasic domain) and Part 3 (excess of SiNPS-monophasic domain).

SANS experiments were carried out using PACE (Léon Brillouin Laboratory-LLB at Saclay, France). For a given wavelength, the range of the amplitude of the transfer wave vector q was selected by changing the detector distance, D . Two sets of sample-to-detector distances and wavelengths were chosen at LLB ($D = 1.0$ m, $\lambda = 10 \pm 1.0$ Å; and $D = 4.7$ m, $\lambda = 10 \pm 1.0$ Å) so that the following q -ranges were respectively available: $2.2 \times 10^{-2} \leq q$ (Å⁻¹) $\leq 2.2 \times 10^{-1}$, and $4.2 \times 10^{-3} \leq q$ (Å⁻¹) $\leq 4.4 \times 10^{-2}$. Measured intensities were calibrated to absolute values (cm⁻¹) using normalization by the attenuated direct beam classical method. Standard procedures to correct the data for the transmission, detector efficiency, and backgrounds (solvent, empty cell, electronic, and neutronic background) were carried out.

This is a powerful method for determining shapes of objects in solution over the range of 1-30 nm. Figure III-9 shows the variations of the scattered intensity as a function of q measured for each of the representative solutions in deuterated water and in the presence of 0.2 M

CH_3COONa and $0.3 \text{ M } \text{CH}_3\text{COOH}$ at $T=20^\circ\text{C}$. It is important to note that the SANS signal is dominated by the SiNPs, as expected from the high value of the SiNPs molecular volume (measurements in $\text{D}_2\text{O}/\text{H}_2\text{O}$ mixture eliminating the signal of chitosan by contrast matching, shown in Figure III-10, corroborate this estimate).

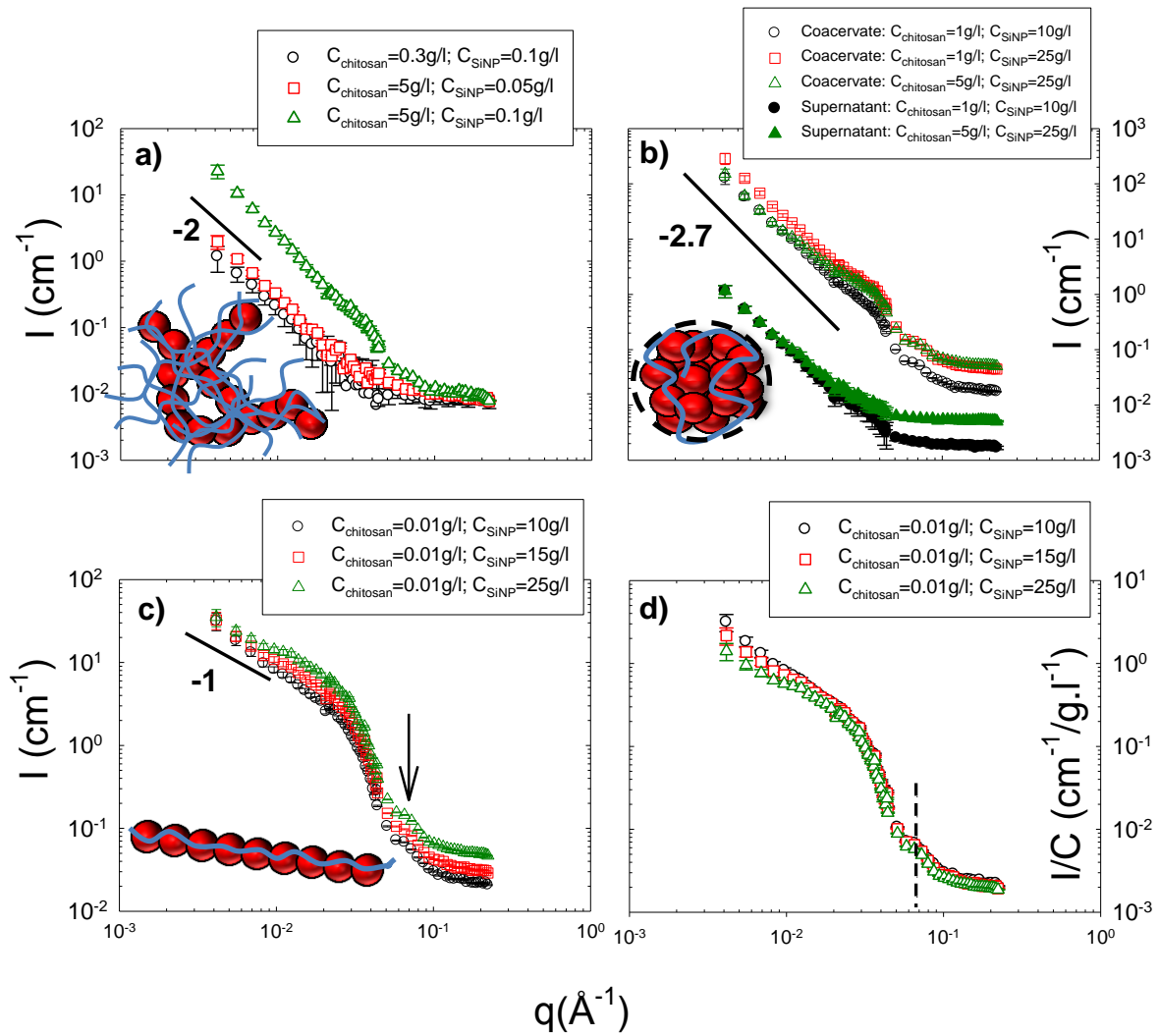


Figure III-9: Variation of the scattered intensity, I , with q obtained by SANS in chitosan/SiNP solutions in D_2O at $\text{pH}=4.5$: (a) dilute SiNP solutions in the presence of an excess of chitosan chains (monophasic domain #1); (b) biphasic domain #2 (for clarity the spectra corresponding to the supernatant phase have been divided by one log unit); and (c) dilute chitosan solutions in the presence of an excess of SiNPs (monophasic domain #3). (d) same as (c) but representation of the variation with q of the ratio I/C_{SiNP}

Part 1: Figure III-9a shows the SANS curves obtained for $C_{\text{chitosan}}=0.3 \text{ g/l} / C_{\text{SiNP}}=0.1$; $C_{\text{chitosan}}=5 \text{ g/l} / C_{\text{SiNP}}=0.05$ and $C_{\text{chitosan}}=5 \text{ g/l} / C_{\text{SiNP}}=0.1 \text{ g/l}$ monophasic mixtures (dilute solutions of SiNPs in the presence of an excess of chitosan). The scattering curve does not

exhibit a Guinier regime with a plateau at low q associated to the finite size of the complexes but instead a $\sim q^{-2}$ behaviour in a rather extended q range, followed by a high q oscillation. This q^{-2} dependence suggests a Gaussian distribution for the NPs inside the complexes, or branched quasi-fractal aggregates. The global size of the complexes being larger than 30 nm.

Part 2: For this biphasic domain, the scattering varies as a $q^{-\alpha}$ law with α ranging from 2.6 to 2.8, characteristic of rather compact fractal aggregates larger than 30 nm (the scattering curves do not exhibit a Guinier regime with a plateau at low q). This behavior is observed in a representative set of samples of the biphasic domain for dense phases as well as for supernatant phases, as seen in Figure III-9b. The power law is followed at large q , as for part 1, by a high q oscillation that will be discussed below.

Part 3: Figure III-9c displays the scattering patterns for chitosan/SiNPs solutions at various SiNPs concentrations (Domain #3 of the phase diagram). The variations of the ratio I/C_{SiNP} of the scattered intensity over the SiNP concentration are illustrated in Figure III-9d. The most interesting feature of Figure III-9d concerns the intermediate and high q -ranges where all the scattering curves superimpose on each other, thus indicating that the self-assemblies have the same structure at the spatial scale corresponding to these q -ranges. Furthermore in the lowest q -range, the q dependence of the scattered intensity tend to join for the lowest concentrations, a power law with an exponent close to -1, which suggests a rod-like structure at the corresponding scale. This variation with q has never been observed in NP-polyelectrolyte complexes at our knowledge. The oscillation observed in the high q -range is the initial part of the oscillating term of the shape dependent form factor of the particle cross-section.

In the low q range, the shape of the scattering curves depends on the NPs concentration. System with a very large excess of SiNPs ($C_{\text{SiNP}}=25$ g/l) tends to exhibit a Guinier regime with the beginning of a plateau in the low q range associated with the average finite size of the scattered objects (here a mixture of rigid-rods and of free SiNPs). This “plateau” is followed by a slight upturn probably associated to the presence of rods that dominate the signal at very low q . For SiNPs concentrations of 10 g/l and 15 g/l the curves show neither a Guinier plateau nor a significant upturn of the scattered intensity in the low q -range: the characteristic q^{-1} rod dependence is measured down to the lowest q , thus indicating that the rods dominating the SANS signal in this concentration domain are relatively long; i.e., larger than 30 nm.

All curves of Figure III-9 exhibit an oscillation occurring at the same value of q for all the systems investigated. However, the absence of a Guinier regime at low q and the contribution of the incoherent background at high q prevented us from determining the global and cross-sectional dimensions of the nanorod aggregates with very high accuracy. Therefore, it was interesting to turn to SAXS experiments at the ESRF high brilliance light source.

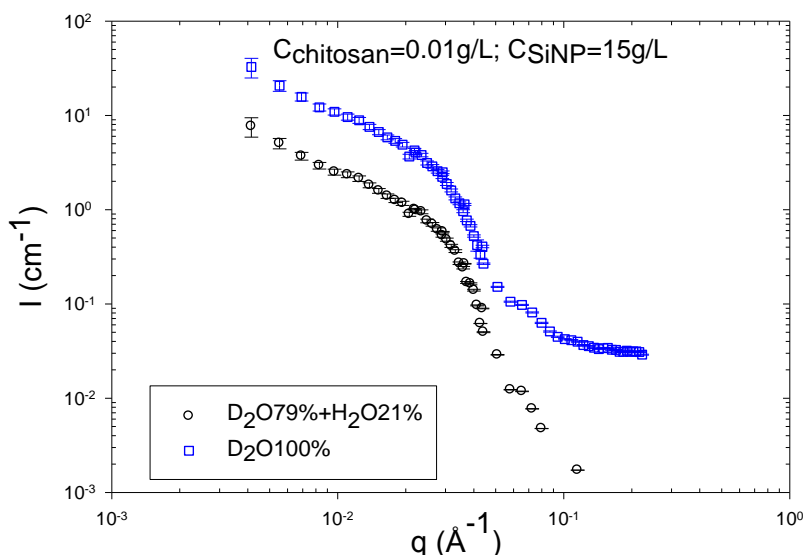


Figure III-10: SANS patterns of sample chitosan 0.01g/L+SiNP 15g/L prepared in 100%D₂O and 79%D₂O/21%H₂O mixed solvent (zero average contrast for chitosan) respectively

III.2.4 Nanorods SAXS characterization

Figure III-11a shows the variations of the ratio I/C_{SiNP} of the scattered intensity over the SiNP concentration versus the scattering wave vector q for nanorod solutions at two different NPs concentrations, $C_{\text{SiNP}}=10$ g/l and 15 g/l. The solutions are the same samples (monophasic) as studied formerly by SANS (see above) and observed several months later. Due to the high mass and concentration of the SiNPs, the SAXS signal is dominated by the scattering of the NPs; the signal of chitosan chains is negligible. The scattering pattern of free SiNPs is also represented in the high q range in Figure III-11a. The scattering curves of the complexes exhibit the same overall behavior for both SiNP concentrations, characterized by the following sequence: a Guinier regime in the low q range associated with the finite size and mass of the scattered objects, one intermediate regime in which the q dependence of the scattered intensity is described by a power law with an exponent close to -1, a axial Guinier regime at higher q corresponding to the size of the cross-section of the assemblies, and finally

well-defined oscillations associated to the shape-dependent form factor of the particle cross-section.

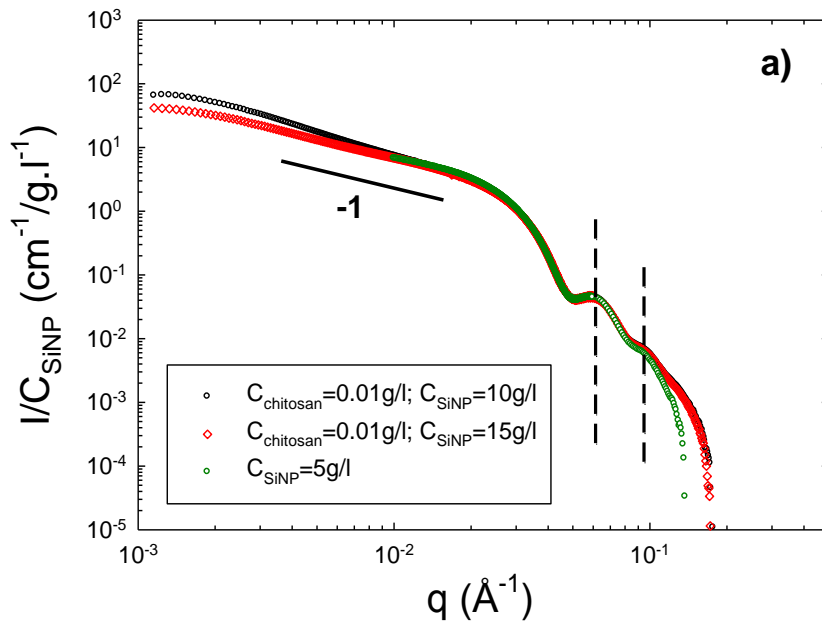


Figure III-11a: Variation of the ratio I/C_{SiNP} with q obtained using SAXS experiments for free SiNPs and in the presence of 0.01 g/l chitosan at $T=20^\circ\text{C}$

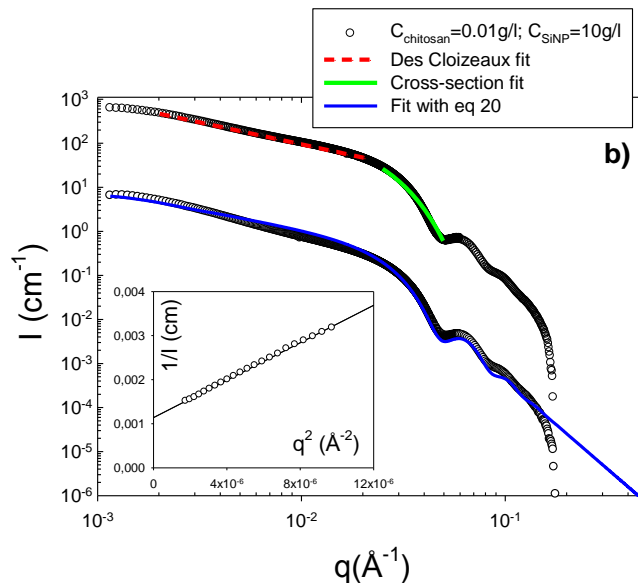


Figure III-11b: SAXS spectra obtained for a 0.01 g/l chitosan/10 g/l SiNP dispersion solution in 0.2 M CH_3COONa and 0.3 M CH_3COOH . Upper curve: the dashed curve represents the fit of the data in the intermediate regime with eq.III-3 and the solid curve represents the fit of the high q data by a Guinier expression for the form factor of the section (eq.III-4). Bottom curve, for clarity the data have been shifted by two log units along the y-axis: the continuous solid line represents the best fit of the data obtained by a combination of spheres and cylinders form factors (see eq III-6). The inset shows the plot of $1/I$ versus q^2 and the best linear fit to the data

Inner conformation: In the intermediate q regime, the scattering curves can be fitted satisfactorily by a rigid rod model. Figure III-11b shows the fit realized for a 0.01 g/l chitosan/10 g/l SiNP solution, that is in the very dilute regime for chitosan, by means of the des Cloizeaux law^[117] derived for rigid rod particles and valid for $qL_p > 2$, where L_p is the persistence length and L_c the contour length.

$$P(q) = \frac{\pi}{qL_c} + \frac{2}{3q^2L_pL_c} \quad \text{III-3}$$

The high q data can be fitted by a Guinier expression for the form factor of the section:

$$V_{chain}P(q) = \frac{\pi S}{q} \exp\left(\frac{-q^2 r_c^2}{2}\right) \quad \text{III-4}$$

Where r_c is the radius of gyration of the cross section. By fitting the two equations above to the experimental data, after dividing by the contrast as for individual particles, one can determine the mass per unit length of the rods, M_L , the section, S , and the radius of gyration, r_c , of the cross section. From the fits of Figure III-11b, we obtain $M_L = (98 \pm 9) \times 10^3$ g/mol/nm, $S = 131 \pm 15$ nm², and $r_c = 6 \pm 0.2$ nm. If the rods consist of straight SiNPs monolayer wires, then the mass per unit length can be calculated to be $\sim (\text{mass/diameter})_{\text{SiNP}} = 3 \times 10^6 / 24 = 125 \times 10^3$ g/mol/nm, a value slightly larger than the experimental determination. This discrepancy may be explained by the contribution of free NPs to the SAXS signal (see next part).

The radius of gyration of the cross-section of such a nanorod is given by:

$$r_c^2 = \frac{R^2}{2} \quad \text{III-5}$$

Using the experimental value of $r_c = 6$ nm, one obtains $R = 8.5$ nm, which is a value in good agreement with the experimental one determined in Figure III-7. In all cases, the determined local structural parameters are consistent with a well-ordered single-strand 1D SiNP self-assembly whose cross-section is that of a single SiNP. This is corroborated by the oscillations observed at higher q that are identical for all the samples for $q > 4 \times 10^{-2} \text{ \AA}^{-1}$ (when $S(q) \sim 1$) and that are reasonably well reproduced with $P(q)$ calculated for the spherical SiNPs with a radius R of 9.2 nm (see Figure III-11 and Figure III-7).

Overall shape of the nanorods: The low q data have been fitted by the classical Guinier expression, $1/I(q) = 1/I(0) \times (1 + q^2 R_G^2 / 3)$, which provides the average radius of gyration, R_G , and the zero-wave vector intensity, $I(0)$, associated to the weight-average molecular weight, M_W ,

of the rods. For rodlike particles with large aspect ratio ($L_c \ll L_p$), $R_G^2 = L^2/12$, where L is the average contour length of the rod. For $C_{\text{SiNP}}=10\text{g/l}$, we obtain $R_G=77\text{ nm}$, $L=267\text{ nm}$ and $M_W=(31\pm 3)\times 10^6\text{ g/mol}$. Inspection of the data calls for two remarks. First, the particles behave as rigid rods, as shown by the comparison between the calculated value $L=12^{1/2}R_G=267\text{ nm}$ and the experimental value of $M_W/M_L=(31\times 10^6)/(98\times 10^3)=316\text{ nm}$. Secondly, the average number of SiNPs constituting a nanorod is, neglecting the Virial effects, $\sim M_{W,\text{nanorod}}/M_{W,\text{SiNP}}\sim 11$ (or $\sim 14-15$ if one considers the ratio between the rod length and the NPs diameter $267/18.4$).

For $C_{\text{chitosan}}=0.01\text{ g/l}/C_{\text{SiNP}}=15\text{ g/l}$ solutions, the zero-wave vector scattered intensity, $I(0)$, is slightly lower due to the enhanced contribution to the signal of the free SiNPs, and thus showing that the proportion of both populations has to be taken into account: free SiNPs and rodlike self-assemblies. The low- q signal is, however, still dominated by the rodlike behavior.

III.2.5 Combined SAS and cryo-TEM measurements of the different shapes

To gain insight into the shape of the NPs self-assemblies, complementary cryo-TEM experiments were performed on solutions characterizing the three parts of the phase diagram, using also TEM, as a support for the discussion.

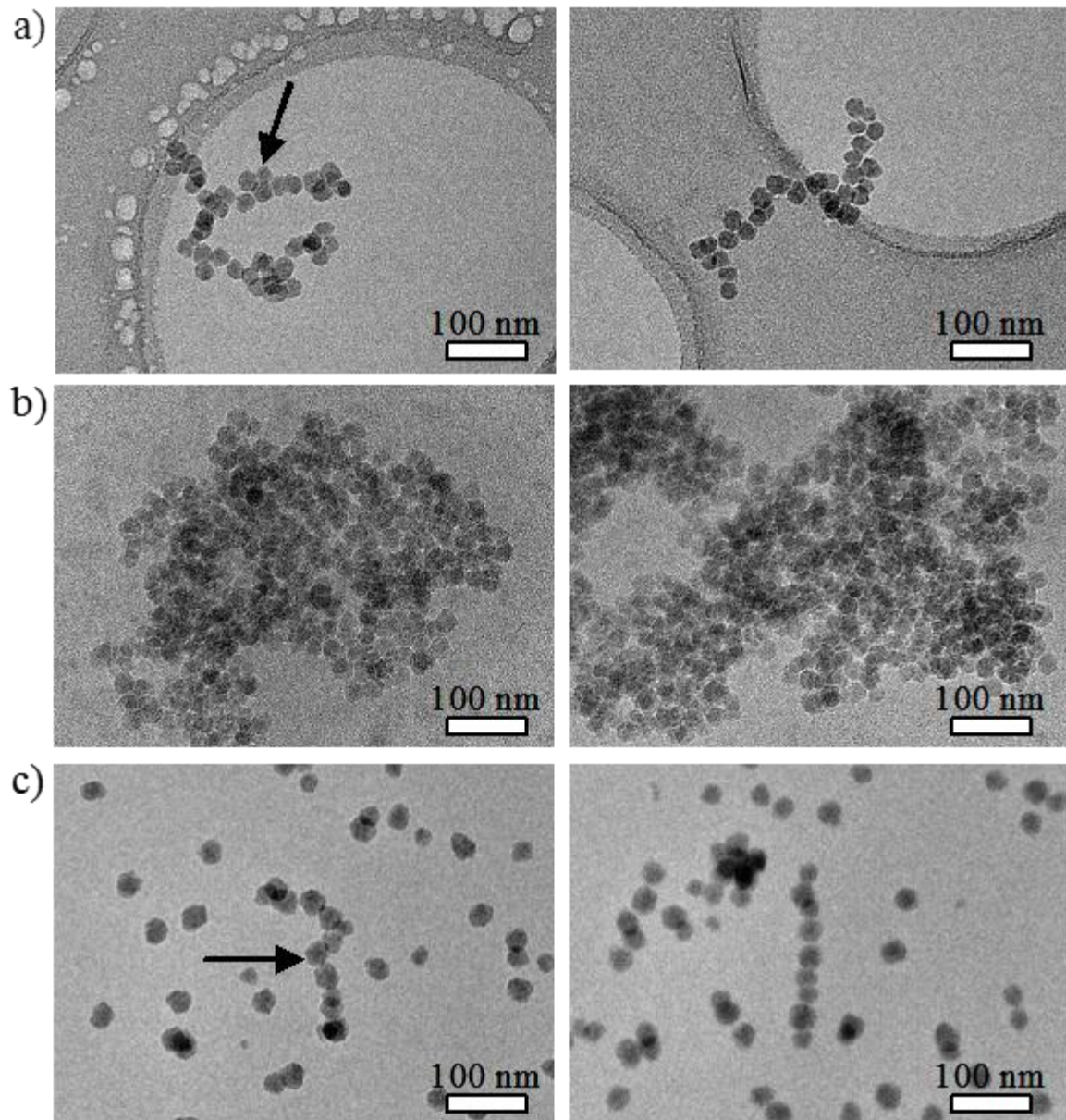


Figure III-12: Cryo-TEM images of a) a vitrified $C_{\text{chitosan}}=5\text{g/l}$ / $C_{\text{SiNP}}=0.1\text{g/l}$ monophasic solution (Part 1); b) a coacervate phase with initial concentrations of $C_{\text{chitosan}}=1\text{g/l}$ and $C_{\text{SiNP}}=10\text{g/l}$ (Part 2); and c) a $C_{\text{chitosan}}=0.01\text{g/l}$ / $C_{\text{SiNP}}=10\text{g/l}$ monophasic solution (Part 3) in the presence of 0.3 M CH_3COOH and 0.2 M CH_3COONa . Scale bar is 100 nm. Some chitosan chains, in white in the pictures, are indicated by black arrows

Part 1, excess of chitosan: Evidence in favor of dilute randomly self-assembled NPs structures of 300-400 nm, as already suggested by the q^{-2} dependence observed in the SANS spectra was provided by cryo-TEM images of solutions containing an excess of chitosan (5 g/l) and 0.1 g/l SiNPs (Figure III-12a). A common observation in these micrographs is that NPs do not form single-strand structures but instead form flexible branched structures with variable lengths, cross-sections, and aggregation numbers (mostly between 20 and 50). Thus an apparent fractal dimension of 2 is in agreement with such branched or contorted structure. Also, no free NPs are observed. Thus, assuming that all chitosan chains are involved in the self-assemblies, we can estimate that the number of chains per complex is around $16 \sim (\text{Number of chitosan chains})/(\text{Number of NPs} \times \langle N_{\text{agg}} \rangle)$, with $\langle N_{\text{agg}} \rangle \sim 30$ the average NPs aggregation number.

Part 2, biphasic domain: Figure III-12b show micrographs of vitrified coacervate phases (concentrated viscous phases). Here, we see dense and globular SiNP aggregates larger than 500 nm composed of most of the NPs and chitosan chains. These observations corroborate the SANS analysis.

Part 3, excess of SiNPs: Imaging of chitosan/SiNP solutions using Cryo-TEM corroborates the SANS and SAXS results indicating the presence of straight rodlike structures in monophasic solution with large excess of NPs. Figure III-12c show representative images that clearly demonstrate the presence of aligned nanorod objects. Some objects (see left hand picture of Figure III-12c) present some kinks. However, they can be somehow disorganized by the cryo-TEM procedure, such that for the structure of the objects in bulk solution we better rely on the SAXS, which definitely shows rodlike behavior. All the rods exhibit uniform diameters of approximately 20 nm, which are in agreement with the diameters calculated from r_c values determined from SAXS data (assuming a circular cross-section). Beyond agreement with SANS/SAXS, TEM gives new information on the rods lengths, which are variable (mostly between 160 and 280 nm). In the light of invariant diameters, and in the absence of branched structures, the observed nanorods are thought to correspond to single strand rigid NP assemblies as already shown by the scattering analysis and the experimental value of the linear mass density.

Looking closer to the complexes, one can distinguish white lines, of less than 1 nm width, on some SiNPs that may be assigned to chitosan binding on nanoparticle surface (indicated by black arrows in Figure III-12). However, the low electronic contrast of the biopolymer does not enable to clearly identify the number of chain per complex and their arrangement in the

nanorods structure. To shed some light on this aspect, we have estimated the amount of chitosan per complexes from SAXS measurements. This simple calculation have been made on the basis of the average number of individual nanoparticles and of the nanorods determined by fitting the scattering pattern by the following equation^[118]:

$$I(q) = I_{rods}(q) + I_{spheres}(q) \quad \text{III-6}$$

Where $I_{rods}(q)$ and $I_{spheres}(q)$ are the scattered intensities related respectively to the form factor of the rods and of the spheres (see eq.II-7). For the rods, we used the classical form factor derived for cylinders:

$$P(q)_{cylinder} = \int_0^{\pi/2} \left[\frac{\sin\left(q \frac{L}{2} \cos \alpha\right)}{q \frac{L}{2} \cos \alpha} \frac{2J_1(qR \sin \alpha)}{qR \sin \alpha} \right]^2 \sin \alpha d\alpha \quad \text{III-7}$$

where α is the angle between the axis of symmetry of the cylinder and q , and J_1 the first-order Bessel function. The best agreement with the data presented in Figure III-9a is obtained for $\phi_{spheres}=4.3 \times 10^{-3}$, $\phi_{rods}=2.3 \times 10^{-4}$, $R_{spheres}=R_{cylinders}=8.5$ nm, $\sigma=0.11$, and for $L_{cylinders}=250$ nm (see bottom curve of Figure III-11a, fit realized with eqs II-7, III-7, III-8, and III-9 using the SASfit program).

The polydispersity in size of the scattered objects have been described by a log-normal distribution, $L(r, R, \sigma)$, where r is the radius, R the mean radius, and σ the variance:

$$L(r, R, \sigma) = \frac{1}{r\sigma\sqrt{2\pi}} \exp\left(-\frac{1}{2\sigma^2} \ln^2\left(\frac{r}{R}\right)\right) \quad \text{III-8}$$

Thus, neglecting the Virial effects (neglecting interparticles correlations), it is classical to define the global scattering intensity by the following relation:

$$I(q) = \phi(\Delta\rho)^2 V \int_0^{\infty} P(q, r) L(r, R, \sigma) dr \quad \text{III-9}$$

Then, considering that SiNPs are in excess and that, according to cryo-TEM, only SiNPs present in complexes display the ribbed texture attributed to chitosan chain binding, one can hypothesize that all the chitosan chains are involved in the complexes. Finally, one derives an average concentration of 1.8 chains of chitosan per nanorods. This result first shows that very few chains are needed to allow SiNPs organisation into nanorods. A second striking point is

that the average contour length of the biopolymers (~ 943 nm) is significantly higher than the average nanorods length (~ 250 nm) suggesting that chitosan chains are somehow wrapped around SiNPs. This could be permitted by adequation between the NPs surface curvature and the chitosan chains bending, controlled by its persistence length. This is possible since L_p (7.5 nm) $\sim R$ (8.5 nm). The number of NPs is $250 \text{ nm}/(8.5 \times 2) = 14.7$, corresponding to a chain length of 62 nm per NPs, i.e. slightly more than one NP circumference (53 nm).

This suggests that the chain wrapping around the SiNP is somehow helical. and thus adds rigidity explaining the single strand rod-like structure. This is in striking contrast with DNA packaging into chromatin, where an almost rigid polymer with bare persistence length (L_p) about 50 nm is compacted around small oppositely charged histone with $R \approx 3.5$ nm.^[70] Here a much more flexible polymer (intrinsic persistence length $L_p \approx 7.5$ nm) can be rigidified, only via electrostatic interactions, into rod like structure by nanoparticles with radius such as $L_p/R \approx 1$.

III.2.6 Conclusion

These results concerning the interaction between semi-flexible polyelectrolytes and 10 nm radius nanoparticles can be commented from different points of view. First, it can be seen as an exploration of the different structures obtained in the phase diagram resulting from an associative mechanism, here involving electrostatic complexation, and in given concentrations range, to phase separation, the so-called “complex coacervation”. The specificities of three kinds of structure are clearly cut for the three phase diagram regions; SANS or SAXS results are in good agreement with cryo-TEM. From these structures in the three regions of the phase diagram, we can try to imagine the mechanisms for a system of chains and particles with possibly strong interactions since all particles are multiply charged and all chain segments are charged.

The obtained shapes are summarized in Figure III-8. When chains are in excess, branched objects are formed made of linear short strands, while when NPs are in excess linear objects appear. In the stoichiometric range, which corresponds to the biphasic regime, more quasi-3D compact objects are formed. They are observed both in the supernatant and in the coacervate (dense) phase. This suggests that the dense objects are formed prior to phase separation. Their shape would be induced by the high number of particles per monomer in the stoichiometric complexes, while more expanded shapes corresponds to an insufficient number of NPs (part 1) or to an insufficient number of chains (part 2). In parts 1 and 3 as well as in the supernatant phase (part 2), it is very likely that individual complexes are formed. For the

coacervate (dense phase in part 2), it seems that individual objects of quasi-identical fractal dimension are obtained (in some cases they appear bigger than the complexes observed in the supernatant but we cannot extrapolate their global size), while they are just concentrated in richer phases. From these points of view, it seems that the shapes of the complexes are dictated by the monomer/NP ratio.

Second, the succession of different shapes is not observed with such consistency in most of the former works, and in particular, rodlike shapes as well defined as here - as seen at the light of SAXS measurements- are rarely observed. This could be due first to the use of a semiflexible polyelectrolyte, and second to a good adequation between persistence length and NPs radius. Thus a second important ratio appears to be L_p/R . Finally the structure of the chain itself may play a role: the chitosan chain possesses gentle helical shape, which can help a lot to make the structure more rigid. The helix could wrap gently the NPs. This rejoins some pictures and evaluation formerly proposed by theorists.^[114] However, while this was proposed for the interaction between one chain and one NP, this is observed here in the case of complexes involving several NPs per chain, where the structure formed renders easy precise check. The use of a natural polyelectrolyte polysaccharide involving such helical structure appears to be a good choice, although the chain anchorages at the surface of the NPs are not specific as they could be for proteins.^[119, 120]

Part B: Variation of persistence length and swapping charge sign

In the previous section, we have studied the complexation between semi-rigid chitosan and ~10 nm silica nanoparticles (SiNP). The intrinsic persistence length (L_p) of the positively charged chitosan is 9 nm in the given solvent condition, and the size of silica nanoparticle Ludox AM30 is 10 nm in radius (R), and this makes the characteristic ratio of $L_p/R \approx 1$. As seen in the previous part, it is possible to obtain well-defined 1D rodlike self-assemblies of SiNPs in the presence of an excess of NPs. Therefore, it is interesting to investigate the role of the polyelectrolyte persistence length on the complexes' dimensions and structure.

It is also interesting to check our conclusion on the semiflexible PELs case on a different polymer, well known in our group, Hyaluroan, which bears negative charge. This is also an opportunity of looking at the effect of the sign of the charges, since in this case the NPs will be silica particles bearing positive charges. Here as in all Chapter III, we keep the same order of magnitude. Smaller NPS being studied in the next chapters.

III.3 Effect of the Polyelectrolyte Persistence Length:

III.3.1 Complexation of 10 nm Radius Silica Nanoparticles with Flexible Poly-L-lysine

In order to vary the ratio L_p/R , the polyelectrolyte poly-L-lysine (PLL), displaying positive charges along its flexible backbone, was chosen, the choice of the second partner, 10 nm SiNPs, remained unchanged.

Within our experimental conditions; i.e., in the presence of an excess of salt (screened conditions), the characteristic ratio between the polyelectrolyte persistence length and NPs radius, L_p/R , is close to 0.1, with $L_p(\text{PLL}) \sim 1$ nm (PLL intrinsic persistence length).

The two components, PEL and NPs have been carefully characterized. For the sake of easier reading, we report these results to the end of the chapter.

III.3.2 Phase diagram of the PLL-SiNP system

SiNPs and PLL solutions were prepared separately in the presence of 0.2M KBr and were diluted at different concentrations. The PLL concentration was ranging from 0.001g/L to 10g/L, whereas that of SiNPs was varying between 0.01g/L and 20g/L. For each concentration pair, the same volume of the two components were mixed and shaken, so that the final concentrations of both components in mixed solution were the half of their initial

concentrations. For example, when 1g/L PLL mixing with 10g/L SiNP resulted in 0.5g/L PLL-5g/L SiNP in mixed solution, and to simplify the notation, it will be noted as PL0.5Si5, so as all the samples in the following sections.

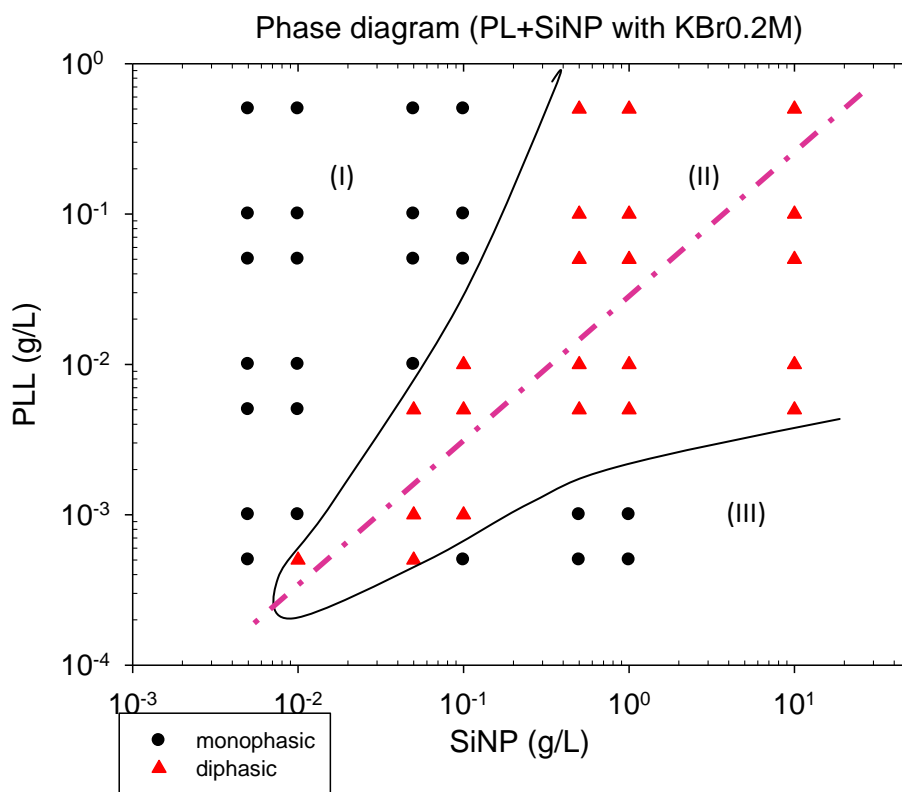


Figure III-13: Phase diagram (one week after mixing, solvent H₂O) of PLL-SiNP system as a function of the flexible polyelectrolyte and NP concentrations in the presence of 0.2M KBr at room temperature. The pink dash lines is indicative, that corresponds to charge stoichiometry $[+)/[-] = 1$

The samples were prepared as described above and were thoroughly shaken to ensure homogenization and then kept at the temperature of observation, here $T=20^{\circ}\text{C}$ (room temperature), for several days before visual examination. When a phase separation is observed, the samples are re-homogenized and set back to rest for a couple of days to confirm the observations. As shown in Figure III-13, there are two major behaviors in the phase diagram. The mixed solutions are monophasic and transparent in the presence of an excess of PLL (domain I), or of SiNP (domain III). A biphasic (domain II) is observed in the intermediate range, where one rich phase of white coacervate coexists with an upper dilute and limp phase (Figure III-14 (c), (d), (f)). The volume ratio of the two phases depends on the concentration ratio. The mixtures at boundaries of the two behaviors may slightly evolve with time. For example, PL0.1Si0.1, PL0.01Si0.1 and PL0.05Si1 samples were monophasic and transparent when initially mixed ($t=0$), but became biphasic at the end of observation

(typically a week after mixing, corresponding to the phase diagram) with the emergence of an unstable phase made of big colloids (Figure III-14 (e)). This phase disappears under shaking, but reappears at rest after a longtime (i.e. 5 days). It might suggest that the formed complexes in these samples are smaller and lighter than the quick precipitated ones in other samples.

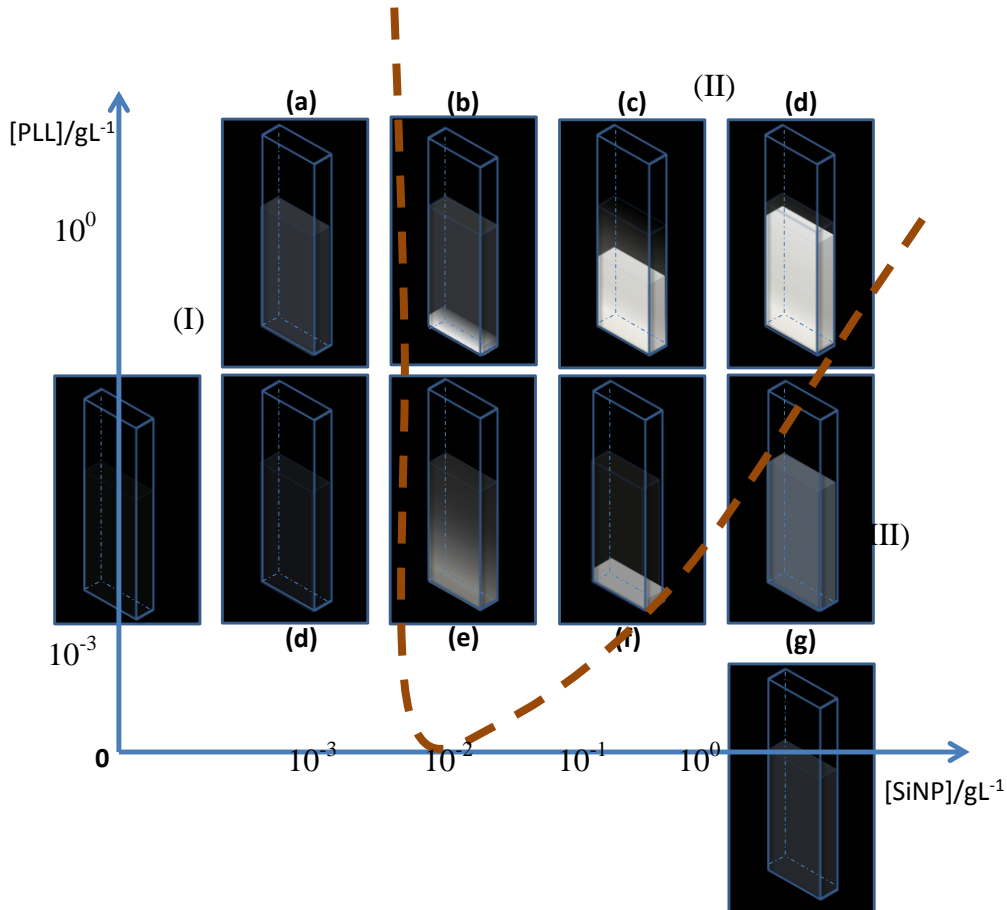


Figure III-14: Macroscopic observation of PLL-SiNP complexes in the different characteristic domains of the phase diagram

Actually, the term ‘excess’ is based on the relative position to the stoichiometric point in charges. Considering that SiNPs are hard spheres, a volume $V = \frac{4}{3}\pi R^3 = 2.6 \times 10^{-18} \text{ cm}^3$ (with $R=8.5 \text{ nm}$ as measured by TEM), a mass of $5.6 \times 10^{-18} \text{ g}$ and a surface area of $S_{\text{sphere}} = 4\pi R^2 = 908 \text{ nm}^2$ can be obtained. According to the supplier, the SiNPs have a surface charge density of 1 electron per nm^2 at $\text{pH}=9$, so they have 1.6×10^{20} negative charges per gram. PLL, as we can see from its chemical formula, has one positive charge every chain unit of 128 g/mol at fully protonated state, so PLL has 4.7×10^{21} positive charges per gram. If the stoichiometric point in charges is defined as the ratio of weight concentrations in g/cm^3 , $[\text{PLL}] / [\text{SiNP}]$, for which the two components neutralize their charges in the complex, we

can roughly estimate the stoichiometric point to be [PLL]: [SiNP]=1: 30. However, as observed in the phase diagram, the boundary of the phase separation occurs much earlier than this ratio, at about [PLL]: [SiNP] =1:10. This is probably due to the fact that at this pH=9, the PLL is only partially protonated, as the pKa of amine is 9~10. Another explanation comes from the Manning condensation increasing the distance between effective charges along the PLL chain to 7.13 Å, the Bjerrum length that is approximately three times larger than the monomer length and then than the distance between two charges. However it has been shown, at least in one case, PSS / lysozyme complexes^[121] that all counterions were decondensed and released in the solution, such that Manning condensation should not be accounted for.

III.3.3 Structure of the PLL-SiNP complexes: SANS characterization

Small angle neutron scattering (SANS) was used at Léon Brillouin Laboratory (beam line PACE). Three configurations were used as usual, 4.7m--13Å and 6Å, and 1m-- 6Å allowing a large q -range: $0.00318\text{Å}^{-1} < q < 0.369\text{Å}^{-1}$.

For each characteristic domain of the phase diagram, the choice of the samples to be prepared was dictated by the wish to get the higher scattering signal. All the samples were prepared in D₂O to have better contrasts and/or lower background and in 2mm thick Hellma cells. As a consequence, the state of phase may differ for the samples at the boundary between monophasic and diphasic domains. Their state before SANS recording is indicated in Table III-1. Importantly, for the biphasic samples, the two phases were measured separately in two different scattering cells after pipetting the upper fluid phase.

PLL (g/L)	NPSi (g/L)	KBr(M)	solvent	Domain of the phase diagram
5	0.01	0.2	D2O	(I)
5	0.05	0.2	D2O	(I)
5	0.1	0.2	D2O	(I)
1	0.05	0.2	D2O	(I)
1	10	0.2	D2O	(II)
0.5	0.05	0.2	D2O	(II)
0.01	0.5	0.2	D2O	(II)
0.01	1	0.2	D ₂ O	(II)
0.001	1	0.2	D ₂ O	(III)
0.01	1	0	D ₂ O	(III)
0.01	10	0	D ₂ O	(III)

Table III-1: list of samples measured by SANS

III.3.3.1 Samples with added salt (0.2M): high ionic strength

First, samples were prepared in the presence of added salt. The concentration of KBr was fixed to 0.2 M (PLL being purchased with Br^- counterions, excess salt KBr was chosen) in order to compare the structure of the complexes with that obtained previously in the chitosan-SiNPs systems in the presence of 0.2 M CH_3COONa .

First, note that all curves will exhibit the first oscillation occurring around $7 \times 10^{-2} \text{ \AA}^{-1}$ and associated to the form factor of the SiNPs cross-section, as soon as the silica content is high enough to have sufficient signal at large q .

I) Monophasic domain (III): a clear difference with semiflexible PEL (in the presence of an excess of SiNPs: samples PL0.001Si1 and PL0.01Si10).

Samples PL0.001Si1 and PL0.01Si10 are representative mixtures corresponding to the domain (III) of the phase diagram (visualized in the bottom right of Figure III-13 and Figure III-14). The ratio between the concentration of PLL and SiNPs is identical for both samples and is the same as that used for characterizing the complexes of SiNPs with semi-rigid chitosan in the same domain III. Both representative samples appear visually as a unique phase but are opalescent and were stable in an observation time scale of several months (as shown above in the visual phase diagram of Figure III-14 (sample g)).

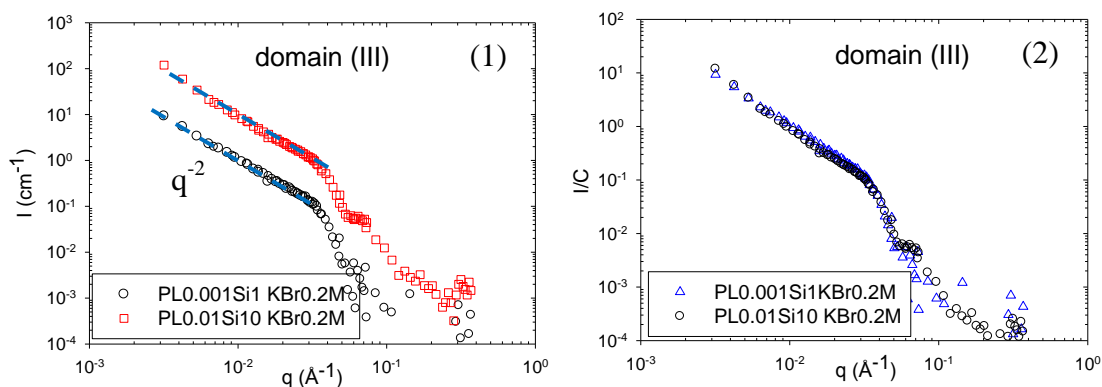


Figure III-15: SANS patterns (1) for representative samples PL0.001Si1 and PL0.01Si10 (domain III of the phase diagram-excess of NPs); (2) in the presence of 0.2M KBr; normalized by SiNP concentration

The scattering patterns obtained using SANS and showed in Figure III-15 do not show any Guinier regime with a plateau at low q associated to the finite size of the complexes but instead a q^{-2} regime behavior in an extended q range, followed by the first oscillation associated to the form factor of the cross-section of the 10 nm radius SiNPs. The variations of the ratio I/C_{SiNP} of the scattered intensity over SiNP concentration are illustrated in Figure

III-15(2). A first mostly interesting feature is that the *scattering curves superimpose on each other* in the whole q -range indicating that *the complexes*, which are larger than 30 nm, *have the same ramified structure*. A second is the low q slope (q^{-2} dependence) suggesting a Gaussian distribution for the SiNPs inside the complexes, or branched aggregates.

We have here a first result which **profoundly differs from that obtained with the semiflexible polyelectrolyte chitosan** (which showed a q^{-1} law due to the formation of nanorods within the same experimental conditions). This suggests a **major role played by the polyelectrolyte persistence length**. Here, PLL, a flexible polyelectrolyte, with $L_p/R \sim 0.1$, cannot induce the formation of 1D structures.

2) **Monophasic domain (I): medium size and medium ramification** (excess of PLL: representative samples PL5Si0.01, PL5Si0.05 and PL5Si0.1)

These three representative samples (not studied in the phase diagram determined for H₂O) that differ from their content in NPs are all homogeneous and transparent (see samples d in visual diagram Figure III-14).

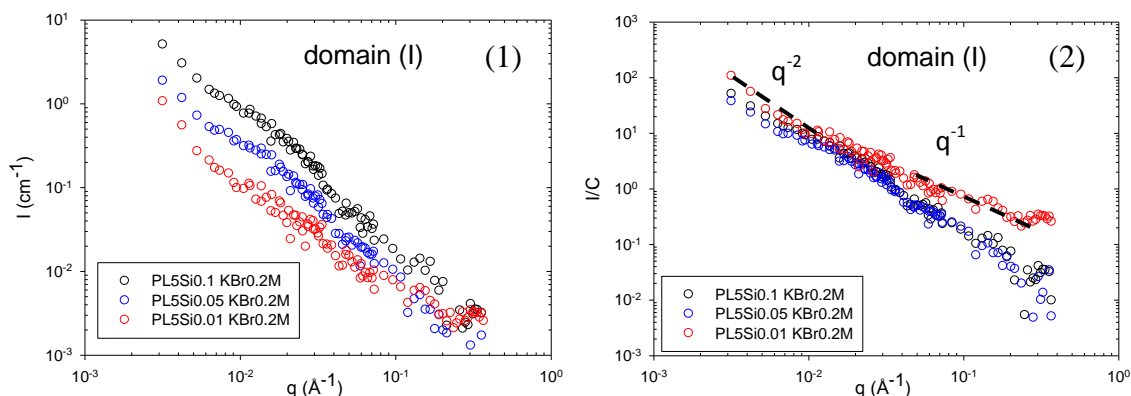


Figure III-16: SANS patterns for representative samples PL5Si0.01, PL5Si0.05 and PL5Si0.1 (Domain I-excess of PLL) in the presence of 0.2M KBr (1); normalized by SiNP concentration (2)

For the lowest SiNP content (PL5SiNP0.01, red curve), the scattering profile exhibits a transition between a Gaussian q^{-2} low q regime, and a q^{-1} domain at higher q characteristic of the PLL rodlike behavior for distance smaller than its persistence length (see Figure III-16 (2)). This ensemble of variations is characteristic of the PLL wormlike chain behavior inside the complexes, the signal of the SiNP being negligible. **When the SiNP content is increased** (blue curve) the high q^{-1} regime is masked and we observe the decrease associated to the cross-section of the SiNPs (see Figure III-16 (2)). The maximum observed at $q \sim 2 \times 10^{-1} \text{ \AA}^{-1}$ may correspond to the second oscillation associated to the form factor of the SiNPs.

Figure III-17 displays over a quite larger q range the scattering pattern of the representative PL5Si0.1 sample, obtained by coupling SANS measurements with static light scattering (SLS, low- q data, rescaled by the ratio of contrasts of the two techniques (see Chapter II). The SLS data, as they extend towards smaller q , display a plateau associated to the Guinier regime of the complexes. Using a classical Zimm analysis, we obtain $R_G=268\text{nm}$ and $M_w=1.69\times 10^9\text{g/mol}$ for the so-formed complexes. The latter can be estimated to be composed of 450 SiNPs at these concentrations, if we neglect the signal arising from the PLL chains in excess (first approximation).

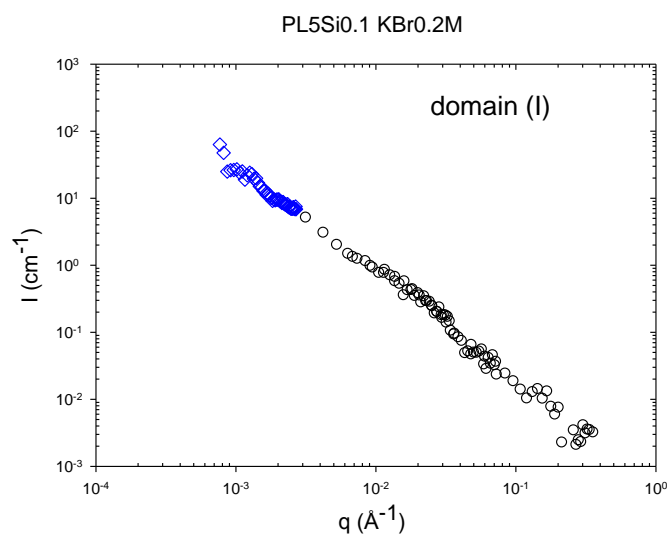


Figure III-17: combined SLS and SANS measurements for sample PL5Si0.1 with 0.2M KBr. The SLS curve was rescaled by the appropriate factor (Chapter II) to match the SANS intensity (cm^{-1})

3) Biphasic domain (II): higher sizes, higher compactness (case of the representative samples PL0.01Si0.5, PL0.01Si1, PL1Si10 in the presence of KBr0.2M)

A first set of samples PL0.01Si0.5 and PL0.01Si1 are both biphasic samples although they do not exhibit a clear interface between the lower and upper phases (Figure III-14 (see samples e)). As it was too difficult to separate the coacervate phase from the supernatant one, the SANS experiments were performed on the entire samples.

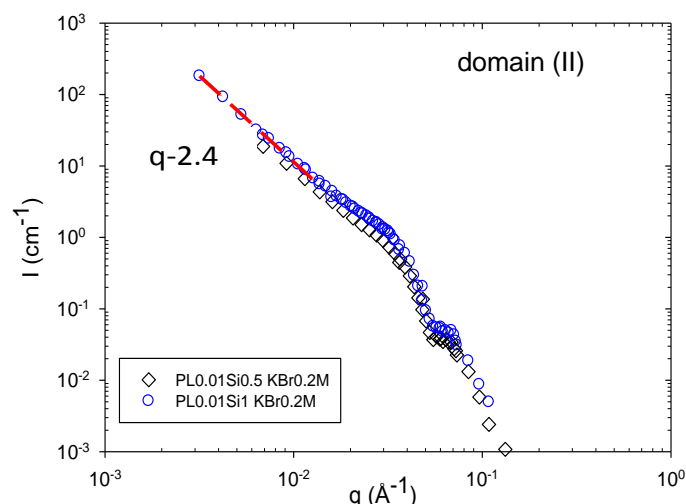


Figure III-18: SANS patterns for samples PL0.01Si0.5 and PL0.01Si1 in the presence of 0.2M KBr

The samples were shaken to be temporarily homogenous, but they might have undertaken phase separation during the measurement. Therefore, the scattering pattern corresponds to the sum of the two contributions: the signal of the coacervate phase as well as that of the supernatant one.

For both samples the scattering varies as a $q^{-2.4}$ law, characteristic of fractal aggregates which are larger than 30 nm since their scattering curves do not exhibit a Guinier regime at low q . The value of the characteristic exponent is smaller than that measured in the coacervate phases in the presence of chitosan, which indicates a less compact structure with PLL at these concentrations. This could explain, only in part, why the interface between coacervate and supernatant is not well defined. This exponent 2.4 is, however, clearly suggests more compact structures than obtained in monophasic domains (I) and (III).

A second representative kind of sample PL1Si10 is more concentrated in polylysine and SiNPs: here the separation between the transparent dilute supernatant phase and the dense and viscous one takes place readily (with a sharp interface). The volume of the coacervate (lower phase) was large enough to ensure the full filling of the 2 mm scattering cell and thus to be studied by SANS (see Figure III-19). The supernatant was not attained by the beam but was not removed from the top of the cell to keep the coacervate hydrated during the measurement.

The exponent of the power law is found close to -2.7, as in the chitosan coacervate systems with similar SiNP concentration, characteristic of rather compact fractal aggregates larger than 30 nm.

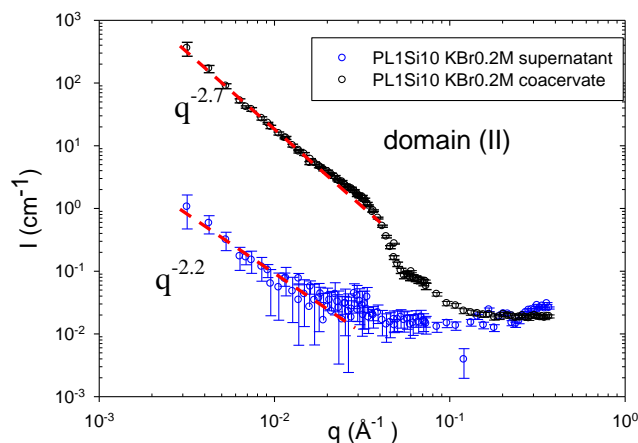


Figure III-19: SANS pattern for representative sample PL1Si10 in the presence of 0.2M KBr (black dots: coacervate phase-domain #II of the phase diagram; blue dots: supernatant of the same sample)

4) Summary on all phases

The results for flexible PEL with similar SiNPs show a clear difference in domain III: the rodlike structure cannot be observed. In the two other domains on the contrary we see mainly important similarities in terms of degree of ramification, as well as in term of phase separation behavior.

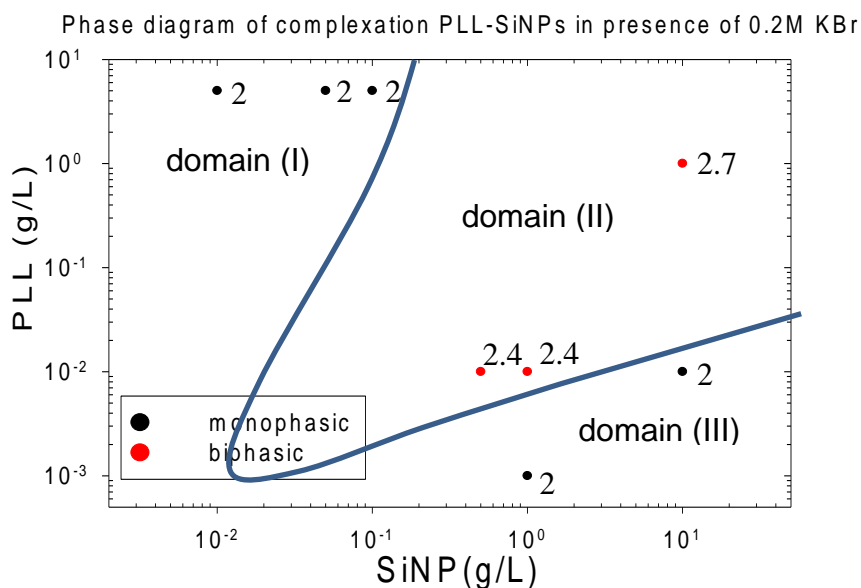


Figure III-20 : Summary of different fractal dimension values corresponding to the samples in the phase diagram

III.3.3.2 Samples with no added salt: low ionic strength

To compare with the case of no added salt, we took representative samples characterized by the same PLL/SiNPs concentration ratio.

In the visual phase diagram (which we did not build systematically in whole), we qualitatively retrieve the same characteristic domains, with boundaries only slightly shifted (to the right hand side by about 4g/L in term of SiNP concentration), for the limit between domain II and III for example. In other words more silica is necessary in absence of salt. Visual observations also indicate that the complexation between the two partners is weaker in the absence of salt, as the coacervate phases are less turbid in absence of 0.2 M KBr.

In the monophasic domain (III) - excess of SiNPs: as shown in Figure III-21, samples with a lower $C_{\text{PLL}}/C_{\text{SiNP}}$ ratio exhibit a Guinier regime at low q associated with the finite size of individual SiNPs. However, after waiting a longer time (3 days) we eventually –observe the beginning of a very small upturn at very low q . When increasing the number of PLL chains, When the ratio between the two concentrations, $C_{\text{PLL}}/C_{\text{SiNP}}$, is increased, one observes the formation of NP self-assemblies with a fractal dimension close to -1.3; i.e., lower than that obtained in the presence of salt. This result indicates **that the complexation is weaker in the absence of salt.**

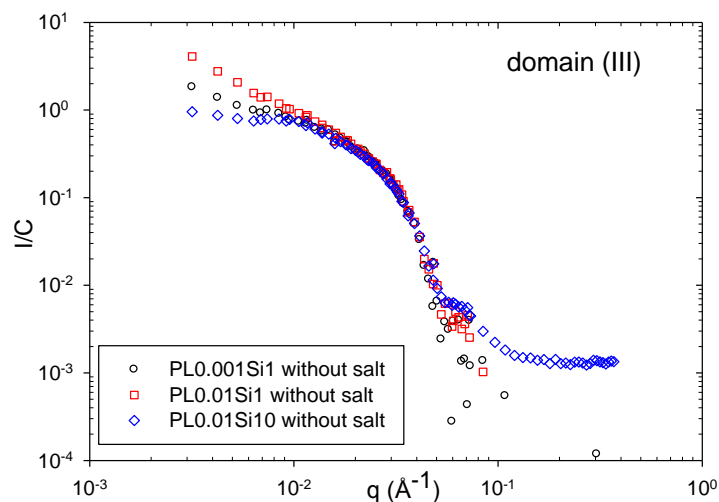


Figure III-21: SANS patterns normalized by the SiNP concentration for representative samples PL0.001Si1, PL0.01Si1 and PL0.01Si10 without addition of salt

A biphasic domain (II) is also observed for appropriate concentration ratios between two partners, like for the representative sample, PL1Si10. However, without addition of salt the coacervate phase is more fluid at equilibrium than that in the presence of an excess of salt. After vigorous shaking, the coacervate phase can still be mixed with the supernatant one,

leading to a quasi-homogenous solution. This was not possible for the same sample in the presence of 0.2 M KBr.

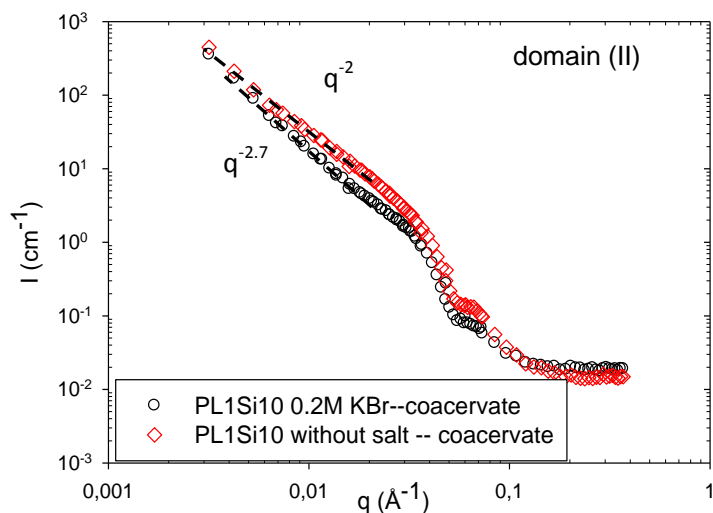


Figure III-22: SANS patterns obtained on coacervates for sample PL1Si10 in the presence of 0.2M KBr and without addition of salt

SANS results (Figure III-22), showing a variation of the scattered intensity with q characterized by a power law with an exponent equal to -2 instead of -2.7 in the presence of salt, corroborate the previous observations indicating that salt-free complexes are less compact. One explanation is that electrostatic repulsions between NPs inside self-assemblies are not totally screened. Therefore, complexes can adopt a looser structure. This will be discussed in more details in the General Summary III-5.

III.4 Swapping the Sign of Charges: Interaction between Semi-flexible Polyanion Hyaluronan and Positively Charged Silica Nanoparticles

III.4.1 Introduction

In the two previous parts, the polyelectrolytes - semi-rigid chitosan or flexible poly-L-lysine - were polycations, whereas the silica particles carried a more pronounced negative surface charge density, this makes the charge ratio of PEL/NP=+/-.

In this section, we would like to reverse the sign of charges of the two components, which means to complex a polyanion with positively charged nanoparticles. In the first place, the studied nanoparticles are still silica nanoparticles but another surface modification was performed to bring positive charges onto their surface. The chosen partner is the polyanion hyaluronan, a natural polyelectrolyte polysaccharide displaying a semi-flexible backbone characterized by an intrinsic persistence length of $L_p \sim 5 \text{ nm}^{[108]}$ and carboxylic groups that provide a negative charge every repeating unit, i.e., every 10.2 \AA (no Manning condensation in this case). Two molar masses were used in order to compare the effect of the chain length on the wrapping of the particles. Also, two ionic strengths were used to see whether it would affect the complexation behaviors as observed with the PLL/SiNPs system.

The materials, SiNP and hyaluronan have been carefully characterized. To make the manuscript easier to read, the results are transferred to the end of the chapter.

Solutions of hyaluronan and SiNPs were dissolved separately in either distilled water or in the presence of 0.1M NaCl, and then diluted at various volume ratios to obtain the desired concentrations at constant ionic strength. The concentration of hyaluronan is ranging from 0.01 to 1.5 g/L, while that of SiNPs from 0.05 to 10 g/L.

III.4.2 Sequence of Phase Behaviors

In this part we will recognize the phase behavior identified in the former sections:

- (I) monophasic and transparent region (Domain (I)) at low SiNP content.
- (II) a two-phase region at intermediate NPs content
- (III) and finally another monophasic domain in excess of SiNPs.

Figure III-23 show these domains for the 92K hyaluronan, first without addition of salt. Some additional comments can be made on the phase separation: For more concentrated samples, as for representative sample H1.5Si10, the separation was observed immediately after the mixing of the two components. For other samples, this process is slower: For example, one has to wait several days to observe a white and thin coacervate phase at the bottom of the cell for samples with less NPs (H0.1Si2). For some other samples, the macroscopic phase separation between two well-defined phases separated by a net interface is not very clear. We can also observe some smoke-like substance suspended in the solution with samples evolving slowly with time and showing a thin layer of white coacervate only after a long time (i.e. one week), especially for mixtures H0.05Si2 and H0.1Si6. It shows the same sequence of phase behaviors for the system in presence of 0.1 M NaCl, but the boundary between domains (II) and (III) is shifted to lower hyaluronan concentrations.

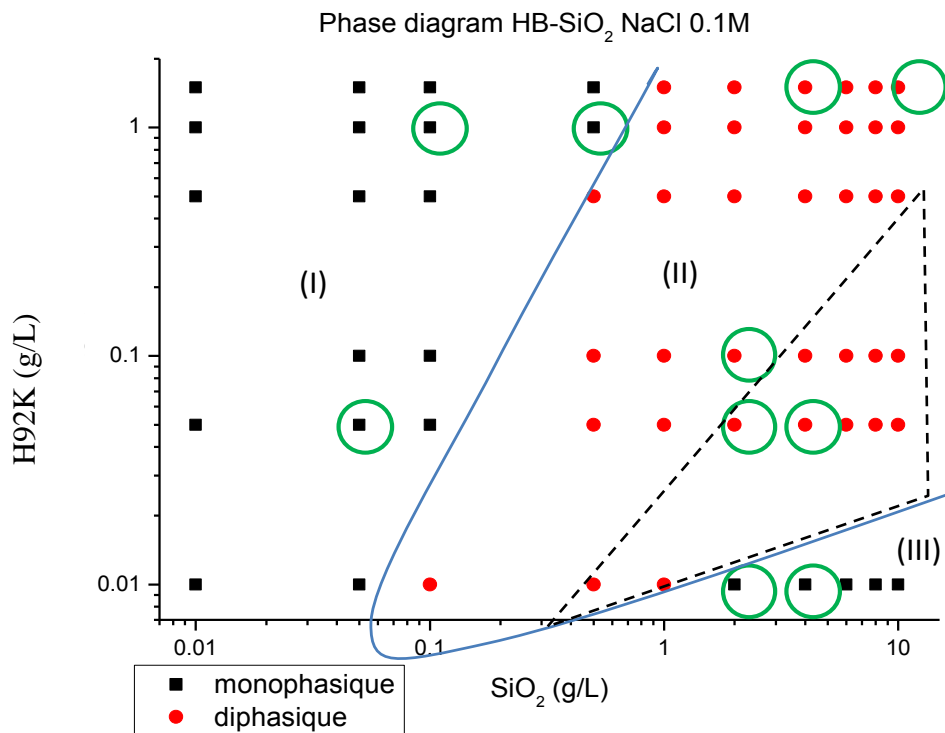
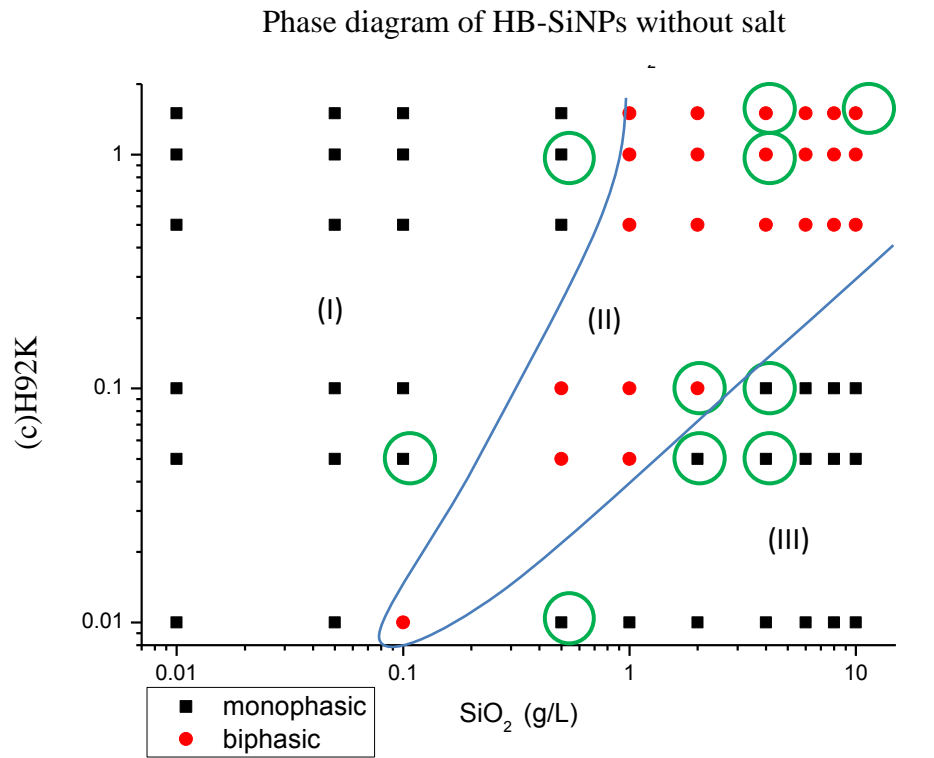


Figure III-23: Sequence of phase behaviors in the 92K Hyaluronan concentration (vertical axis) / positively charged SiNPs (horizontal axis) at pH=4 and in the presence of 10^{-4} M HCl plane, at room temperature, without addition of salt (above) and with 0.1M NaCl. The points surrounded by green-circles correspond to samples studied by SANS

For small hyaluronan molecular weight (40K), the same shift was observed for 0.1 M NaCl (Figure III-24 and Figure III-25). Strikingly, the lower bound of domain (II) is quasi-**vertical**, at [SiNP]=0.5g/L or [SiNP]=0.1g/L in the presence or not of added salt (this will be discussed in the Conclusion).

In summary we have a neat effect of the addition of 0.1 M NaCl: an increase of the area of the biphasic domain. This obviously suggests that the electrostatic screening of the charges induces an easier complexation: the electrostatic repulsion is more balanced by the Van der Waals attraction (see Summary III-5). This confirms the observations for the PLL/SiNPs mixtures; this behavior is independent on the chain flexibility and on the sign of charge.

The chain flexibility may however play a role in the structure of the complexes: this is established in the next paragraph.

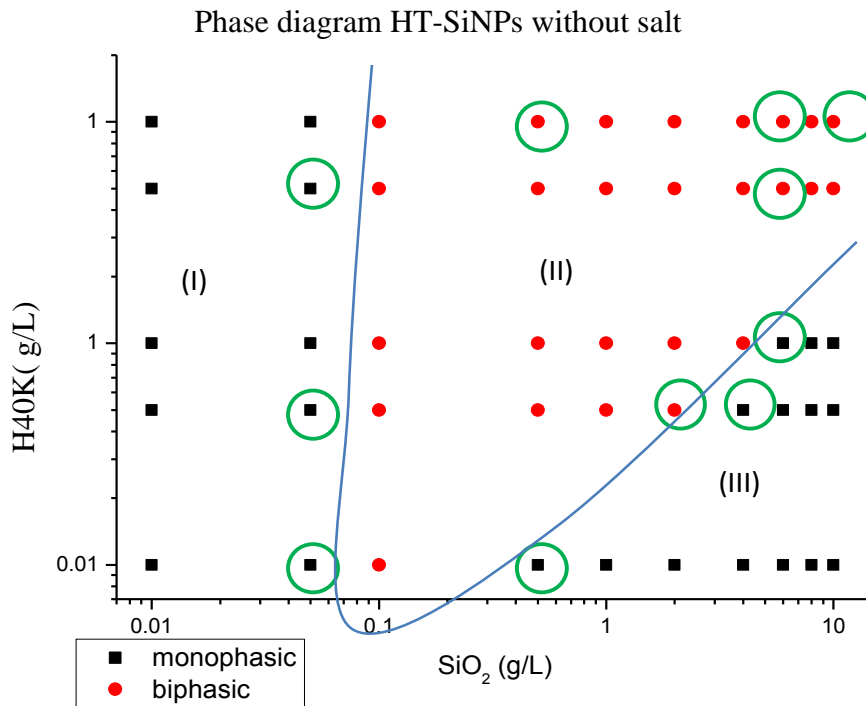


Figure III-24: Phase diagram of mixed 40K hyaluronan TBPM-SiNP system without salt addition

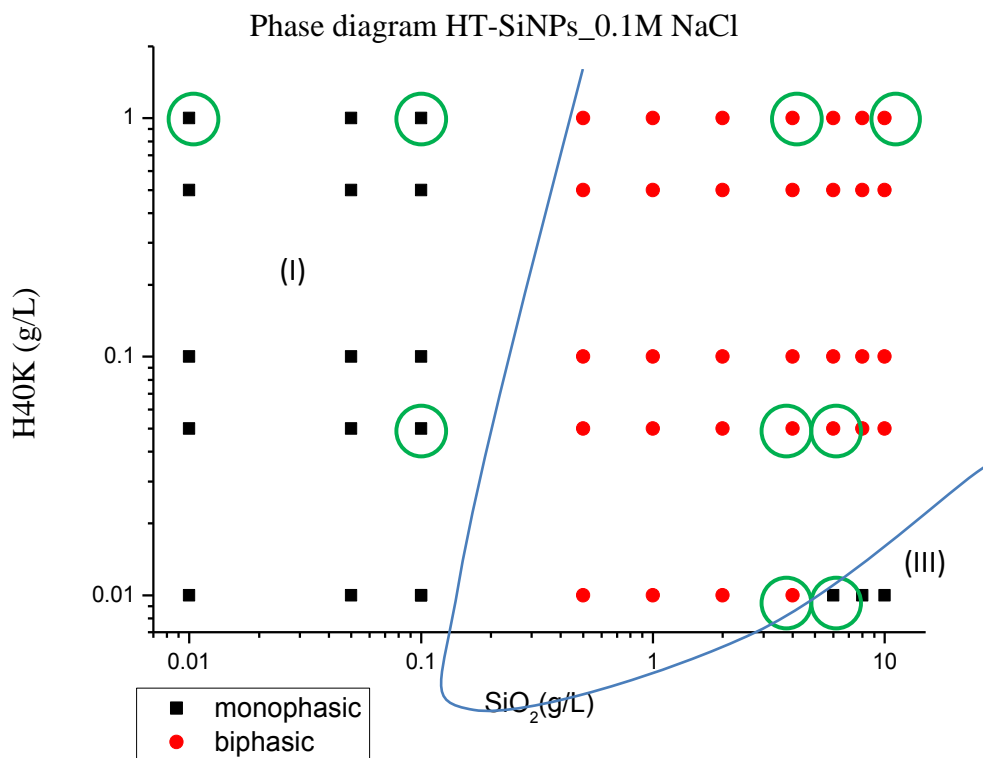


Figure III-25: Phase diagram of mixed 40K hyaluronan TBPM-SiNPs system in the presence of 0.1M NaCl

III.4.3 Structure of the Hyaluronan/SiNP complexes: similarities with the inversed charges case

SANS experiments were performed at Saclay on the beam-line PACE using three different configurations: 4.5m-17Å; 3m-12Å; 1m-6Å, allowing a total q-range varying from 2.4×10^{-3} to $3.7 \times 10^{-1} \text{Å}^{-1}$. It is important to recall that the SANS signal is mainly arising from the SiNPs as expected from the pretty high value of the particles volume. The effect of the hyaluronan molecular weight (92K and 40K), i.e., of the hyaluronan chain length on the particles wrapping, as well as that of the ionic strength (with or without addition of 0.1 M NaCl) was investigated. The choice of the selected representative mixtures depends on the available volume of the coacervates as well as on the content of the NPs determining for the quality of the signal.

III.4.3.1 92 K Hyaluronan/SiNP system without addition of salt

The 92 K hyaluronan chain length is, $L_c=235$ nm, a value larger than the particles circumference (~ 100 nm), makes complexation between HA and several NPs possible.

a) Monophasic domain (III): excess of SiNP

First the scattering profiles collected for representative mixtures in the presence of an excess of NPs are presented in the following Figure III-26.

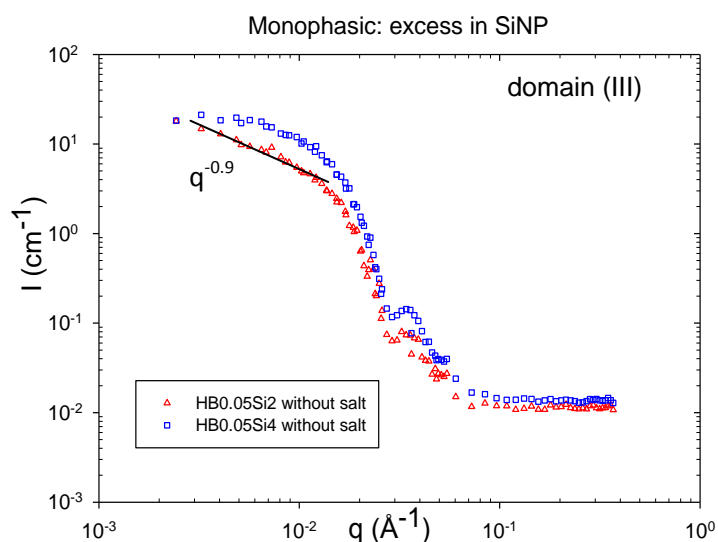


Figure III-26: SANS from salt-free 92K hyaluronan-SiNP mixtures in domain III

Representative sample H0.05Si2 is situated close to the boundary between the biphasic (II) and the monophasic domain (III). Its neighbor, H0.05Si4, was prepared with the same HA concentration but the concentration of SiNPs is twice (hence an identical incoherent

background level at high q , not subtracted, indicating a similar content of hydrogen arising from the polymer). Both curves exhibit the same first oscillation associated to the form factor of the particles. Note that no precipitation occurred during the measurements.

The curve obtained for sample H0.05Si4 exhibits a Guinier regime in the low q range. A Zimm analysis q (Figure III-27) gives $R_G = 22.2\text{nm}$, a value slightly larger than that of individual Ludox CL SiNPs, 16 nm. This discrepancy may be attributed to the wrapping of several HA chains on the surface of the particles.

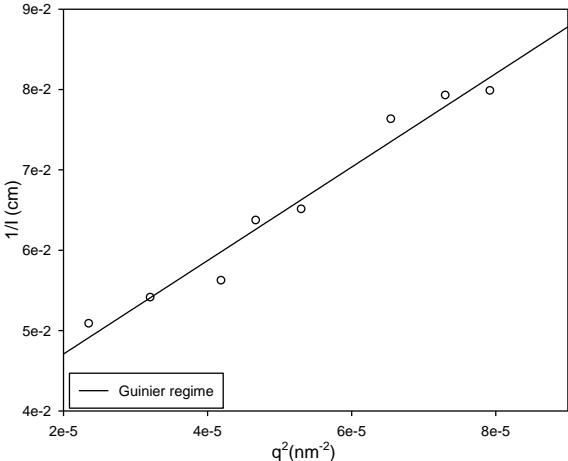


Figure III-27: Guinier plot obtained for sample H0.05Si4

On the contrary, the scattering profile of sample H0.05Si2 (more silica) exhibits an upturn towards the small q indicating a complexation process between HA chains and several nanoparticles. The apparent fractal dimension is 0.9, a value characteristic of 1D nanostructures.

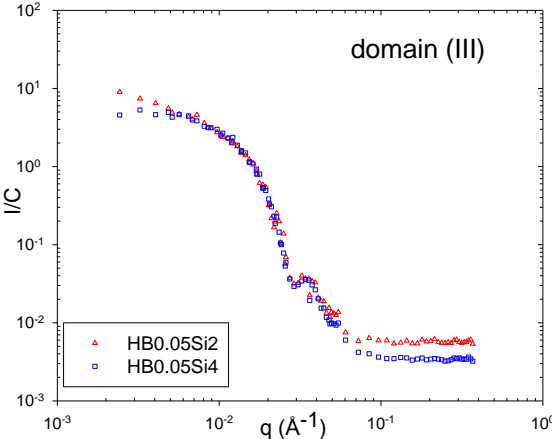


Figure III-28: SANS pattern for representative samples H0.05Si2 and H0.05Si4, normalized by the SiNP concentration (domain III)

Such q^{-1} variation at low q is much better defined when the HA content is increased (Figure III-29). In this case, it can be fitted by a rigid rod model in order to obtain the linear mass density of the aligned SiNPs in the complexes, M_L . We obtain $M_L = 19305\text{g/mol}/\text{\AA}$, five times lower than that calculated for straight monolayer wires of SiNPs in close contact: $(\text{mass/diameter})_{\text{SiNP}} = 3.38 \times 10^7\text{g/mol}/340 = 99411\text{g/mol}/\text{\AA}$; a result suggesting that the unidimensional complexes have a rather loose structure of “dashed rods” (in absence of salt).

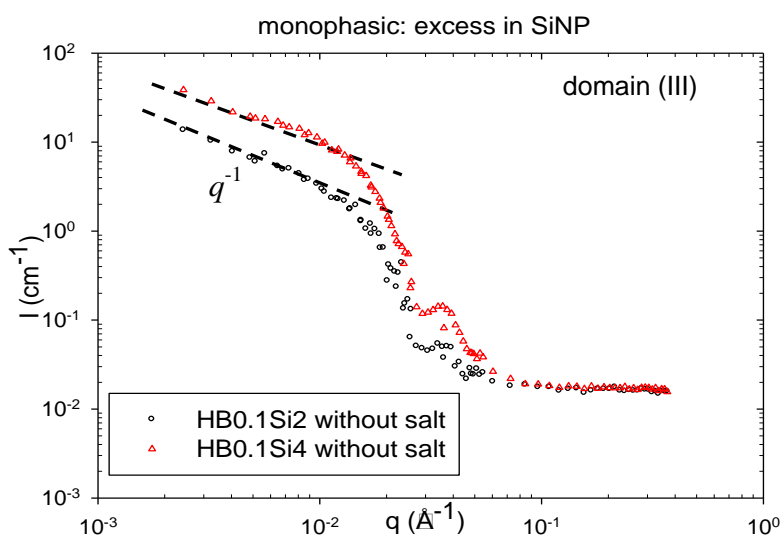


Figure III-29: SANS patterns of sample H0.1Si2 and H0.1Si4 without addition of salt. Samples, mixed in D_2O , were monophasic during the spectrum recording

b) Monophasic domain(I): Representative sample H1Si0.5 with an excess of polyelectrolyte

Due to the pretty low scattered signal in the low q range, it was not possible to collect data in this part of the profile and then to determine the complexation characteristics. However, the lowest q part at medium q (Figure III-30) shows a slight upturn compared to sample H0.01Si0.5 of same SiNP concentration in domain (III) suggesting a higher fractal dimension and thus a more ramified structure, as observed in former systems.

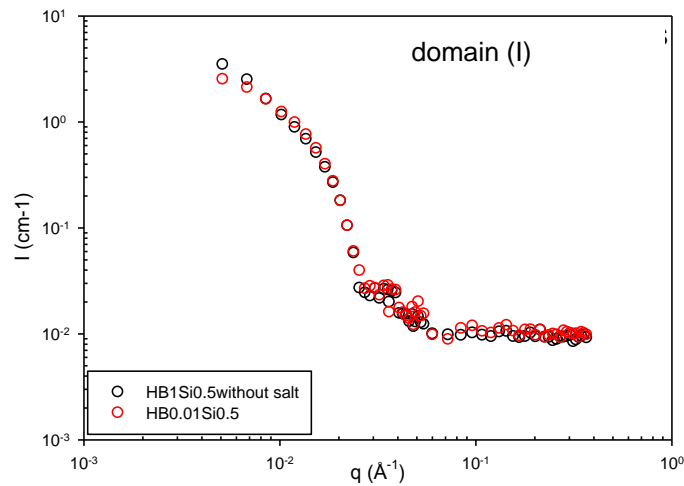


Figure III-30: SANS patterns for samples H1Si0.5 and H0.01Si0.5 without added salt

c) Biphasic domain:

In this domain reminiscent of complex coacervation, the separation can be quick, and the supernatant very clear and transparent, for relatively large amount of NPs. For example, for sample H1.5Si10 (Figure III-31), the scattering intensity is negligible for the supernatant. For the coacervate, it varies clearly as a $q^{-2.2}$ in the low q range.

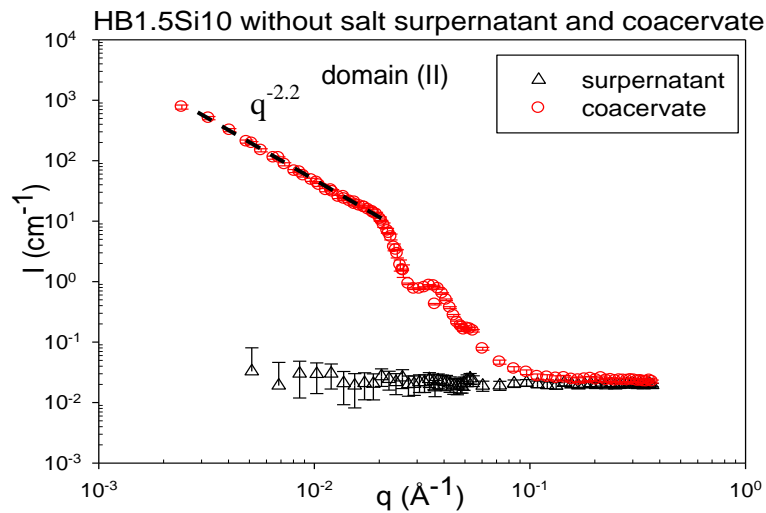


Figure III-31: SANS patterns obtained for sample H1.5Si10: coacervate and supernatant. For lower NPs contents samples, the supernatant stays turbid and the scattered intensity varies like in the coacervate with a $q^{-2.2}$ law (see Figure III-32). Loose ramified objects are observed both in the supernatant and in the coacervate. This suggests, as observed for the chitosan/SiNP systems, that the dense objects are formed before separation.

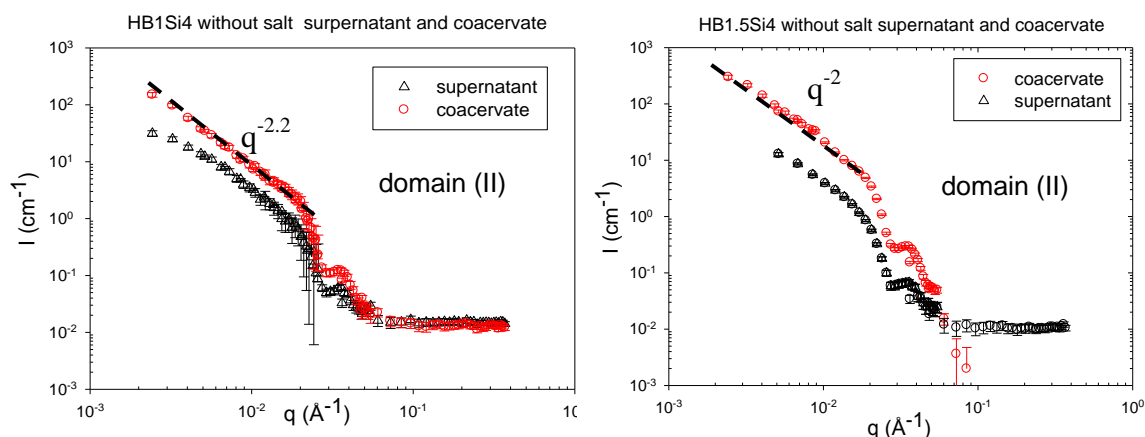


Figure III-32: SANS patterns of samples H1Si4 and H1.5Si4 without addition of salt: supernatant and coacervate spectra

There is however a difference between coacervate and supernatants, for which one observes the slight beginning of a Guinier regime. A basic analysis for the supernatant of sample H1Si4 gives $R_G=63$ nm. Complexes remaining in the supernatant may have an overall smaller size, even if their fractal dimension is the same than for coacervates.

III.4.3.2 Effect of salt addition on 92 K Hyaluronan/SiNP systems (0.1M NaCl): increasing compacity in different ways.

The effect of salt addition on the phase diagram, suggesting the importance of electrostatic screening already evoked above in this Chapter, is confirmed by SANS:

- in both monophasic domains it leads to complexes larger than 30 nm. In monophasic domain (I), the variation of the scattered intensity with q is a power law with an exponent equal to -1.5; i.e., larger than that measured without addition of salt. Conversely, in monophasic domain (III), the scattering displays the same characteristic q^{-1} rodlike behavior as for salt-free solutions, but with a higher linear mass density: $M_L=30807$ g/mol/Å. This is however still lower than that calculated for compact straight necklaces of SiNPs in close contact.

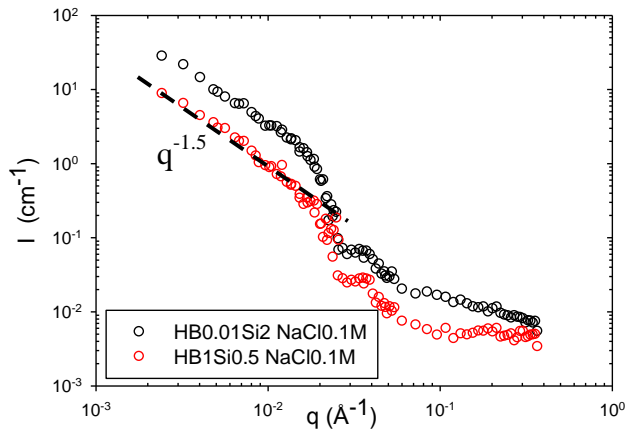


Figure III-33: SANS patterns for samples H0.01Si2 (domain III) and H1Si0.5 (domain I) in the presence of 0.1M NaCl

- in biphasic domain (II) (Sample H1.5Si10), the separation, much faster in the presence of salt. The white coacervate falls down immediately and is very viscous and gel-like, whereas the supernatant is very clear, transparent, and fluid. This is accompanied by a larger fractal exponent value for the coacervate (Figure III-34): -2.4, a value definitively larger than -2.2 or -2 determined for salt-free mixtures. The scattering of the supernatant is negligible.

Interestingly, for the first time we see a peak. Its abscissa $q^*=0.018\text{\AA}^{-1}$ corresponds to a distance $d=2\pi/q^*=350\text{\AA} \sim 2R$, between two particles in close contact.

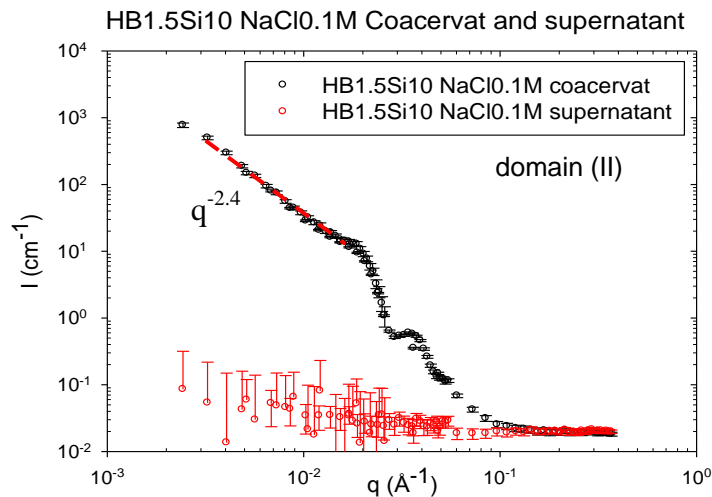


Figure III-34: SANS for sample H1.5Si10 with 0.1M NaCl for both coacervate and supernatant phases. The black arrow indicates the maximum at $q^* = q^*=0.018\text{\AA}^{-1}$

III.4.3.3 Effect of the Hyaluronan Chain Length: 40K HA/SiNP

Salt-free system: short length limits NPs aggregation

a) Monophasic domain (III): excess in SiNP

Although both representative samples H0.05Si4 and H0.1Si6 are opalescent, with a degree of turbidity higher than for SiNPs alone at the same concentration, the SiNPs show no aggregation in the SANS q range (Figure III-35: both spectra gives $R_G=17\text{nm}$, and $M_w=3.2\times 10^7\text{g/mol}$ (values characteristic of individual NPs)).

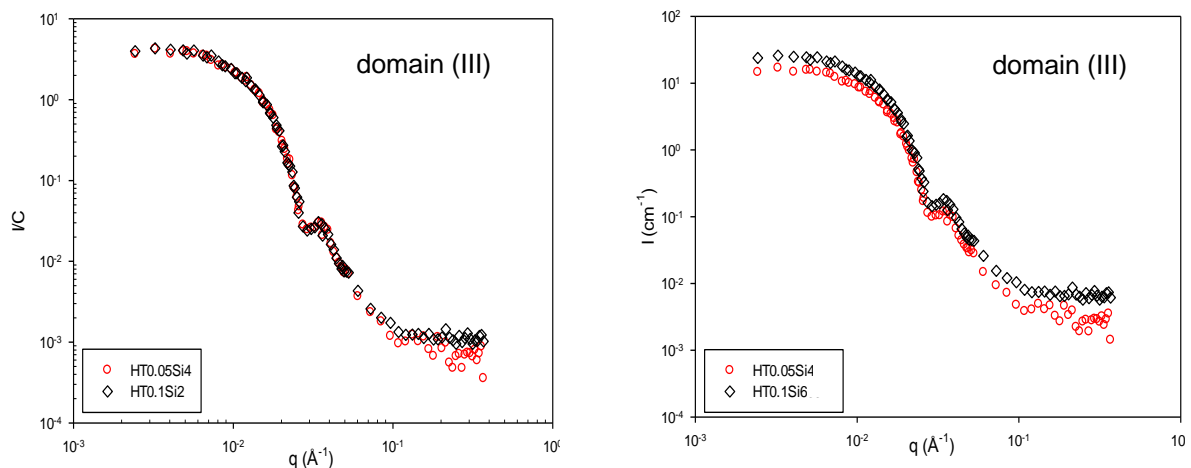


Figure III-35: SANS patterns for samples H0.05Si4 and H0.1Si6 without addition of salt (a) and normalized by the SiNP concentration (b)

b) Monophasic domain (I): excess in hyaluronan:

The quality of the scattering pattern obtained for the representative sample H0.5Si0.05 is poor, but we can distinguish the Guinier regime associated to individual SiNPs.

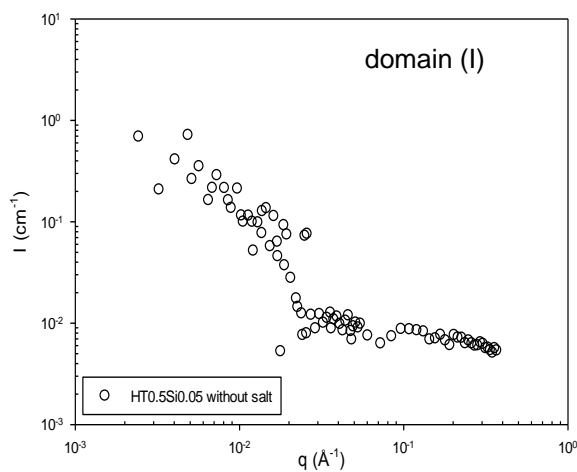


Figure III-36: SANS pattern for salt-free sample H0.5Si0.05

The important result is: neither in monophasic domains (I) nor in monophasic domain (III), is complexation of several SiNPs observed for short HA chains. A simple calculation shows that

the average contour length, $L_c \sim 100$ nm, of 40K hyaluronan chains is slightly shorter than the silica NP circumference (138 nm), suggesting that they can wrap around SiNPs but are too short to bridge two or more of them.

c) Biphasic domain (II): representative samples H1Si6 and H1Si10 without salt addition

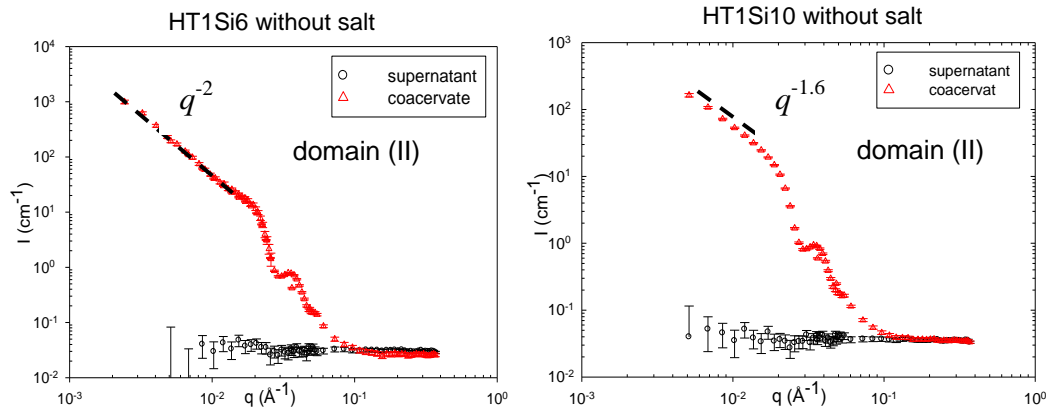


Figure III-37 : SANS patterns of samples HT1Si6 and HT1Si10 without addition of salt, for both phases: coacervate and supernatant

Though SiNP aggregation is not observed at all in monophasic domains, the characteristic biphasic domain (II) is still observed. In particular, for high enough NPs content (far from the lower quasi-vertical domain boundary), the interface between coacervate and supernatant is well defined and sharp. In this case, SANS experiments could be performed separately on the supernatant and the coacervate. For representative samples H1Si6 and H1Si10, the supernatants are very poor phases as shown by their pretty low scattering (Figure III-37). While for sample H1Si6 the fractal dimension in coacervates is close to 2, suggesting a ramified structure (reaction limited aggregation), a lower dimension ($q^{-1.6}$ law) obtained for the lower fraction of HA in H1Si10 reveals a looser particle-particle connection.

The most interesting conclusion here is that even short chains can complex several NPs in coacervates; i.e., in a regime where NPs are concentrated and close to each other.

III.4.3.4 Effect of salt for the short Hyaluronan 40K-SiNP system: increasing compacity.

We will briefly summarize the main results for this case.

In monophasic domain (III), **no difference with the no salt case** (superimposed spectra in Figure III-38): the absence of complexation between several particles is also observed.

In monophasic domain (I), **the complexation seems favored by salt**. In spite of poor counting statistics (the low concentration of SiNP), we detect a $q^{-1.3}$ law.

Finally, in the biphasic domain (II), we observe both **an enhancement of phase separation and of complex compactness** due to salt. We could again distinguish:

- Representative Samples H0.05Si6 and H0.05Si8 close to the boundary with the monophasic domain (III), for which one has to wait a while (i.e. 3 days) before observing a phase separation. The interface between the two phases is not sharp, the supernatants are opalescent and turbid, and the coacervate phases had a too small volume to focus the neutron beam. The results are obtained on the supernatant only: one observes a $\sim q^{-1}$ law in Figure III-40. The degree of ramification increases a little with the SiNP concentration ($q^{-1.2}$). This behavior was observed several times in the presence of an excess of SiNPs in monophasic domain (III). If the precipitated phase is made of charge neutralized complexes, we may believe that complexes in the supernatant are made of few polyelectrolyte chain and abundant SiNPs.
- Representative samples H1Si6 and H1Si10, more concentrated in HA, and where the phase separation is more pronounced (transparent supernatants, viscous coacervates) show ramified structures in the coacervate with an exponent close to -2.2. Once again, this exponent increases when salt is added.

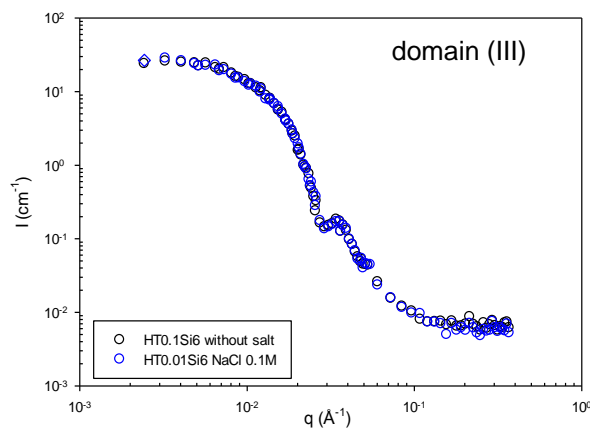


Figure III-38 : SANS pattern in domain III for sample HT0.01Si6 in the presence of 0.1M NaCl, compared to spectrum without addition of salt (same concentration)

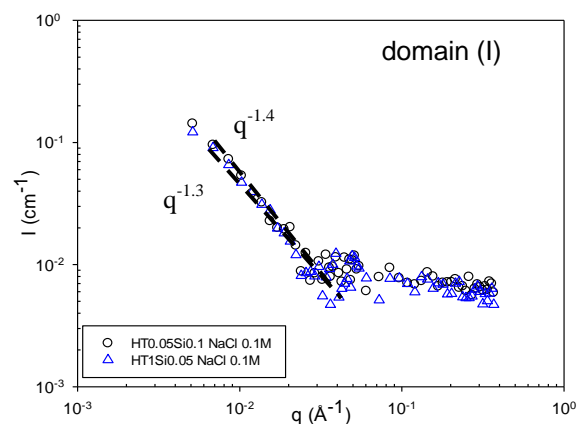


Figure III-39: SANS pattern in domain I for samples H0.05Si0.1 and H1Si0.05 in the presence of 0.1M NaCl

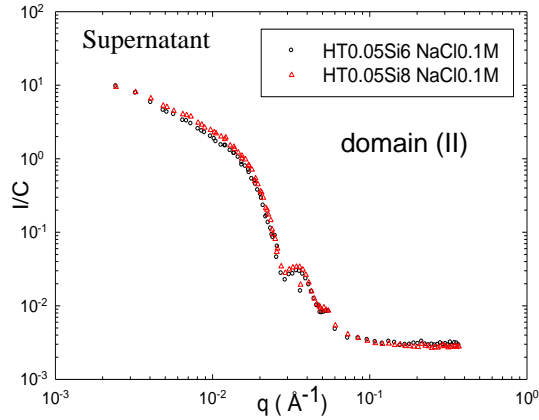


Figure III-40 : SANS patterns in domain II for supernatants of samples H0.05Si6 and H0.05Si8 in the presence of 0.1 M NaCl, normalized with SiNP concentration

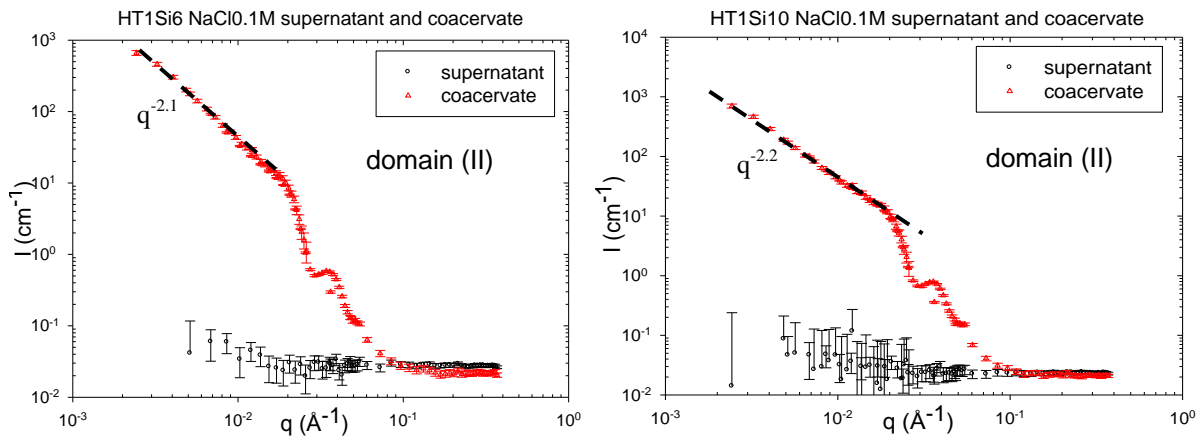


Figure III-41: SANS patterns for samples HT1Si6 (a) and HT1Si10 (b) in the presence of 0.1M NaCl, for both supernatant and coacervate phases

III.4.3.5 Summary on the effect of mass

We observe that the behavior of complexation depends on HA molar masses: the boundaries between monophasic and biphasic domains are shifted. This is unexpected if it is only influenced by the charge ratio of the two components (the charge ratio ($e^-/g^- / e^+/g^+$) should not vary). This suggests that, for 40K HA, the PEL contour length is too short for an efficient wrapping of several NPs.

III.4.4 General summary: some common trends to all systems

The results obtained with the different systems studied in this chapter are summarized in the following Table:

	313K Chitosane/SiNP ⁻	54K PLL/SiNP ⁻		92 K HA/SiNP ⁺	
L_p/R^*	9 nm/9.2 nm~1	1 nm/9.2 nm~0.1		5 nm/17 nm~0.3	
PEL contour length, L_c , with $L_c > 2\pi R$	943 nm	130 nm		235 nm	
	Excess salt: 0.2 M CH ₃ COONa	Salt-free	Excess salt: 0.2 M KBr	Salt-free	Excess salt: 0.1 M NaCl
Monophasic domain (I): excess in PEL	Fractal exponent equal to -2: Ramified or branched structures.	Too poor statistics	-2		~ -1.5
Biphasic domain (II): coacervate	-2.7: More dense and compact structure for the complexes	-2	Between -2.4 and -2.7	Between -2 and -2.2	-2.4
Monophasic domain (III): excess in NPs	-1: Well-defined single-strand nanorods	Beginning of an upturn with exponent~-1.3	-2	-1: Nanorods with holes	-1: More compact nanorods

Table III-2: Summary of the results: Fractal exponent for the power law characterizing the variation of the scattered intensity as a function of q in the low q regime. $*L_p$ is the intrinsic persistence length determined using a wormlike chain model fit of the data; R represents the real NPs radius determined by fitting the data by means of the form factor expression derived for hard spheres

The PEL-large nanoparticles systems investigated here present several notable features:

Complexes involving several NPs are favored with polyelectrolytes displaying a long backbone (large contour length).

- 1) For all investigated systems, the shape of the phase diagram is reminiscent of complex coacervation due to electrostatic attraction between polyelectrolytes and oppositely charged NPs. Three similar characteristic domains are visualized for all systems: two monophasic domains in the presence either of an excess of PEL or NPs, and a biphasic domain for intermediate concentration ranges.

- 2) In the presence of added salt and of NPs (monophasic domain III), well-defined single-strand nanorods can be obtained with semiflexible polyelectrolytes with $L_p/R \geq 0.3$. For nanoparticles as large as the SiNP studied in this Chapter, a semiflexible backbone for the PEL seems to be a necessary condition to obtain such nanorods (To reach such a ratio for flexible chain ($L_p \sim 1$ nm) we would need very small NPs ($R < 3$ nm) as will be studied in Chapter V).
- 3) In the presence of an excess of PEL (monophasic domain I), more ramified or Gaussian-like structures are obtained.
- 4) More compact and dense structures are obtained in coacervates as well as in monophasic domains in the presence of added salt (0.1 M) as shown by the larger fractal exponent determined in the presence of salt (-2.7 for coacervates in the presence of salt instead of ~ -2.1 for salt-free systems).
 - a) A first explanation is electrostatic screening between complexes: in salt-free solutions, electrostatic repulsions between NPs inside self-assemblies are not totally screened. Therefore, complexes can adopt a looser structure. “Dashed nanorods” (without systematic contact between all NPS) have been observed without addition of salt. The addition of salt may modify the behavior of the complexation process in the following ways: (i) the biphasic domain II for salt-free mixtures is more extended. For biphasic samples, the presence of an excess of salt induces a quick (of order of minutes) phase separation with a clear and net interface. (ii) the structure of the formed complexes is more compact, and we may observe in some cases the characteristic peak associated to the particle-particle distance in close contact.
 - b) A second explanation of higher compacity could be the effect of screening on the elementary species, the effectiveness of charges at the surface of either SiNPs or hyaluronan chains. In particular, for hyaluronan chains- which are semi-rigid PEL, the persistence length is the sum of the intrinsic contribution and of the electrostatic one. The latter decreases with salt as the square of Debye Hückel length κ^{-1} , in another word, $I^{-1/2}$ (I being the ionic strength). Thus semiflexible chains become more flexible in the presence of salt and therefore the wrapping around the NPs could be more efficient.

5) Let us comment a little more on the shape of the phase diagram. The most natural is to think that electrostatically formed complexes will separate in two phases when they are neutralized. Thus, the neutralization line should correspond to a given concentration ratio as both components have fixed number of charges per gram. In practice, we observe several differences with this simple case. First, the biphasic domain is not limited to the line of electrostatic stoichiometry $[+]/[-] = 1$, on the contrary, it is quite wide. It means that the mixture precipitates before it attends the neutralization point. This argument can be associated to the fact that for some biphasic samples, the supernatant still contains some complexes of smaller size with the same fractal dimension. This can be explained by the fact that even if they are not neutral, the electrostatic repulsion can be balanced by attractive forces, such as VdW ones. This can induce precipitation depending on the concentration of neutral objects. A simplest situation would then be that the boundaries correspond to stoichiometric lines with $[+]/[-] < 1$. But this implies that the attractive forces are proportional to the global charge (assuming also that all complexes have the same $[+]/[-]$, i.e; without “disproportionation”). However, according to the shape of our phase diagrams, the ratio between PEL and SiNP concentrations is not constant: the separation lines do not correspond to stoichiometric lines (with stoichiometry). For example, from the position of the first boundary in Hyaluronan/SiNPs systems, between the monophasic domain (I) and the biphasic domain (II), the lines are more vertical: we can see that, the more concentrated the PEL solution, the less is the number of SiNPs per chain in monophasic domain (I), the line being thus shifted to the left. One possible explanation is that, staying on a given PEL/SiNP ratio, when increasing the PEL concentration, the global size of complexes is bigger than the one of complexes formed with smaller PEL concentration, due to steric avoidance between chains. Then these bigger objects require more net repulsive charges to counteract the attractive Van der Waals force, thus precipitate at lower SiNP fraction. Another explanation of precipitation before neutralization point is that a free chain may prefer to bind onto aggregated SiNPs instead of individual ones. The driving force for this can be that semi-rigid chains cannot completely fold on the SiNP, so locally, some area of their stay strongly charged, and thus can attract other free chains. In this way, more chains there are, less SiNPs are needed to neutralize complexes. In the Figure III-42 below we show that between the two situations (simple cases have been chosen), the right

hand side one (b) with an aggregate of 7 NPS with two chains plus one individual SiNP can be more advantageous than the left hand side one (a) (2 chains, 8 NPs). This is actually an example of disproportionation of neutralization, a system coexisting with a more neutral object (2 chains, 7 NPs) and an individual SiNP, here not neutralized at all.

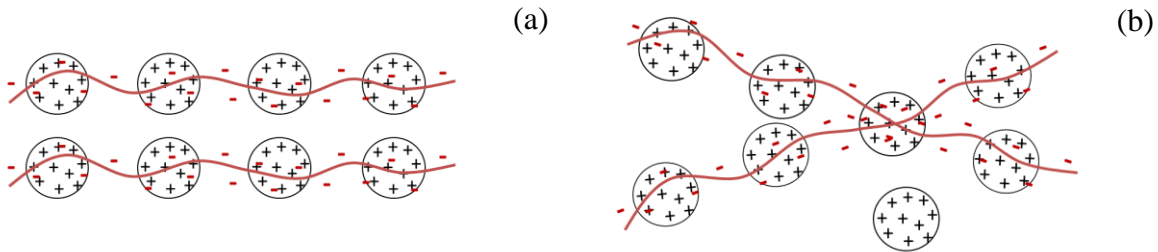


Figure III-42 : Illustration of two possible complex structures with the same concentration ratio. (a) uniform distribution of charge for all complexes ; (b) disproportionation of charge distribution

Other types of disproportionation exist as proposed by Zhang and Shklovskii^[25], who give a complete theoretical analysis of the phase diagram, including the width of the biphasic zone, the salt dependence, the size (or the extension?) of the individual or collective complexes , through only electrostatic repulsion and electrostatic attraction (due to short scale correlations).

III.5 Appendix 1 of Chapter III: Silica particles and Poly-L-lysine.

Poly-L-lysine (PLL, chemical formula $(C_6H_{12}N_2O)_n$) is a natural homopolymer composed of L-lysine amino acids and produced by bacterial fermentation (the human body cannot synthesize it). Each unit of the chain contains an amino group ($-NH^{3+}$) that renders the whole chain positively charged with $pK_a=9$

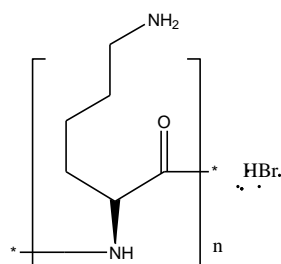


Figure III-43: Chemical formula of poly-L-lysine (PLL). The monomer mass and length are 128 g/mol, and 3.55 Å, respectively

Polylysine can be electrostatically absorbed onto the cell surface of the bacteria and is commercially used in food preservation industry. Also, many researches have been focused on the complexation of polylysine with DNA through electrostatic interactions between the positively charged amino groups of PLL and the negatively charged phosphate groups of DNA.

Here, PLL was chosen because it displays positive charges and a flexible backbone characterized by a persistence length, L_p , close to 1 nm, which makes a contrast with chitosan. The poly-L-lysine hydrobromide used in our study was purchased from Sigma-aldrich (CAS Number 25988-63-0, M_w 30,000~70,000) in its powder state and was used as purchased.

The poly-L-Lysine was prepared in aqueous solution in the presence of 0.2M of KBr. The concentration of additional salt KBr was fixed at 0.2M to keep the same ionic strength than that of chitosan solutions previously studied. Within these experimental conditions, all the amino groups are protonated and PLL is fully charged displaying a charge approximately every 3.5 Å; i.e, every 7 Å after Manning correction.

The molar weight of PLL was determined by static light scattering (SLS) using a classical Zimm analysis (see chapter II; here a single concentration was used).

First, the refractive index increment, dn/dc , of PLL in 0.2M KBr aqueous solutions was determined. For these experiments, five concentrations of PLL were prepared, and for each concentration, the value of the refractive index was measured three times and then averaged.

The value of the $dn/dc=0.1645 \text{ cm}^3/\text{g}$ was obtained from the slope of the plot showing the refractive index of the solution, n , versus the PLL concentration, c (see Figure III-44)

C_{PLL} (g/L)	Index n	deviation
0	1,33591	6,0E-5
2	1,33612	5,4E-5
5	1,33671	8,7E-6
7	1,33697	4,9E-5
10	1,33765	5,6E-6

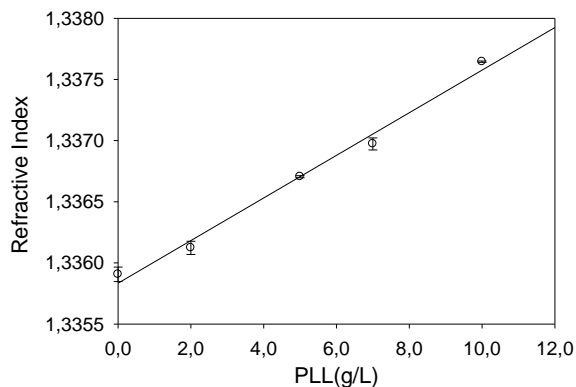


Figure III-44: Refractive index, n , as a function of the PLL concentration in the presence of 0.2M KBr at room temperature

The scattering constant $K= 1.975 \times 10^{-7} \text{ cm}^2 \cdot \text{g}^{-2} \cdot \text{mol}$ was then calculated using eq. II-12 with $\lambda=632.8 \text{ nm}$ and the solvent refractive index, $n=1.33$.

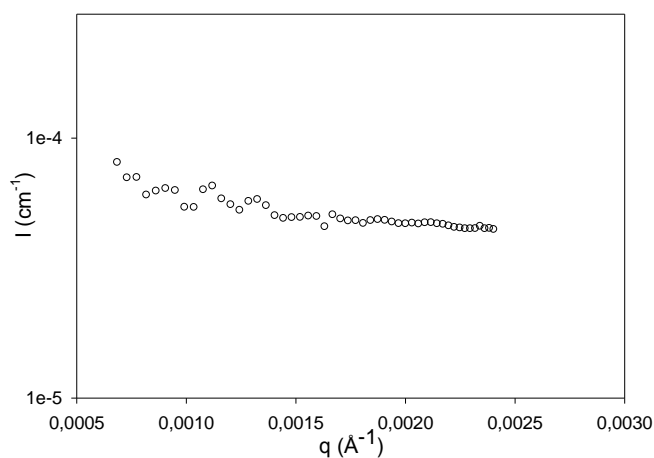


Figure III-45: Absolute intensity (excess Rayleigh ratio in cm^{-1}) versus q obtained by SLS for a PLL solution at 5g/L in the presence of 0.2M KBr (dilute regime characterized by a concentration below the overlap concentration c^* separating the dilute and semidilute regimes)

Figure III-45 shows the variation of the scattered intensity, I , with q for a 5 g/l PLL dilute solution in the presence of 0.2 M KBr and obtained using SLS measurements at room temperature (θ varying from 30° to 130° and corresponding to a q -range of 6×10^{-4} - $2.5 \times 10^{-3} \text{ \AA}^{-1}$).

Considering that the experiments were performed in the dilute regime ($c \ll c^*$, confirmed by the results obtained below and the viscosity close to the one of water), the weight-average molecular weight, M_W , and the radius of gyration of the chains, R_G , were obtained by plotting the product KC/R as a function of q^2 (see eq.II-14). The extrapolation to $q^2=0$ gives $M_W=54000$ g/mol, whereas the slope of the plot gives $R_G=4.6$ nm. As every monomer unit of mass of 128 g/mol bears one positive charge, we can evaluate that there are 422 positive charges per PLL chain.

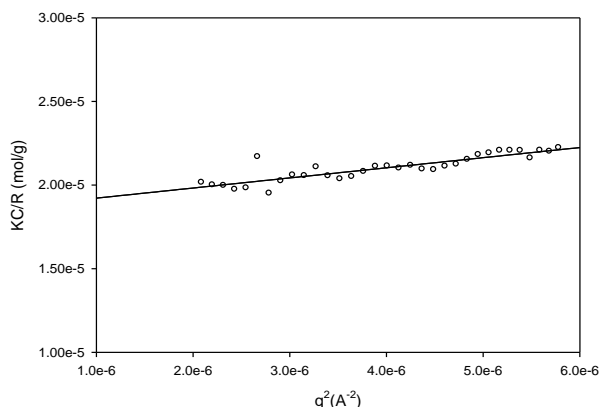


Figure III-46: Extrapolation of KC/R versus q^2 for PLL at 5g/L in presence of 0.2M KBr. R represents the Rayleigh ratio; i.e., the SLS absolute intensity in cm^{-1} (see Chapter II)

The hydrodynamic radius, R_H , of PLL was also obtained by DLS performed at 90° and at room temperature. The cumulant analysis gives $R_H=7.9\text{nm}$, a value slightly larger than that obtained for the radius of gyration. This discrepancy can be explained by the presence of a slow mode of low amplitude in the time correlation function and disturbing the cumulant analysis in the short time range. (see Figure III-47).

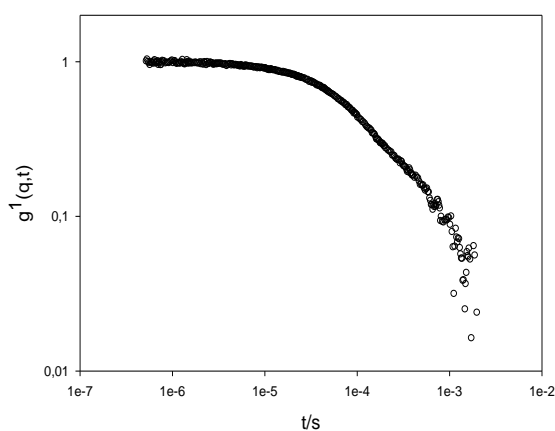


Figure III-47: DLS performed on a 5g/L PLL dilute solution in the presence of 0.2M KBr at 90° and 20°C

III.6 Appendix 2 of Chapter III: Positively charged SiNP and Hyaluronan

III.6.1 Positively charged SiNP (Ludox CL)

The available commercial positively charged SiNPs are provided by Grace under the reference Ludox CL. Ludox CL is a modified silica colloidal dispersion where the SiNPs are coated with aluminum oxide Al_2O_3 (3% according to the supplier) using aluminium chloride to reverse the surface charge density. Therefore, these modified silica particles carry a more pronounced positive charge on the surface of the NPs (see Figure III-48).

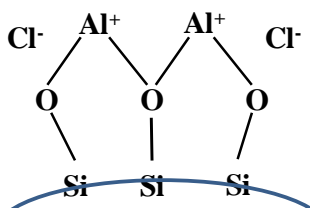


Figure III-48: SiNPs carrying a positive surface charge density (Ludox CL)

Positive Al^+ ions are bonded to the SiNP surface through the silanol groups.

Ludox CL was kindly donated by Grace, and was used as received without further purification. The supplier provided two different sizes, referenced Ludox CL-CAL25 and Ludox CL-CAL50, and corresponding to a diameter of 25 and 50 nm, respectively. However, according to our DLS measurements, both of them are bigger than the values claimed by the supplier.

For the DLS measurements (Malvern ZetaSizer apparatus), the original 30w.t% stock was diluted into a 10^{-4} M HCl solution to ensure a pH value of 4 and a good stability of the positively charged particles in the presence of 0.1M NaCl and also without addition of excess salt. The solutions were then directly filtered into the light scattering cells before the measurements.

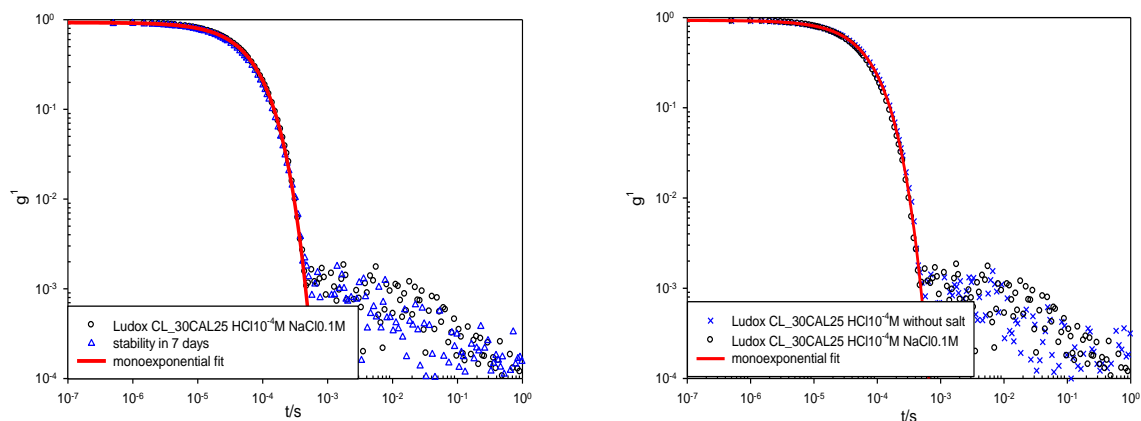


Figure III-49: Scattered field autocorrelation function, $g^{(1)}(q,t)$, at 173° for a 1 g/l Ludox CL30CAL25 10^{-4} M HCl solution in the presence of 0.1M NaCl. The correlation function obtained without addition of salt is also represented for comparison

Within these experimental conditions, the scattered electric field autocorrelation function is clearly monomodal, as illustrated by Figure III-49. From the cooperative characteristic relaxation time one obtains an apparent hydrodynamic radius, R_H , of 21.9 nm and 22.2 nm respectively in the presence or not of excess salt. The slight difference, which is in the error bar, could be attributed to the screening of the repulsive interactions in the presence of 0.1 M NaCl. Also silica particles are monodisperse in size as seen by the polydispersity index calculated using the cumulant procedure: $k_2/k_1^2=0.057$. The stability with time of the Ludox CL-CAL25 colloidal suspensions was also checked using DLS by performing new experiments 7 days after samples preparation, and no changes in the autocorrelation curve were observed.

On contrary, Ludox CL30CAL50 suspensions were, for unknown reasons gel-like instead of liquid-like in the case of the 30CAL25 product. Also, diluted solutions cannot be easily filtered through the $0.2\mu\text{m}$ porous membranes. Though the unfiltered solution gives also a good autocorrelation function and seems to be quiet monodisperse in size with a radius of 46.5 nm, lack of knowledge, it was not further used for the complexation experiments.

The radius of gyration of the cationic SiNPs, which is too small to be determined by static light scattering, was obtained by small angle x-ray scattering (SAXS) experiments at the beamline ID02 at ESRF (Grenoble, France). Samples were prepared in 1mm capillaries and three configurations were used: wavelength $\lambda=1\text{\AA}$, distance sample to detector of 1 m for a q range varying from 0.11 nm^{-1} to 6.25 nm^{-1} ; distance 10 m for a q range of $9\times 10^{-3}\text{ nm}^{-1}$ - 0.63 nm^{-1} , and finally Bonse-Hart for a q range extending from $1.32\times 10^{-3}\text{ nm}^{-1}$ to 0.20 nm^{-1} .

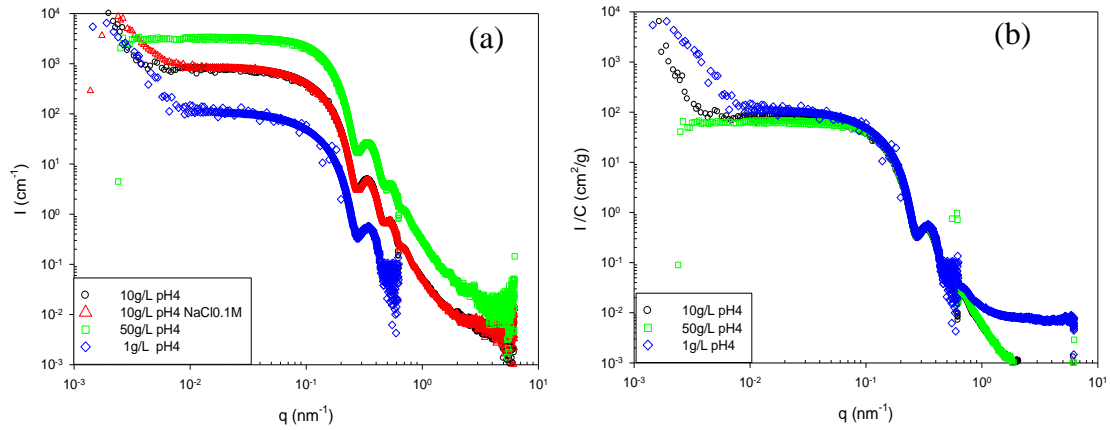


Figure III-50: SAXS patterns of SiNP Ludox CL at different concentrations at pH4: (a) Absolute intensity I (cm^{-1}) – q (nm^{-1}); (b): Intensity normalized by concentration I/C - q . Data collected on the beamline ID02 at ESRF

Three concentrations of SiNPs were prepared at pH=4: 1, 10, and 50 g/L. For the concentration of 10g/L, 0.1M NaCl was added to the solution to test the effect of excess salt on the SiNPs stability. Indeed, the presence of 0.1M NaCl in the system do not destabilize the SiNPs at pH=4 as seen by the superimposition of the data in Figure III-50(a) representing the SAXS patterns for a 10g/L solution with and without addition of salt. (b) the representation I/C was displayed to show the superimposition of the data in the intermediate and high q regimes, thus indicating that the structure of the SiNPs is similar in the whole investigated concentration range. The upturn occurring at very low q for 1 g/L and 10 g/L solutions with the Bonse-Hart configuration, may be attributed to the delicate capillary subtraction close to the beamstop.

The scattering curves exhibit then the same behavior characterized by a Guinier regime in the low q range associated to the size of the SiNPs. The low q range data have been fitted by a classical Guinier expression, which provides the average radius of gyration, R_G , and the zero-wave vector scattered intensity, $I(0)$, associated to the mass of the scattered objects:

$$\frac{C}{I(q)} = \frac{C}{I(0)} \left(1 + \frac{q^2 R_G^2}{3} \right)$$

Figure III-51 shows the plots representing $1/I$ versus q^2 and the best linear fits. We obtained $R_G=16$ nm for all concentrations.

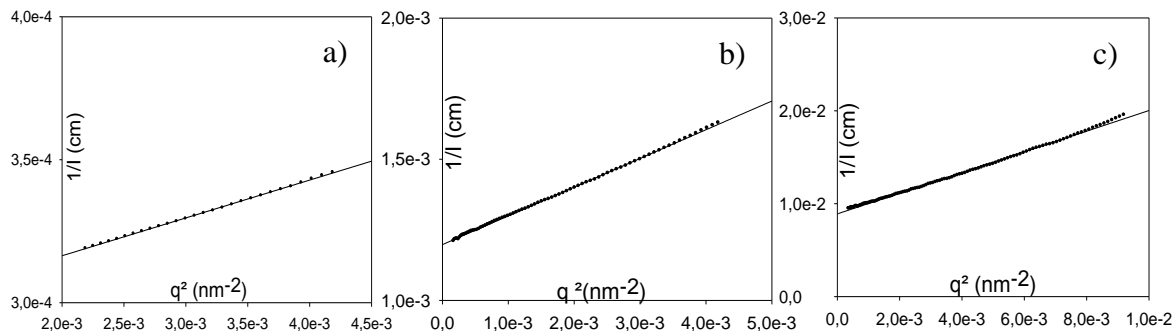


Figure III-51 : Variations of the ratio $1/I$ with q^2 in the low q range for SiNP solutions at various concentrations: a) 50g/L; b) 10g/L; c) 1g/L

After extrapolation of the ratio C/I ($q^2 \rightarrow 0$) to zero-concentration (see Figure III-52), we obtained the weight-average molecular weight of the particles: $M_W = 3.38 \times 10^7$ g/mol, with eq.II-38.

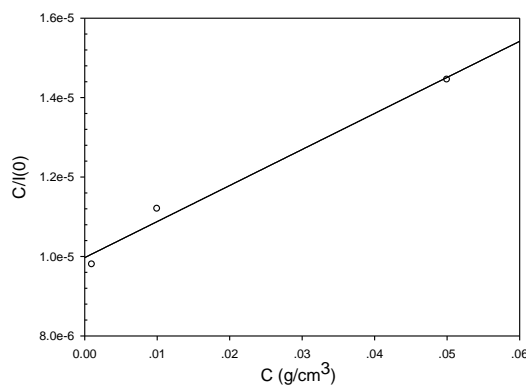


Figure III-52: Variation of the ratio $C/I(0)$ with the silica concentration

The positive slope of the line indicates that the pH=4 HCl solution is a good solvent for the cationic SiNPs and gives a value for the second Virial coefficient $A_2 = 4.54 \times 10^{-5}$ cm³.g⁻².mol ($1/I = 1/I(0) + 2A_2C$).

The high q data can be fitted satisfactorily by means of the form factor expression derived for hard spheres of radius R . The form factor oscillations, damped by the size distribution, are well-reproduced with this model as shown in Figure III-53 giving $R = 17$ nm, a value slightly larger than that obtained using DLS.

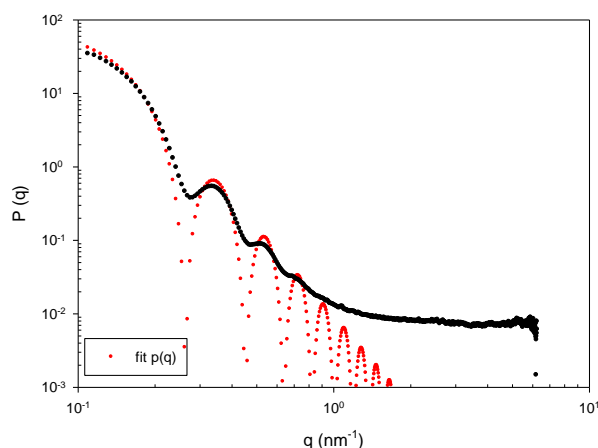


Figure III-53: Variation of the SiNPs form factor, $P(q)$, with q and the fit of the data using the form factor expression derived for monodisperse hard spheres. The concentration is 1g/L

The characteristics of the cationic SiNPs Ludox CL obtained using the various scattering techniques are collected in the following table.

	SiNP Ludox CL
R_H (nm)	22.2
R_G (nm)	16
R (nm)	17
Zeta Potential (mV)	17.8 (in the presence of 0.1M NaCl)
M_w (g/mol)	3.37×10^7

Table III-3 Cationic SiNP characteristics

III.6.2 Hyaluronan

Hyaluronan (HA) is a linear semi-rigid polyelectrolyte with the repeating disaccharide structure poly(((1→3)-β-D-GlcNAc-(1→4)-β-D-GlcA)), with global formula $C_{14}H_{20}NO_{11}Na$, for the Sodium salt form (see extended formula in Figure III-54), monomer molar mass of 401.3/mol and monomer length close to 10.2 Å. HA is found in animals (10 grams are contained in human body) where it is mainly produced by fibroblasts and other specialized connective tissues cells. It is a common component of synovial fluid and extracellular matrix and one of its assumed functions in the body is joint lubrication.

In joints as well in other situations, HA seems to have complex roles and its associations and interactions with proteins or other biomolecules are known to participate to many biological mechanisms that can even be opposite depending on the molecular mass.^[119] Large masses are involved in ovulation, embryogenesis, regeneration, while small masses are found in inflammatory processes, and very short ones are involved in the mobility of cancerous cells and stimulate neo-vascularization of tumors. In pharmacology, HA is widely used in

dermatology, ophthalmology, and rheumatology. In this last domain, different formulations of hyaluronic acid are used for arthritic patients, while proof of their efficiency remains to be established.

Among the group of glycoaminoglycans (GAGs), HA is the only one that is not covalently associated with a core protein. Being charged, like DNA, HA has specific interactions with proteins (Habp, HA bonding proteins, like CD44 which is important in cancer for example). In addition, HA has a repetitive primary structure that allows also nonspecific binding with proteins, via electrostatic interactions identical along the chain, contrary to DNA. The charge density of the HA depends on pH of the solution since the dissociation coefficient of the carboxyl groups is pH-dependent; such complexes depend therefore on pH (as well as on ionic strength).

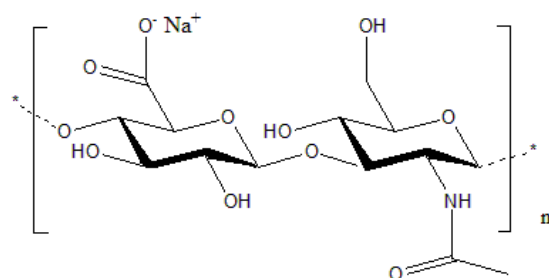


Figure III-54: Molar formula of hyaluronan

As a polyelectrolyte, it can then be complexed with other oppositely charged nanoparticles or polycations by electrostatic interaction. In order to investigate the effect of the chain length on the complexation, two different molecular weights were investigated, referenced “Bashyal” (hyaluronan medium molar weight, noted HB) and “TBPM” (low molar weight, noted HT) by the supplier Soliance (Pomacle, France). Bacterial hyaluronan was purified under the Na salt form and used as received without further purification.

Light Scattering Characterization: First, the molecular weight and size of the chains in dilute regime were determined for both hyaluronan references using light scattering experiments. The solutions were prepared in the presence of 0.1M NaCl to ensure the screening of the electrostatic interactions necessary for a chain molecular weight determination, at a concentration of 0.25g/L that is below the overlap concentration $c^* = M_w / (4\pi N_{Av} R_G^3) \sim 4$ g/L. Figure III-55(a) shows the correlation function obtained for a medium HA molecular weight (“Bashyal” commercial reference). The autocorrelation function is well described by a stretched exponential indicating that our sample is polydisperse in size. The results obtained by applying the Contin procedure to our data and presented in Figure III-55(b) confirms this

trend by showing a broad distribution of the scattered intensity as a function of the hydrodynamic radius. The average apparent hydrodynamic radius is equal to $R_H=14.6\text{nm}$.

From the extrapolation of the ratio KC/R to $q^2=0$ (see Figure III-56), we obtained the average molecular weight of the sample equal to $M_w=9.2\times 10^4\text{g/mol}$. The slope of the plot is too weak to allow the determination of the radius of gyration.

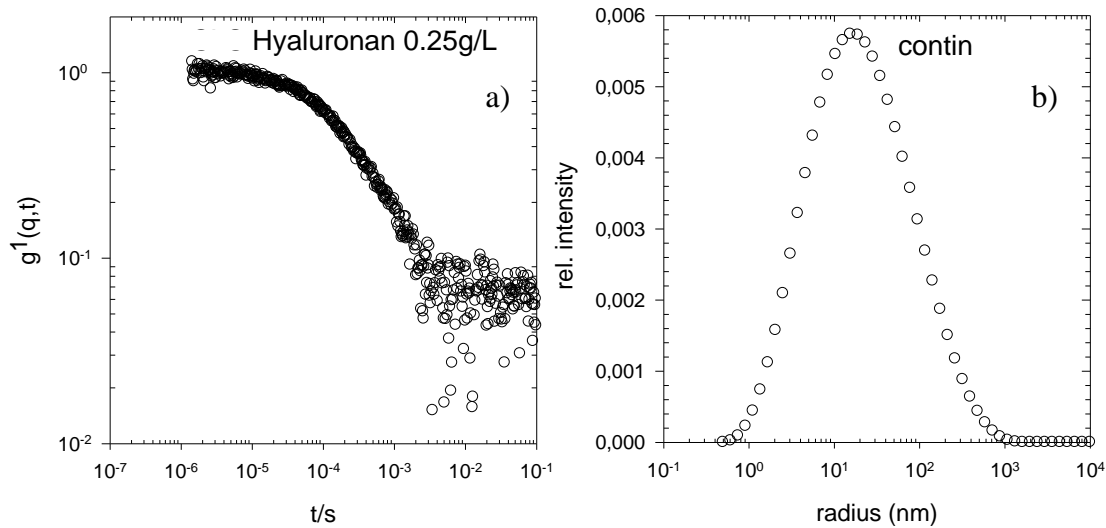


Figure III-55: DLS on hyaluronan “bashyal” (medium molecular weight): a) time auto-correlation function of the scattered electric field; b) Distribution of the scattered intensity as a function of the size obtained by applying the Contin method to our data

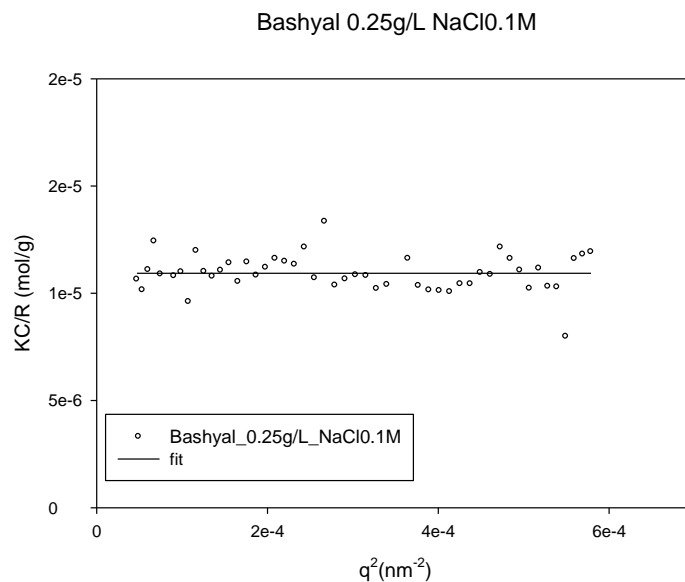


Figure III-56: SLS realized on hyaluronan “bashyal”: plot of KC/R versus q^2

For the HA sample referenced TBPM (small molecular weight), the auto-correlation function clearly became bimodal and can be clearly described by the sum of two relaxations widely

separated in time. Fast and slow modes are diffusive with characteristic times inversely proportioned to q^2 . The Contin analysis provided R_H (fast) =8.1nm, and R_H (slow) =100nm (see Figure III-57b)

In case of coexistence of two populations, the total scattered intensity is dominated by the contribution of the bigger population, the latter corresponding to HA chain aggregates.

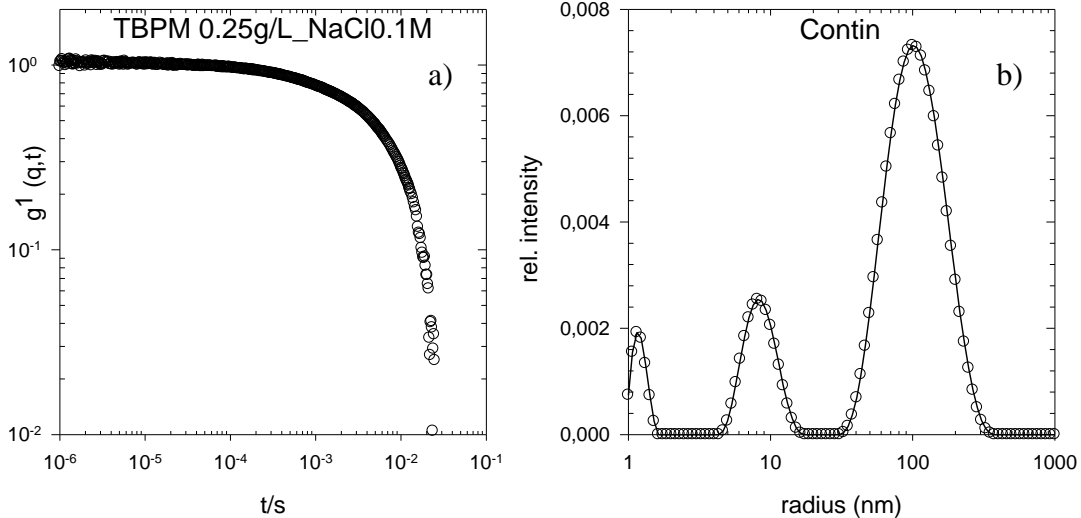


Figure III-57: DLS experiments realized on hyaluronan referenced “TPBM” (small molecular weight) at a scattering angle of 30°: a) Scattered electric field auto-correlation function; b) Distribution of the scattered intensity obtained by applying the Contin procedure to our data

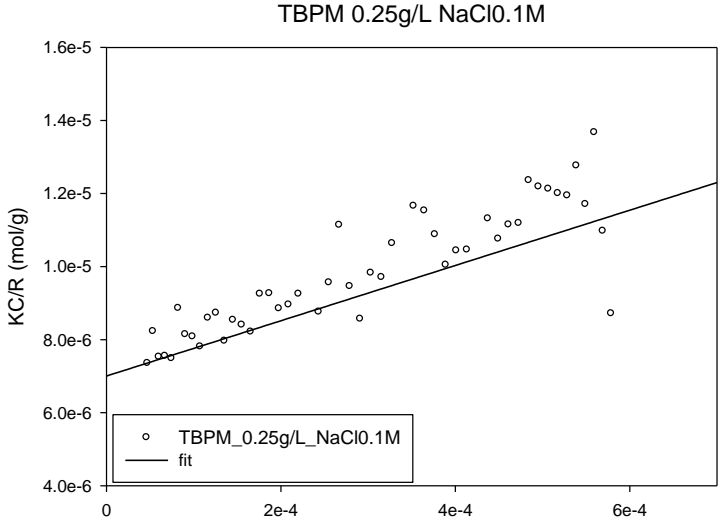


Figure III-58: KC/R versus q^2 for HA referenced “TPBM” (small molecular weight)

$$\begin{aligned}
g^1(q,0) &= A_f e^{-0/\tau_f} + A_s e^{-0/\tau_s} = A_f + A_s = 1 \\
\left(\frac{A_f}{A_s}\right)_{90^\circ} &\approx \left(\frac{A_f}{A_s}\right)_{q=0} = \left(\frac{I_f}{I_s}\right) = \frac{K \times M_{wf} \times C_f}{K \times M_{ws} \times C_s} = \left(\frac{R_{Hf}}{R_{Hs}}\right)^{5/3} \times \frac{C_f}{C_s} \\
I_{total} &= I_f + I_s = A_f I_t + A_s I_t \\
I_{fast} &= A_{fast} \times I_{total} = K \times M_{wfast} \times C_{fast} \\
C_f + C_s &= 2.5e^{-4} \text{ g/cm}^3
\end{aligned}$$

where K is the scattering constant. One obtains $C_{fast}=2.40 \times 10^{-4} \text{ g/cm}^3$ and $C_{slow}=1.04 \times 10^{-5} \text{ g/cm}^3$ that represent respectively the concentrations, of small chains and of aggregates, the total concentration of the solution being equal to the sum of these concentrations. Knowing both concentrations it is easy to calculate the molecular weight associated to individual HA chains and to aggregates, and we obtain: M_w (fast)= M_w (HA chains) = $4.0 \times 10^4 \text{ g/mol}$ and M_w (slow)= M_w (aggregates) = $2.6 \times 10^6 \text{ g/mol}$ a pretty high value corresponding to aggregates made of 65 HA chains. The proportion of aggregates, which were probably not totally eliminated during the purification process, is pretty low.

Knowing the molar weight of HA “basyal” 92K and of HA “TPBM” 40K, we can now estimate the number of negative charges per chain. Assuming that every monomer unit is bearing one charge, we found 237 and 106 charges per chain for 92K and 40K HA, respectively.; i.e., 1.6×10^{21} charges/g.

III.7 Appendix 3 of Chapter III: SAXS pattern of system HA-SiNP, using Bonse- Hart configuration

Here we also present some SAXS results of 92K Hyaluronan-SiNPs complexes performed on ID2 at ESRF, particularly extends to very low q range using Bonse-Hart configuration. These samples, though having the same ionic strength in final, were prepared differently of those presented in the text. It means that the hyaluronan was diluted in the presence of 0.2M NaCl while hyaluronan was diluted in pH=4 condition without additional salt. These tests prove that the complexes have even larger size than 1000 nm. However, for samples taking long time to phase separate, we measured actually the mix of two phases at metastable stage.

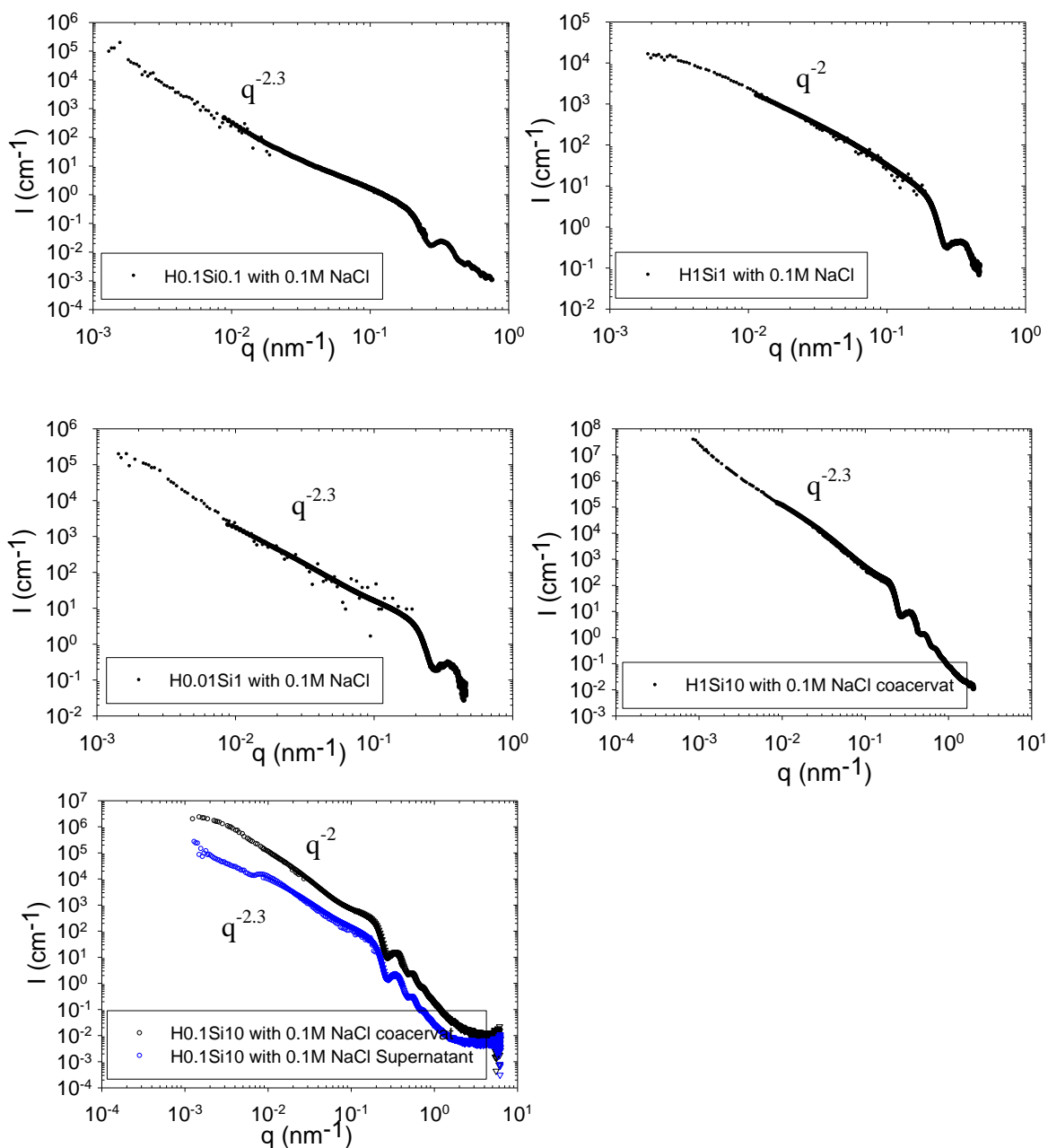


Figure III-59 : SAXS patterns of HA-SiNPs complexes samples at different ratios performed on beamline ID02 at ESRF, using particularly Bonse-Hart configuration at very low q

III.8 Appendix 4 of chapter IV: The double layer model and the estimate of the particle charge

The effective charge of the particle with a charged surface is not easy to define, because part of the counterions may stay associated to the particle, and reduce its charge. This part depends on the technique of measurement of the charge, and this is never simple to estimate. One usually uses the so-called double layer model. The first model due to **Helmholtz** considered the balance between thermal agitation (entropy) and electrostatic attraction (field defined as for a capacitor). However, when even a small amount of salt is present, electrostatic screening of this field must be added to the model, what is done by the **Gouy-Chapman** model. Finally this is not satisfactory since some c.i. or other ions are trapped at the surface by physical or chemical interactions other than electrostatic ones.

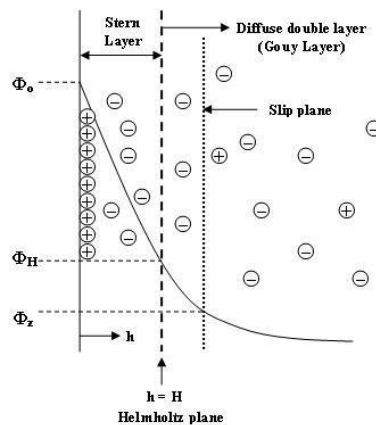


Figure III-60 : Illustration of double layer model

These effects are accounted for by a double layer, with a first so-called « **Stern** » layer, and a « second » layer being the c.i. located at larger distance beyond the Stern layer and attracted to the surface charge via the screened Coulomb force (Gouy-Chapman). It is loosely associated with the object, because it is made of mobile ions, and is thus called the **diffuse layer**.

When measuring the mobility m_e , the question is to estimate which fraction of the c.i. moves with the particle: it is comprised within a so-called slipping layer, again uneasy to predict. Electric potential at this plane is called zeta potential, or ζ -potential, and should be measured using in particular electrophoresis, in practice using a « zeta-meter » which measures the velocity v of the particles under a given applied electrical field E .

$$\mu_e = v / E$$

III-10

The most known and widely used theory of electrophoresis was developed in 1903 by Smoluchowski^[122] :

$$\mu_e = \varepsilon_r \varepsilon_0 \zeta / \eta \quad \text{III-11}$$

where ε_r is the dielectric constant of the dispersion medium, ε_0 is the permittivity of free space ($C^2 N^{-1} m^{-2}$), η is dynamic viscosity of the dispersion medium (Pa·s), and ζ is zeta potential. Here the central assumption is that the zeta potential is the electrokinetic potential of the slipping plane.

The Smoluchowski theory does not include electrostatic screening as characterized by the Debye length κ_{DH}^{-1} . The spatial distribution of the counterions cloud acts on the way the electric force exerted by a field on these counterions is transferred on the particle. This must be important for electrophoresis. The first limit, for which Smoluchowski theory is valid, is "thin DL":

$$\kappa_{DH}^{-1} \ll R \quad \text{III-12}$$

It is valid for most aqueous systems because the Debye length is only a few nanometers in such cases. It breaks down only for nano-colloids in solution with ionic strengths close to water. In such case^[123], we have:

$$\mu_e = 2\varepsilon_r \varepsilon_0 \zeta / 3\eta \quad \text{III-13}$$

In practice we see only a factor 2/3 difference between the two models, while the uncertainty about the definition of the slipping plane is large.

Moreover the formation of complexes is very likely to obey to a different role of the counterions. Namely they can be released in the solution. **Therefore the chemical charge, as can be measured by titration should be the important parameter for complexation.** This will be discussed in the two cases corresponding to SiNP and AuNP, in Chapter III and Chapter V respectively.

CHAPTER IV
SYNTHESIS OF GOLD
NANOPARTICLES (AuNP)

IV. Synthesis of gold nanoparticles (AuNP)

IV.1 Introduction

The fabrication and functionalization of gold nanoparticles attract continuous attentions since several decades for their potential applications in the fields of physics, chemistry, biology, and medicine as well as material science, due to their discovered novel properties.^[124] The shape and size dependent localized surface plasmon resonance (LSPR) of gold nanoparticles, which is the origin of their special optical properties, has been developed for the detection of single-base mismatches in DNA hybridization.^[125] The spherical AuNPs with specific target groups have been employed as analytical probes in biotechnological systems, such as diagnostic, biological imaging for their abilities of scattering near infrared light under dark-field microscopy^[126, 127], while, the absorption of near IR enables them to produce heat rapidly to eradicate targeted tumors.^[128] The large surface area/volume ratio of AuNPs make them good therapeutic agent carrier as their surface can be coated with hundreds of molecules.^[129] The covalent assembly of functionalized AuNPs exhibits switching behaviors can be used for organic field-effect transistor (OFET) based memory devices.^[130] The organization of gold nanoparticles in 1–3 dimensions was found to hold unique electrical properties, caused by Coulomb charging and molecularly supported electron transfer, which in principle fulfill the requirements of applicability in future microelectronics.^[131] In addition, AuNPs are best candidates of catalyst in many chemical reactions, for AuNP surface binds much more strongly to supports like titania and iron oxide, and the thermodynamic stability of adsorbed intermediates for catalytic reactions can either increases or decrease strongly with decreasing AuNP sizes.^[132, 133]

From the non-exhaustive examples cited above, one can conclude that the trend today is the fabrication of AuNP based objects in controllable ways: (i) the well-defined size and surface charge of AuNP itself by functionalization and (ii) the aggregation of controlled numbers of AuNPs organized in desirable dimensions.

Besides the multiple promising applications they hold if we master the controllable aggregation, gold nanoparticles are chosen for our study of complexation for the specific reasons. Firstly, a number of relatively mature synthesis methods can be consulted to obtain AuNPs with controllable size and uniform surface charges, which is crucial for the understanding of complexation systems, however the use of AuNPs are rarely mentioned in this domain. Secondly, AuNPs adapts well to our mainly used characterization techniques,

thanks to their good contrasts in transmission electronic microscopy (TEM), Small Angle X-ray scattering (SAXS) and ultraviolet visible spectroscopy (UV-vis) without supplementary magnetic interactions, even in diluted systems. Nevertheless, the inconvenient is also obvious: (i) the price and time cost of the synthesis of AuNPs limit the realizable number of experiences, (ii) compared to its large density (19g/cm^3), the neutron scattering length density of gold lies within normal values, so does the contrast with water, thus the necessary mass concentration for a good signal is high and costly (the situation is far better for X rays which are sensitive to the electronic number Z).

Anionic polyelectrolyte with persistence length (L_p) lower than 10nm such as hyaluronan and sodium polystyrene sulfonate retain mainly our attention because their behavior in solution (Variation of the persistence length with the concentration and the ionic strength, level of counterions condensation, etc) have been thoroughly studied in the past by F. Boué and E. Buhler.^[109] In this context, the goal of this chapter is to establish a robust protocol for the synthesis of cationic, monodisperse and water dispersible AuNPs with radius of less than 10nm based on the existing results of the literature. Moreover, in order to keep the advantages of our low polydispersity, these AuNPs should not aggregate during re-concentration by centrifugation which permit access to a large range of AuNPs concentration, and also to redisperse in different solvents (e.g. deuterated one like D_2O) for SAXS as well as SANS measurements.

IV.2 Wet chemical synthesis of water dispersible cationic AuNPs

AuNPs can be prepared by a large number of approaches including wet chemical synthesis, radiolysis, LASER ablation or even sonolysis, etc.^[134] We have chosen the former approach because it is the most studied. Moreover, it not only simplifies the manipulation, but also allows the control of several parameters (size, shape, functions) at one time.

Wet syntheses of AuNPs in solution are based on the reduction from Au (III) or Au (I) in form of gold salt to Au (0), followed by a nucleation-growth mechanism.^[135] The first step of gold reduction is quite easy because gold is highly electronegative with a standard redox potential: $E^\circ_{\text{SHE}} = +1.69\text{V}$ for Au^{1+} . The growth process can be controlled and the particles be stabilized by a capping agent present in the reaction media that associates with the particle surface. The scientific interest for this kind of synthesis has started in the middle of the nineteenth century when Michael Faraday published a comprehensive paper about the preparation and properties of gold sols.^[136] Together with the development of analytical

techniques like electronic microscopy or light scattering, the initial synthetic pathway has been optimized to enable the control of particle size, shape and polydispersity by using different kinds of reducing and/or capping agents. Today, two different approaches are most often considered for the synthesis of spherical AuNPs: the Turkevich and the Brust approaches. In the following, we will present and discuss the results obtained by these two procedures.

IV.2.1 Turkevich method

IV.2.1.1 General Principle

In 1951, Turkevitch proposed to use sodium citrate (Figure IV-1) as both reducing agent and stabilizer. This approach has been successively optimized^[135, 137-139] and is probably the most well-known for synthesizing gold colloids in water with diameter ranging between 3 nm^[139] and 70 nm.^[138] In short, the initial Turkevitch synthesis procedure consists to add small quantity of sodium citrate solution (typically 5 mL of a sodium citrate solution at 1 vol.%) into a boiling aqueous chlorauric acid solution (typically 95 mL of a chlorauric acid solution containing 5 mg of Au) under vigourous mechanical stirring. According to the authors this method is “highly reproducible and gives spherical particles with a mean diameter of about 20.00 nm ± 0.15 nm and a root-mean-square deviation of 12.5 %”

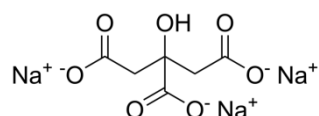


Figure IV-1: Chemical structure of trisodium citrate

To our knowledge, no completely established mechanism have been proposed so far to explain the formation of citrate stabilized AuNPs. The “organizer” mechanism (Eq. IV-1, IV-2) initially proposed by Turkevitch^[140], is the most often discussed but without clear experimental proof so far.^[141] The first step involves reducing Au from Au(III) to Au(I) (Eq. IV-1) and oxidizing the trisodium citrate into dicarboxy acetone (Eq.IV-2):



The second step is the disproportionation of aurous species to gold atoms:



The disproportionation step requires three aurous chloride molecules to combine. This may be facilitated by dicarboxy acetone, which, according to Turkevich et al. plays the role of

organizer through the formation of a complex. An illustration of such complex is presented in Figure IV-2. In the chain-like structure pictured here, three Au⁺ can be tethered by a minimum of two dicarboxy acetone molecules so that the overall stoichiometry of the reduction reaction can then be written as follow:

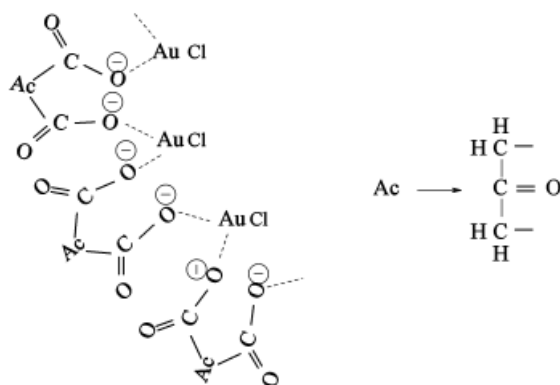


Figure IV-2 : Scheme of complex of aurous species and dicarboxy acetone extracted from ref [140]

Although Turkevitch indicates^[140] that the mean particle size and the root-mean-square deviation can be varied by playing on the temperature and reagent concentration, it is only recently that the synthesis procedure has been optimized to control these critical parameters.

The variation of AuNPs' size can be realized by adjusting the ratio of citrate/Au(III), or the addition of sub reductant, such as tannin, or just the pH of Au(III) salt solution. Many publications revealed the combined effects of these parameters.

For instance, in 1981, Slot and Geuze show that the size of AuNPs can be decreased from 20 nm down to 3 nm by using tannic acid (Figure IV-6 (a)) together with sodium citrate to play the role of reducing and protective agents.^[139] This effect is not observed when using either tannic acid or sodium citrate alone meaning that a synergistic effect exist. The exact mechanism leading to this effect is still unclear.

In 2006, Plech et al.^[138] show that the increase of $C_{\text{Au}}/C_{\text{citrate}}$ would increase the final size of AuNPs, and the initial C_{Au} would determine the polydispersity of the AuNPs, as confirmed by both diameter measured by TEM and the wavelength of absorption peak of UV (see Figure IV-3). Combining these two parameters, in order to get monodisperse AuNPs, the optimal $C_{\text{Au}}/C_{\text{citrate}}$ should be below 1 and the maximum C_{Au} should be less than 0.8mM.

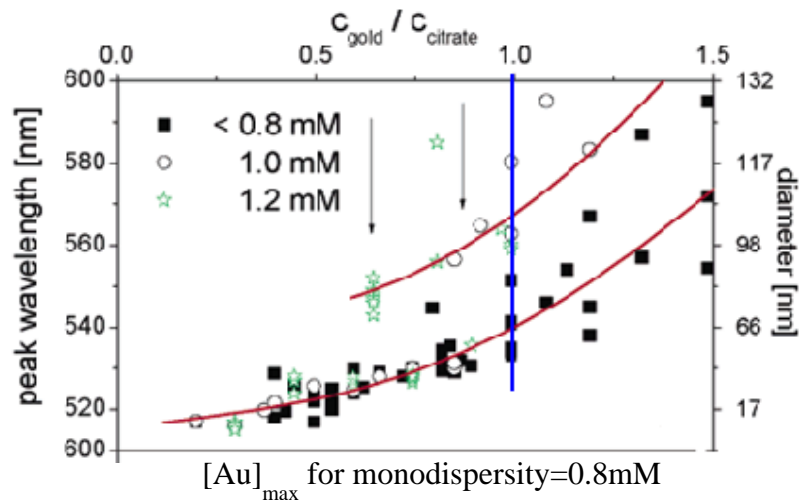


Figure IV-3: Figure extracted from ref [137] showing the influence of $C_{Au(III)}/C_{citrate}$ ratio on the final size of AuNP prepared by Turkevich method

This study has been completed in the same year by Peng et al.^[137] which shows that the pH value of the solution can also vary the final size of AuNPs. First, it is important to note that the pH is dependent of citrate/Au ratio as $HAuCl_4$ is an acid and sodium citrate a conjugate base of a weak acid (i.e. citric acid). As showed in Figure IV-4, pH increases significantly from 3.3 to 7 when the ratio of $C_{citrate}/C_{Au}$ increases from 1 to 10, and becomes stable after ratio attends 10. This is mainly due to the three pKa of the polyprotic citric acid that serves as a buffer before the pKa₃. Also, the Au(III) can have different conjugation forms of different reactivity with Cl^- and OH^- according to the variable pH as illustrated in Figure IV-4

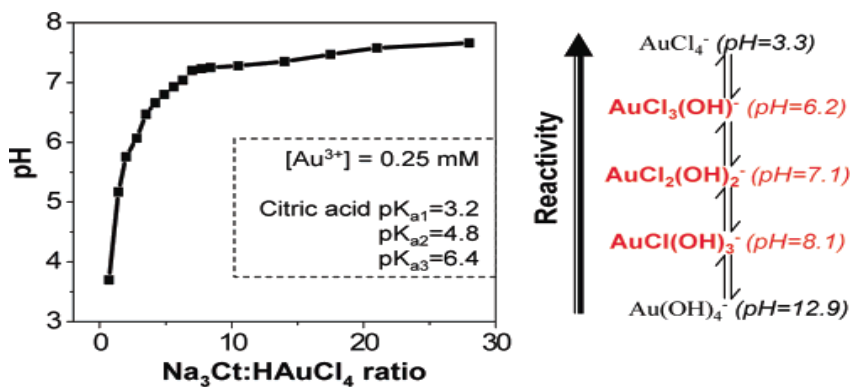


Figure IV-4: Effect of pH on the reactivity of conjugated Au(III). Figure extracted from Ref [137]

Besides the initial C_{Au} and the ratio of $C_{Au}/C_{citrate}$, the effect of pH have been studied independantly from C_{Au} and $C_{Au}/C_{citrate}$ by addition of HCl or NaOH.^[137]

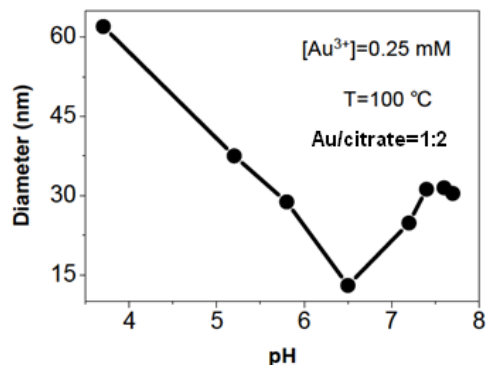


Figure IV-5: Effect of pH on the final diameter of AuNP. Figure extracted from ref [137]

As shown in the Figure IV-5, keeping the initial $C_{Au}=0.25\text{mM}$ and the ratio of $C_{Au}/C_{citrate}=0.5$ constant, the AuNPs' diameter decreases from 60 to 10nm when the pH increases from 3.3 to 6.5, and pH=6.5 is a turning point, afterwards, the size increases until 30 nm and becomes stable above pH=7.5. From this result, the optimal condition to favour reproducibility is to achieve pH=7.5 by adding NaOH.

IV.2.1.2 Materials

Gold (III) chloride trihydrate: $\text{HAuCl}_4 \cdot 3\text{H}_2\text{O}$ >99.99%, trisodium citrate and 2-mercaptoethanol (Figure IV-6 (b)) were purchased from Sigma –Aldrich, and used as received without particular treatment. All solutions were prepared in milliQ water with $R=18\text{M}\Omega$.

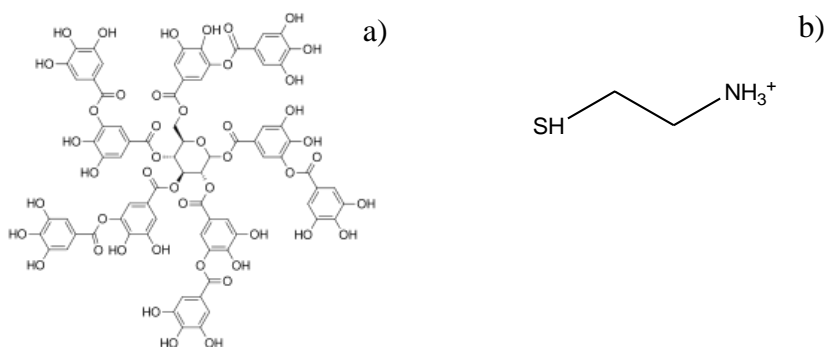


Figure IV-6: chemical structure of a) tannic acid and b) 2-mercaptoethanol

IV.2.1.3 Preparation of citrate stabilized AuNPs

Due to the hygroscopic character of gold salt, we never stock gold salt in powder state, instead, at the first opening of a gold salt batch, we always prepare a mother solution at 10g/L

in milliQ water using all the powder. These mother solutions were stocked in dark area for period not exceeding 3 months for all the following experiences.

1) Preparation of citrate stabilized AuNPs with $R_H > 10$ nm

Here, we took the standard method, as described by Turkevitch and Frens.^[135] The gold (III) mother solution was diluted to obtain 50mL at $C_{Au} = 2.54 \times 10^{-4}$ mol/L with milliQ water in a pre-rinsed three-necked round flask. The yellow orange solution was heated to boil without reflux by a bath thermostat to ensure the homogeneous temperature distribution and was vigorously stirred at ~ 900 rpm with a teflon-coated magnetic bar. When the solution had started to boil, 2.5ml of preheated citrate solution (variable citrate/Au molar ratios tested) was all added at once. After 15min of vigorous stirring at 100°C , the heating source was removed and the solution was allowed to cool down to the room temperature under the same vigorous stirring. The yellow color in the aqueous solution due to the presence of AuCl, turned clear over dark blue and finally left a deep wine red color within several minutes indicating the formation of gold nanoparticles.

$\text{Na}_3\text{Ct} : 2.5\text{ml}$

$\text{HAuCl}_4 : 0.25\text{mM}, 50\text{ml}$

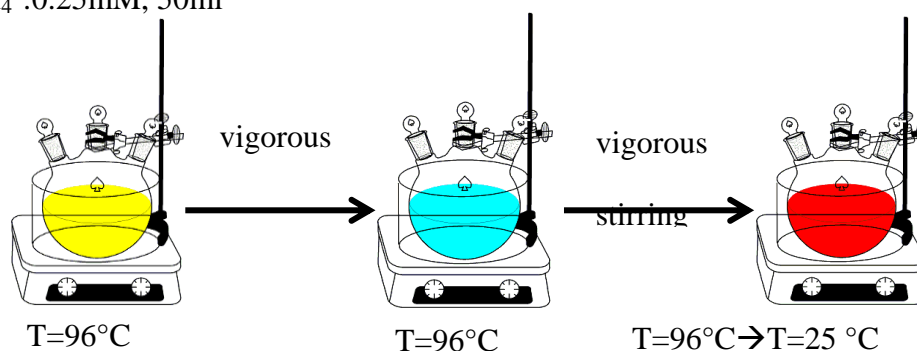


Figure IV-7: Scheme of AuNPs' synthesis by Turkevitch approach for AuNPs with $R_H > 10$ nm

2) Preparation of citrate stabilized AuNPs with $R_H < 10$ nm

For AuNPs smaller than 10nm in radius, the protocol of Slot^[139] was used. For the total volume of 50mL, 0.5ml mother solution of Au(III), 1 vol.% tannic acid 0.5mL, and 0.5ml, 0.025mol/L K_2CO_3 , 1 vol.% sodium citrate 2ml, were prepared. The molar ratio of $C_{Au}/C_{\text{citrate}}$ was equal to 0.187. As the tannic acid is easily oxidized, for each synthesis, the tannic acid was freshly prepared. The 0.5ml mother solution of Au(III) was diluted with 40ml of MilliQ water to attain $C_{Au} = 0.25\text{mM}$ in a pre-rinsed three-necked round flask, and then heated at 60°C without reflux by a bath thermostat under vigorous stirring. Meanwhile, the mixed solution of

tannic acid, K_2CO_3 and sodium citrate was diluted to 10ml in a vial and also heated separately at $60^\circ C$ by a bath thermostat. These two solutions were mixed together at $60^\circ C$ under vigorous stirring during 45min. After that, the heating temperature was raised to $100^\circ C$ during 15min with reflux, and then cooled to room temperature without stopping stirring.

IV.2.1.4 Results and discussions

We now show the characterizations of the synthesized NPs in solution. We would like to insist on the accuracy in size distribution, in particular the size distribution around the average small size value (polydispersity) but first of all the absence of aggregation, which is **very important for how we want to use the NPs in the future**.

1) Effect of Au/citrate ratio on the size of AuNPs (without extra adjustment of pH)

Keeping the same initial $C_{Au}=0.25mM$, and the same heating temperature at $96^\circ C$ without reflux (to avoid inhomogeneous temperature), the effect of the ratio of $C_{Au}/C_{citrate}$ on AuNP size was tested. As shown in Figure IV-8, the size of AuNPs increases with the ratio of $C_{Au}/C_{citrate}$, which is consistent with the literature ^[137] (see Figure IV-3). All of the obtained AuNPs were almost monodisperse with pdI ranging between 0.16 and 0.23.

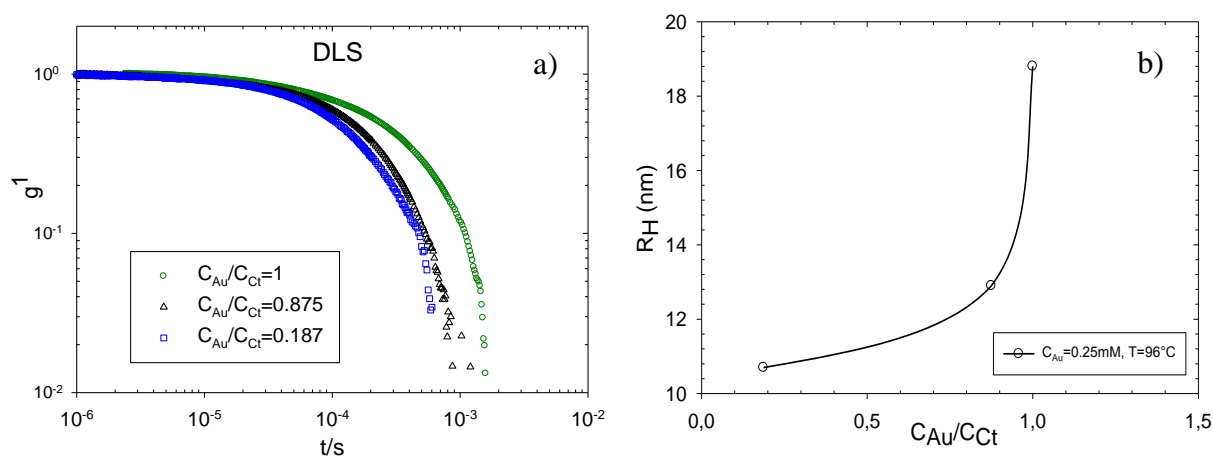


Figure IV-8: a) Correlation functions $g^{(1)}(90^\circ, t)$ on AuNPs dispersions prepared with different initial $C_{Au}/C_{citrate}$ ratio; b) Evolution of AuNPs' apparent hydrodynamic radius as a function of $C_{Au}/C_{citrate}$ molar ratio

1) Effect of pH on the size of AuNPs (ratio of $C_{Au}/C_{citrate}$ constant)

Keeping the same initial $C_{Au} = 0.25mM$, the ratio $C_{Au}/C_{citrate} = 0.58$, and the heating temperature was fixed to $96^\circ C$ without reflux, the effect of pH on the size of AuNPs was studied. The pH was varied by adding NaOH or HCl.

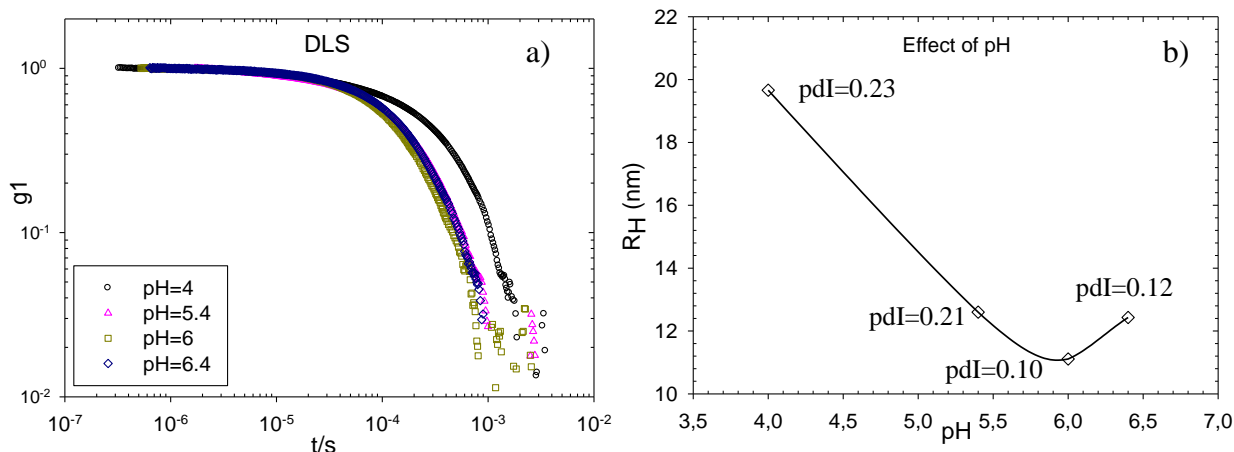


Figure IV-9: a) Auto-correlation functions $g^{(1)}(90^\circ, t)$ of AuNPs prepared at different pH; b) Size evolution of AuNPs in function of pH

As we can see from Figure IV-9, at pH=4, we obtained the biggest size of AuNPs, and it decreases when we raise the pH. We obtained the smallest particles at about pH=6, and after that minimum, the size increases. In the point of view of polydispersity, the AuNPs are much more monodisperse at pH>6. This tendency is in qualitative agreement with the report of Peng (see Figure IV-5), the difference in the absolute value of pdI has to be appreciated together with the fact that Peng measured size by TEM, instead of, in our case, DLS which we believe probes the system on a much more statistical way (including the problems of the large aggregates).

2) Effect of heating temperature of AuNPs

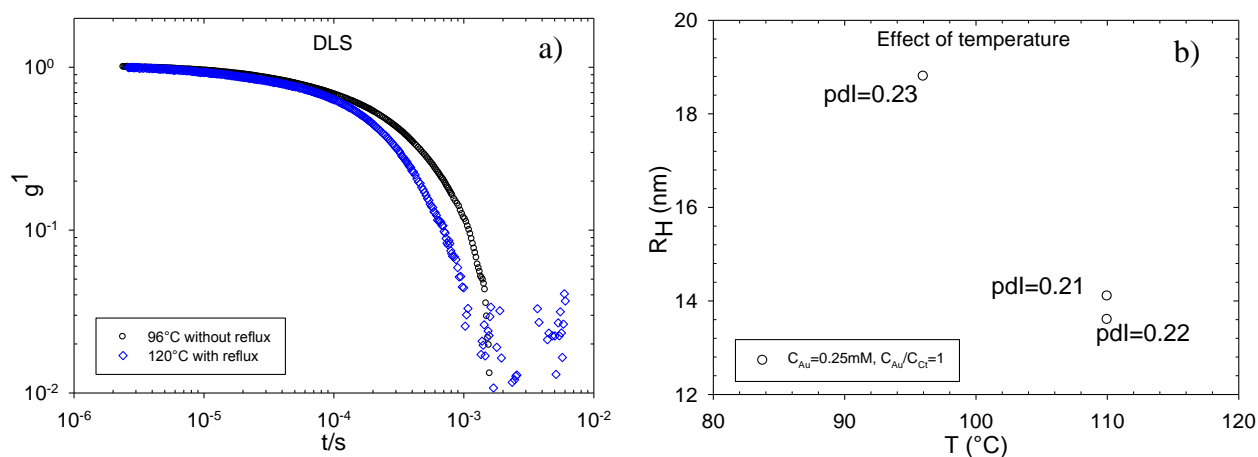


Figure IV-10: a) Auto-correlation functions $g_1 \sim t$ obtained at 90° on AuNPs prepared at different bath temperature; b) Effect of heating temperature on the size of AuNPs

For the same initial Au(III) concentration $C_{Au}=0.25\text{mM}$, same ratio $C_{Au}/C_{Cit}=1$ and the same $\text{pH} = 7.5$, two heating temperatures were tested at 110°C with reflux and at 96°C without reflux. As shown in Figure IV-10, heating at 120°C resulted in AuNPs of smaller size.

3) Use of tannic acid

The use of tannic acid reduces effectively the AuNPs' size, as demonstrated in Figure IV-11, while the initial Au (III) concentration and Au/Citrate concentration ratio remains unchanged. The addition of K_2CO_3 was supposed to further reduce the size of AuNPs, however, it was not applicable in our case.

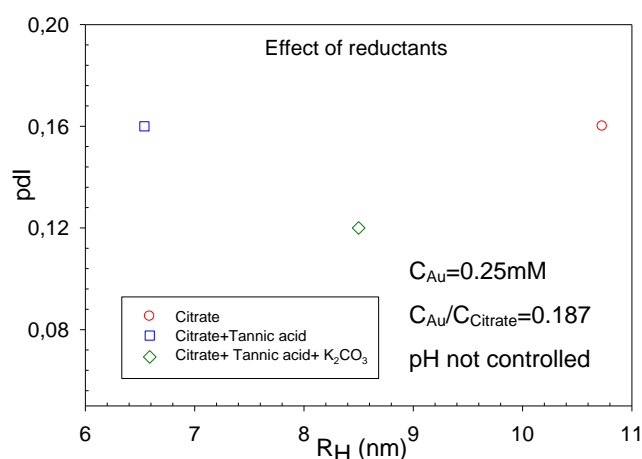


Figure IV-11: Comparaison of size by using different reductants

In summary, we have shown that AuNPs with apparent hydrodynamic radius ranging from 6.5nm to 18.8nm can be prepared in water by playing on the following parameters: ratio of $C_{Au}/C_{citrate}$, pH of system, heating temperature and addition of tannic acid. These particles are quite well defined with pdI comprise between 0.1 and 0.23.

However, the surface of these particles is decorated by adsorbed citrate giving rise to an anionic surface charge. In the following paragraph we present result concerning the exchange of citrate by cationic thiolated ligand.

IV.2.1.5 Ligand exchange: attempts towards positive charge.

It is possible to substitute thiol-ligand for citrate, due to the fact that thiols/Au's covalent bond is more stable than the binding of Au with the carboxyl groups of citrate. Kunitake^[142] proposed a direct way, which is to add an anionic thiol ligand simultaneously with the sodium citrate during the reduction, which resulted in anionic thiol ligand stabilized AuNPs. He emphasized that the addition of thiol ligand before the citrate would make impossible the

reduction of gold, while the addition of thiol after the citrate is not applicable either, because that would cause incomplete exchange and the coexistence of two populations, the citrate-stabilized AuNPs together with thiol-stabilized ones. A more universal method is to change the ligand once the citrate-stabilized AuNPs are formed. It consists to remove the excessive citrate by centrifugation or dialysis and then add a 10 times^[143] more concentrated (molar ratio) thiol ligand solution into the diluted citrate stabilized AuNP solution during long time stirring. After completion of the exchange, the solution is again purified by dialysis to remove the citrates which have been released in solution.^[144]

The amount of substituent ligand is usually 10 times in excess compared to what is needed for full coverage and can be calculated by eq.IV-5:

$$n_{\text{ligand}} = \frac{\text{Number of AuNPs-citrate}}{0.74 \times \left(\frac{R}{0.146}\right)^3} \times \frac{4\pi R^2}{0.214} \times 10$$

Number of ligand per particle

IV-5

where n_{Au} (mol) and n_{ligand} (mol) are respectively the quantity of Au and thiol ligand; 0.74: the compacity of the FCC structure; R(nm): core radius of AuNPs; 0.214: a thiol ligand footprint^[145] in nm²; 0.146: atom radius of gold in nm.

Unfortunately, in 2009, while we were starting our experiments of ligand exchange, Punter et al.^[146] showed that irreversible aggregation occurs systematically when one tries to exchange citrate by cationic ligand. The scheme below (Figure IV-13) illustrates why the aggregation during oppositely charged ligand exchange is unavoidable.

As showed in Figure IV-12, the right pH range to stabilize anionic ligand as sodium citrate is above 3, and the right pH range to stabilize cationic ligand (NH₃⁺) is below 10.

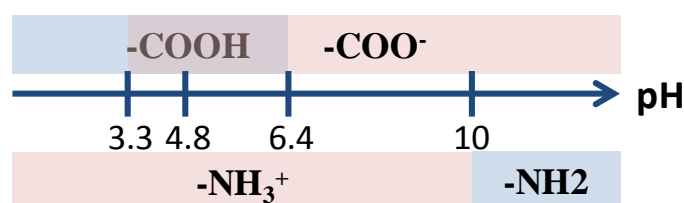


Figure IV-12: Stability of carboxylic acid/carboxylate ion and amine/ammonium ion at different pH

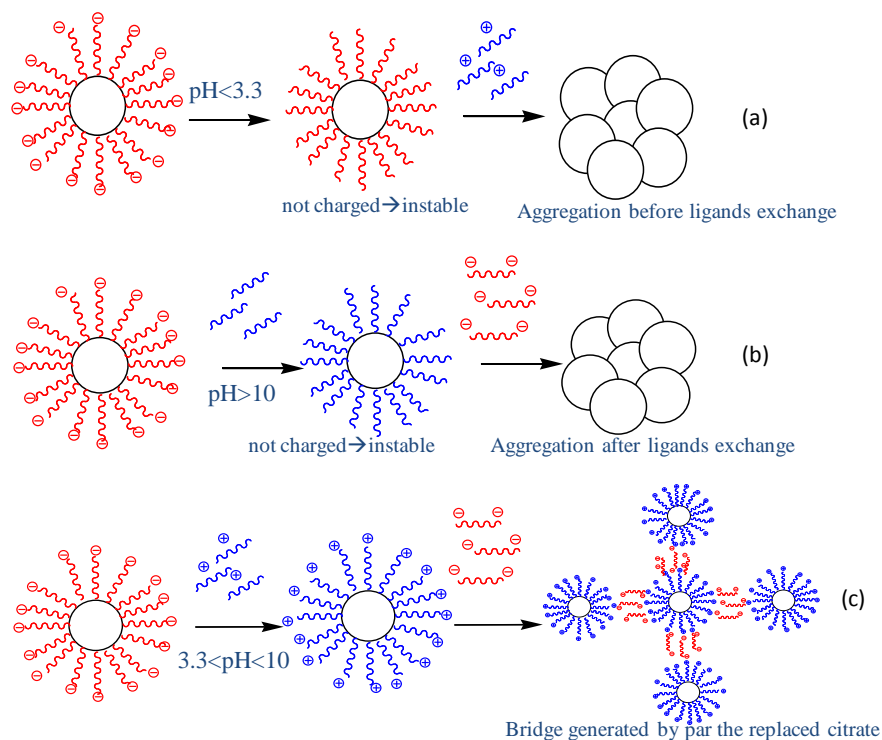


Figure IV-13: Scheme of three possibility of aggregation generated by exchange of oppositely charged ligand

- If the starting pH is below 3.3, the AuNPs-citrate are not charged, and would aggregate immediately before the exchange.
- If the starting pH is above 10, the AuNP-thiol would aggregate immediately after the exchange.
- If at the beginning, the pH of AuNP-citrate is between 3 and 10, then after ligand exchange, the replaced citrate would serve as bridge between AuNP-thiol by electrostatic attraction, as citrate has three carboxylate groups.

We have checked the validity of the different scenario. While using the route a, the AuNP citrate sedimented immediately after addition of HCl. While taking the route b, the pH was adjusted to 11 by adding NaOH, but shortly after the addition of uncharged ligand, the AuNP sedimented. The route c is more complicated. Considering the three pKa of citrate, the initial pH of AuNP citrate was adjusted to three corresponding values. The AuNPs did not sediment macroscopically after ligand exchange as seen in the previous two schemes, but the change of color of AuNP solution during the ligand exchange was observed, and the cumulant analyse of DLS results revealed that the AuNPs were effectively aggregated (Table IV-1)

Option 1: pH = 8.3 \Leftrightarrow Citrate (- / - / -) and Ligand (+)

Step	$R_{app,H}$
Freshly prepared AuNPs – citrate after synthesis	7.2nm
AuNPs after 2 days' dialyze at the same pH	<8.5 nm
AuNPs after adjustment of pH to 8.3	9.2 nm
After ligand exchange at pH=8.3 (ligand prepared in the same pH)	53.1 nm

Option 2: pH = 5.7 \Leftrightarrow Citrate (0 / - / -) and Ligand (+)

Step	$R_{app,H}$
Freshly prepared AuNPs – citrate after synthesis	7.2 nm
AuNPs after 2 days' dialyze at the same pH	<8.5 nm
AuNPs after adjustment of pH to 5.7	8.6 nm
After ligand exchange at pH=5.7 (ligand prepared in the same pH)	12 nm*

* Change of color from wine red to mauve was observed during the exchange. Loss of AuNPs during the stirring (adsorbed on the stirring bar), DLS result based on the remaining very dilute solution may not be reliable.

Option 3: pH = 4 \Leftrightarrow Citrate (0 / 0 / -) and Ligand (+)

Step	$R_{app,H}$
Freshly prepared AuNPs – citrate after synthesis	7.2 nm
AuNPs after 2 days' dialyze at the same pH	<8.5 nm
AuNPs after adjustment of pH to 4	9.3 nm
After ligand exchange at pH=4 (ligand prepared in the same pH)	53.4 nm

Table IV-1 Step by step DLS results on AuNP dispersions during the ligand exchange in 3 pH conditions.

In summary, we have shown that irreversible aggregation occurs systematically when one try to exchange citrate by cationic ligand in agreement with the recent article of Puntès et al.^[146]

IV.2.2 Brust Method**IV.2.2.1 General principle**

This method was described by Brust et al. in 1994. In contrast to the citrate reduction method, the AuNPs are synthesized in an organic media and sterically stabilized by organic molecules having thiol, amide or acid groups. Brust method requires organic solvents to disperse the

Au(III) salt and uses strong reductants such as NaBH₄, Tetrabutylammonium bromide (TBAB), etc.^[147]. The reduced AuNPs usually have small sizes (1-2nm in diameter). The addition of stabilizing agents can obviously increase AuNP' size by interfering the contact between Au (III) surface and reductant, thus slowing down the reduction process.^[148] An increase of AuNP size can also be realized, up to 20nm, by using the initial 1-2nm AuNP as seeds dispersed in a Au (III) salt solution containing a milder reductant.^[149]

In short, the initial synthesis procedure consists to add dodecanethiol to the organic-phase (AuCl₄-dodecanethiol=1:1 mole:mole), followed by reduction with BH₄⁻, leads to dodecanethiolate protected Au clusters having a 1-3 nm range of core diameters.

Subsequent reports^[150] have shown that, instead of dodecanethiol, a wide range of alkanethiolate chain lengths (C3-C24), ω-functionalized alkanethiolates, and dialkyl disulfides can be employed in this same protocol.

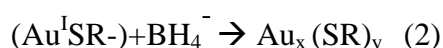


Figure IV-14 Chemical equations of reduction of Au (III) by Brust method^[151]

The details of reactions 1 and 2 have not been completely dissected; however, the reaction's behavior is consistent with a nucleation-growth-passivation process: (i) Larger thiol/gold molar ratios give smaller average AuNPs core sizes and (ii) fast reductant addition and cooled solutions produce smaller, more monodisperse AuNPs. (iii) Quenching the reaction immediately following reduction produces higher abundances of very small core sizes (2 nm).

Based on the Brust method, there are also other many deviations in regard to the protecting ligand structures.^[134, 152, 153] Instead of synthesizing alkanethiolate/AuNPs which are nonpolar, one can use highly polar ligands and synthesize water-soluble AuNPs, in modified syntheses.^[154] A shorter and easier one step protocol using highly polarized ligands can be performed,^[155] but has its fatal defaults: it requires relatively large quantity of ligand at the beginning, compared to the dosage in the ligand exchange. For example, for 7.5mg HAuCl₄, it would cost 90mg ligands at the reduction stage to compare with the 6.3mg at the ligand exchange stage, which induces a much higher cost in regard of the price of the commercial ligands.

IV.2.2.2 Materials and methods

1) Materials

Gold (III) chloride trihydrate: $\text{HAuCl}_4 \cdot 3\text{H}_2\text{O}$ >99.99%, Didecyldimethylammonium bromide (DDAB) $\geq 98\%$, Dodecylamine (DDA) $\geq 99\%$, Tetrabutylammonium bromide (TBAB) $\geq 98.0\%$, Toluene 99.8%, Methanol, Ethyl acetate 99.8% were purchased from Sigma-Aldrich and N,N,N-trimethyl-(11-mercaptoundecyl) ammonium chloride (TMA) $\geq 98\%$ was purchased from Prochimia surfaces. All these products were used as received without further purification.

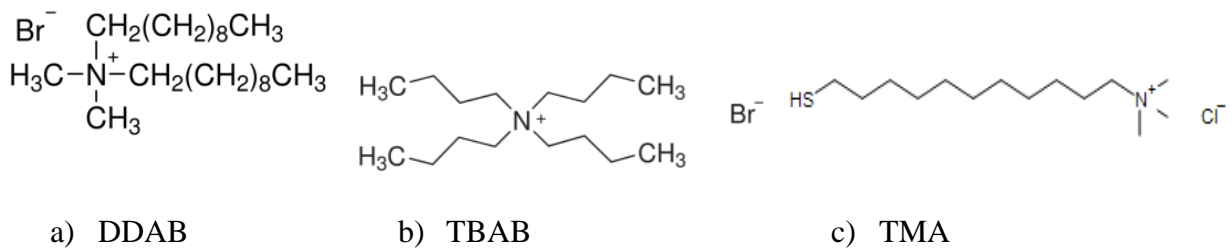


Figure IV-15: Chemical structure of a) didecyldimethylammonium bromide; b) Tetrabutylammonium bromide and c) N,N,N-trimethyl-(11-mercaptoundecyl) ammonium chloride

2) Technical methods

Dynamic light scattering (DLS): Dynamic light scattering was monitored at 25°C on a NanoZS (Malvern Instrument) equipped with a 4 mW HeNe LASER operating at $\lambda = 632.8$ nm. The normalized time autocorrelation functions of the scattered intensity, $g^{(2)}(q,t)$, were measured at 173° . The attenuators were selected automatically by the program in function of sample concentration. Samples dispersed in toluene were filtrated by PTFE filter with membrane size of $0.4 \mu\text{m}$ and samples dispersed in water were filtrated by cellulose filter with membrane size of $0.2 \mu\text{m}$.

Conventionally, we use polydispersity index (pdI) to describe the polydispersity of system. PdI can be calculated from second order cumulant fit, where we obtain R et ΔR , and

$$\Delta R/R = \sigma = \sqrt{\frac{k_2}{k_1^2}} = \sqrt{pdI}.$$

Small angle neutron scattering (SANS): The small angle neutron scattering experiment (for batch N°2) was performed at LLB, Saclay on beamline PACE. The three configurations were $13\text{\AA}-4.7\text{m}$, $4.5\text{\AA}-4.7\text{m}$ and $5\text{\AA}-1\text{m}$, for the q -range from $6.24 \times 10^{-4} \text{\AA}^{-1}$ to $1.64 \times 10^{-3} \text{\AA}^{-1}$, from $9.17 \times 10^{-3} \text{\AA}^{-1}$ to $9.77 \times 10^{-2} \text{\AA}^{-1}$ and from $4.35 \times 10^{-2} \text{\AA}^{-1}$ to $4.42 \times 10^{-1} \text{\AA}^{-1}$. To get a better

contrast, the AuNP mother solution was ultrapurified 3 times against D₂O to transfer all the AuNP into D₂O environment.

Small angle X-ray scattering (SAXS): The SAXS experiment was performed at SOLEIL on beamline SWING. The configuration was 1 Å- 3m to get the q -range from $7.3 \times 10^{-3} \text{Å}^{-1}$ to 0.52Å^{-1} . The aqueous AuTMA dispersions were prepared in 1.5mm quartz capillary.

Transmission electron microscopy (TEM):

TEM images of AuNP were obtained with JEOL 2010 electron microscope operating at 200keV. Samples were prepared by casting a single drop of a 1g/L aqueous solution onto a standard carbon-coated Formvar films on copper grids (200 mesh) and drying in air for more than 30 min

Ultraviolet visible spectroscopy (UV-vis): The UV-vis spectroscopy was performed on Cary 50 Scan UV-Visible Spectrophotometer of brand Varian. The diluted AuNPs were filled in the 5mm thickness Hellma cell (quartz). The absorbance values were recorded after baseline correction.

Electrophoretic mobility (μ) measurements: The measurements of the electrophoretic mobility were carried out at 25°C by means of the laser Doppler electrophoresis technique using the previously described NanoZS (Malvern Instrument). To avoid electro-osmosis the applied electric field is automatically reversed in a periodic manner during the measurement, by a series of slow field reversal and fast field reversal. The AuNP dispersions were diluted at 1g/L in water without addition of salt.

The final electrophoretic mobility has been obtained by averaging the results of 10 measurements.

IV.2.2.3 Preparation of thiol ligand stabilized AuNPs

The protocol used in this thesis combined two previous publications ^[149, 156] with slight modifications, and is composed of three major steps:

- First step is to reduce Au(III) in the presence of DDA.^[149] Both Au(III) and DDA are dispersed in a DDAB /toluene mixed solution. DDAB, a simple artificial cationic lipid, is used as a protective reagent for the formation of monolayer-protected gold nanoparticles in an organic medium. The synthesized AuDDA have diameter of 3 nm and are dispersed in toluene.
- The second step is to exchange the ligand against TMA and redispersed into water.

- The third step is to purify TMA-coated AuNPs by eliminating the excess of ligand. ^[156]

Step-1 Synthesis of AuDDA

Appropriate amount of didodecyldimethylammonium bromide (DDAB) was dissolved in toluene to make a stock solution with 100mM concentration. Then 7.5 mg $\text{HAuCl}_4 \cdot 3\text{H}_2\text{O}$ was dissolved in 2.5 mL of DDAB solution by bath sonication for at least 5 minutes, leading to orange red color. After that 90 mg of dodecylamine was dissolved by bath sonication until the solution became transparent pale yellow. Finally, 25mg TBAB dissolved in 1mL DDAB solution was injected at once to the gold salt solution during vigorous magnetic stirring (900rpm). Dark brown color appears immediately and is stable for more than 24h.

Step-2 From AuDDA (-) in toluene to AuTMA (+) in water

A toluene dispersion of DDA-capped gold particles (3.5ml) was quenched with 17.5 ml of methanol to give black precipitate. The supernatant solution with excess of capping agent and surfactant was decanted, and the precipitate was washed with methanol (3 times 8.5 ml), dissolved in toluene (8.75 ml), to which a thiol solution TMA (6.3mg) in 0.875ml methanol was added drop by drop upon stirring. Dark precipitate of TMA-coated AuNPs appeared in one minute, and was allowed to settle down after 20 min with a continuous magnetic stirring (760rpm). The mother-liqueur solution was decanted, and the solid was washed 3 times with 9 mL of ethyl acetate. The precipitate was then dissolved in 6 ml of water under gentle manual agitation

Step-3 Purification and concentration

In spite of former claim that ethyl acetate would be a solvent of the ligand, the AuTMA dispersion obtained after step 2 still contains a large excessive of ligand at this stage. This might form mesophases in the system according to the streak texture (schlieren) that we observe. This is also probably responsible of the long modes seen in Nano-ZS measurements, which can be first analyzed as large aggregates. This important problem was solved by eliminating the excess ligand by centrifugation with a “Vivaspin” container (MWCO =10K; V =7ml). This device of filtration allows concentrating the solution at the same time of purification, without causing extra aggregation.

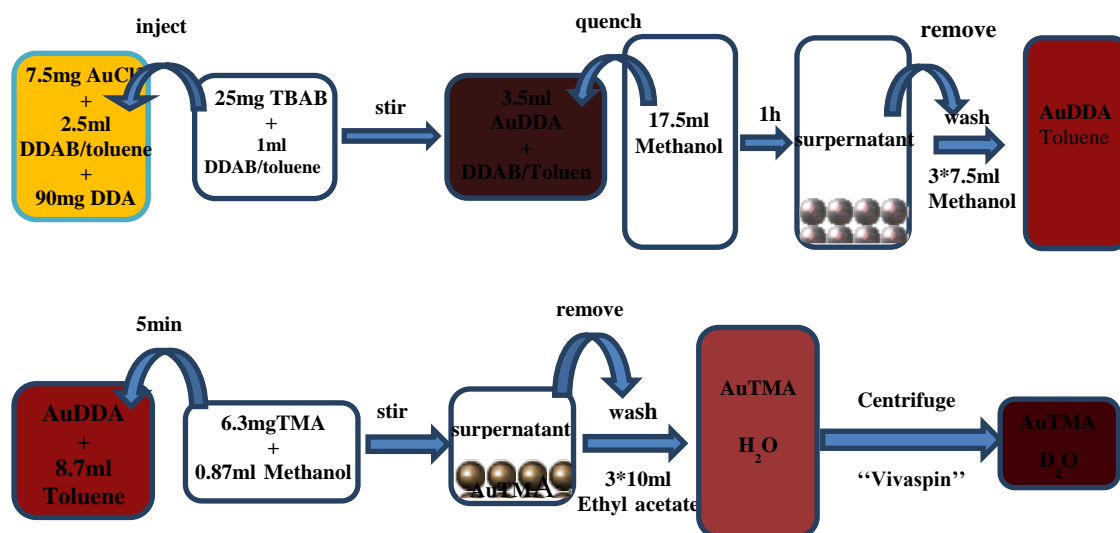


Figure IV-16: Scheme of AuTMA synthesis AuTMA

IV.3 Characterization of AuNPs obtained by the Brust's method

During this thesis, two main batches of AuTMA (each one was a set of about twenty independent small quantity of synthesis) were prepared at different time for the complexation study presented in the next chapter. These two batches are similar in chemical and physical properties, only have 30% difference in size because the Au(III) salt used in the synthesis steps was different for batch n°1 ($\text{HAuCl}_4 \cdot 3\text{H}_2\text{O}$) and for batch n°2 (AuCl_3). Here we just present a series of consistent results.

IV.3.1 Size and shape of gold nanoparticle

IV.3.1.1 Dynamic light scattering: monitoring sizes during the synthesis.

AuNPs were characterized after the three main steps of the synthesis. As shown in Figure IV-17, DDA stabilized AuNPs obtained in toluene after the first step are quite monodisperse ($\text{pDI} = 0.078$) with an average $R_{\text{H,App.}} = 4\text{nm}$.

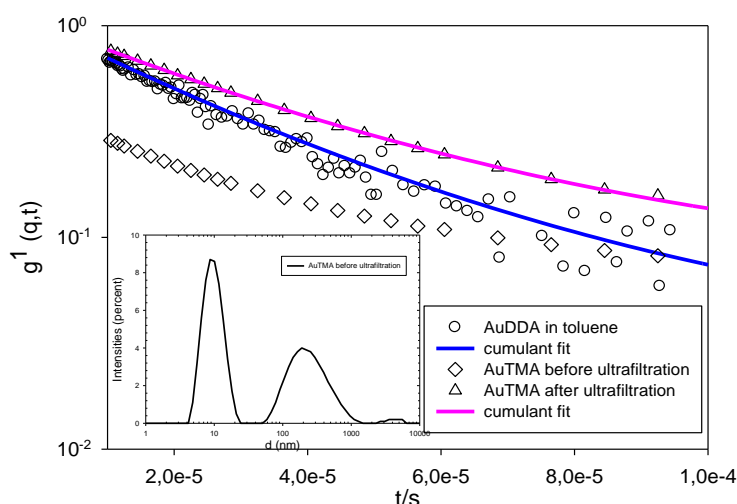


Figure IV-17: Semilogarithmic representation of auto-correlation function $g^{(1)}(173^\circ, t)$ of AuNPs-DDA in toluene (black open circle), AuNPs-TMA in water before (black open diamond) and after ultrafiltration (black open triangle). The two former samples correspond to the same single synthesis while the latter sample have been obtained by gathering AuNPs-TMA prepared out of different synthesis performed in the same conditions. The continuous lines correspond to the best adjustment of cumulant fit. The inset give the size distribution of AuNPs-TMA in water before centrifugation derived from the Contin analysis

After the exchange of ligands and redispersion of AuTMA in water (step 2), one observes an increase of the size ($R_{app,H} = 5.1$ nm) and of the polydispersity (pdI = 0.67). The high value of the pdI suggests the presence of a second relaxation. This trend is confirmed by applying the Contin procedure to our data that shows the presence of a slow mode in the distribution of the scattered intensity as a function of R_H (see inset of Figure IV-17). Indeed, according to this analysis, two main populations can be distinguished in the solution with average size of $R_{app,H} = 5$ nm and 140 nm (see inset of Figure IV-17). To check if this effect is related to the AuNPs or to the excess of ligand that may form mesophases, we gathered about twenty times synthesized AuTMA and filtered our aqueous dispersion under centrifugation using the Vivapsin filtering device. After this treatment (i.e. step 3), we obtain a single population AuTMA with $R_{app,H} = 4.9$ nm and pdI=0.176. One can hypothesize that the increase in polydispersity between AuNPs-DDA (step 1) and AuNPs-TMA (step 3) is related not anymore to a slower population, but just to the standart deviation of the sizes obtained in the twenty different synthesis.

IV.3.1.2 Small angle neutron scattering (SANS)

We have then studied AuNPs by SANS to obtain their R_G and state on the possibility to redisperse these nanoparticles in pure D_2O .

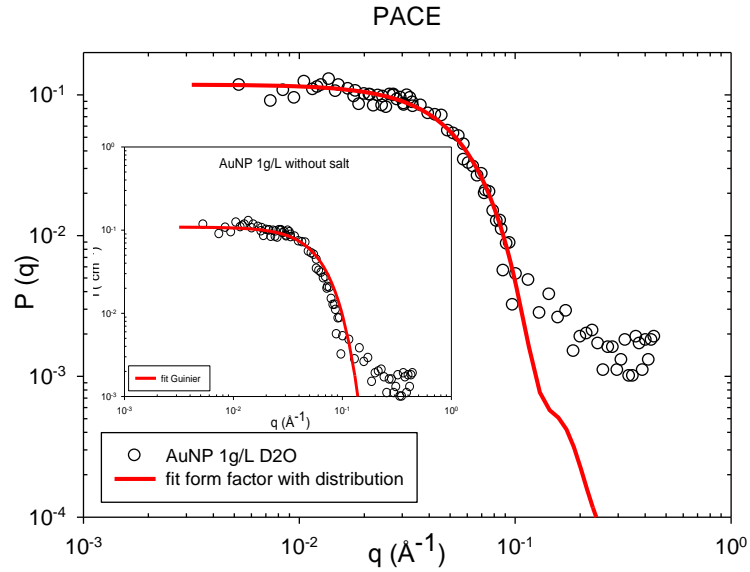


Figure IV-18: SANS pattern of AuNPs-TMA at 1g/L in D₂O without salt performed on beamline PACE and fitted by the form factor $P(q)$ with log-normal distribution (inset: simple fit of the Guinier equation, see Chapter II)

The fit of the data with the form factor derived for hard spheres gives the $R=32 \text{ \AA}$ with log-normal size distribution $\sigma=0.17$, and the fit of Guinier platform give the $R_G=27 \text{ \AA}$. It is worth mentioning that this R_G is consistent with the characteristic ratio R_G/R_H with $R_H=R$ for hard

spheres: $\frac{R_G}{R} = \frac{2.7}{3.2} = 0.845$ since $\frac{R_G}{R} = \sqrt{\frac{3}{5}} = 0.775$ is expected for hard spheres.

Thus we have shown that AuNPs are spherical and can be redisperse in pure D₂O without aggregation.

IV.3.1.3 Small angle X-ray scattering

The SAXS measurement of mixed AuTMA in water were performed on beamline Swing at Soleil.

By fitting with the form factor $P(q)$ of hard sphere (see Figure IV-19), the $R=1.7\text{nm}$ with the log-normal dispersion $\sigma=0.2$ was obtained. The R here is the core radius of the sphere. The reason for the low q upturn seen in the Figure is unknown since the absence of aggregation has been checked by SANS. It may be due to the inadequate subtraction of the capillary contribution.

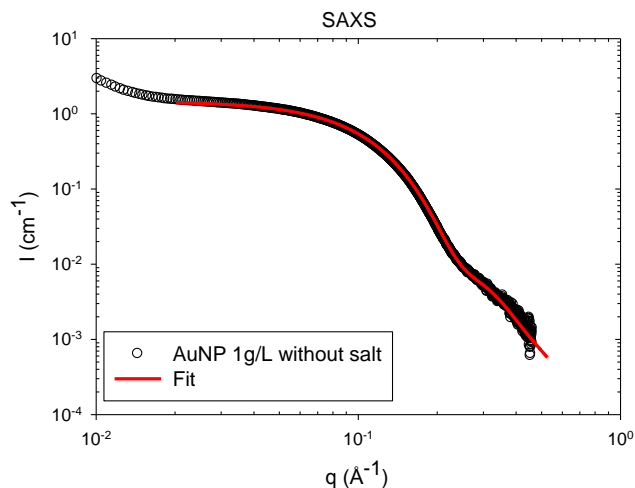


Figure IV-19: SAXS pattern of AuNPs-TMA at 1g/L in H₂O without salt performed at beamline SWING and fitted by the form factor $P(q)$ with log-normal distribution. The reason for the low q upturn is unknown since the absence of aggregation has been checked by SANS. The R from SANS is bigger than R from SAXS, this difference is because that SANS measures the whole AuNP including the ligand TMA, while SAXS measures only the AuNP core (see contrasts in Figure IV-20). As mentioned in chapter II, the scattering signals are the product of several items:

$$I(\text{cm}^{-1}) = \Delta\rho^2 V \Phi P(q) S(q) \quad \text{II-38}$$

As shown in Figure IV-20, the scattering length densities of components are different in SANS and SAXS.

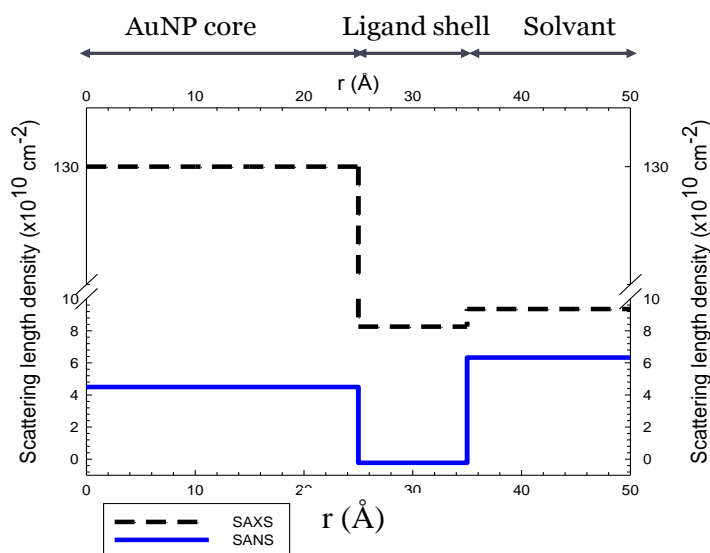


Figure IV-20: Illustration of scattering length density of components in samples for SANS and SAXS

Consequently, the contrasts arising from the scattering length density difference between components and solvent are also different in SANS and SAXS:

- in neutron scattering, the AuNP core and the ligand TMA contributes significantly to the scattering signals, as both of them have sufficient scattering length density difference with the D₂O solvent.
- in X-ray scattering on the contrary, the density difference between ligand TMA and solvent H₂O is almost negligible, which means the majority of signals come from the AuNP core. This explains why R from SANS is larger than R from SAXS. We can deduce here that $R_{\text{SANS}} - R_{\text{SAXS}} = d_{\text{ligand shell}} = 1.5 \text{ nm}$

IV.3.1.4 Transmission electronic microscopy

We have completed the characterization of AuNPs by determining their size and shape in the direct space thanks to TEM. Indeed, due to the strong electronic density of Au and the low electronic density of the grafted thiol ligand and of the underlying membrane of the grid, it is possible to image the AuNPs core only by this approach.

TEM images of AuNPs (Figure IV-21(a)) show us a circular section of AuNPs' core in accordance with the fitted form parameters and the ratio R_G / R_H .

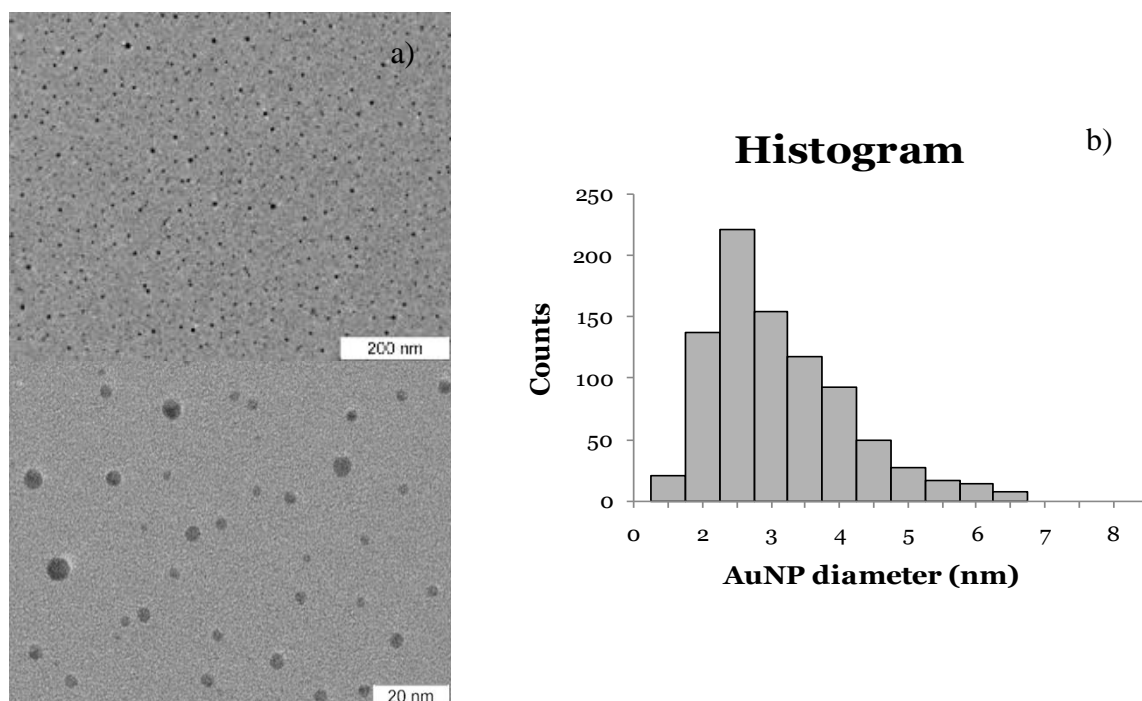


Figure IV-21: a) TEM images obtained at two different magnifications on the same final AuNPs-TMA sample extracted from batch n°1; b) Histogram of AuNPs-TMA (batch n°1) size obtained by a statistical study of different TEM images

An arithmetic mean $\frac{\sum_i n_i R_i}{\sum_i n_i}$ giving $\langle D \rangle = 3.3$ nm, with $\sigma = 30\%$ was obtained from direct

measurement based on 860 nanoparticles of the same dispersion. To compare with sizes obtained from scattering methods, which are based on weight average molar mass

$$M_w = \frac{\sum_i n_i M_i^2}{\sum_i n_i M_i}, \text{ the } \langle R \rangle_{M_w} \text{ can be calculated in the same way and we find}$$

$$\langle R \rangle_{M_w} = \sqrt[3]{\frac{\sum_i n_i R_i^6}{\sum_i n_i R_i^3}} = 2.33 \text{ nm.}$$

Several AuNP solutions from individual synthesis were studied by TEM as well as the final mother solution (from which all the samples were made) obtained by mixing the several solutions. Comparing Figure IV-22 with Figure IV-21, it can be seen that individual synthesis are more monodisperse than the mixed mother solution (Figure IV-21), which means that the polydispersity of mother solution is due to the deviation between each individual synthesis.

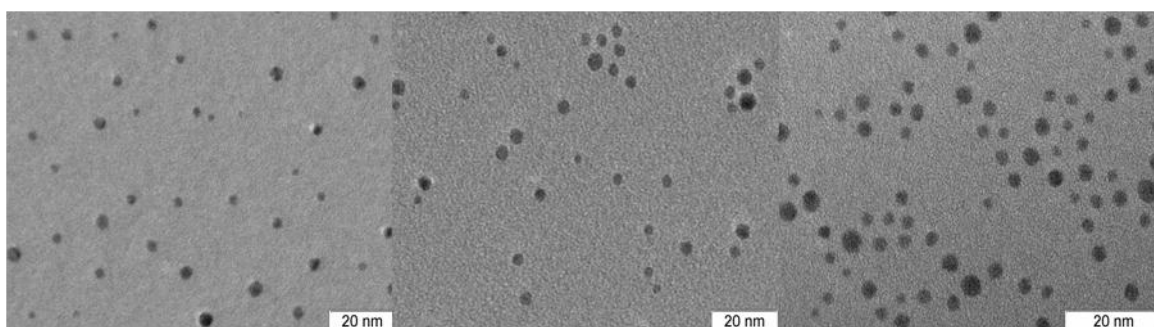


Figure IV-22: TEM images of three individual syntheses of AuNPs using the same protocol and the same magnification

IV.3.1.5 Ultraviolet-visible spectroscopy

Our AuNPs have a specific surface plasmon resonance (SPR) around 520 nm, which is strongly related to their nm size as known from literature, which also tells us that from the color we can already have qualitative information about the size: the small size AuNPs have the wine red color, while big size or aggregated AuNPs dispersions are mauve. However other factors (dielectric environment) may influence this maximum. We will now try to obtain quantitative informations about AuNPs' size and aggregation state with UV-. In a second step, our approach enable us to determine the AuNPs' concentration as shown in the next paragraph.

At first sight, a direct way appear to be the measurement of λ_{\max} , the abscissa of the maximum in the absorption curve $Abs(\lambda)$. However, if we want to be quantitative, we are perturbed by the inaccuracy of the relation ^[143] between the AuNP core diameter and λ_{\max} in the λ range 510 – 520 nm, i.e. when the size is small, between 1nm and 5nm. One reason could be environment. Therefore we decided to use another approach: the diameter can be calculated from the following expression ^[143]:

$$D = \exp\left(B_1 \frac{A_{spr}}{A_{450}} - B_2\right) \quad \text{IV-6}$$

with the experimental parameter $B_1=3.00$, $B_2=2.2$, A_{spr} is the surface Plasmon resonance peak absorption value, A_{450} is the absorption value at $\lambda=450\text{nm}$. ^[143]

The AuNPs mother dispersion was diluted by 10, 20, 50, 80 and 100 times. This enables first to check that, while the values A_{spr} and A_{450} vary slightly with concentration, the average ratio of A_{spr}/A_{450} stays constant and equal to 1.13 as shown in Figure IV-23-b. From eq. IV-6, this value has enabled us to calculate an average core diameter of 3.3nm, which is in good agreement with $\langle D \rangle$ measured by TEM. We note that the peak abscissa does not vary with concentration.

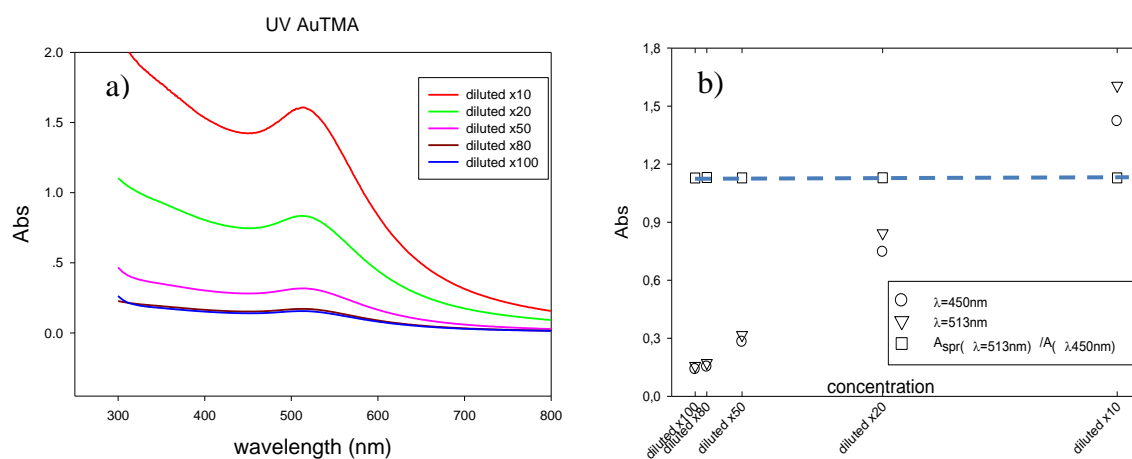


Figure IV-23: UV-visible measurements for AuNP-TMA dispersed in water at different dilution.

IV.3.1.6 Summary on the size results from the different techniques

We summarize in Table IV-2 the sizes determined by the different methods of characterization of the same batch.

	$R_{H,app}$ by intensity	R_G by intensity	R by Mw	R by number
DLS	4.9nm, batch #1 4.0nm, batch#2 (global)			
TEM			2.3nm, batch #1 (core)	1.7nm, batch #1 (core)
UV				1.7nm, batch #1 (core)
SANS		2.7nm, batch #2 (global)	3.2nm, batch #2 (global)	
SAXS		NA	2.2nm, batch #1 1.7nm, batch #2 (core)	

Table IV-2: List of AuNP size based on measurement of DLS, TEM, UV, SANS and SAXS

All of these techniques have given us consistent and/or complementary information on size, shape and polydispersity of AuNPs.

IV.3.2 Determination of AuNP mother solution concentration

One of the inconveniences of Brust's method is the rather unknown productivity of synthesis. Thus it is also important to determine the concentration of the mother solution from the direct syntheses. In this point of view, UV-visible spectroscopy is a practical method for such small quantity weakly concentrated dispersions.

The absorbance at 513 nm was recorded for each sample at different dilution and plotted versus the relative molar concentration of the solution (from the results shown in Figure IV-23-b). According to the Beer-Lambert law, there is a linear evolution with the relative concentration:

$$A = \epsilon l C \quad \text{IV-7}$$

where $l = 0.5$ cm is the thickness of sample cell.

To know C , we need to know ϵ . Regardless of the capping ligands on the particle surface and the solvents used to dissolve the nanoparticles, the linear relationship between the logarithms of extinction coefficients and core diameters of AuNP can be used as a calibration curve to determine the concentration of AuNP-ligand dispersions.

$$\ln \epsilon = k \ln D + a \quad \text{IV-8}$$

where k and a are parameters for spherical AuNPs in aqueous solvents that have been obtained theoretically^[157] equal to 3.36 and 8.1, and experimentally^[158] equal to 3.32 and 10.8

respectively. Eq. IV-8, using the core diameter $\langle D \rangle = 3.3$ measured from TEM (or UV-vis). The concentration $C = 1.17 \times 10^6$ mol/L can be deduced from the slope of the curve Abs(C).

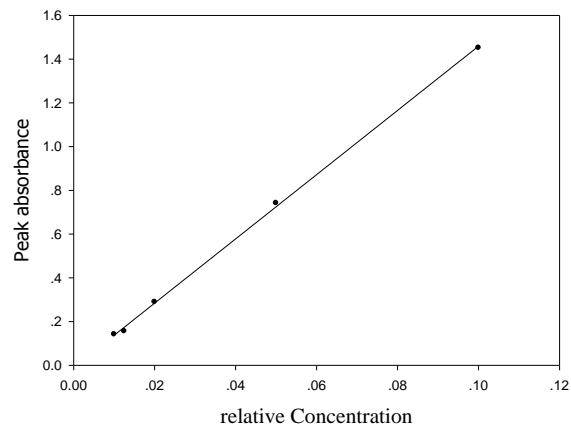


Figure IV-24: Extrapolation of the SPR absorbance vs relative concentration

Using the density of gold (fcc) is 19.3 g/cm^3 , the molar mass $M = 2.4 \times 10^5$ g/mol can be calculated for AuNPs with diameter $D = 3.3 \text{ nm}$ from

$$M = V\rho N_A = \frac{4}{3}\pi\left(\frac{D}{2}\right)^3\rho N_A \quad \text{IV-9}$$

Thus, the concentration of AuNP mother solution is 2.7 g/L

IV.3.3 Surface charge of AuNP

1) surface charge determined by electrophoretic mobility

The electrophoretic mobility of the AuNP-TMA have been measured on a dispersion at 1 g/L , and without added salt. Assuming a full dissociation of the ionic groups, resulting in an elementary positive charge per charged ligand and a surface area per charge of about 0.214 nm^2 ^[145], one can estimate that each AuNPs with core radius 1.7 nm is surrounded by a closely packed monolayer constituted of ~ 170 ligands at $C_{\text{AuNPs}} = 1 \text{ g/L}$ leading to a bare charge of $170e$ or $94e$ if one take into account Manning condensation. Considering that our AuNPs have typical R_H around 5.1 nm according to DLS, it appears that our measurements were performed for $\kappa R_H \approx 0.44$ or $\kappa R_H \approx 0.33$ if one take into account Manning condensation.

In this condition, Huckel's formula can be applied to derive the electrical charge per nanoparticles, Z_{eff} , from the measured electrophoretic mobility $\mu = 1.73 \cdot 10^8 \text{ m}^2 \cdot \text{V}^{-1} \cdot \text{s}^{-1}$ which is an average of 10 measurements with the standard deviation $\sigma = 11\%$:

$$Z_{\text{eff}} = 6\pi\mu\eta R_H \approx +9e/\text{AuNP} \text{ or } \approx +0.25e \cdot \text{nm}^{-2}$$

where η is the solvent viscosity at 25 °C. This result indicate that our nanoparticles are effectively positively charged and display an electric charge. The value is far below the one expected in the limit case of a closely packed TMA ligand monolayer with a full dissociation of the ionic groups.

However, it appears that the above determined surface charge is well below the value obtained by SANS (next paragraph) and titration (next chapter) that is 190 ligands per particle. This number is in fair agreement with the calculation performed for a closely packed monolayer making us furthermore confident in this value rather than the former one. So why the surface charge determined by electrophoretic mobility should be inappropriate?

A technical reason may be that, in the default configuration, the Nano-ZS device uses the so-called “Mixed Mode Measurement” (M3) sequence which consists of a periodically reversing of the applied field during the measurement. This sequence is composed of a series of slow field reversal and fast field reversal. According to the supplier this mode avoid electro-osmosis effect arising from the cell’ walls which carry a surface charge and thus enable the measurement of the particle velocity in the middle of the cell rather than at the stationary layer that is situated in the vicinity of the wall. We believe that in our case the AuNPs could diffuse to the oppositely charged electrode surface during the slow field reversal due to their very low size and their high surface charge. This assumption is supported by the observation that the electrode surface depicts a mauve color even after one measurement. According to this scenario the electrophoretic measurements are thus probably skewed by the electrode polarization and the aggregation of an unknown proportion of AuNPs on the electrode surface. But we can also consider a more general physical reason, which is discussed in detail in Chapter III: the charge responsible for electrophoretic mobility includes some counterions condensed around the particle, which may not be the case for electrostatic complexation (see Chapter III).

2) surface charge determined by calculation of ligand number

The surface charge of synthesized AuNPs can be determined by calculating the number of ligand functionalized at the surface of AuNP core, as we know that each chain of ligand owns one positive charge. The calculation is made using the expression of Pedersen model, which gives the an analytical expression of the scattering of a single corona, at $I(q=0)$:

$$P_{Pedersen}(Q, R_{AuNP}, R_G) = V_{core}^2 \Delta\rho_{core}^2 P_{sphere}(Q, R_{SiO_2})$$

$$\begin{aligned}
& + N\Delta\rho_{chain}^2 V_{chain}^2 P_{chain}(Q, R_G) \\
& + 2NV_{core} V_{chain} \Delta\rho_{core} \Delta\rho_{chain} S_{core-chain}(Q, R_{AuNP}, R_G) \\
& + N(N-1)\Delta\rho_{chain}^2 V_{chain}^2 S_{chain-chain}(Q, R_{AuNP}, R_G) \quad \text{IV-10}
\end{aligned}$$

Using the values from Figure IV-18, we obtain N=190 ligand per particle. Assuming that all the ligands are solvated (in acidic state), thus all charged, a single AuNP can have maximumly 190 positive charges. This value is much higher than the one given by zetameter discussed in Appendix 4 of Chater III.).

IV.4 Conclusion

We have been attempting at the synthesis of positively charged –cationic- NP, a rare object, in a non-aggregated form. First we have been able to synthesize **anionic** AuNPs quite monodisperse ($0.1 < \text{pdI} < 0.23$), having hydrodynamic radius between 6.5 and 18.8nm. These AuNPs can be prepared by Turkevitch derived approaches. However, the citrate at surfaces cannot be exchanged by cationic ligands without aggregation, so it is not appropriate for our study.

Hence, we have synthetized small AuNPs by Brust type approach. We have found a way to transform them into cationic NPS without aggregation. These well characterized AuNPs are stable enough to be highly concentrated and then redispersed in either H₂O or D₂O in function of scattering interests and in presence of salt without having aggregation. In the following chapter, these AuNPs will be considered as model NPs for the study of anionic PEL/small cationic NPs complexation.

CHAPTER V

COMPLEXATION OF
POLYELECTROLYTE AND
NANOPARTICLES OF SMALL
SIZE (2~5NM)

V. Complexation of polyelectrolyte (PEL) and nanoparticles (NPs) of small size (2~5nm)

V.1 General introduction

In this chapter, we will study the electrostatic complexation between polyelectrolyte and nanoparticles of small size. Decreasing R will extend the range of L_p/R which concerns most of our study. For this purpose, again, the same two polyelectrolytes with different flexibility as before are used, flexible sodium polystyrene sulfonate (PSSNa) and semi-flexible hyaluronan (HA), both of them are negatively charged. The small particles are AuNPs ($R \approx 4\text{nm}$) and were synthesized by ourselves and well characterized using the protocol described in the previous chapter. The question is: are the features of complexation only explained by the parameter L_p/R ? We will see that not only the behaviors are different from systems with larger particles, but also the differences between AuNPs complexed with flexible PSSNa and semiflexible HA are not exactly the same as for silica particles. Besides, salt effect was also studied. For each composition, two salt concentrations were proposed, without salt added or with additional 0.1M NaCl. As before, salt effects are clear, in particular on phase diagram and on different fractal dimension or compacity of the complex formation. All this will be developed now.

V.2 Complexation of sodium polystyrene sulfonate (PSSNa) and gold nanoparticles (AuNPs)

V.2.1 Materials

V.2.1.1 Sodium polystyrene sulfonate

Sodium polystyrene sulfonate (PSSNa) was purchased from supplier PSS and used as received. PSSNa is derived from polystyrene, the sulfonate group adds to the polymer one negative charge per monomer unit.

PSSNa is a flexible polyelectrolyte, well known for its intrinsic persistence length as short as 0.9 nm. The Mw of PSSNa powder used in all experiments is 80KDa, according to the supplier's GPC measurement.

The variation of the electrostatic contribution to the persistence length with the concentration and the ionic strength has been studied in detail by the LLB group^[159], as well the level of counterions condensation, the hydrophobicity effects, the effect of added divalent coions: this PEL is well known from us.

Sodium polystyrene sulfonate: $C_8H_7SO_3Na$

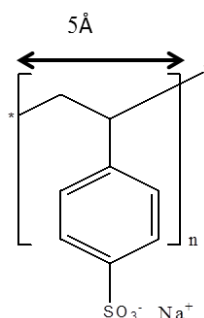


Figure V-1: chemical formula of PSSNa

V.2.1.2 Positively charged AuNPs

The synthesis and characterization of AuNPs used for complexation in this chapter were described in the last chapter. Hence we just recall the main characteristics. For the batch No°1, AuNPs have an Au core size of 2.2nm in radius, and a shell of ligands of about 1.5nm, which make the global size of about 3.7 nm in radius. For batch No°2, AuNPs have an Au core size of 1.7nm and the global size of 3.2nm. The water soluble AuNPs were stabilized by the positively charged ligand TMA, which has thiol groups on the one end to make covalent bond with Au core surface, and ammonium groups on the other end of the chain to bring repulsive positive charges.

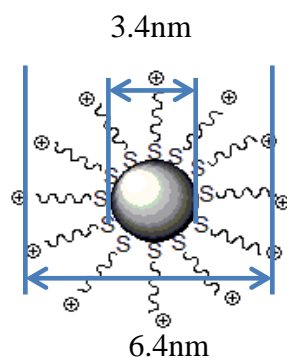


Figure V-2: sketch of TMA stabilized AuNPs for batch No°2

At the last step of synthesis, the AuNPs were collected together for further purification, using centrifugation in special containers (“vivaspin”). For samples prepared for small angle neutron scattering, AuNPs should be purified against deuterated water (D_2O) from the point of view of contrast (while obviously it is simpler to do it in H_2O). In practice, due to the experiment schedule and limited quantity of synthesized AuNPs, we could not follow

precisely this principle. For X-rays, we assume that the physical properties of AuNPs are identical in D₂O and H₂O; thus, since the contrasts of AuNP/D₂O and AuNP/H₂O are almost the same in X-ray scattering, we did not distinguish samples prepared in D₂O or H₂O and it will not be specified each time in the following sections. For neutron scattering, on the reverse this will be noted each time, because the background due to incoherent scattering is much larger in H₂O, which often results in poor statistics. To sum up, we have made successively two batches of mother solution of AuNPs, one in D₂O and another in H₂O. In priority, samples studied at DESY and at ILL (D11) were prepared in H₂O, and samples performed on SWING and PACE were prepared in D₂O. These two batches may have little difference in core size.

V.2.2 Complexation PSSNa-AuNPs without salt

V.2.2.1 Description of phase diagram

Samples were prepared by mixing the same volume of PSSNa and AuNP solution. After being shaken for a while, they were allowed to stabilize for three days before the observation was made.

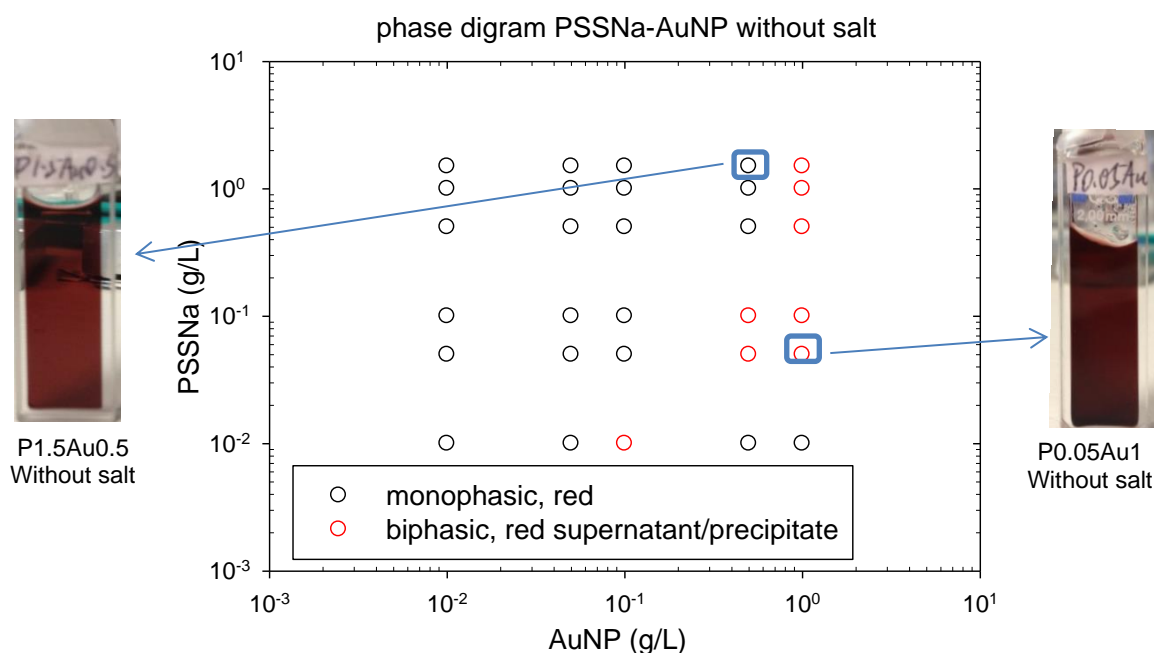


Figure V-3: Phase diagram of PSSNa-AuNP complexation behaviors at different concentration pairs without salt

In the phase diagram, two monophasic domains (I, left hand side, and III, right hand side), and one biphasic domain (II) were observed. In I, samples exhibit the same red color as the diluted solution of AuNP alone at the same concentration. When the AuNP is in excess (domain III),

the samples are deep red. Whether they phase separate or not can be rather difficult by visual observation, as they can have little precipitate in suspension. But as there is no gradient in color from top to bottom of the solution, we assume that the sample is monophasic. In the middle of the diagram, the samples are biphasic, with the red color supernatant (color of AuNP solution alone) and precipitate fallen onto bottom. Just after mixing, these samples cannot be distinguished from the others that stay monophasic all the time. The process of precipitation may take from several hours to several days before the biphasic samples get stabilized.

V.2.2.2 Inner structures of complexes

The structure can be investigated using X-rays, which is dominated by the scattering of the gold particles. SAXS measurements were first performed on beamline A2 at DESY, Hambourg. Samples were chosen from the last two columns of the phase diagram, for which the scattering is higher because the Au particles concentration is higher. All the samples were freshly prepared in the capillary of 2mm thickness three days before the experiments. The equivalent volume of AuNP and PSSNa solution was first mixed in the glass vial, then the well mixed solution was quickly transferred to the capillary, and the precipitates were allowed to settle down in the capillary in case of biphasic ones.

During the experiment, the vertical position of the capillaries was adjusted so that the X-ray beam could shoot at different altitude of the capillary.

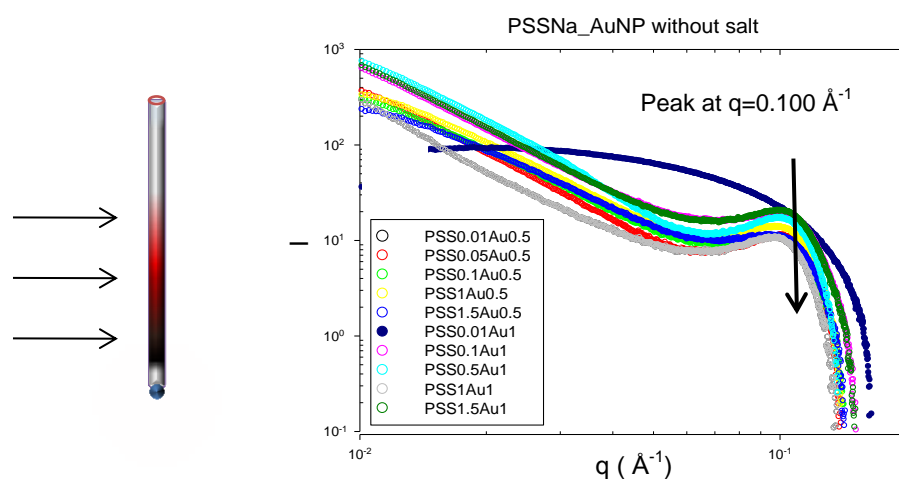


Figure V-4: SAXS pattern of complexes PSSNa-AuNP without salt performed on beamline A2, Desy. The sketch at left showed how the capillary was measured at different height. Here, we just plot the results corresponding to a X-ray beam pointed at the middle of capillary. First, all the curves have a peak at around $q=0.100\text{\AA}^{-1}$ except for the sample PSS0.01Au1,

corresponding to an interparticle distance of 6.28nm. The characteristic peak is a typical sign of the fact that an important fraction of nanoparticles are stuck to each other inside the complex. This distance is between the double of the radius of the particle R_{NP} of AuNP core and the double of R_{NP} of AuNP including ligand. It means that the ligand shells of two particles may be able to interpenetrate each other.

A different profile is obtained for PSS0.01Au1, which much resembles the one of the AuNP solution alone. This can be explained by the fact that in this sample, there is a very small amount of complexes compared to the quantity of non complexed AuNPs, which dominate the scattering signal.

Normally, one can extract information from the low q part of the curve. Here we see slope in log-log, which could indicate the fractal dimension of the formed complex. However, for these given experiments at DESY, a reliable transmission value is missing, and the capillaries are of poor quality. Therefore it is nearly impossible to from the signal of the capillary, each capillary having a different thickness of capillaries. We consider the apparent slope cannot be trusted here. Under these conditions it is also difficult to tell whether a Guinier regime (which would indicate a size of the objects) appears or not.

For these reasons, it was interesting to check the slopes of curves at low q small angle neutron scattering, for which the thickness of the cells (Hellma cell) is much more uniform. The SANS experiments were performed at ILL Grenoble at beam line D11. All samples were freshly mixed a few minutes before the experiment, using the same mother solutions and in the same way as for SAXS. In the time range of experiments, all the samples were still macroscopically homogenous. It is to be regretted that limited by the quantity of mother solution of AuNP, the samples were all prepared in H₂O, which is indeed not suitable for SANS experiments. For the reason of poor contrast and weak concentration, the signal was weak compared to incoherent scattering background, making the data at high q range not exploitable. This preparation method is valid for most of the samples in SANS experiment at D11 if not specially mentioned.

Representative samples were chosen for measurements at configuration of 5 Å, 20m, giving (depending on which figure below) a q range from 0.003 Å⁻¹ to 0.04Å⁻¹, or sometimes 5 Å , 40 m (0.0017 Å⁻¹ to 0.022Å⁻¹), and even 10 Å , 40 m (0.00076 Å⁻¹ to 0.012Å⁻¹).

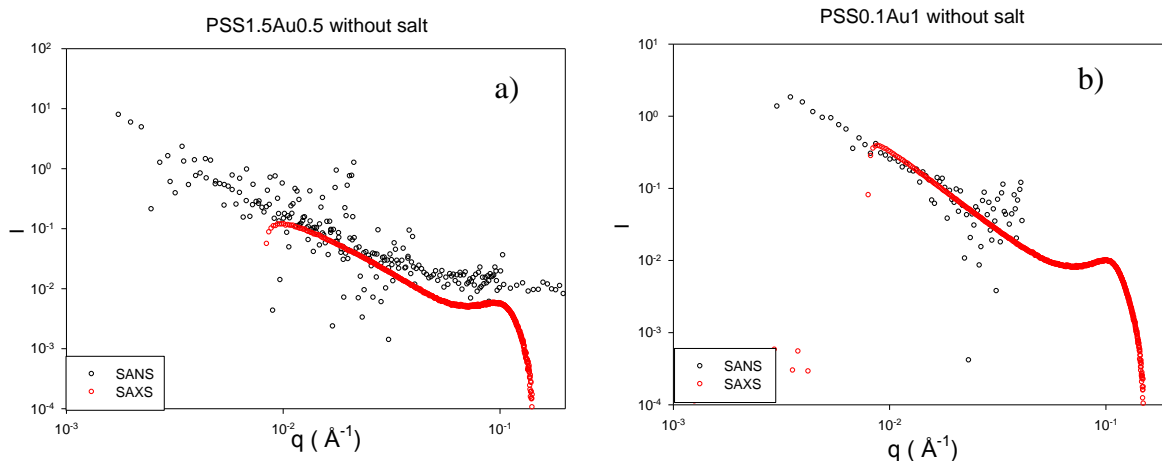


Figure V-5: combination of SANS and SAXS patterns of sample PSS1.5Au0.5 and PSS0.1Au1 without salt. The intensity of SANS was adjusted arbitrarily to joint two curves. By shifting arbitrarily the SAXS curves (vertical direction), it is possible to combine the SAXS to SANS, and we find a good continuity at low q , indicating that the complexes formed at the beginning of mixing stay stable in the solution between recordings at the two configurations.

A more precise work was made using SAXS on beam line SWING at SOLEIL, where the full q range covers from 10^{-3} to 0.5 \AA^{-1} and the scattering curve could be calibrated by transmission and solvent subtraction. We plot on Figure V-6 the results for which the X-ray beam was focused on bottom of the capillary.

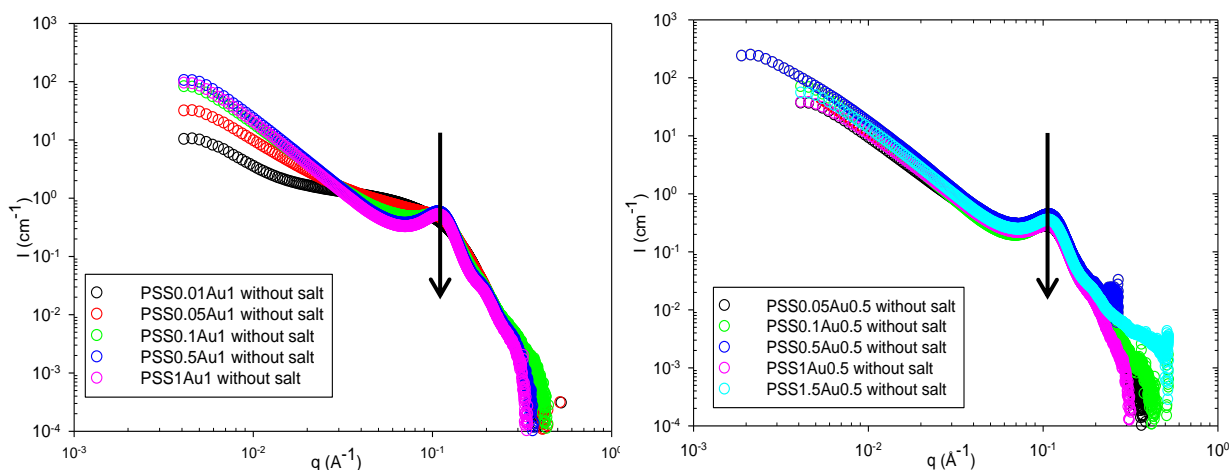


Figure V-6: SAXS patterns of complexes samples at different PSSNa-AuNPs ratios in the absence of salt

All the samples except PSS0.01Au1, show a peak at $q=0.106 \text{ \AA}^{-1}$, corresponding to an interparticle distance of 5.92nm, which is between the double of core radius and double of global radius (core + shell).

The evolution of slopes at low q was also analyzed. The slope varies between 1.7 and 2.5, and it arrives its maximum 2.5 at ratio PSSNa/Au=0.2 (g/L/g/L). Below that ratio, the slope decreases with the increase of PSSNa's concentration. Above that ratio, the slope decreases with the increase of AuNP's concentration.

Discussions of the reproductibility: We find that the slope at low q may vary for the same identical composition of some samples measured at ILL and SWING. This is the case, for example, of sample PSS0.1Au0.5 without salt (see Figure V-5(b) and Figure V-7(b)). The reason is that the SANS at ILL was measured immediately after the mixing, when the separation of phase were not completed yet, while the SAXS at DESY and SWING was measured only after the final state of complexes was reached. It is possible that at beginning of mixing, samples form less compact ramified structures which become more compact afterward. Actually, at A2 DESY, the X-ray beam was shot at the middle of capillary, and the bottom of the capillary for SWING. The plot shows that at different attitude of capillary, the complexes do not have the same structure. This phenomenon occurs when the PSSNa is in excess.

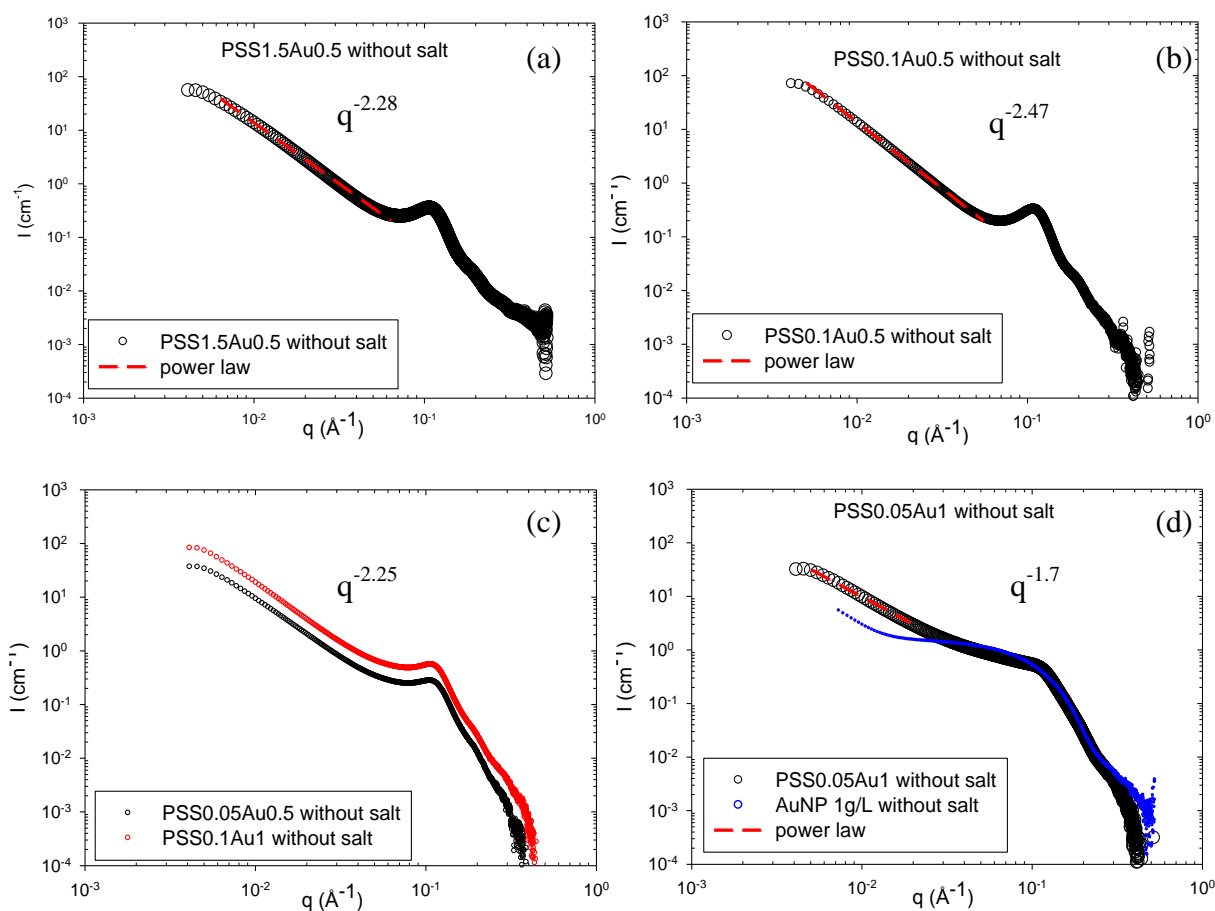


Figure V-7: SAXS pattern measured at same heights in the capillary on beamline SWING of sample PS1.5Au0.5(a), PSS0.1Au0.5(b), PSS0.05Au0.5, PSS0.1Au1(c) and PSS0.05Au1(d) in the absence of salt. The evolution of PSSNa/AuNP ratio reflects the evolution of fractal dimension

For certain samples we find the quite good reproducibility for SANS and SAXS experiments; they correspond to the case where the separation of phase occurs shortly after mixing, suggesting that the final state is reached already.

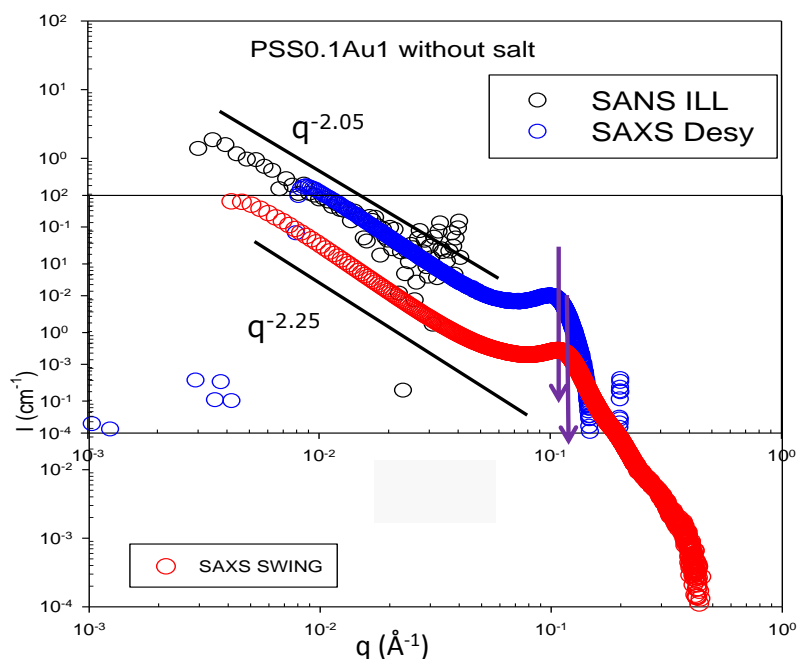


Figure V-8: SANS and SAXS patterns of sample PSS0.1Au1 without salt showing good agreement between the curves; the curve of SAXS was shifted arbitrarily

We can see from Figure V-8 that for sample PSS0.1Au1 without salt, the curve of SAXS at low q has about the same slope as for SANS, which means that the formed complexes have the same structure in the rich and poor phase, and became stable soon after the mixing. The slight shift of characteristic peak is due to the fact that the AuNPs from the first batch (for ILL and DESY) are 30% bigger than from the second batch (used for SOLEIL).

Structure and stoichiometry: In conclusion, the evolution of the fractal dimension of the complexes, which is the main characteristic of the evolution of complexes' structures, shows a consistent dependence on the position in the phase diagram. When AuNPs are in large excess, the scattering signal is fully dominated by the individual AuNPs and we see only the Guinier platform of the individual NP form factor, with no upturn due to aggregation. There is a critical ratio of PSSNa/AuNP at which the complexes are most compact, above that ratio, the excess of PSSNa leads to a ramified aggregation of AuNPs. Below that ratio, the supplemental AuNPs in the solution also results in a ramified structure, but more linearized compared to the former ones (fewer and longer branches). Actually, the concentration ratio of PSSNa/AuNP corresponds to a ratio of opposite charges for the two components in given conditions. Finally, a last characteristic, shown by a set of several SANS and SAXS results, is that under certain conditions, the phase separation may undergo more than one stage, and the complexes could rearrange to reach a more compact structure.

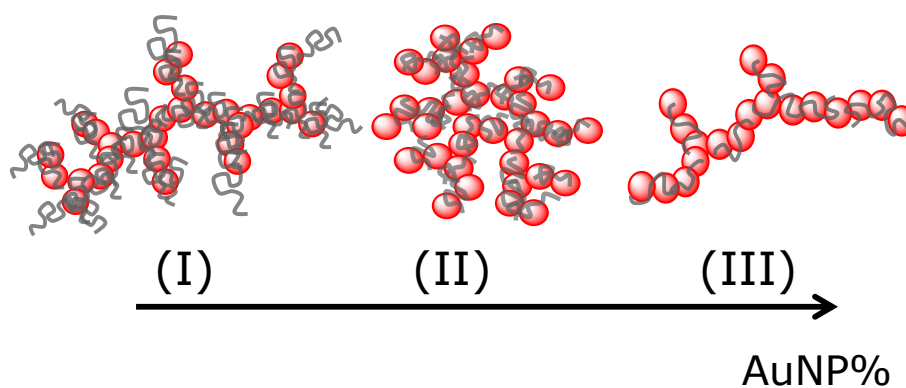


Figure V-9: Evolution of complexes' structures with the increase of AuNPs concentration

V.2.3 Complexation PSSNa-AuNPs in screened conditions (0.1M NaCl)

V.2.3.1 Description of phase diagram and state of the samples

Samples used to form complexes PSSNa-AuNP with 0.1M NaCl were prepared by mixing the equivalent volume of AuNP saltless solution and PSSNa solution with 0.2M NaCl at different concentration pairs. Similarly, after being shaken for a while, they were allowed to stabilize for two weeks before the observation of the phase diagram was made.

Unlike the saltless systems, the complexation in the presence of 0.1M NaCl exhibits a different behavior. For the monophasic region in the left of the diagram, the solutions are similar to the saltless ones. However, for the biphasic region, there are two types of biphasic samples. One type is already familiar, with deep red supernatant and a few precipitate at the bottom. The second biphasic behavior occurs at a fixed AuNP/PSSNa concentration ratio of 10, which draws what we will call the “stoichiometric line”. This behavior is valid for all the cases even at very low absolute concentration, like PSS0.005Au0.05. It is distinguished from the other biphasic region by the unique feature that black insoluble grains formed within one second once two components mixed, and sediment onto the bottom of vial immediately, leaving the supernatant clear and colorless. For biphasic samples above this stoichiometric line (AuNP/PSSNa concentration ratio of 10 g/L/g/L), the supernatants actually have a gradient in concentration (i.e. in color through visual observation), while for samples below this stoichiometric line, the supernatants are rather homogeneously red. For all biphasic samples, the presence of 0.1M NaCl leads to quicker phase separation than for saltless systems.

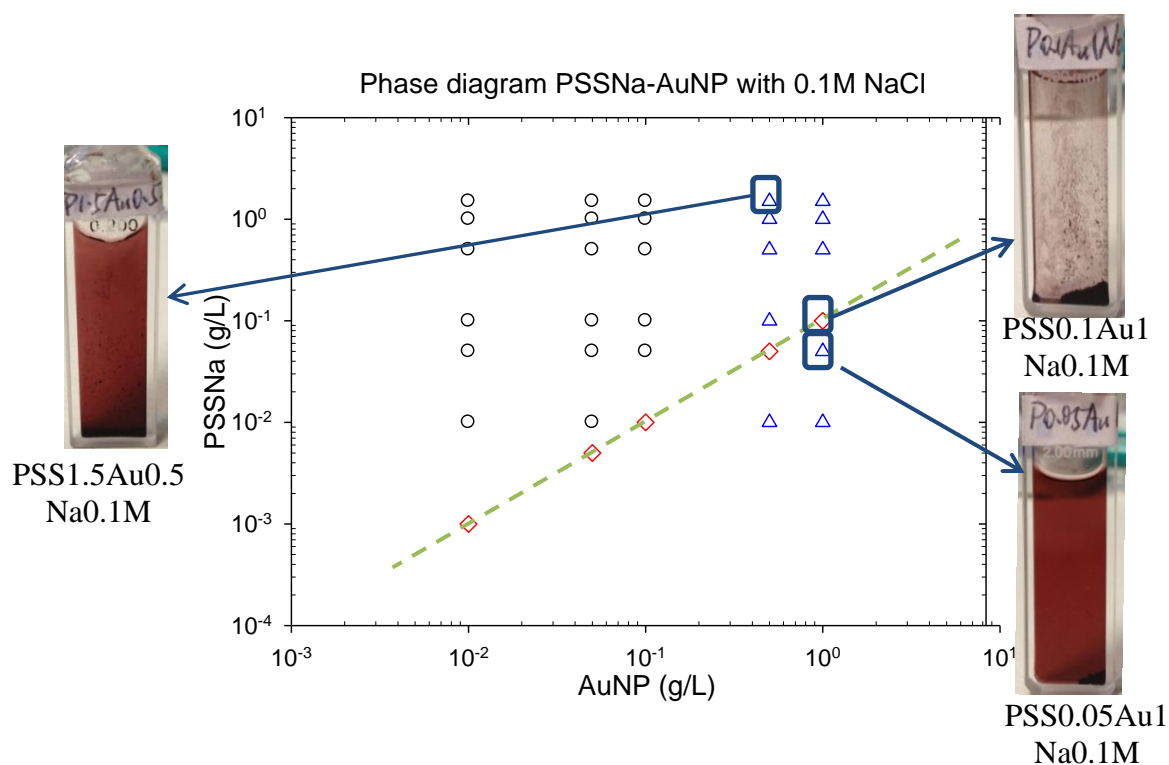


Figure V-10: Phase diagram of PSSNa-AuNP complexation behaviors of AuNP-PSSNa at different concentration pairs in the presence of 0.1M NaCl

V.2.3.2 Inner structures of complexes

1) Biphasic samples on the stoichiometric line

In the first time, samples of AuNP/PSSNa concentration ratio of 10 (“stoichiometric line” discussed above) were examined by SAXS on beamline A2, DESY. The X-ray beam was aimed at both the top of supernatant and the bottom of the precipitate.

First, above all, for both samples, the curves have a characteristic peak at 0.101\AA^{-1} , corresponding to the distance of 6.2nm, shorter than the previous saltless cases and other samples with 0.1M NaCl as well. It means that inside the aggregation, AuNPs are closer to each other. Second, it is surprising that the supernatant scatters still a lot, as it is completely transparent suggesting that there are no NPs there. Also it is abnormal that the sample PSS0.05Au0.5 has higher intensity than PSS0.1Au0.1. The reason for this is just that some insoluble grains were not able to sediment completely in the capillary Note that during preparation of this sample, we succeeded in introducing manually an additional amount of precipitates from PSS0.05 Au0.5 into the capillary. For this reason, a few grains were left in the supernatant (obviously the quantity is not comparable to what is in the bottom of capillary:

as seen in the Figure V-11, for both samples, the curves for supernatant are lower than precipitate).

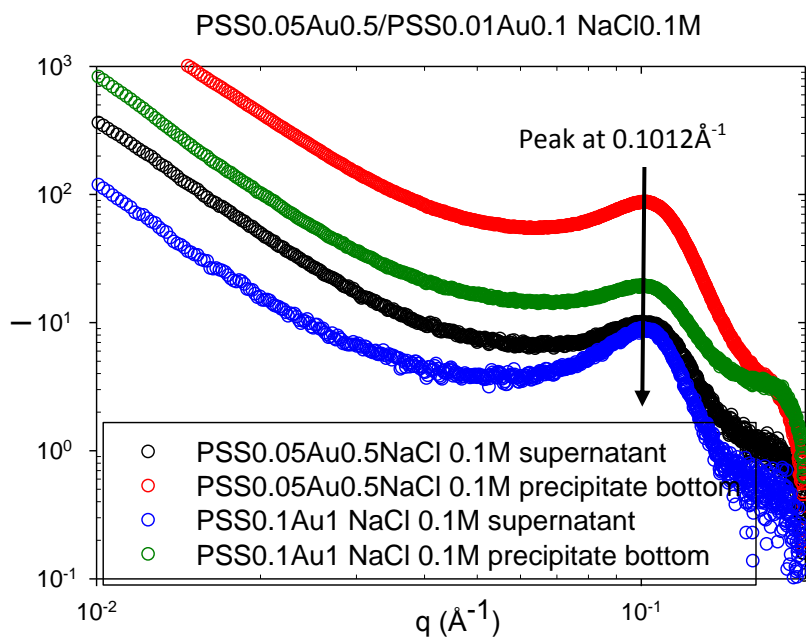


Figure V-11: SAXS pattern of complexation AuNP-PSSNa in the presence of 0.1M NaCl for samples of AuNP/PSSNa concentration ratio of 10 performed on beamline A2, DESY

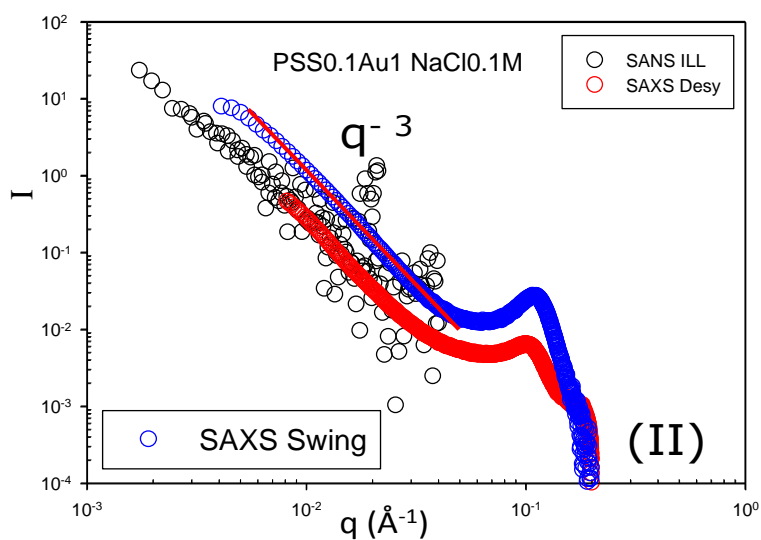


Figure V-12: Combined SANS and SAXS patterns of sample PSS0.1Au1 in the presence of 0.1M NaCl. The intensity was shifted arbitrarily for the sake of clarity

A measurement for the same composition made on A2 at DESY was repeated on beam line D11, ILL and beamline SWING, Soleil. Plotting the three results together, in Figure V-12, we see that three scattering curves are parallel, showing the reproducibility of the dense compact complexes' structure at this ratio.

2) Other biphasic samples

In a second time, we discuss the scattering for the other biphasic type of samples as plotted in Figure V-13. These samples all show a characteristic peak around $q=0.102 \text{ \AA}^{-1}$ (SWING) and 0.097 \AA^{-1} (A2), corresponding to an interparticle distance of 6.16nm and 6.48nm respectively. Except for the samples on the stoichiometric line, the presence of 0.1M NaCl seems to shift the peak towards the left, which also means distances slightly larger than the interparticle distance for samples made of same concentration ratio. The variation is however small.

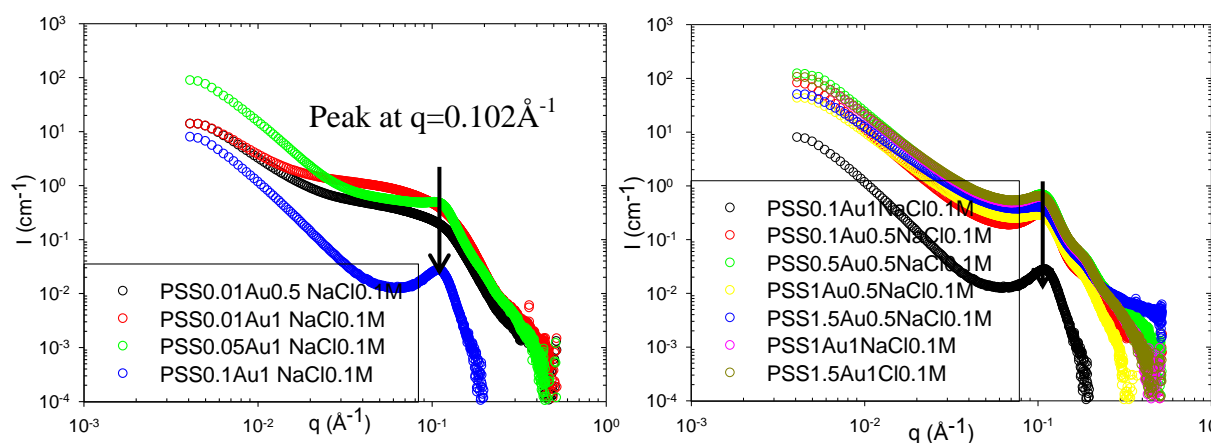


Figure V-13: SAXS patterns of PSSNa-AuNPs biphasic samples at different concentration pairs performed on beam line SWING: (a) for samples situated below the stoichiometric line of phase diagram; (b) for samples situated above the stoichiometric line of phase diagram

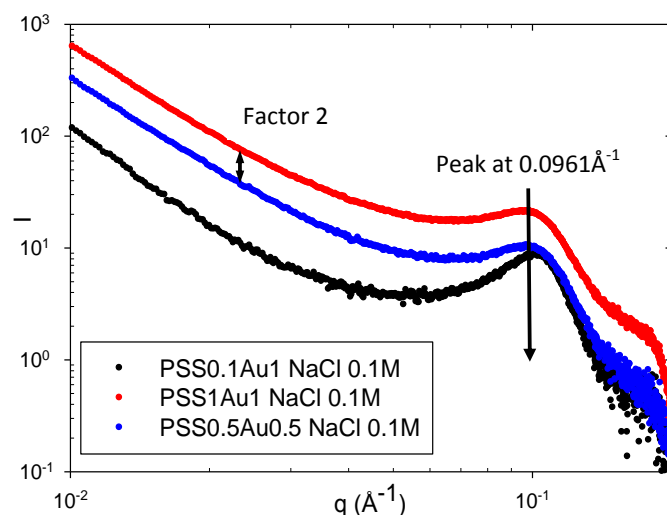


Figure V-14: SAXS pattern of complexation AuNP-PSSNa in the presence of 0.1M NaCl for sample PSS1Au1 (red) and PSS0.5Au0.5 (blue), and sample PSS0.1Au1 for comparison. In Figure V-14, it is obvious that sample PSS0.5Au0.5 (blue) and PSS1Au1 (red) have exactly the same behavior, except that there is a gap of factor 2 in intensity level, which corresponds well to the difference in absolute sample concentration. Compared to the sample PSS0.1Au1 (black), the characteristic peak at 0.096\AA^{-1} is slightly left shifted, as mentioned before.

The different structures of complex in supernatant and precipitate are also examined. For sample from the same biphasic region PSS0.1Au0.5, the position of peak does not move, but the slope at low q is different. The supernatant may contain complex having smaller size as the beginning of Guinier regime has already appeared.

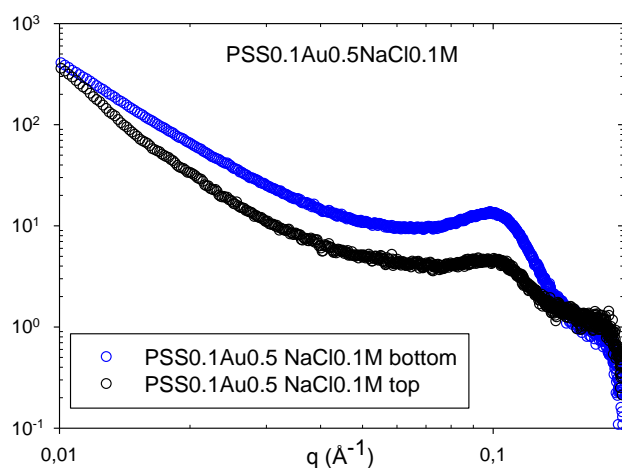


Figure V-15: SAXS pattern of sample PSS0.1Au0.5 with 0.1M NaCl performed on beamline A2, DESY at different altitude of capillary

Note that these two compositions were investigated at lower q using D11 to complete the DESY measurements. Remarkably, the SAXS and SANS agree together. This is true for all samples measured by both SAXS and SANS

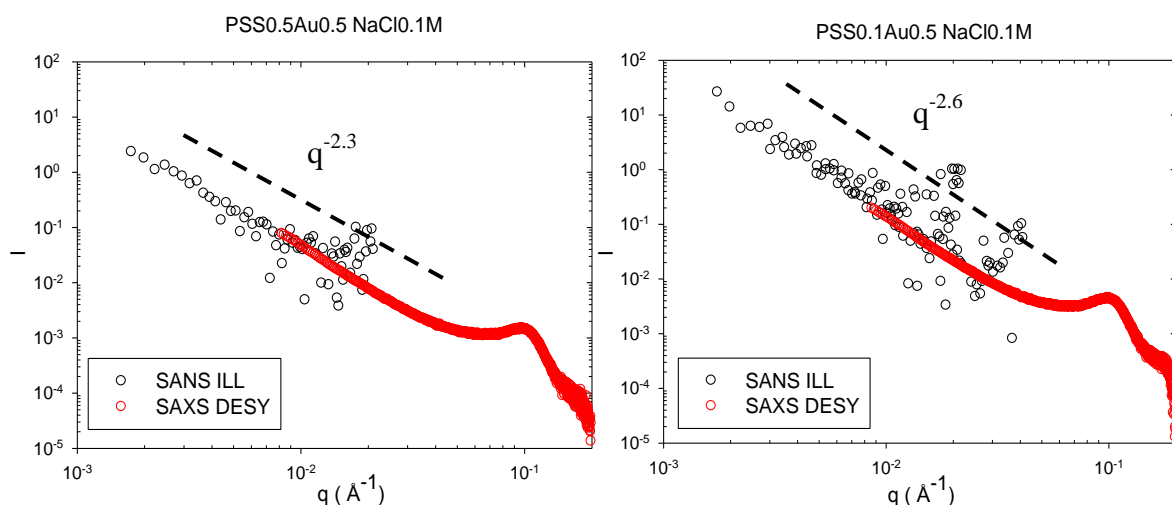


Figure V-16: Combined SANS and SAXS patterns for sample PSS05Au0.5 and PSS0.1Au05 in the presence of 0.1M NaCl. The SANS curves are shifted arbitrarily to join the SAXS curves

The slope at low q varies between 2.2 and 2.6, depending on the PSSNa/AuNPs' concentration ratio.

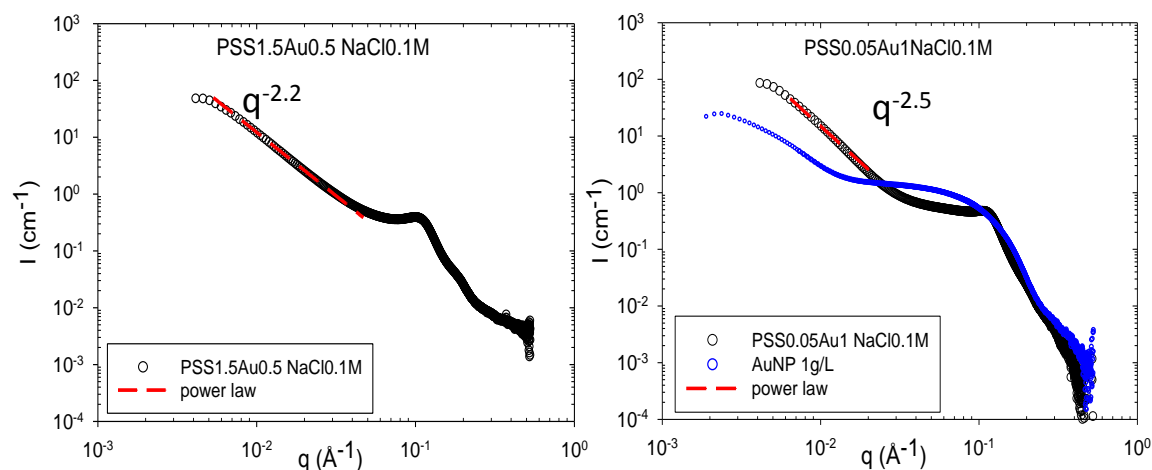


Figure V-17: SAXS pattern of (a) sample PSS1.5Au0.5 (above the stoichiometric line) and (b) PSS005Au1 (below the stoichiometric line) in presence of 0.1M NaCl performed on beamline SWING

Similarly, we find that the fractal dimension of complexes varies with the PSSNa/AuNPs concentration ratio. At stoichiometric point (ratio PSSNa/AuNPs=0.1), complexes have the most compact structure (q^{-3}), before this ratio, the fractal dimension decreases with the

increase of PSSNa's concentration, and after this ratio, the fractal dimension decreases with the increase of AuNP's concentration, as shown in Figure V-18

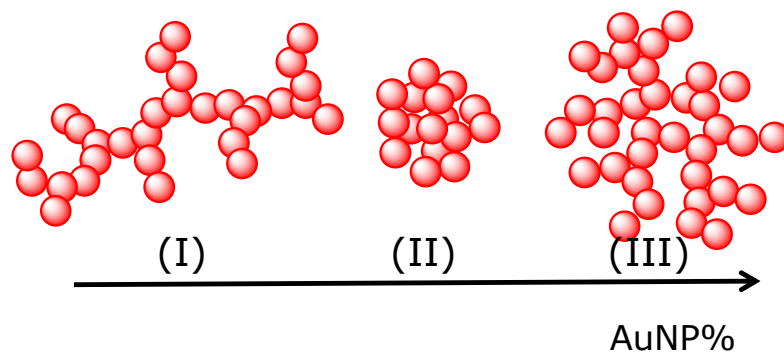


Figure V-18: Evolution of complexes' structures with the increase of AuNPs concentration

V.3 Complexation of Hyaluronan (HA) and gold nanoparticles (AuNPs)

V.3.1 Introduction

At the same time of studying complexation of AuNPs with PSSNa, another natural polyelectrolyte, hyaluronan was chosen to complex also AuNPs. Different from PSSNa with persistence length $L_p = 0.9\text{nm}$, hyaluronan is semi-flexible with persistence length L_p of about 5nm, depending on ionic strength condition. Comparing with complexation PSSNa-AuNPs, we could get information of effect of chain flexibility on complex structure, meanwhile, comparing with complexation hyaluronan-SiNPs, we could get information of effect of nanoparticle size on complex structure.

V.3.2 Materials

V.3.2.1 Hyaluronan

The same batch of hyaluronan used for complexation of hyaluronan (92K) with silica nanoparticles was used here. The powder was dissolved in milliQ water (or 0.1M NaCl solution) at room temperature and was stirred for at least 48hours before further dilution. The mother solution of hyaluronan at 3g/L was then diluted into different concentrations, and was filtered by 0.2 μm cellulose membrane to discard the impurities. The hyaluronan solutions used for complexing AuNPs were all freshly prepared (within one week).

V.3.2.2 AuNPs

Same AuNPs used for complexation PSSNa-AuNPs were used for complexation Hyaluronan-AuNPs. Two batches of AuNPs mother solutions were used, the first one for experiments at DESY and ILL, and the second one for experiments at Soleil and LLB. The first batch AuNPs has an average R_G of 3.8nm, while the second one is 30% smaller.

V.3.3 Complexation Hyaluronan-AuNPs without salt

V.3.3.1 Description of phase diagram

Samples were prepared in the same way as for PSSNa-AuNPs complexation, but the phase diagram is more complicated, as it contains one monophasic domain, two biphasic domains and one triphasic domain. When AuNP concentrations are inferior to 0.1g/L, the samples are monophasic with red color. When both components concentrations increase, the phase separation occurs.

The biphasic samples may have:

- one phase of red supernatant and one phase of precipitates at bottom,
- or one phase of red supernatant with gradient in concentration and one dense red layer on the bottom of the vial (it is difficult to determine whether it is a viscous liquid or a solid-like precipitate).

In triphasic samples, there are one red supernatant with gradient in concentration, one dense black layer on the bottom and one phase of very small quantity of precipitate (about one mm height in a Helma cell of thickness 2mm), in the form of solid grains of a hundred μm typically.

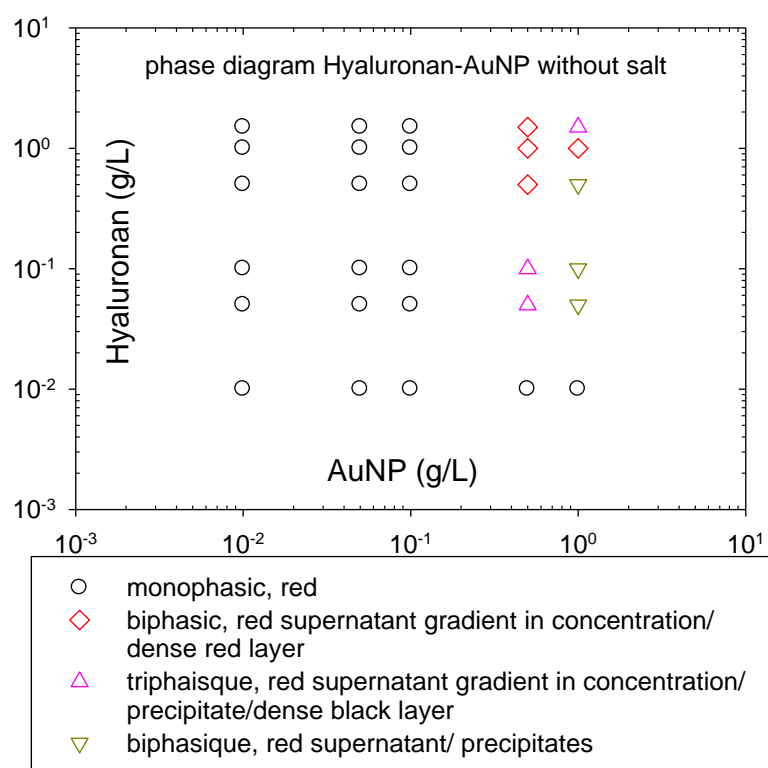


Figure V-19: Phase diagram of Hyaluronan-AuNP complexation behaviors of at different concentration pairs without salt

The process of phase separation would take a few days, especially for the formation of a red or black dense layer on the bottom of glass vials. Unlike the granular precipitates, the constituent of this layer is immobilized at the surface, with a constant thickness of a few tenth of μm .

V.3.3.2 Inner structures of complexes

Choice of samples

As in precedent experiments, we chose in the first time, samples situated in the two last columns of phase diagram were performed on beamline A2 (due to larger concentrations providing larger signals). Samples were first added into the glass vials as for the phase diagram, and were quickly transferred into 2mm capillaries after mixing, and phase separation was allowed to take place inside the capillaries.

Various scatterings

In a first place, we plot the scattering of all the samples measured at the middle height of capillaries.

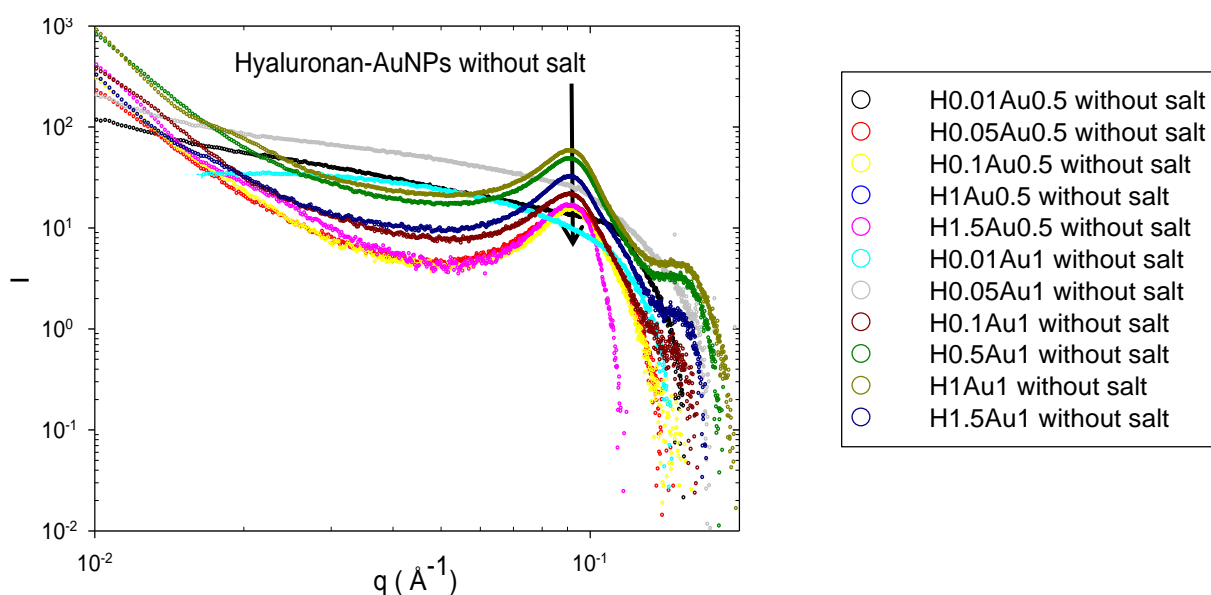


Figure V-20: SAXS pattern of Hyaluronan-AuNP complexes in the absence of salt at different concentration ratios performed on beamline A2, DESY

At first sight, the SAXS patterns of samples Hyaluronan-AuNPs look very similar to those of AuNP-PSSNa. Indeed, they also have a characteristic peak at high q , and an ascending slope towards low q , except for sample H0.01Au1, H0.01Au0.5 and H.05Au1, where the excess of individual AuNPs in supernatant dominate the signals. However, if we look closer, we find that the curves have a significantly boarder and deeper hollow between the low q peak, and the upturn around $q=0.02 \text{ \AA}^{-1}$. The latter might be followed by a Guinier platform of the finite size of complexes that we will discuss later.

The characteristic peak is situated at 0.091 \AA^{-1} , corresponding to a distance of 6.90nm. Compared to complexation AuNP-PSSNa without salt, complexes Hyaluronan-AuNPs without salt have a looser particle-particle arrangement.

Structure in different phases

In the second place, we would like to know whether complexes in different phases of the same sample have the same structure. To this purpose, we've chosen three samples, two biphasic and one triphasic. The analysis of scattering curves measured at different altitude of capillary provided us a lot of information concerning the complexes structures in different phases.

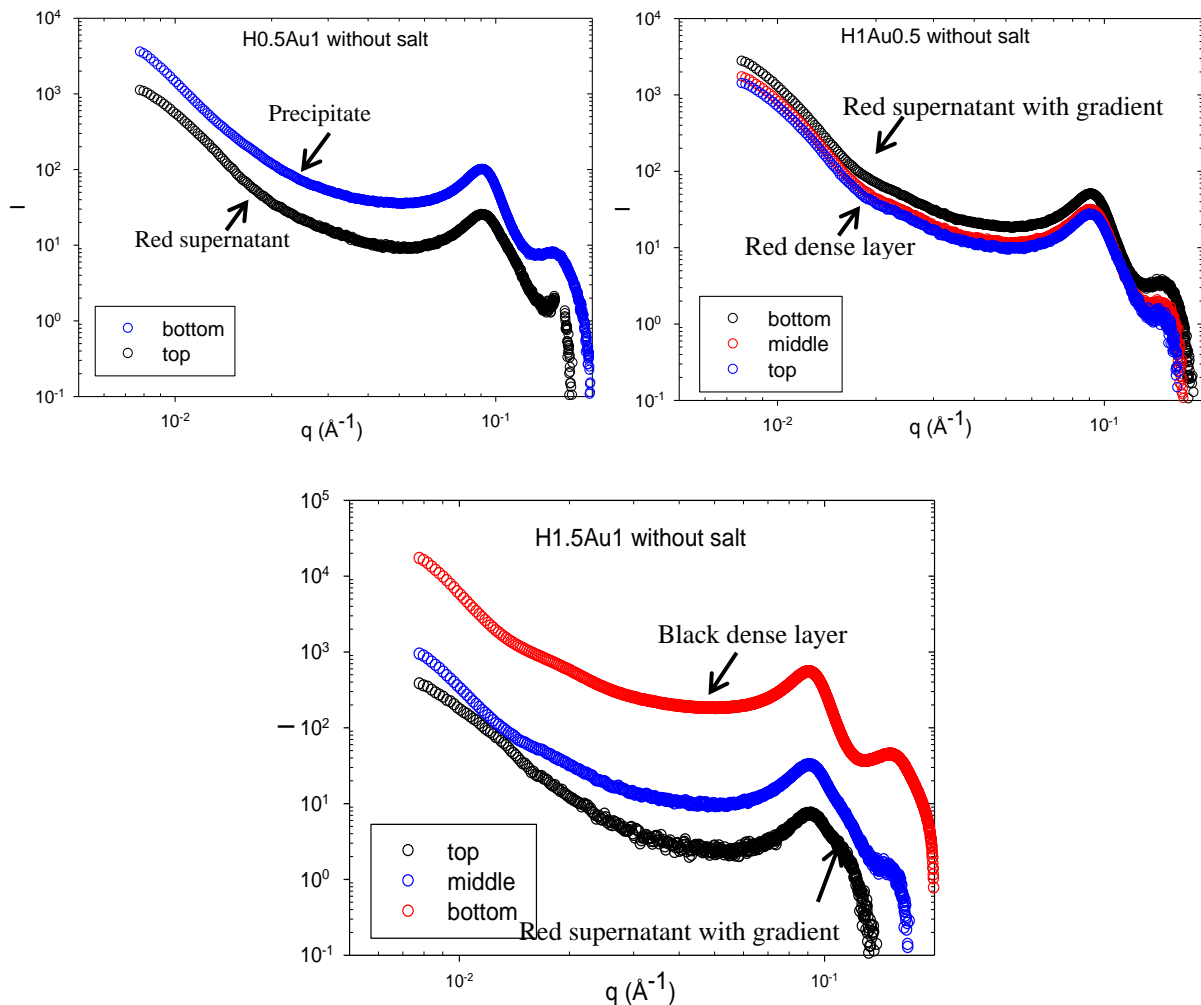


Figure V-21: SAXS pattern of Hyaluronan-AuNPs complexes at different ratio and at different height of capillary measured on beamline SWING, at SOLEIL

From Figure V-21, we can clearly figure out the scattering curves from different phases of the same mixture:

- For biphasic sample H0.5Au1 without salt, we see two distinct curve shapes: one for the precipitate situated at bottom of capillary, and one to the red supernatant. The supernatant contains complexes of smaller size as we see already the appearance of a Guinier plateau, while the scattering pattern of precipitate continues to uprise towards low q .

-For biphasic sample H1Au0.5 without salt, the patterns look alike each other at three different height (with some difference in absolute intensity). We could deduce that the red dense layer is made of complexes coming possibly from the red supernatant, and being concentrated in the bottom.

- For triphasic sample, H1.5Au1 without salt, the scattering from the red supernatant at the top of capillary looks similar to those from the red supernatant of the other two samples. Meanwhile, the scattering of the black dense layer is a little different from the one of the red dense layer of sample H1Au0.5: the upturning point appears at lower q (0.013 \AA^{-1} instead of 0.017 \AA^{-1}). Concerning the scattering of the precipitate, we unfortunately could not figure it out, because it is overlapped by the one of the black dense layer.

We now discuss the extension to low q range which we have been able to make in some cases by connecting the X rays patterns with the low q SANS pattern. As seen in Figure V-22 this allows determining the finite size of complexes by extrapolating the Guinier plateau to zero q . As mentioned above, at ILL, we measured actually the sample at the earlier stages of phase separation, so the $R_G=40\text{nm}$ obtained here is most probably corresponding to the same size as for small complexes in the supernatant after decantation as measured at DESY. We just note that the same $R_G=40\text{nm}$ from a Guinier plateau at SOLEIL for the supernatant of sample H0.1Au1 without salt, while the Hyaluronan content is much smaller. It may be argued that in this case the complexes stay in a first stage and do not grow anymore.

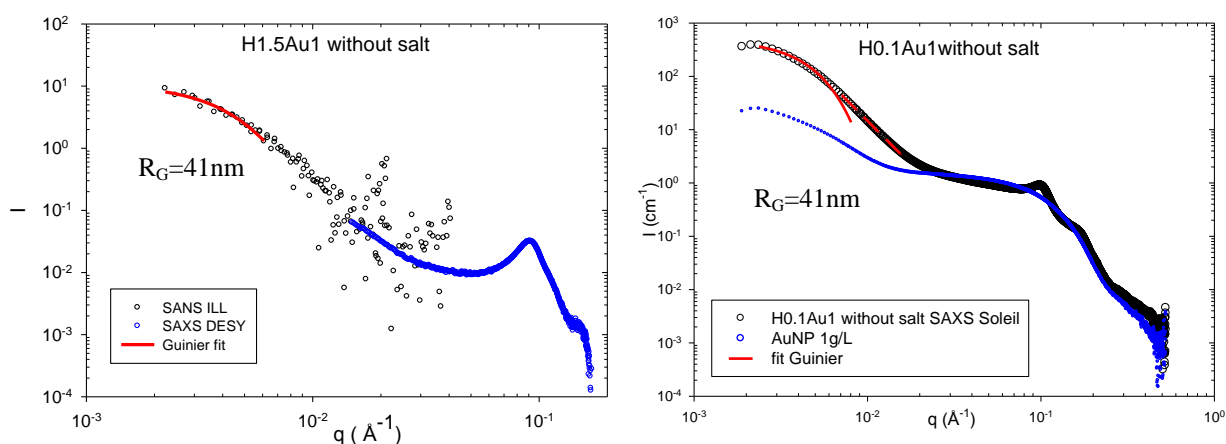


Figure V-22: Combined SANS and SAXS patterns of sample H1.5Au1 without salt and SAXS pattern of sample H0.1Au1 without salt

Still speaking of low q , the SAXS experiments in this range (accessed on beamline SWING) show also that sometimes, rather than having a Guinier plateau at $q=3 \times 10^{-3} \text{ \AA}^{-1}$, the scattering patterns of some biphasic samples continue to ascent following a power law of exponent $-\alpha$,

$1.3 < \alpha < 1.7$. It is not certain whether or not it means that these complexes are formed of 40nm objects with a secondary arrangement at larger scale (e.g. fractal of dimension α), and whether such secondary arrangement is responsible for the formation of the dense layer.

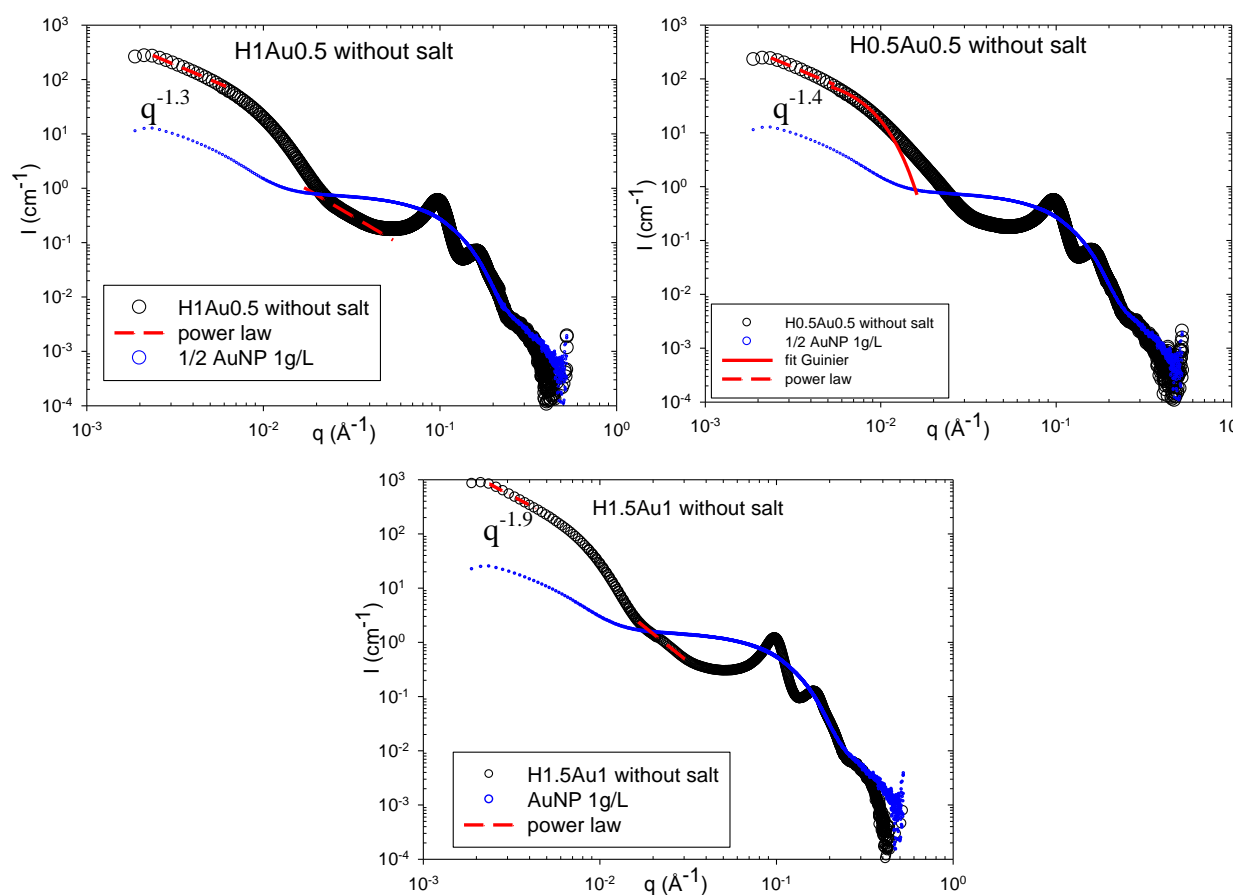


Figure V-23: SAXS patterns of sample H1Au0.5, H0.5Au.5 and H1.5Au1 without salt, performed on beamline SWING at SOLEIL

Second peak

Another important feature we could get from SAXS results performed at SOLEIL, is the very clear second peak at about $q = 0.163 \text{ \AA}^{-1}$ following the first one (at DESY we had imprecise transmission measurements and did not work at large q). Compared to the pattern of AuNPs alone, we find that the second peak does not match the oscillation of the form factor of single sphere.

The first peak at $q = 0.097 \text{ \AA}^{-1}$ corresponds to an AuNP-AuNP interparticle distance of 6.48nm, which is slightly larger than the distance between two particles covered with ligands. The

origin of the second oscillation can be simply a higher order peak as found in crystalline structure. This may allow estimating the degree of order in the system.

V.3.4 Complexation Hyaluronan-AuNPs with 0.1M NaCl

V.3.4.1 Description of phase diagram

Samples were prepared in the same way by mixing equal volume of AuNP and Hyaluronan solutions at different concentration ratios. The hyaluronan solutions contain 0.2M NaCl and the AuNP solution was saltless, so the final mixed solutions contain 0.1M NaCl.

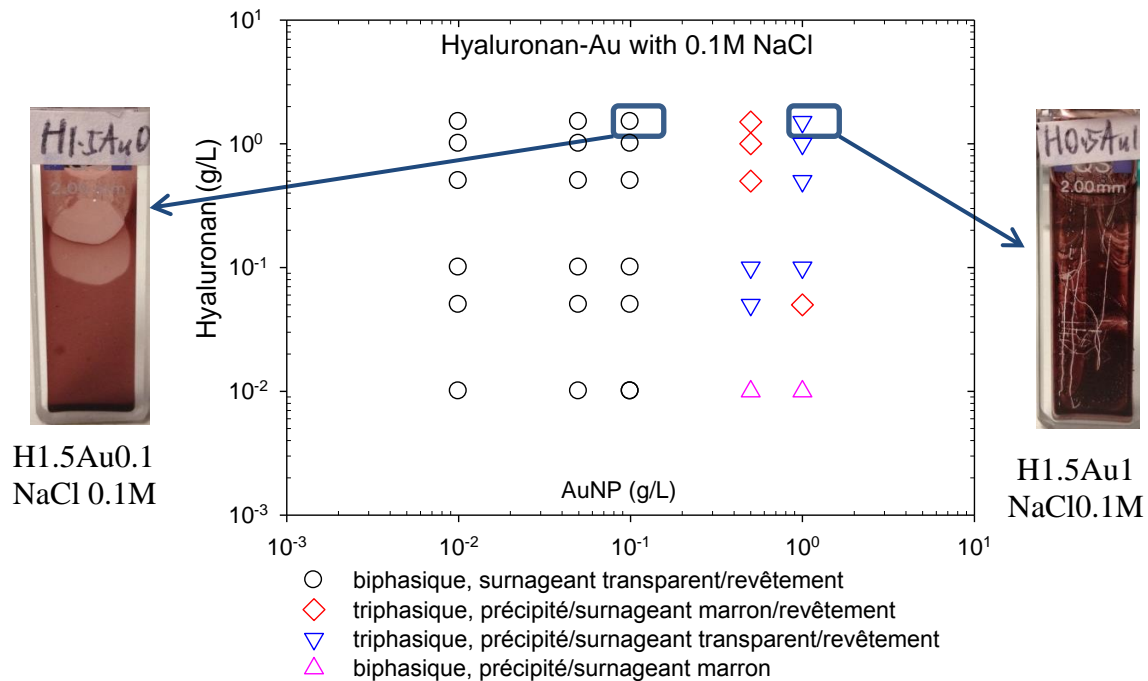


Figure V-24: Phase diagram of complexation hyaluronan-AuNP in the presence of 0.1M NaCl

Unlike the precedent three cases, the phase diagram of complexation AuNP-Hyaluronan with 0.1M NaCl does not have monophasic domain. Even at very low concentration of both components, the mixed solutions are biphasic. For all the samples showed in phase diagram, at the very beginning of mixing, the solutions tend to become more and more turbid, and the color changes from red to purple. The dense complex phase finally settles down and separates from its supernatant. This process is faster, so the evolution is easier to detect, when both components are at high concentrations. The latest visual observation is done before measurements (after typically two weeks).

For mixed solutions with $C_{\text{AuNP}} < 0.1\text{g/L}$, all samples are biphasic with a clear boundary between the upper transparent supernatant and a dense deep purple layer deposited on the bottom of the glass vial (see Figure V-24, picture of a cell at the left hand side of the phase diagram).

For mixed solutions with $C_{\text{AuNP}} > 0.1\text{g/L}$, some samples are biphasic, having precipitate and deep purple supernatant, and some others are triphasic, having:

- precipitate, deep purple supernatant and dense deep purple layer
- or precipitate, transparent supernatant and dense deep purple layer (Figure V-24, picture of a cell at the right hand side).

Note that it is possible that the difference between purple supernatant and transparent supernatant is just a matter of time. Giving more time to the system to evolve, the purple supernatant would condense to the dense layer if the solutions are not perturbed.

Reorganization of the aggregates: It is interesting to note that when one additional drop of concentrated Hyaluronan was added to the sample H0.05Au0.5 NaCl0.1M which had already become purple and had shown separation, the sample aspect returned to the aspect observed at the beginning of mixing, the homogenous but very opalescent red. However, without additional hyaluronan, even upon sonication, the sample would not return to its initial state. The choice of adding hyaluronan instead of adding AuNP was made to simplify the observation, since the addition of AuNP could deepen the color of the solution.

In summary, this qualitative test shows that it is possible to reorganize the complex composition and structure by changing the ratio of two components. It also proves that, during the complexation, ligands always stay at the surface of AuNPs.

V.3.4.2 Inner structures of complexes

Details of special sample preparation: Samples from the last two columns of phase diagram were freshly prepared for the SAXS experiments performed on beam line A2, DESY. For samples having dense purple layer, a thin piece of Kapton was shaped to stick on the cap of the vial. When two components solutions were well mixed, a drop of mixed solution was quickly transferred to capillary and was allowed to phase separating inside. At the same time, the vial was inverted so that after a while, the dense phase was thus deposited on a round piece of Kapton film, with the supernatant covering above. Shortly before the SAXS experiment, the piece of Kapton film was taken out of the cap, and quickly recovered by another piece of Kapton, so that we could measure the complexes still hydrated. We call these samples ‘on-Kapton’ samples.

For the data treatment, the capillary samples were calibrated after empty capillary subtraction, and the Kapton samples were calibrated after Kapton subtraction of the signal of a double layer of Kapton film (“empty Kapton”).

Scattering shape: Typically, these “on Kapton” samples produce a characteristic peak at around $q=0.0854 \text{ \AA}^{-1}$, corresponding to a distance of 7.35nm, 2 times the R_G including ligand TMA. It is the longest interparticle distance in all the described cases. These samples do not exhibit much difference at high q range.

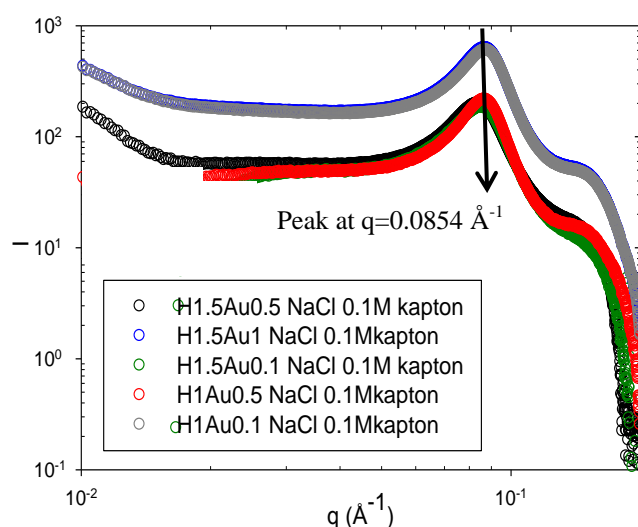


Figure V-25: SAXS patterns of Kapton sample H1.5Au0.5, H1.5Au1, H1.5Au0.1, H1Au0.5 and H1Au0.1 in the presence of 0.1M NaCl, performed on beamline A2, DESY

The precipitate phase (small solid grains around a few 100 μm), unfortunately, is lacking in our investigation: due to the small quantity of grains, they were not collected to be measured. The third phase, the supernatant, was measured.

Effect of the height of measurement

The sample H0.1Au1 was supposed to be a triphasic sample with precipitate grains, transparent supernatant and a dense purple layer. However from the time of preparation to the time of measurement, the phase separation was not yet completed. Therefore the supernatant still contains some non-decanted precipitates, such that in Figure V-26 below the supernatant has a characteristic peak at the same position of q as “on-Kapton” samples. We also see that the concentration of complex increases from top to the bottom of the capillary, and at the low q , we can already see the different upturn tendency.

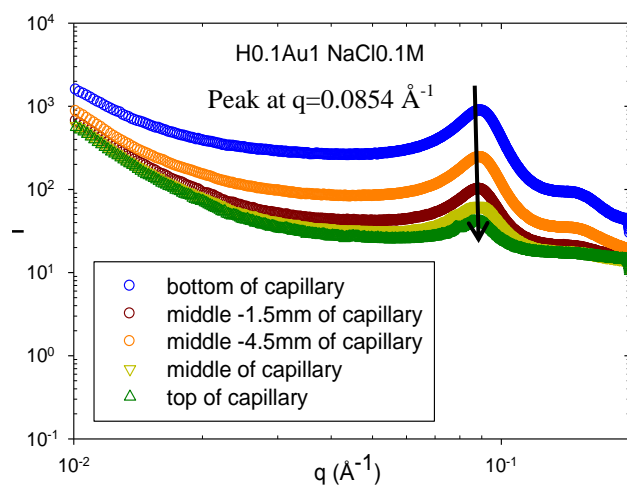


Figure V-26: SAXS pattern of sample H0.1Au1 with 0.1M NaCl measured from top to bottom of capillary, performed on beamline A2, DESY

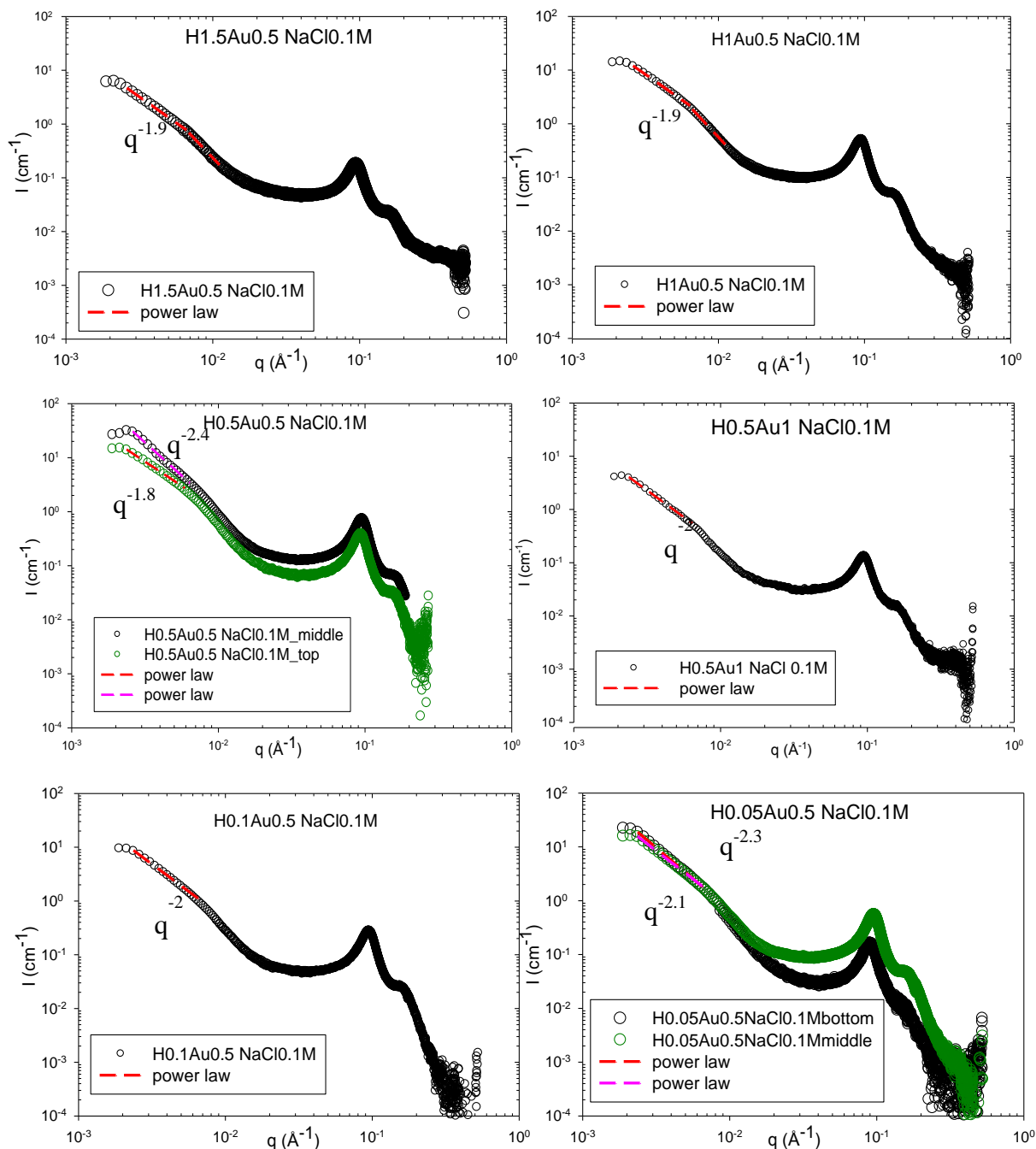


Figure V-27: SAXS patterns of samples prepared at different hyaluronan-AuNPs concentration pairs and performed on beamline SWING, SOLEIL

Effect of the composition. We can see from Figure V-27 that regardless of concentration ratio of two components, the different samples have similar scattering patterns at medium q , with the first characteristic peak at $q=0.092 \text{ \AA}^{-1}$ and the second one at $q=0.160 \text{ \AA}^{-1}$. At low q , they have an upturn following the power law with the exponent of around -2. More precisely, the exponent may vary a little, according here also to the different height at which the

complexes are situated. Like what reported just above, usually the complexes for the same sample have less fractal dimension at top of capillary than at a lower position.

Following phase separation

Small angle technique: For these samples with added salt, the process of phase separation could be followed by SANS experiment. Sample H1.5Au0.5 with 0.05M NaCl was freshly prepared in D₂O. The original solutions are hyaluronan 3g/L with 0.1NaCl and AuNP 1 g/L without salt.

In Figure V-28, the decreasing slope fitted by a q^{-4} power law reveals the Porod regime of the complexes, which stands for compact objects having a well-defined narrow interface with the solvent in the corresponding spatial range.

The kinetics of complex formation was followed by successive measurement on the same sample. As time runs, the compact objects grow: to account for this effect, the configuration was adjusted to access lower q range. However because of the required relative long duration of recording, the new measurement at configuration of smaller angles cannot catch up the evolution as fast as the growth speed.

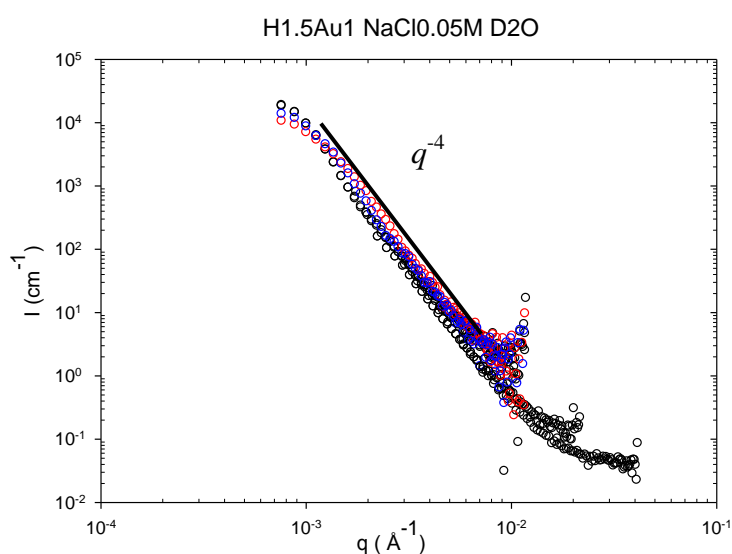


Figure V-28: SANS patterns of sample H1.5Au05 with 0.05M NaCl, performed on beamline D11 at ILL

Optical microscopy: We also developed visual observation at MSC we also used a light microscope with the aid of Marie-Alice Guedeau-Boudeville, confined immediately after mixing between two quartz plates separated by a ring of soft plastic gum, of thickness adjustable to less than 1 mm. This also prevents evaporation by introducing the liquid sample,

between plate and platelet. Phase separation into microscopic droplets (30 to a hundred microns) could be first observed, followed by slow falling down of the droplets, which adhered on the bottom plate. When letting time passing (up to a night) we could observe that the adhered droplets had merged together (see Figure V-29). This is a direct observation of the liquid-liquid phase separation, following the first stages detected by SANS and showed just above (see Figure V-28, see also in Figure V-29 the progressive growth of such droplet as shown by the red circle), though it was not the same composition.

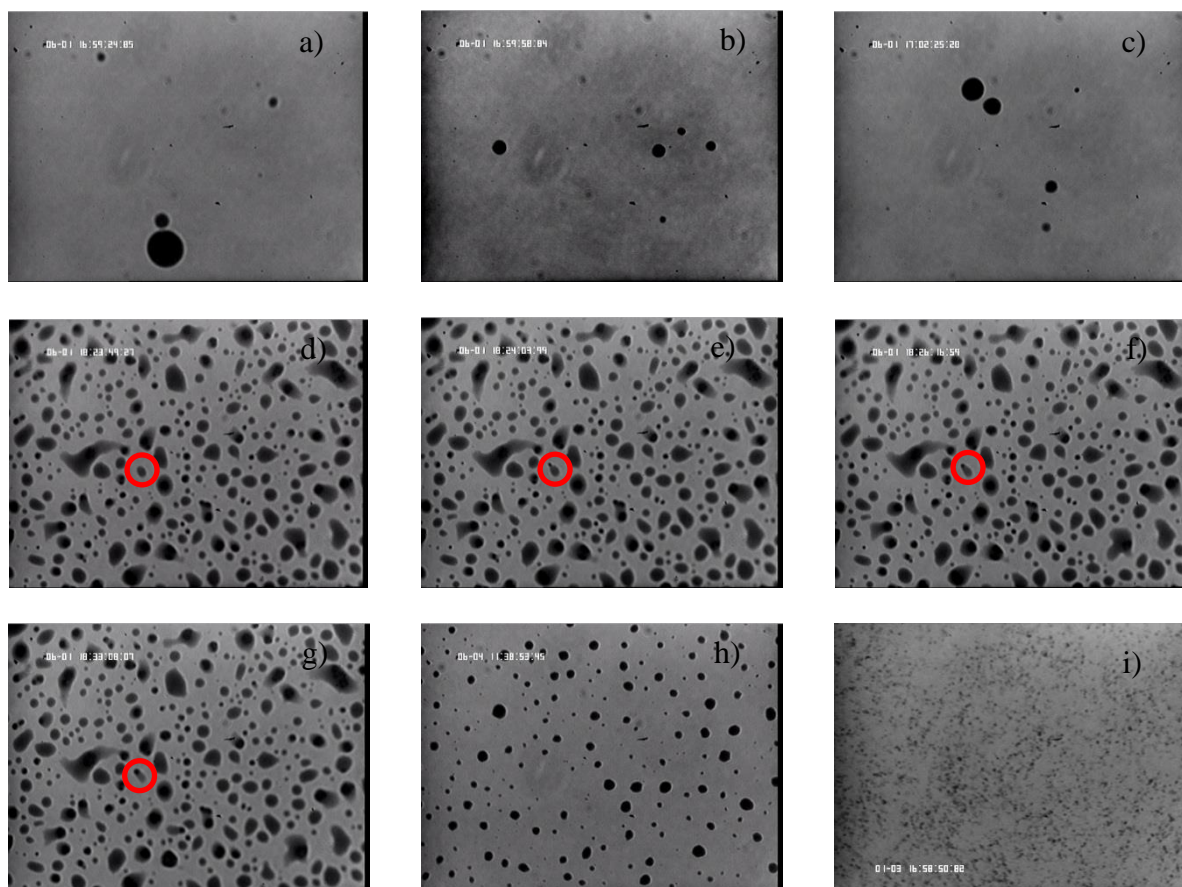


Figure V-29: optical microscopy photos (zoom \times 100) of freshly prepared sample H0.5Au1 confined between two quartz plates hermetically sealed. Photo (a), (b) and (c) were taken in the first 5 minutes after preparation; (d), (e), (f) and (g) were taken successively on the same site at about 15minutes after preparation, where the red circles point out a local phase merging; (h) was taken after 3 days, and (i) was taken after five month (zoom \times 20)

Finally, the last photo of Figure V-29 shows the same sample after 5 months: the droplets have vanished and some small dots probably made of denser precipitates are visible (see Figure V-39).

UV-visible spectroscopy: Since, for following the evolution after mixing, the SANS and SAXS measurements are limited by the need of high AuNPs concentration, UV-visible spectroscopy is more suitable for low AuNP concentration samples. As mentioned before, in

the presence of 0.1M NaCl, whatever the concentration ratio, all samples exhibit a change of color followed by the phase separation. So we choose the samples at low AuNP concentration (the evolution of which is easier to follow) to see the complexes size evolution.

The sample H0.1Au0.1 was mixed directly inside the 1mm thickness cell. The evolution of complex growth was recorded every five minutes until the complex phase was settled down and beyond the measurement window.

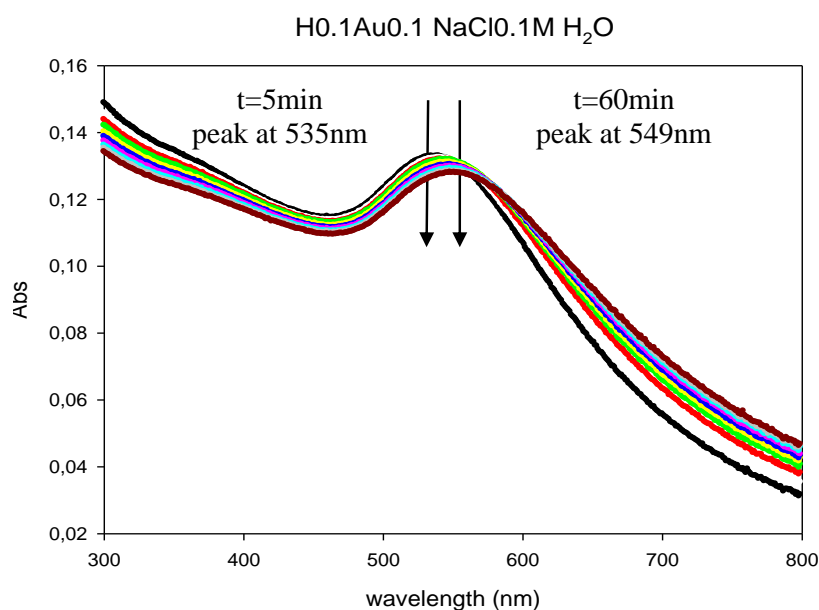


Figure V-30: UV-visible spectrum of sample H0.1Au0.1 with 0.1M NaCl, and kinetics was recorded every 5 minutes

As showed in Figure V-30, the red shift of peak towards longer wavelength is consistent with the observation of change in color from red to mauve. We recall that the solution of AuNPs alone have the peak of absorption at 519nm, corresponding to the AuNP size of 3nm. The evolution of size happened so quickly that even at the first measurement, the peak was already shifted to 535nm. As mentioned above (eq. V-1), the red shift of absorption peak indicates the growth of AuNP aggregation. Here the slight decrease in absorption peak altitude maybe due to the sediment of complex phase, as the laser was aimed at the upper part of the solution. The peak at 549nm corresponds to the AuNP size of about 80nm in diameter. We could not follow further the evolution of the sample; from SAXS and SANS results, we know that the 80nm size was not yet the final state.

V.3.4.3 Crystals in samples

An unexpected result in this system is that, besides the regular complexes, the scattering patterns of some samples exhibit a colloidal crystal like behavior. This phenomenon was

observed repeatedly, at DESY and on SWING at SOLEIL, on different samples of same composition, and only for Ha-AuNP complexes in presence of salt.

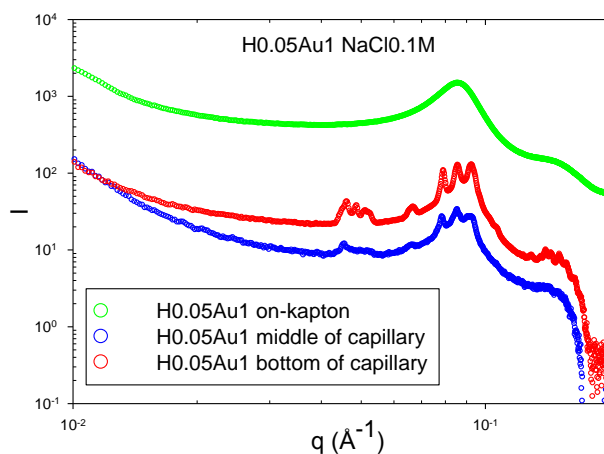


Figure V-31: SAXS patterns of sample of H0.01Au1 with 0.1M NaCl, both supernatant in top (blue) and bottom (red) of capillary and on Kapton (black)

Moreover, at the position of $q=0.0854 \text{ \AA}^{-1}$, instead of one peak, the sample H0.05Au1 display a massif of three finer peaks at $q=0.0793 \text{ \AA}^{-1}$, 0.0858 \AA^{-1} and 0.0927 \AA^{-1} . Note that the center of the massif has not moved.

	Massif 1 (\AA^{-1})			Massif 2 (\AA^{-1})	Massif 3 (\AA^{-1})		
Middle of capillary	0.0455		0.0523	0.0664	0.0786	0.0856	0.0932
Bottom of capillary	0.0462	0.0489	0.0517	0.0670	0.0793	0.0858	0.0927
Kapton						0.0854	

Table V-1 List of peak positions of sample H0.05Au1

The same situation was observed for sample H0.01Au0.5 with NaCl0.1M, as showed in , and the positions of massifs were listed in Table V-2.

	Massif 1 (\AA^{-1})		Massif 2 (\AA^{-1})				Massif 3 (\AA^{-1})	
Middle of capillary	0.0428	0.0451	0.0736	0.0793		0.0963	0.0136	
Bottom of capillary	0.0433	0.0453	0.0740	0.0822	0.0864	0.0964	0.01340	0.1469
Kapton	0.0428	0.0443	0.0725	0.0814	0.0845	0.0925	0.1330	0.1439

Table V-2 List of peak positions of sample H0.01Au0.5 (recorded on beamline A2/DESY)

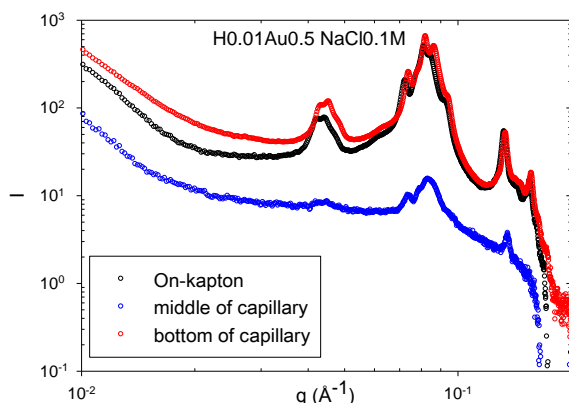


Figure V-32: SAXS pattern of sample of H0.01Au0.5 with 0.1M NaCl, both supernatant in top (blue) and bottom (red) of capillary and on Kapton (black)

On beamline SWING, we have observed this phenomenon **for the second time**. On 2D image, we find three principal concentric ring zones (I, II, III), and for each ring zone, there are at least three adjacent rings, more or less intensive. By regrouping the 2D image, we get the I-q plot with three massifs made of several fine peaks. The peak abscissas are close to what observed at DESY, though slightly different; this can be explained by the differences in the size of the AuNPs. More “satellite” rings appear in the SWING measurements, probably because of the better resolution used.

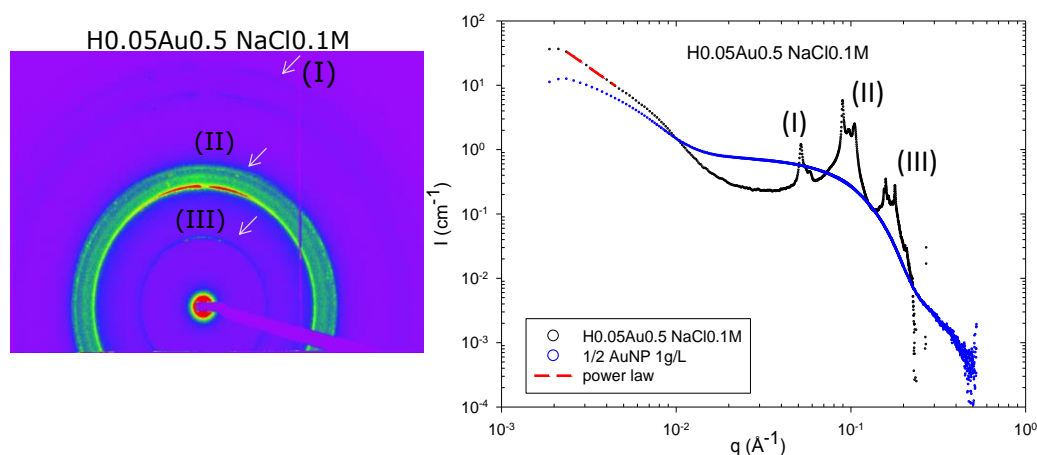


Figure V-33: SAXS patterns of sample H0.05Au0.5 with 0.1M NaCl; 2D image (left) and regrouped I-q plot (right)

	Massif 1 (\AA^{-1})			Massif 2 (\AA^{-1})					Massif 3 (\AA^{-1})		
Peak position	0.0516	0.0547	0.0580	0.0895	0.0971	0.1051	0.1550	0.1583	0.1640	0.1706	0.1782
Intensity	0.7835	0.5775	0.5244	3.1842	2.4012	1.9905	0.4130	0.3470	0.1985	0.1604	0.1752

Table V-3 List of peak positions and intensity of each peak of sample H0.05Au0.5 with 0.1M NaCl

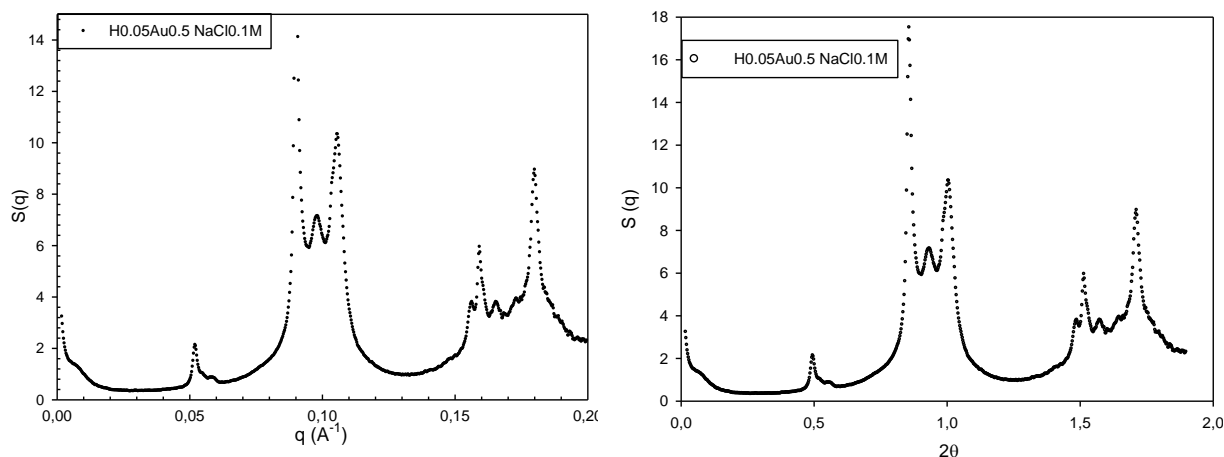


Figure V-34: $S(q)$ (scattering $I(q)$ normalized by the form factor $P(q)$) pattern of sample H0.05Au0.5 with 0.1M NaCl. Left: in q units. Right: in theta units.

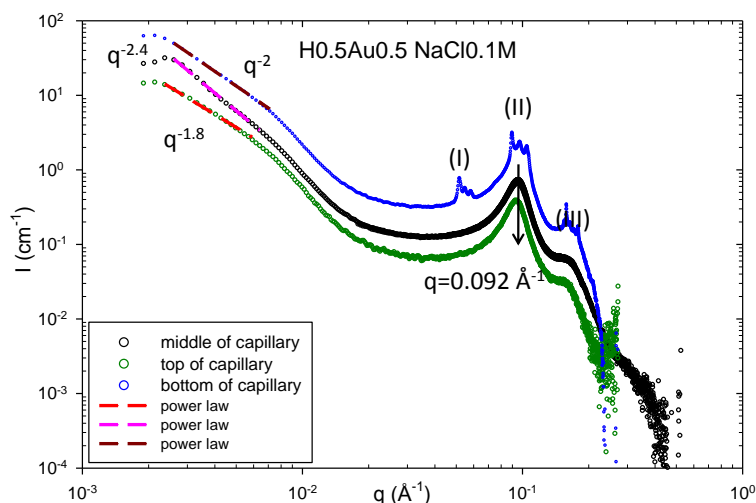


Figure V-35: SAXS patterns of sample H0.5Au0.5 with 0.1M NaCl

Comparing these samples, H0.05Au1 with 0.1M NaCl (Figure V-31), H0.01Au0.5 with 0.1M NaCl (Figure V-32), H0.05Au0.5 with 0.1M NaCl (Figure V-33) and H0.5Au0.5 with 0.1M NaCl (Figure V-35) we find that the positions of massifs and peaks remain the same for complexes composed of different concentration ratios, however, the intensity of each adjacent peak of the massif varies case by case. For example, for the massif (II), sample H0.05Au0.5 with 0.1M NaCl have the lowest intensity at the centric peak and the neighboring peaks (right and left) have much higher intensity, while the intensity of sample H0.5Au0.5 with 0.1M NaCl declines from left (lower q) to right (higher q).

V.3.5 Discussion on crystals

The mechanism of the formation of these colloidal crystals is not yet understood. It is not clear whether this phenomenon is related to the preparation procedure like most of classical crystallizations that are controlled by kinetics, or whether it only depends on concentration ratio and ionic strength, and is controlled by thermodynamics. Hopefully, further characterizations could bring more information. Until now we initiated several attempts, which remain at the preliminary stage.

V.3.5.1 Nature: composition, size

First where are the crystals located? In all cases, they coexist with the complexes and with Ha or NPs in excess. They may be on the walls of the capillary, in the liquid phase, or at the bottom. In the same capillary, the crystals are preferentially situated at the bottom of capillary (see Figure V-31, Figure V-32, Figure V-34). Even if we detect the diffraction patterns at middle of capillary, usually they miss some peaks compared to the pattern measured at bottom of capillary (only some of the “bows” are seen on some 2D images). This goes with the fact that on 2D image instead of continuous diffraction rings, the concentric circles are composed of single spots (grainy structure). This could correspond to different ordered regions inside a given small crystal (macles), with a limited number of crystals, or to a larger number of separate small monocrystals. In this case, in average in the volume of the beam, of order 1 mm^3 , we have of the order of 100 different crystals. The larger number of spots at the bottom of the capillary suggest either that more crystals becomes visible while falling, or that the most visible grow in more polycrystals .

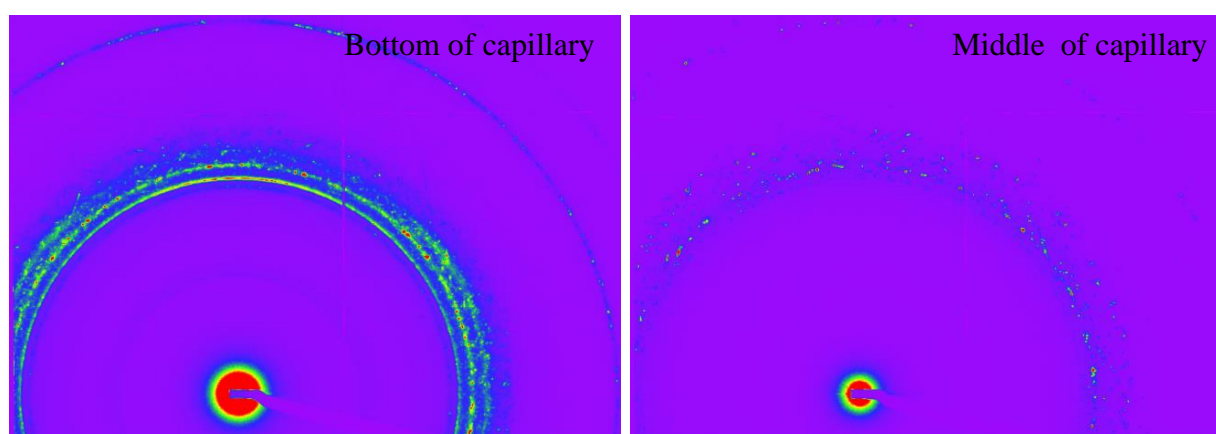


Figure V-36: 2D SAXS patterns of sample H0.01Au1 with 0.1M NaCl: measured at bottom of capillary (left) and middle of capillary (right) respectively

It is interesting to consider some 2D images with small numbers of spots, in order to evaluate the width of diffraction of a single crystal. Though a detailed analysis remains to be done, we can crudely conclude that the spot width is of the same order as the one in the radial average: the signal is dominated by the scattering from crystals large enough to show width smaller than some 0.2 degrees. Note that the granularity of the rings may depend on the ring: on the main group of rings of Ha 0.01 Au1, the internal ring is more regular, the others showing more separate spots.

On some images we notice some “texture”, i.e. some azimuthal regions of maximum intensity, suggesting a preferred orientation. Those are not distributed on all the rings of a same group of rings (corresponding to a “massif” in radial average). We can also note that the azimuthal reinforcement is different on the two figures.

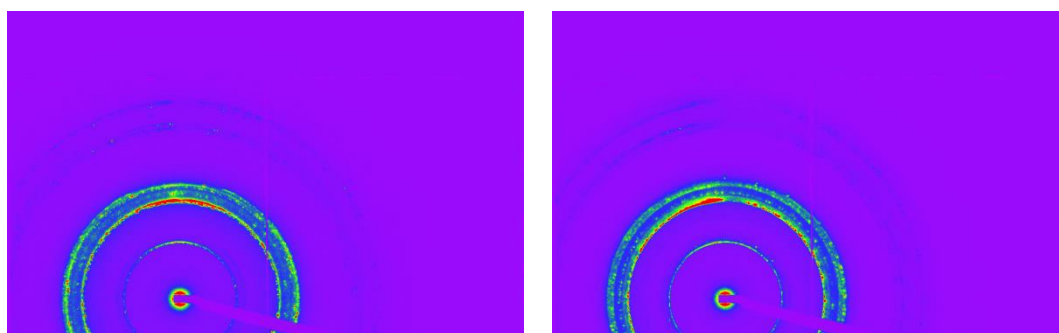


Figure V-37: 2D SAXS patterns of sample H0.5Au1 with 0.1M NaCl: measured at different height of capillary (left: higher; right: lower). 2D images showing preferred orientation on some of the rings only

V.3.5.2 Composition

What is the composition of the crystals? They could be made of:

- pure HA. In this case we could wonder about the signal, since the scattering length density of Ha is low; however the crystal would contain sodium ions, inducing higher signal. Pure AuNP giving strong signals. However, here in water, the AuNP are charged, thus repel each other and are not expected to crystallise

Moreover, the most striking feature is that the crystals peaks are always centered just at the abscissa of the maximum of the wide maxima associated to the complexes. This supports strongly the idea that the crystals are made of both Ha and AuNPs, and are an ordered version of the complexes. Note that they will be stabilized by the release of the counterions of both species, Na⁺ and Cl⁻.

V.3.5.3 Size: Test of detection

We can address the size of the crystals using two different routes. The first one is through real space images of the solution.

- Visual inspection using optical microscopy has been undergone first on a freshly prepared solution (of the same composition of crystal pattern observed on SAXS) between a plate and a platelet (Orme des Merisiers). We basically observe some dendritic deposits of small transparent crystals of size between 10 and several 100 microns, which are very likely to be salt (NaCl) crystals, and did not observe any darker crystals which could more likely be made of AuNPs.

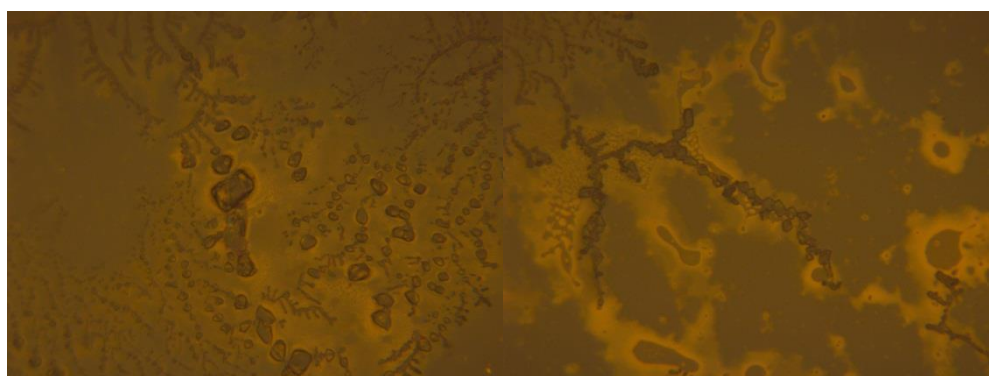


Figure V-38: optical microscopy images of freshly prepared Hyaluronan-AuNPs mixed sample in the presence of 0.1M NaCl

- Second, at MSC, as detailed above, we tried to follow crystallisation using a light microscope with the aid of Marie-Alice Guedeau-Boudeville, mixtures were made, quickly confined between two quartz plates separated by a ring of soft plastic gum, of thickness adjustable to less than 1 mm. This also prevents evaporation. After that phase separation into microscopic droplets could be observed, followed by slow falling down of the droplets, which adhered on the bottom plate and after up to a night, merged together, we had to let (due to failure of the microscope) a long time pass and observed the same samples 5 months later. Photos in Figure V-29 show that all droplets vanished and transformed into small dark dots made of aggregated AuNPs deposited on the glass, while the solution remained perfectly clear. The question is whether we can observe crystals among these dots (see Figure V-39).

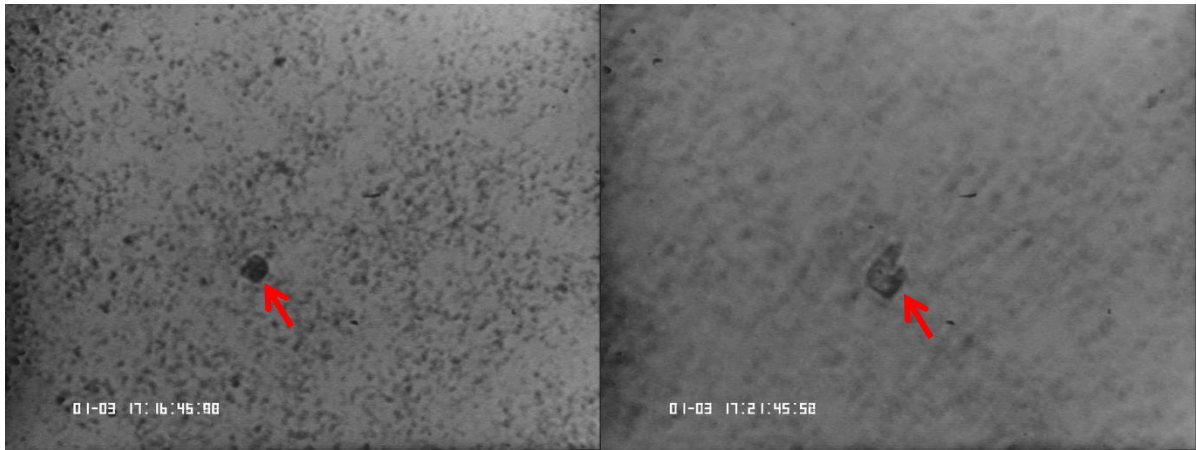


Figure V-39: optical microscopy photos (zoom \times 100) of sample H0.5Au1 observed after 5 months of preparation. The red arrows point at objects probably being crystals in question

- cryo-TEM observations were made owing to the kind help of Gervaise Mosser, Collège de France. We have tried to find the crystals using cryoTEM on FEI Tecnai Spirit G2 TEM microscope operating at 120 kV. Most of the observations resulted in images of the grids covered by a compact layer of AuNP packed together. Larger aggregates can be however observed, without any crystalline aspect, nor crystalline electronic diffraction. It is not possible to conclude on the bulk behavior since it is possible that the AuNPs are attracted by the grid. It is by the way easy to visualize the ligands around the Au NPs, and also confirm the size distribution. As the sample was mixed shortly before being vitrified (within 1min after the phase separation began), we are not sure if the waiting time was sufficient for the formation of crystal.

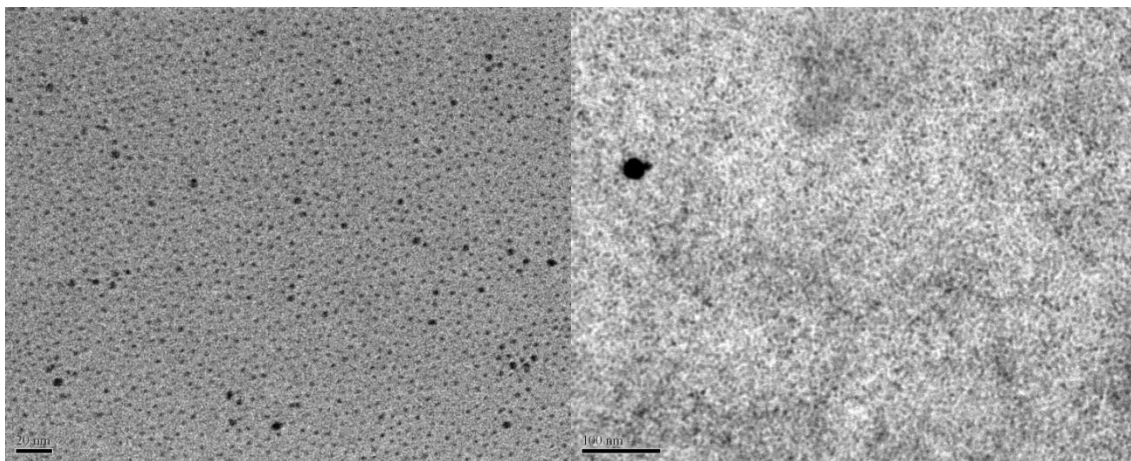


Figure V-40: CryoTEM images of vitrified sample H0.5Au0.5 in the presence of 0.1M NaCl

- Finally, we quote another possible exploration, formerly used by other authors on small microcrystals: Scanning Electron Microscope of solutions evaporated on solid substrates such as mica sheets show a large number of these crystals, made of proteins^[33, 160]. One can however fear that the free AuNPs and the complexes mask the microcrystals, and that washing procedures may redissolve them.

A second route is the reciprocal space: the width of the diffraction peaks can be used to deduce the sizes of the crystals, through the Scherrer law, which surprisingly is independent of the characteristic distance between planes. Therefore it appears to be the same for inter atomic distances and inter-nanoparticles. The values apparent on the diagrams are of order 0.1-0.2 degrees, i.e. $t \sim 0.0017$ to 0.0034 rad. Applying

$$t = \frac{K\lambda}{B \cos \theta_B} \approx \frac{\lambda}{B} \quad \text{V-2}$$

with θ_B (rad) small, $\lambda = 0.15$ nm, and K a constant of order 1. We find $B = 0.15 / (0.003) > 50$ nm.

Finally, note that using SANS (neutron radiation), we could not detect the same rings maybe because of the weak signal but more probably because of the large incident wavelength distribution, which spreads the signal out.

V.3.5.4 Structure

- 1) The multiple peaks.

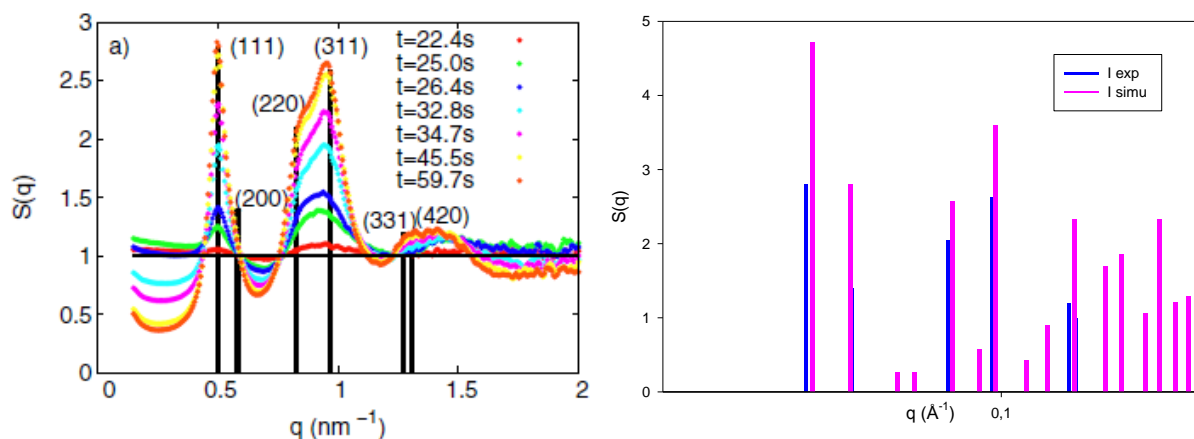
As remarked, the spectra are presenting by radial average, several adjacent peaks, usually of order 3 (sometimes even 5). These adjacent peaks form a group, which we can also call a “massif”. This corresponds in 2D images to groups of “adjacent” elementary “thin rings”. Although this maybe a classical case in crystallography, we have not yet found some similar situation in the literature. We will however try to compare with other cases of AuNP nanocrystals.

We first quote the work of Abecassis et al^[161], who observed by X ray (ID02, ESRF) some crystalline diffraction from suspensions of AuNPs synthesized with routes similar to ours (including the thiol ligand nature). This is observed only a few seconds after the initial formation of the nanoparticles. It is likely that the NPS are polydisperse, with polydispersity close to ours, which does not prevent from crystallization. Since the NPs were dispersed in an organic, non-polar solvent (toluene), the origin of the aggregation is proposed to be a potential

with Van der Waals attractive part; a VdW attraction also goes well with the particle size dependence of the phenomenon (stronger for large NPs). The crystal size could be measured from the oscillations of the form factor at low q and was found equal 85 nm.

The peaks are sensibly wider (factor 5) than in our observation, which agrees with this size. They were indexed with reference to a fcc lattice with a parameter of 21.5 nm leading to 15.2 nm for the center to center between closest neighbors, in agreement with the NP size including the ligand. Some simulations of the scattering are proposed; they predict much more peaks than observed, in particular at high q , which is not commented by the authors but maybe due to a less ordered arrangement than assumed. No splitting is predicted nor observed.

We can compare the diagrams predicted or observed by Abecassis et al with ours, using a log scale in q abscissa. If the crystal structure is homothetic to ours, we could observe a superposition of the peaks abscissa by simple translation. Testing such translation, we observe that a rather high number of peaks are found, which could explain the “satellite” peaks, whereas other peaks are not accounted for. But a simple shift in log scale is not enough: a distorsion is observed when increasing q , suggesting, in a very crude approach, that the lattice structure of our crystals is more complex. This could be associated to the presence of the PEL chain in our crystal.



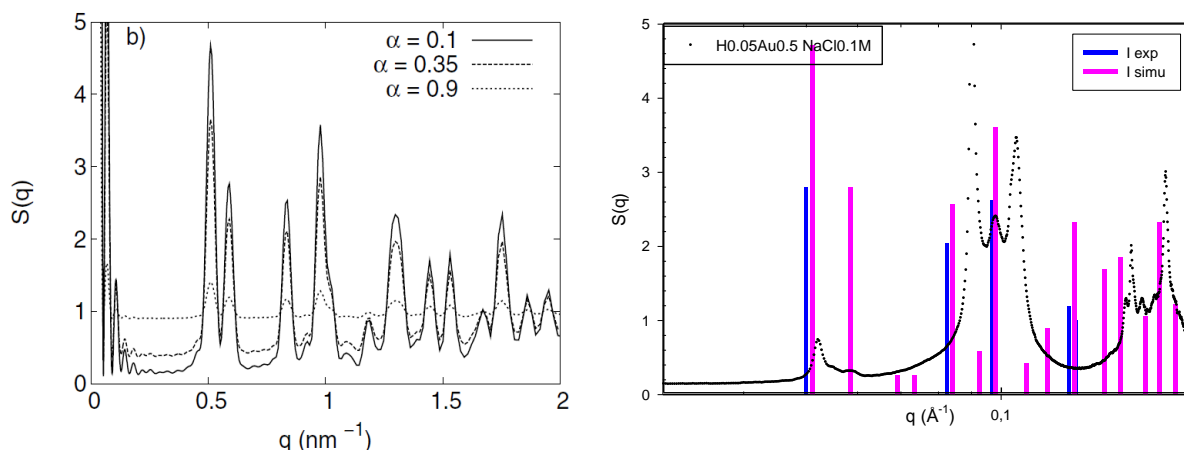


Figure V-41: Comparison of peak positions (up left: experiment data extracted from ref [161], down left: simulation data extracted from ref [161]; up right: peak position of both experimental and simulation data from ref xx and replotted in logarithm coordinate; down right: superposition of our experimental data in logarithm coordinate with former simulation of Abecassis et al)

Another reported case is the one of electrostatic aggregates from two kinds of NPs oppositely charged^[156] (Grzybovski). Here the crystal size is very small, as can be inferred from the width of the peaks (several degrees). Again the NPS are polydisperse, which does not prevent the formation of crystals of a given and unique set of lattice parameters.

From these literature results, we cannot account in detail for the adjacent peaks. A possibility not discussed up to now is that they are just coming from a few different crystals. This is apparently in contradiction with the large numbers of spots in the rings: the few crystals present would be made of numerous “macles”. If the lattice structure is the same for the different rings, the three peaks from a given massif should show the same ratio with the respective three peaks of another massif. This is observed in some cases (i.e. H0.5Au0.5), but not in all cases. Note that the exact abscissa of the peaks may be modified under the influence of the underlying scattering from aggregates (in Figure V-34 only the AuNP form factor was removed not the scattering from the aggregates).

Note also that in measurement made at DESY, the abscissas of the peaks are slightly different from the ones observed at SWING. This may be due to the different sizes of the NPS used in the two experiments.

Generally speaking, the splitting of the peaks corresponds to some symmetry breaking, starting from a basic crystal arrangement. Here, we refer to an indexation proposed to us by Arsen Goukasov, using the software “Fullprof” (Juan Rodriguez-Carvajal) and looking for the highest symmetry compatible with the data. This can be represented in real space as a

hexagonal arrangement in x, y plane ($a = b = 7.9$ nm), which agrees with close packing of Au NPs of the sizes used here, and different lattice parameter along the c axis: $c = 12.1$ nm (Hexagonal Group SG 175, P 6/m, $\alpha = \beta = 90^\circ$ and $\gamma = 120^\circ$). The first peak at the lowest q (with harmonics observable at larger q) is important since it signals the larger size of 12 nm. To cope with such anisotropy, an intermediate layer of lower particle density has to be introduced. This model can account for most of the peaks, but not all, (i.e. the peak in the middle of second massif at $q=0.0971 \text{ \AA}^{-1}$, surrounded by two crystalline peaks). We note that, it is exactly the characteristic peak position of complexes coexisting with these crystals. However, the complex peak is much wider than the middle peak observed here, so it is very probable that the peak does come from crystal of a different lattice (fcc coexisting with the hexagonal lattice). Ignoring this at the moment, one can thus think that the compact AuNP planes pack together with intermediate planes or lines containing particles arranged with Hyaluonan. This could be produced by organization of Hyaluronan along the AuNPs.

This could be put in relation with the mauve color of the spectra due to specific shift, suggesting specific privileged size with probably the creation of a thick layer of HA around the NPs, which would modify the dielectric environment. The occurrence of this “mauve shift” should be better understood.

Projection 001

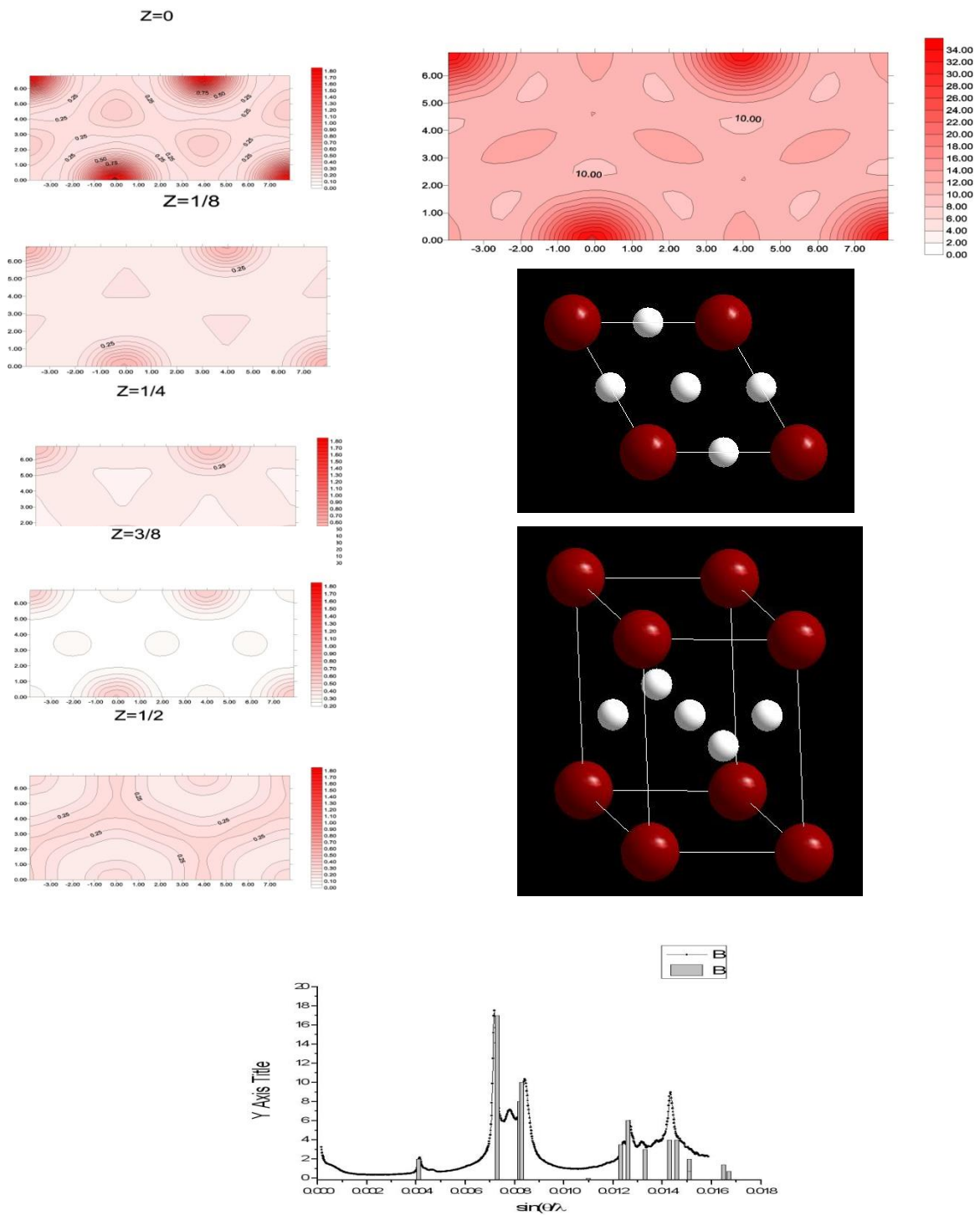


Figure V-42: peak indexation by Hexagonal lattice model and its horizontal projection suggested by software “Fullprof”, thanks to Arsen Gukasov, of HA-AuNP crystalline sample

V.4 Conclusion

In this chapter, two types of complexation were studied, the complexation of PSSNa and AuNPs and of hyaluronan and AuNPs. The main differences between PSSNa and hyaluronan are the chain flexibility and the number of charges per chain which is related to the M_w . For each type of complexation, the effect of salt concentration was compared, as the ionic force can also influence the effective charges of both AuNP and polymer and thus the electrostatic interaction according to Debye-Hückel model.

1) Effect of salt

The effect of salt concentration on interparticle distance and fractal dimension were analyzed mainly based on the second batch of AuNPs and SWING results. For complexes of same compositions, two ionic strengths were compared-with additional 0.1M NaCl in the solution and without salt added.

i) PSSNa-AuNP

- Visual observation

First, in the visual observation, we can compare phase diagrams (see Figure V-3/ Figure V-10 and Figure V-19/Figure V-24).

With added salt:

- The biphasic domain has a broader area in the case of system with additional 0.1M NaCl. In practice the lower bond is shifted to the left (lower concentrations of AuNPs lead to separation with added salt).
- We see a distinct behavior concerning samples situated on the *stoichiometric line* of phase diagram with composition of concentration ratio $C_{\text{PSSNa}} \text{ (g/L)}/C_{\text{Au}} \text{ (g/L)} = 1:10$. In stand of a separation liquid/liquid, samples here have a rapid solid/liquid separation with a phase of black insoluble grains and a phase of totally transparent supernatant.

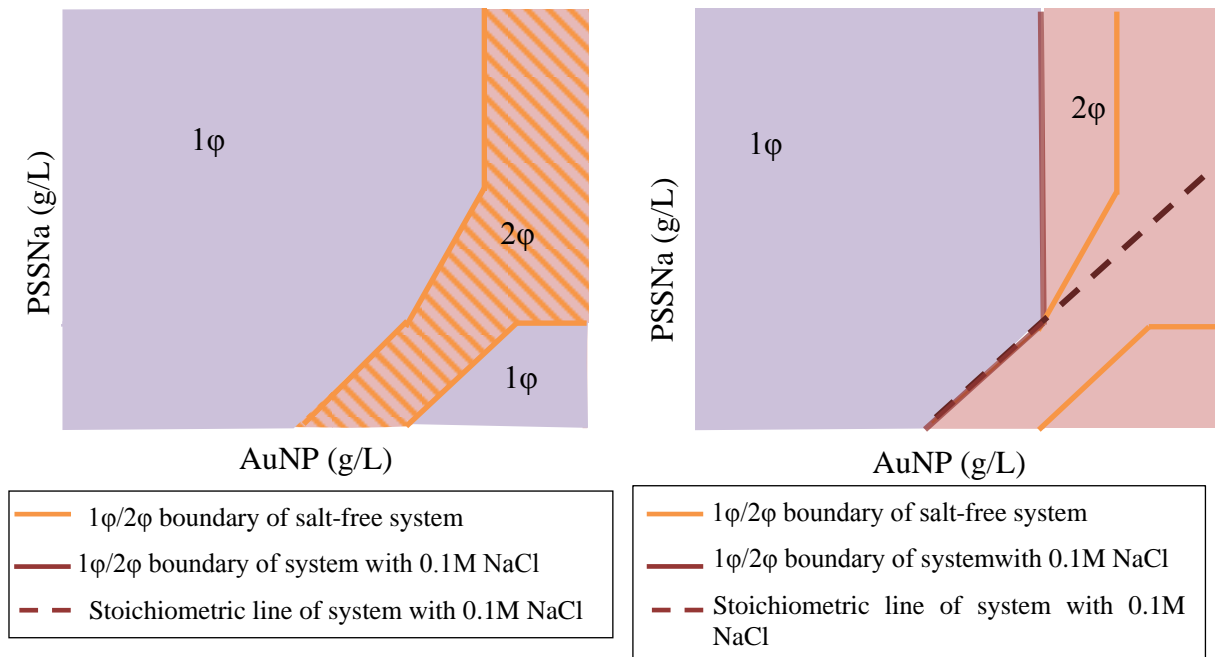


Figure V-43: Simplified phase diagram of PSSNa-AuNP complexation

- Scattering pattern

Typical shape: In general, complexes formed by mixing PSSNa-AuNP solutions have a typical pattern with (from low to high q) a quasi-linear part (in log-log plot, i.e. a $q^{-\alpha}$ law) at low q , one principal characteristic peak at around $q=0.102 \text{ \AA}^{-1}$, often followed by a second peak less intensive, and at even larger q , by the oscillation of form factor of AuNP. We can associate the low q slope to a $q^{-\alpha}$ variation, with α a fractal dimension, and since α is varying between 1 and 2 – 2.5, we can think of a more or less ramified structure.

Effect of salt: If we compare the linear part at low q of samples with/without added salt of the same composition, we can see that samples in the presence of 0.1M NaCl have a higher slope, i.e. a higher exponent (α of $q^{-\alpha}$). Hence, adding salt increases the apparent fractal dimension, in other words the degree of ramification (except for the last ratio value PSSNa/AuNP=3) and a higher interparticle distance. The difference is more distinct at low ratio, in other words, when AuNPs are in excess. The explanation might be that in both minority of NPs and excess of NPs, the complexes can be respectively negatively or positively charged. In consequence, the aggregation is limited by the repulsive interaction in both situations (see General Discussion). Now, adding salt will screen this repulsion, which favors the aggregation towards a more compact structure.

Quantification: fractal dimension and peak position: We can see from Figure V-44, for a given salt concentration of PSSNa/AuNP, the fractal dimension first increase with the

increase of PSSNa/AuNP ratio, and after the maximum value of α is reached, it then decreases continuously. The evolution of fractal dimension is consistent with the evolution of peak position. This is valid for both cases, with and without added salt. We find that this ratio for maximum fractal dimension ($\alpha = 3$) actually corresponds to the stoichiometric line for system in the presence of 0.1M NaCl where samples have transparent supernatant and precipitated grains.

ratio	α	Peak position	α	Peak position
PSSNa/AuNP	0M NaCl	0M NaCl	0.1M NaCl	0.1M NaCl
1.5/0.5	2.3	0.107	2.2	0.101
1/0.5	2.2	0.107	2.3	0.102
1.5/1	NA	NA	2.3	0.102
1/1	2.3	0.108	2.5	0.104
0.5/1	2.4	0.109	NA	NA
0.1/0.5	2.5	0.109	2.6	0.107
0.1/1	2.2	0.106	3	0.108
0.05/1	1.7	No peak	2.5	0.105
0.01/0.5	NA	NA		No peak

Table V-4: Evolution of fractal dimension and peak position in function of PSSNa/AuNP ratio

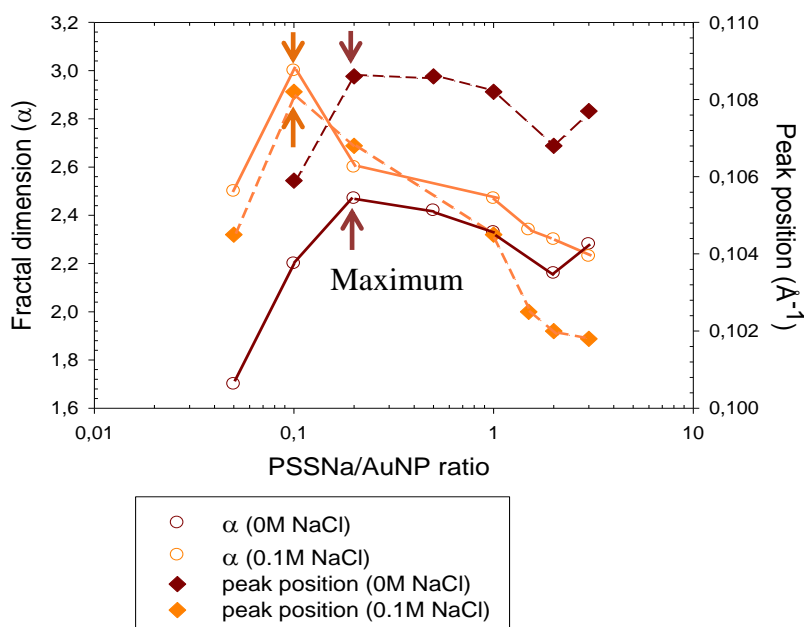


Figure V-44: The evolution of fractal dimension α and peak position in function of PSSNa/AuNP ratio

- ii) HA-AuNP
- Visual observation

For complexes HA-AuNPs, the phase diagrams are different. With no salt added, the diphasic zone is slightly less extended at low Ha concentration, and includes triphasic samples, while with added salt 0.1M NaCl, all samples become diphasic or triphasic, with rapid phase separation. The biphasic and triphasic domains have boarder areas than salt free system. The biphasic domain of salt free system actually covers the triphasic domain of system with added salt. Moreover, for the biphasic or triphasic samples at different composition, the two or three phases in which the system has been separated are of different kind (solid/liquid or liquid/liquid). The separation of phase undergoes very quickly with added salt, and is coupled with the change of color from red to mauve, while for salt free samples, the phase separation takes normally more than one day before to be visible by eye. The mauve color is observed only in the case of HA with added salt.

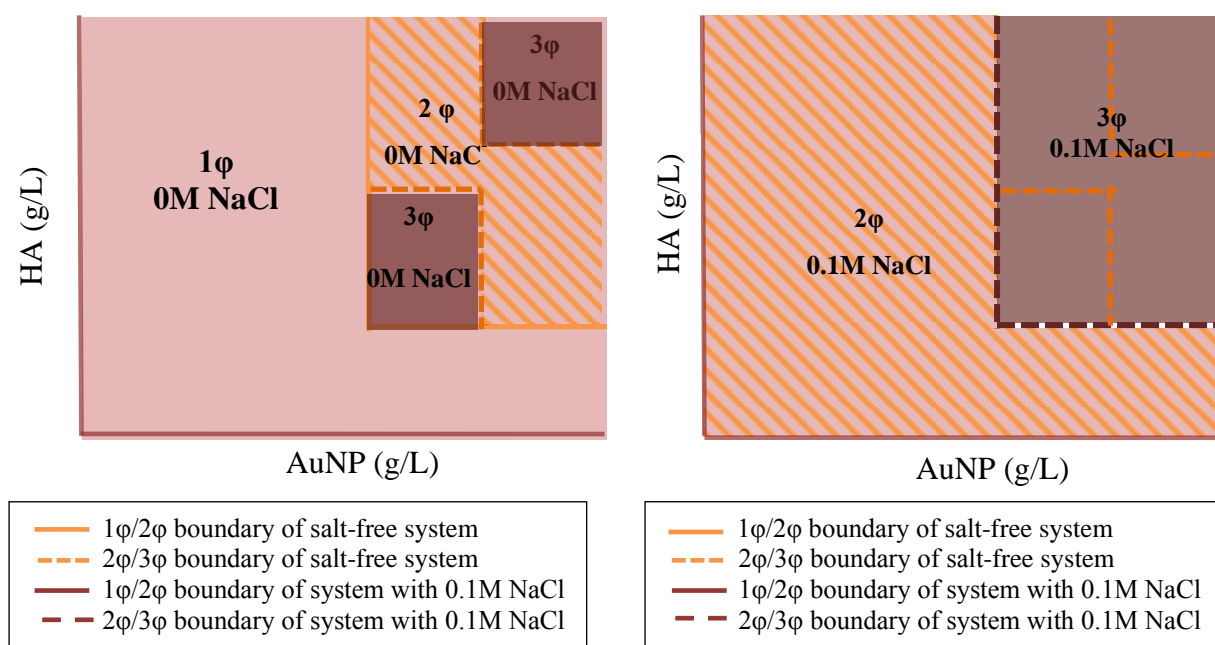


Figure V-45: Simplified phase diagram of HA-AuNP complexation

- Scattering pattern

For the amorphous complexes, the salt free complexes have similar scattering patterns as the ones with added salt (the formation of crystals will be discussed later below). At high q , there is a continuous upturn limited by the accessible q range, followed by the cross section of the secondary structure. At medium q , a big hole with a short upturn joins the cross section. These two characteristics still do not make these systems easy to distinguish. The hole is succeeded at larger q by the 1st peak, at around $q=0.098\text{\AA}^{-1}$ (salt free), or slightly shifted towards lower q at around $q=0.095\text{\AA}^{-1}$ (0.1M NaCl). At around $q=0.16\text{\AA}^{-1}$, a second peak appears. *This is*

different from what observed for PSSNa. For system in the presence of 0.1M NaCl, it looks like a flat shoulder, while in the salt free system, it can be very pointed when HA is in excess. Eventually, the right flank of 2nd peak is ended with the oscillation of AuNP's form factor; this is observed with both HA and PSSNa.

ratio	1 st Peak position	1 st Peak position
HA/AuNP	0M NaCl	0.1M NaCl
1.5/0.5	0.0976	0.0954
1/0.5	0.0976	0.0944
1.5/1	0.098	0.0949
1/1	0.098	0.0945/0.0954
0.1/0.5	0.0986	0.095
0.1/1	0.0976	0.092/0.096
0.05/1	No peak	NA
0.01/0.5	No peak	No peak

Table V-5: Evolution of peak position in function of Hyaluronan/AuNP ratio

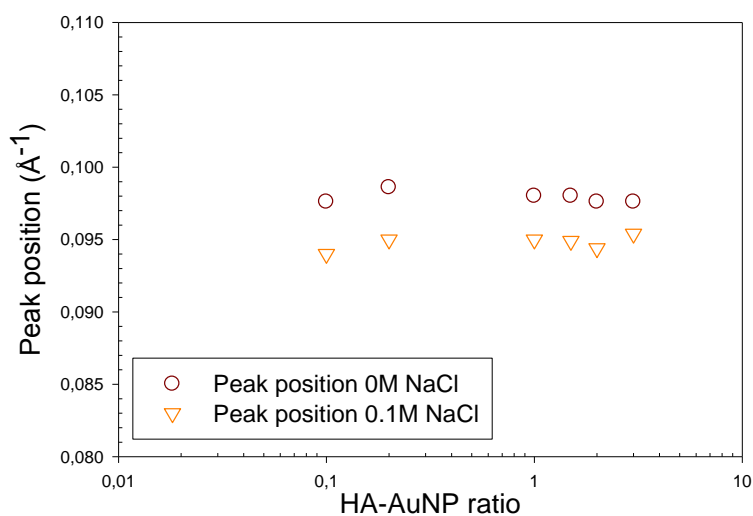


Figure V-46: Comparison of peak position at different ratio for complexes HA-AuNP at two different ionic strength

As for PSSNa-AuNP, we see for HA-AuNP that complexes formed in high ionic strength have a larger interparticle distance. The difference is however small. One can attribute it to the closer particle-particle contact as the effective charge density being reduced by screening chain and nanoparticle can lead to larger distance between the NPs ^[77]. Another possibility is just that the larger AuNPs particles, being more charged, are less screened out than the small ones, and therefore are more frequent in the complexes. The interparticle distance would then be higher. But this situation would be favored in large excess of NPs, which is not observed.

iii) Effect of chain flexibility

The origin of such large differences in scattering pattern between PSSNa and HA is believed to be due to the different flexibility of polyelectrolyte used for the complexation, for $L_p=0.9$ in case of PSSNa and $L_p=5$ in case of HA.

Such difference results firstly in the peak position of scattering pattern. As we can compare Table V-4 and Table V-5, for the same ionic strength, complexes PSSNa-AuNPs have smaller interparticle distance (peak situated at higher q) than complexes HA-AuNPs at the same salt concentration. This phenomenon is in good agreement with theoretical simulations^[78], which show that for a flexible chain, the NPs are close to each other with considerably many NP-NP contacts, while for rigid chain, the NPs are sequentially arranged along the chain with few NP-NP contacts.^[78]

Secondly, the low q increases before the peaks are totally different. For complexes PSSNa-AuNPs, we observe a continuous increase, following a power law of unique exponent value α . It is likely that the aggregation of AuNPs is controlled by the same unique process. Whereas for complexes HA-AuNPs, there are successively two slopes following two values α of power law exponent.

Another fact worth remarking is that in our system, the AuNPs are very strongly charged (according to the approximate calculation, 190 ligand molecule per AuNP of 3.4nm in diameter, giving 5 charges \AA), whereas the polyelectrolyte has a much less linear charge density (0.18 charge/ \AA for PSSNa, 30 times less; 0.1 charge/ \AA for HA, 54 times less).

In this condition, one extended chain (more rigid) of HA may not be able to fully cover one AuNP surface to neutralize its charges, so complexed AuNPs are undercharged. It is thus possible that several HA chains are adsorbed on the surface of one AuNP in different directions, and that the remaining part of these chains, maybe the one most accessible from the outside, can further complex more AuNPs to finally form a more compact structure. We think in such case, the process of complexation undergoes two stages. The first stage refers to the formation of elementary complexes, concerning normally several polymer chains with several nanoparticles in the dilute system. These elementary complexes might still have remaining charges coming from one of the components (hence so called “undercharged in term of AuNPs” or “overcharged in term of HA”). Depending on the composition of these complexes, they could have enough repulsion to overcome Van der Waals attraction, and thus be stable. If the remaining charges are not able to provide sufficient repulsion to balance Van

der Waals attraction, the second stage gets involved, and these elementary complexes get eventually close to each other to form larger complexes. This is shown Figure V-47(b).

The PSSNA/AuNP case is notably at variance of the Ha/AuNP: the PSS flexible chain wraps more easily the nanoparticle, as the charge of one PSSNa chain is equivalent in absolute value to the one of two AuNPs, so in the ideal situation (high ionic strength and stoichiometric ratio), one PSSNa chain can almost complex two AuNPs and become nearly neutral,. Meanwhile, the chain may stay more extended. At low ionic strength, at the same ratio, the complexed AuNPs may be more undercharged, thus aggregates may have a rather ramified and less compact structure.

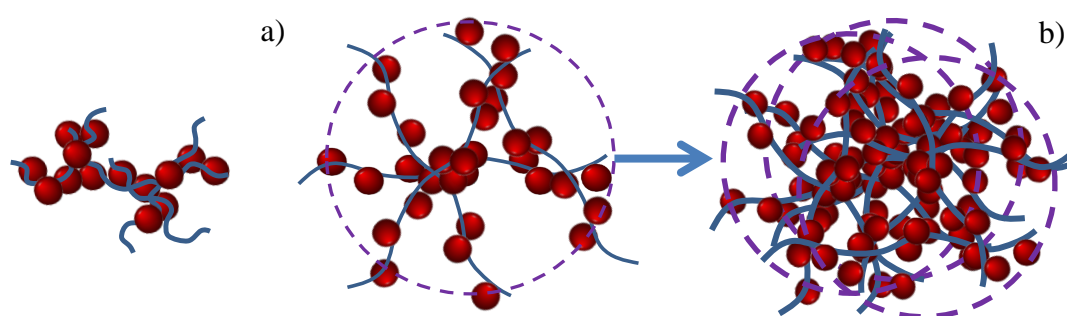


Figure V-47: a) Complex of PSSNa-AuNPs; b) Complex of HA-AuNPs

General Conclusion

In this thesis, we have studied five different complexation systems with the aim of building model systems. These systems are composed of charged PEL and oppositely charged NPs, but with different flexibility of PEL chains and different size of NPs. They exhibit in some extent, some general behaviors, but also several important differences from case to case.

Phase diagram

The phase diagrams, which are made by visual observation, show features quasi-general to all systems, with three successive domains:

- domain I, with low concentration in NPs and excess of PEL, samples are monophasic, of similar aspect –turbidity, color- than NPs alone at the same concentration.
- domain II, when the concentration of NPs is increased, and where the electrostatic interaction leads to the phase separation. In this domain II :
 - in the cases of colorless colloidal SiNPs, the separation can be observed by transparency: it seems to be in most cases a liquid/liquid separation. The lower rich liquid phase (usually called “coacervate”) scatters strongly light (white color), while the supernatant is more or less transparent. The volume ratio of two phases varies as a function of components ratio. It is not clear whether some rich phases are composed of solid precipitates, or can lead to such precipitates in a second stage.
 - in the cases of red color AuNPs, the phases appear macroscopically different (keeping in mind that the strong absorption by gold renders observation difficult). In some cases it is certainly a liquid-liquid phase separation as shown for Ha/AuNP, by the Porod scattering seen at short time by SANS, and as seen at a later time by optical microscopy (in these cases it seems that in a second stage solid particles form and precipitate, see Chap. V). In other cases, closer to stoichiometric line, a solid phase falls at the bottom. The ratio of two components determines whether the supernatant is transparent or dilute red, and whether the solid phase is a dense red layer or black grains.
- domain III: with low concentration in PEL and NPs are in excess, we “re-enter” a monophasic domain. Unlike the first monophasic domain, this time, samples are opalescent, more turbid than the solution of NPs alone at the same concentration,

which suggests the formation of larger objects. This evolution is in good agreement with most reported studies.

If the aggregations of NPs are driven by electrostatic interaction between PEL and NPs, the boundary between two domains must be influenced by the charge stoichiometric ratio between the two species. This addresses the problem of evaluating the charge of the particles, more precisely the charge relevant in the complexation process. We find that the values obtained using the mobility (using a zetameter) are too low. In short, we believe that the condensed counterions (noted c.i.), i.e. the ones comprised under the “slipping plane” neutralize in part the charge, which lowers the mobility, while during electrostatic complexation a part of these condensed c.i. are released far from the complex. Hence they are not present anymore close to the particle, which increases the particle charge effective for complexation. To evaluate the total charge of silica we use literature data and find the stoichiometric line well in the middle of the biphasic domain. For AuNPs, we have two equivalent separated evaluations: literature, and SANS. Using them, we obtain a stoichiometric line, which corresponds, like for silica, with the specificity of the scattering and of the precipitate phase.

Since we can estimate the degree of charge, we can then conclude, for all cases considered, on a **basic mechanism for precipitation**: when adding more charged particles we reach a dynamic concentration of less charged objects above which separation occurs because attractive forces win over repulsive one. This can occur before the stoichiometric line. But we do not know the distribution of global charge over the NPs. Besides polydispersity, disproportionation can occur (coexistence of neutral and more charged objects). Moreover, we have compared the effect of salt for some systems (PLL-SiNPs, HA-SiNPs, PSSNa-AuNPs and HA-SiNPs). All systems show a broader area of diphasic domain, because salt screens electrostatic repulsion, which favors the attractive forces. This process is accelerated when the NPs are concentrated.

We also see that the boundaries between I and II, or II and III, are not exactly lines of same ratio for all concentrations. This can be due in particular to the different dependence of van der Waals force on the volume of the complexes, and to the way more or less rigid chains can neutralize NPs (see Chap.V).

Scattering patterns

The typical scattering patterns for the complexes in all systems except for HA-AuNPs are composed of form factor of NPs at high q “followed” (when going towards $q = 0$) by the increasing slope towards low q . In case of small size AuNPs, with PSSNa, we also see a characteristic peak in the middle of two regimes, due to an interparticle distance. In case of large size SiNPs, we rarely observe such peak (or it is less distinct). This can be explained: the absence of visible inter-particles peak is often observed when structures are less compact.

It is also noticeable that, for the same systems, the three domains of phase diagram correspond to three series of slope value as crudely summarized in the table below.

	Large size SiNPs	Small size AuNPs (with PSS only)
Monophasic domain I (excess in PEL)	-2 or less than -1.5	-2
Diphasic domain II (intermediate ratio)	2-3	2-3
Monophasic domain III (excess in NPs)	-1 (semiflexible PEL) -2 (flexible PEL)	-1.7 (limit with domain II; monophasic at the time of measurement)

The great similarity point of these systems is the evolution of fractal dimension (absolute value of slope) as a function of NPs content. The fractal dimension first increases with the increase of NP content and then decreases after NP content exceeds a maximum complexing ratio. This ratio corresponds to the biphasic domain. The ionic strength of system may shift the NP content for maximum fractal dimension, but will not change the tendency. A very frequent fact is that when complexes are still present in the supernatant (absence of salt), their scattering shows the same apparent fractal dimension than in the coacervate (possibly with lower size). This general evolution of the dimension is nicely confirmed by the real space pictures obtained from TEM in one system. In practice, point by point comparisons are difficult to make because the Si and Au samples behaved differently (e.g. most of measurements for Au concern the diphasic phase, or close to it), so we report to the Discussion of each chapter.

Although we always have a general decrease of apparent dimension when entering domain III, the value is clearly different for flexible PEL from the one for the semiflexible, chitosan and hyaluronane, where it reaches 1, the value for rodlike objects. We discuss this below in term of L_p/R

In the case of complexes HA-AuNPs, the scattering is different. It reflects the formation of very compact clusters, yielding a strong interparticle peak, followed at low q by a hole, like the scattering from a concentrated solution, and the rearrangement of these clusters into aggregates of fractal dimension equal to the slope at very low q . This is close to former observations of complexes at higher concentration (Gummel et al). When salt is added, these compaction features are enhanced.

Effect of L_p/R

At the starting of this thesis work, we proposed L_p/R as a key parameter that would influence the structure of formed complexes. After examining all the systems, we think that L_p/R has a role with no doubt, but not general to all cases:

The **doubtless role of L_p/R** is found in the monophasic domain III of phase diagram, where NPs are in excess, the NPs can form one dimensional nanorods with semirigid PEL, when $L_p/R \geq 0.3$ (Chitosan-SiNPs, HA-SiNPs). On the contrary, the flexible PEL, when $L_p/R < 0.3$ can easily wrap around NPs to neutralize the charges, which leads to a ramified structure (fractal dimension=2).

However, the comparisons are difficult to be made between SiNPs and AuNPs. For example, we did not find rodlike structure in HA-AuNPs ($L_p/R = 1.25$), the Au complexes being much more compacts:

- one physical reason is that AuNPs are much more charged, so with the same ratio L_p/R , PEL chains are not able to wrap to partially neutralize AuNPs. By consequence, many chains must approach at the same time near the AuNPs, which makes transform the partially linear or less ramified structures into objects which are more compact.
- another practical reason is that due to the lower of AuNPs concentration attainable limits (cost) we actually did not reach the monophasic domain with excess in AuNPs, except in the lower right corner (very low Ha content), where we measured scattering signals from individual AuNPs. To visualize complexes, we would have to increase the concentrations of HA and thus of AuNPs, requiring too high quantity of the latter to reach rodlike complex structure.

Besides of the effect L_p/R , other effects may also account for the different structure resulting from large size SiNPs and small size AuNPs.

- First, we think of charge density of polymer. The distance between two charged sites is equal to 2.5 Å for PSSNa, but should be equal to 7.5Å if we take Manning condensation into consideration. However, Manning condensation is likely to play no more role if the polymer condensed ions are displaced from the surface: they are released in the solution, as favored in entropy. This effect was already noted for the c.i. of the NPs, in the discussion above about the stoichiometric line.
- Second, gold has a much higher density than silica (19g/cm³ vs 2.2g/cm³). This leads to different kinetics of phase separation (precipitation in particular).
- SiNPs are inorganic colloidal NPs that tend to form ramified structure –apparently fractal- by themselves where they are alone in solution (sol-gel transitions). SiNPs can attach in line one to another, sometimes due to dissolution and reprecipitation processes. This is not the case for AuNPs, which are more resistant to aggregation once properly liganded. However some fractal structures are observed for AuNP in presence of PSS.
- AuNPs are much smaller. Therefore the growth of compact structures may be achieved faster, more easily, while in the case of silica the larger fractal aggregates may stay trapped because the kinetics are slower.

Perspectives:

In this thesis, we established a frame of systems that can help to understand more profoundly the role of L_p/R on the formation of complexes. Due to the time limit, these systems are not fully developed. For example, the radius of AuNPs can be increased by seed-growth synthesis, which enables to compare the effect of size using NP made of the same species (Au). Also, the salt effect can be studied more subtly by varying gradually the salt concentration (ex. 0M, 0.05M, 0.1M, 0.15M and 0.2M), and the timing of addition (ex. before or after mixing of components). The effect of the PEL chosen should be explored more, in particular in the semi-rigid case; we used two different polysaccharides which have different structures, in particular at the local scale (more or less helicoïdal conformation).

Obviously, much more can be done if we combine electrostatic effects with other interactions, such as hydrogen bonds, as often found in nature. Finally, a more careful account of the different processes of phase separation and their link with the now better known structure of

the complex would be useful in practice and complete a multi-scale approach of the complexity of these systems, including some out of equilibrium problems.

Bibliography

- [1] Flory, P. J., *Principles of polymer chemistry*, Cornell University Press, Series **1953**, Ithaca, New York
- [2] Rice, S. A., Nagasawa, M., *Polyelectrolyte solutions, a theoretical introduction*, Academic Press, Series **1961**, London, New York
- [3] Oosawa, F., *Polyelectrolytes*, M. Dekker, Series **1971**, New York
- [4] Doi, M., Edwards, S. F., *The theory of polymer dynamics*, Oxford University Press, Series **1986**, New York
- [5] Hara, M., *Polyelectrolytes : science and technologies*, Marcel Dekker, Series **1993**, New York
- [6] des Cloizeaux, J., Jannink, G., *Les polymères en solution*, Les éditions de Physique, Series **1987**
- [7] Fontanille, M., Gnanou, Y., *chimie et physico-chimie des polymères*, Dunod, Series **2002**
- [8] Barrat, J.-L., Joanny, F., *Theory of Polyelectrolyte Solutions*, John Wiley & Sons, Inc., Series **2007**
- [9] Manning, G. S., *J. Chem. Phys.*, **1969**, 51(3): 924-934
- [10] Odijk, T., *J. Polym. Sci. Pol. Phys*, **1977**, 15(3): 477-483
- [11] Skolnick, J., Fixman, M., *Macromolecules.*, **1977**, 10(5): 944-948
- [12] Fixman, M., *J. Chem. Phys.*, **1982**, 76(12): 6346-6353
- [13] Odijk, T., *Macromolecules.*, **1979**, 12(4): 688-693
- [14] Odijk, T., Houwaart, A. C., *J. Polym. Sci. Pol. Phys*, **1978**, 16(4): 627-639
- [15] Barrat, J. L., Joanny, J. F., *Europhys. Lett.*, **1993**, 24(5): 333-338
- [16] Callen, H. B., *Thermodynamics*, Wiley, Series **1985**, New York, N.Y.
- [17] Buhler, E., Boué, F., *Eur. Phys. J. E*, **2003**, 10(2): 89-92
- [18] Overbeek, J. T., Voorn, M. J., *J. Cell. Physiol. Suppl*, **1957**, 49(Suppl 1): 7-22; discussion, 22-26
- [19] de Vries, R., Stuart, M. C., *Curr. Opin. Colloid In*, **2006**, 11(5): 295-301
- [20] Kudlay, A., de la Cruz, M. O., *J. Chem. Phys.*, **2004**, 120(1): 404-412

- [21] Kudlay, A., Ermoshkin, A. V., de la Cruz, M. O., *Macromolecules.*, **2004**, 37(24): 9231-9241
- [22] Kumar, R., Audus, D., Fredrickson, G. H., *J. Phys. Chem. B*, **2010**, 114(31): 9956-9976
- [23] Hong, J. W., Henme, W. L., Keller, G. E., et al., *Adv. Mater.*, **2006**, 18(7): 878
- [24] Mengarelli, V., Auvray, L., Zeghal, M., *EPL* **2009**, 85(5): 58001
- [25] Zhang, R., Shklovskii, B. I., *Physica A: Statistical Mechanics and its Applications*, **2005**, 352(1): 216-238
- [26] Svensson, A. V., Johnson, E. S., Nylander, T., et al., *ACS App.Mater.Interf.*, **2010**, 2(1): 143-156
- [27] Goddard, E. D., *J. Am. Oil Chem. Soc.*, **1994**, 71(1): 1-16
- [28] Dias, R., Mel'nikov, S., Lindman, B., et al., *Langmuir.*, **2000**, 16(24): 9577-9583
- [29] Kogej, K., *Adv. Colloid Interfac*, **2010**, 158(1-2): 68-83
- [30] Li, D. C., Kelkar, M. S., Wagner, N. J., *Langmuir.*, **2012**, 28(28): 10348-10362
- [31] Wang, C., Tam, K. C., *J. Phys. Chem. B*, **2004**, 108(26): 8976-8982
- [32] Voisin, D., Vincent, B., *Adv. Colloid Interfac*, **2003**, 106: 1-22
- [33] Koltover, I., Salditt, T., Safinya, C. R., *Biophys. J.*, **1999**, 77(2): 915-924
- [34] Morawetz, H., Hughes, W. L., *J.Phys.Chem.*, **1952**, 56(1): 64-69
- [35] Morawetz, H., Sage, H., *Arch. Biochem. Biophys.*, **1955**, 56(1): 103-109
- [36] Margolin, A. L., Sherstyuk, S. F., Izumrudov, V. A., et al., *Eur. J. Biochem.*, **1985**, 146(3): 625-632
- [37] Parker, D. E., Glatz, C. E., Ford, C. F., et al., *Biotechnol. Bioeng.*, **1990**, 36(5): 467-475
- [38] Gao, J. Y., Dubin, P. L., Muhoberac, B. B., *J. Phys. Chem. B*, **1998**, 102(28): 5529-5535
- [39] Matsudo, T., Ogawa, K., Kokufuta, E., *Biomacromolecules*, **2003**, 4(6): 1794-1799
- [40] Cousin, F., Gummel, J., Clemens, D., et al., *Langmuir.*, **2010**, 26(10): 7078-7085
- [41] de Kruif, C. G., Weinbreck, F., de Vries, R., *Curr. Opin. Colloid In*, **2004**, 9(5): 340-349

- [42] Cousin, F., Gummel, J., Combet, S., et al., *Adv. Colloid Interfac*, **2011**, 167(1-2): 71-84
- [43] Cousin, F., Gummel, J., Ung, D., et al., *Langmuir.*, **2005**, 21(21): 9675-9688
- [44] Gummel, J., Boué, F., Clemens, D., et al., *Soft Matter*, **2008**, 4(8): 1653-1664
- [45] Gummel, J., Boué, F., Deme, B., et al., *J. Phys. Chem. B*, **2006**, 110(49): 24837-24846
- [46] Gummel, J., Cousin, F., Boué, F., *J. Am. Chem. Soc.*, **2007**, 129(18): 5806
- [47] Gummel, J., Cousin, F., Boué, F., *Macromolecules.*, **2008**, 41(8): 2898-2907
- [48] Xia, J. L., Dubin, P. L., Kokufuta, E., *Macromolecules.*, **1993**, 26(24): 6688-6690
- [49] Park, J. M., Muhoberac, B. B., Dubin, P. L., et al., *Macromolecules.*, **1992**, 25(1): 290-295
- [50] Feldheim, D. L., Grabar, K. C., Natan, M. J., et al., *J. Am. Chem. Soc.*, **1996**, 118(32): 7640-7641
- [51] Min, Y., Akbulut, M., Kristiansen, K., et al., *Nat.Mater.*, **2008**, 7(7): 527-538
- [52] Nuzzo, R. G., Allara, D. L., *J. Am. Chem. Soc.*, **1983**, 105(13): 4481-4483
- [53] Heinz, R., Rabe, J. P., *Langmuir.*, **1995**, 11(2): 506-511
- [54] Driver, S. M., Woodruff, D. P., *Langmuir.*, **2000**, 16(16): 6693-6700
- [55] Williams, J. A., Gorman, C. B., *J. Phys. Chem. C*, **2007**, 111(34): 12804-12810
- [56] Love, J. C., Wolfe, D. B., Haasch, R., et al., *J. Am. Chem. Soc.*, **2003**, 125(9): 2597-2609
- [57] Mekhalif, Z., Riga, J., Pireaux, J. J., et al., *Langmuir.*, **1997**, 13(8): 2285-2290
- [58] Ruckenstein, E., Li, Z. F., *Adv. Colloid Interfac*, **2005**, 113(1): 43-63
- [59] Cai, Y., *Langmuir.*, **2009**, 25(10): 5594-5601
- [60] Allara, D. L., Nuzzo, R. G., *Langmuir.*, **1985**, 1(1): 45-52
- [61] Shafi, K., Ulman, A., Yan, X. Z., et al., *Langmuir.*, **2001**, 17(5): 1726-1730
- [62] Helmy, R., Fadeev, A. Y., *Langmuir.*, **2002**, 18(23): 8924-8928
- [63] Sahoo, Y., Pizem, H., Fried, T., et al., *Langmuir.*, **2001**, 17(25): 7907-7911
- [64] Yee, C., Kataby, G., Ulman, A., et al., *Langmuir.*, **1999**, 15(21): 7111-7115

- [65] White, M. A., Johnson, J. A., Koberstein, J. T., et al., *J. Am. Chem. Soc.*, **2006**, *128*(35): 11356-11357
- [66] Warner, M. G., Hutchison, J. E., *Nat.Mater.*, **2003**, *2*(4): 272-277
- [67] Niemeyer, C. M., Simon, U., *Eur. J. Inorg. Chem.*, **2005**, (18): 3641-3655
- [68] Coffey, J. L., Bigham, S. R., Li, X., et al., *Appl. Phys. Lett.*, **1996**, *69*(25): 3851-3853
- [69] Han, J., Ohara, S., Sato, K., et al., *Mater. Lett.*, **2012**, *79*(0): 78-80
- [70] Zinchenko, A., Yoshikawa, K., Baigl, D., *Phys. Rev. Lett.*, **2005**, *95*(22)
- [71] Decher, G., *Science*, **1997**, *277*(5330): 1232-1237
- [72] Kotov, N. A., Magonov, S., Tropsha, E., *Chem. Mater.*, **1998**, *10*(3): 886-895
- [73] Sukhorukov, G. B., Donath, E., Lichtenfeld, H., et al., *Colloid Surface. A*, **1998**, *137*(1-3): 253-266
- [74] Gaponik, N., Radtchenko, I. L., Gerstenberger, M. R., et al., *Nano Lett*, **2003**, *3*(3): 369-372
- [75] Donath, E., Sukhorukov, G. B., Caruso, F., et al., *Angew. Chem. Int. Edit.*, **1998**, *37*(16): 2202-2205
- [76] Akinchina, A., Linse, P., *Macromolecules.*, **2002**, *35*(13): 5183-5193
- [77] Jonsson, M., Linse, P., *J. Chem. Phys.*, **2001**, *115*(7): 3406-3418
- [78] Jonsson, M., Linse, P., *J. Chem. Phys.*, **2001**, *115*(23): 10975-10985
- [79] Chodanowski, P., Stoll, S., *J. Chem. Phys.*, **2001**, *115*(10): 4951-4960
- [80] Ulrich, S., Seijo, M., Laguecir, A., et al., *J. Phys. Chem. B*, **2006**, *110*(42): 20954-20964
- [81] Skepö, M., *J. Phys. Chem. B*, **2004**, *108*(17): 5431-5437
- [82] Cherstvy, A. G., Winkler, R. G., *J. Chem. Phys.*, **2006**, *125*(6): 064904-064911
- [83] Netz, R. R., Joanny, J.-F., *Macromolecules.*, **1999**, *32*(26): 9026-9040
- [84] Schiessel, H., Bruinsma, R. F., Gelbart, W. M., *J. Chem. Phys.*, **2001**, *115*(15): 7245-7252
- [85] Skepö, M., Linse, P., *Macromolecules.*, **2003**, *36*(2): 508-519
- [86] Ou, Z. Y., Muthukumar, M., *J. Chem. Phys.*, **2006**, *124*(15)

- [87] Gucht, J. v. d., Spruijt, E., Lemmers, M., et al., *J. Colloid Interf. Sci.*, **2011**, 361(2): 407-422
- [88] Boroudjerdi, H., Netz, R. R., *J. Phys-condens. Mat.*, **2005**, 17(14): S1137-S1151
- [89] Boroudjerdi, H., Netz, R. R., *Europhys. Lett.*, **2005**, 71(6): 1022-1028
- [90] Cummins, H. Z., Pike, E. R., *Photon correlation and light beating spectroscopy*, Plenum Press, Series **1974**, New York and London
- [91] Higgins, J. S., Benoît, H. C., *Polymers and Neutron Scattering*, Clarendon Press, Series **1994**
- [92] Lindner, P., Zemb, T., *Neutron, x-ray and light scattering: introduction to an investigative tool for colloidal and polymeric systems : proceedings of the European Workshop on Neutron, X-Ray and Light Scattering as an Investigative Tool for Colloidal and Polymeric Systems, Bombannes, France, 27 May-2June, 1990*, North-Holland, Series **1991**, Amsterdam ; New York
- [93] Schmitz, K. S., *An introduction to dynamic light scattering by macromolecules*, Academic Press, Series **1990**, San Diego
- [94] Provencher, S. W., *Comput. Phys. Commun.*, **1982**, 27(3): 213-227
- [95] Provencher, S. W., *Comput. Phys. Commun.*, **1982**, 27(3): 229-242
- [96] Koppel, D. E., *J. Chem. Phys.*, **1972**, 57(11): 4814-4820
- [97] Cooper, C. L., Goulding, A., Kayitmazer, A. B., et al., *Biomacromolecules*, **2006**, 7(4): 1025-1035
- [98] de Jong, H. G. B., Kruyt, H. R., *Proc. K. Ned. Akad. Wet.*, **1929**, 32(6/10): 849-856
- [99] Kayitmazer, A. B., Strand, S. P., Tribet, C., et al., *Biomacromolecules*, **2007**, 8(11): 3568-3577
- [100] Buhler, E., Guetta, O., Rinaudo, M., *Int. J. Polym. Anal. Ch.*, **2000**, 6(1-2): 155-175
- [101] Buhler, E., Rinaudo, M., *Macromolecules.*, **2000**, 33(6): 2098-2106
- [102] Esquenet, C., Buhler, E., *Macromolecules.*, **2001**, 34(15): 5287-5294
- [103] Esquenet, C., Terech, P., Boué, F., et al., *Langmuir.*, **2004**, 20(9): 3583-3592
- [104] Esquenet, C., Buhler, E., *Macromolecules.*, **2002**, 35(9): 3708-3716
- [105] Pedersen, J. S., Schurtenberger, P., *Macromolecules.*, **1996**, 29(23): 7602-7612
- [106] Burchard, W., Kajiwara, K., *Proceedings of the Royal Society of London Series a-Mathematical and Physical Sciences*, **1970**, 316(1525): 185

- [107] Sharp, P., Bloomfield, V., *Biopolymers.*, **1968**, 6(8): 1201-&
- [108] Buhler, E., Boue, F., *Eur. Phys. J. E*, **2003**, 10(2): 89-92
- [109] Buhler, E., Boue, F., *Macromolecules.*, **2004**, 37(4): 1600-1610
- [110] Rasmusson, M., Wall, S., *Colloid Surface. A*, **1997**, 122(1-3): 169-181
- [111] Van der Meeren, P., Saveyn, H., Bogale Kassa, S., et al., *Phys. Chem. Chem. Phys.*, **2004**, 6(7): 1408-1412
- [112] Evans, D. F., Wennerström, H., *The colloidal domain: where physics, chemistry, biology, and technology meet*, Wiley-VCH, Series **1999**
- [113] Lindquist, G. M., Stratton, R. A., *J. Colloid Interf. Sci*, **1976**, 55(1): 45-59
- [114] Holm, C., Joanny, J. F., Kremer, K., et al., *Polyelectrolyte theory*, Springer-Verlag Berlin, Series 166 **2004**, Berlin
- [115] Lee, J., Popov, Y. O., Fredrickson, G. H., *J. Chem. Phys.*, **2008**, 128(22)
- [116] Nizri, G., Makarsky, A., Magdassi, S., et al., *Langmuir.*, **2009**, 25(4): 1980-1985
- [117] des Cloizeaux, J., *Macromolecules.*, **1973**, 6(3): 403-407
- [118] Jouault, N., Nguyen, R., Rawiso, M., et al., *Soft Matter*, **2011**, 7(10): 4787-4800
- [119] Morfin, I., Buhler, E., Cousin, F., et al., *Biomacromolecules*, **2011**, 12(4): 859-870
- [120] Ruff, Y., Buhler, E., Candau, S. J., et al., *J. Am. Chem. Soc.*, **2010**, 132(8): 2573-2584
- [121] Gummel, J., *Structures et mécanisme de formation de complexes polyelectrolyte-proteine*, 228, Thèse doctorat, Ecole doctorale physico-chimie du sud de Paris, Université d'Orsay, 2006
- [122] Von Smoluchowski, M., *Bull. Int. Acad. Sci. Cracovie*, **1903**: 184
- [123] Hückel, E., *Physik.Z.*, **1924**, 49(25): 204
- [124] Eustis, S., El-Sayed, M. A., *Chem. Soc. Rev.*, **2006**, 35(3): 209-217
- [125] Storhoff, J. J., Elghanian, R., Mucic, R. C., et al., *J. Am. Chem. Soc.*, **1998**, 120(9): 1959-1964
- [126] Loo, C., Lowery, A., Halas, N. J., et al., *Nano Lett*, **2005**, 5(4): 709-711
- [127] Perrault, S. D., Chan, W. C. W., *P. Natl. Acad. Sci. USA*, **2010**, 107(25): 11194-11199
- [128] Stuchinskaya, T., Moreno, M., Cook, M. J., et al., *Photochem. Photobiol. Sci*, **2011**, 10(5): 822-831

- [129] Brown, S. D., Nativo, P., Smith, J. A., et al., *J. Am. Chem. Soc.*, **2010**, *132(13)*: 4678-4684
- [130] Gupta, R. K., Ying, G., Srinivasan, M. P., et al., *J. Phys. Chem. B*, **2012**, *116(32)*: 9784-9790
- [131] Schmid, G., Simon, U., *Chem. Commun.*, **2005**, (6): 697-710
- [132] Campbell, C. T., Sharp, J. C., Yao, Y. X., et al., *Faraday. Discuss.*, **2011**, *152*: 227-239
- [133] Thompson, D. T., *Nano Today*, **2007**, *2(4)*: 40-43
- [134] Daniel, M.-C., Astruc, D., *Chem. Rev.*, **2004**, *104*: 293-346
- [135] Frens, G., *Nature-Physical Science*, **1973**, *241(105)*: 20-22
- [136] Faraday, M., *Phil. Trans. R. Soc. Lond.*, **1857**, *147(1)*: 145-181
- [137] Ji, X. H., Song, X. N., Li, J., et al., *J. Am. Chem. Soc.*, **2007**, *129(45)*: 13939-13948
- [138] Kimling, J., Maier, M., Okenve, B., et al., *J. Phys. Chem. B*, **2006**, *110(32)*: 15700-15707
- [139] Slot, J. W., Geuze, H. J., *Ultramicroscopy*, **1984**, *15(4)*: 383-383
- [140] Turkevich, J., Stevenson, P. C., Hillier, J., *Discuss. Faraday Soc*, **1951**, (11): 55
- [141] Kumar, S., Yang, H. Z., Zou, S. Z., *J. Phys. Chem. C*, **2007**, *111(35)*: 12933-12938
- [142] Yonezawa, T., Kunitake, T., *Colloid Surface. A*, **1999**, *149(1-3)*: 193-199
- [143] Haiss, W., Thanh, N. T. K., Aveyard, J., et al., *Anal. Chem.*, **2007**, *79(11)*: 4215-4221
- [144] Ivanov, M. R., Bednar, H. R., Haes, A. J., *ACS Nano*, **2009**, *3(2)*: 386-394
- [145] Woehrle, G. H., Brown, L. O., Hutchison, J. E., *J. Am. Chem. Soc.*, **2005**, *127(7)*: 2172-2183
- [146] Ojea-Jimenez, I., Puentes, V., *J. Am. Chem. Soc.*, **2009**, *131(37)*: 13320-13327
- [147] Brust, M., Walker, M., Bethell, D., et al., *J. Chem. Soc. Chem. Commun*, **1994**, (7): 801-802
- [148] Zhang, L., Sun, X., Song, Y., et al., *Langmuir.*, **2006**, *22(6)*: 2838-2843
- [149] Jana, N. R., Peng, X., *J. Am. Chem. Soc.*, **2003**, *125(47)*: 14280-14281
- [150] Pengo, P., Polizzi, S., Battagliarin, M., et al., *J. Mater. Chem.*, **2003**, *13(10)*: 2471-2478

- [151] Templeton, A. C., Wuelfing, M. P., Murray, R. W., *Accounts. Chem. Res.*, **2000**, *33*(1): 27-36
- [152] Ingram, R. S., Hostetler, M. J., Murray, R. W., et al., *J. Am. Chem. Soc.*, **1997**, *119*(39): 9279-9280
- [153] Leff, D. V., Brandt, L., Heath, J. R., *Langmuir.*, **1996**, *12*(20): 4723-4730
- [154] Warner, M. G., Reed, S. M., Hutchison, J. E., *Chem. Mater.*, **2000**, *12*(11): 3316-3320
- [155] Clifffel, D. E., Zamborini, F. P., Gross, S. M., et al., *Langmuir.*, **2000**, *16*(25): 9699-9702
- [156] Kalsin, A. M., Fialkowski, M., Paszewski, M., et al., *Science*, **2006**, *312*(5772): 420-424
- [157] Jain, P. K., Lee, K. S., El-Sayed, I. H., et al., *J. Phys. Chem. B*, **2006**, *110*(14): 7238-7248
- [158] Liu, X., Atwater, M., Wang, J., et al., *Colloid. Surface. B*, **2007**, *58*(1): 3-7
- [159] Spiteri, M. N., Boué, F., Lapp, A., et al., *Phys. Rev. Lett.*, **1996**, *77*(26): 5218-5220
- [160] Barty, A., Caleman, C., Aquila, A., et al., *Nature Photonics*, **2012**, *6*(1): 35-40
- [161] Abecassis, B., Testard, F., Spalla, O., *Phys. Rev. Lett.*, **2008**, *100*(11): 11504

Résumé en Français

La complexation électrostatique entre un polyélectrolyte et des nanoparticules de charges opposées attire beaucoup d'attentions pour de nombreuses applications dans différents domaines. Dans le cadre de cette thèse, nous nous sommes intéressés particulièrement au rôle du rapport L_p/R sur la formation des complexes. Pour varier ce paramètre sur une grande gamme, nous avons pris des systèmes modèles issus de combinaisons de quatre polyélectrolytes de rigidité différente et trois types de nanoparticules chargées de tailles différentes, dont des nanoparticules d'or chargées positivement synthétisées par nous-mêmes. Pour chaque système, nous avons d'abord caractérisé le comportement macroscopique des complexes en fonction des concentrations, par un diagramme de phase (deux domaines monophasiques encadrant un domaine diphasique). Ensuite, à l'aide des techniques de diffusion du rayonnement -lumière, rayons-X et neutrons, nous avons comparé les différentes structures des complexes (taille, dimension fractale, D_f). Ces structures sont confirmées par cryo-TEM. Pour $L_p/R \approx 1$, nous auto-assemblons des NPs en bâtons solubles dans le domaine monophasique du diagramme de phase en excès de NPs. Dans les autres domaines, les structures sont branchées avec des dimensions fractales de 1.5 à 2.5. En plus de L_p/R , nous avons aussi montré que le sel, en écrantant les répulsions électrostatiques entre complexes, accélère la séparation de phase et accroît la compacité de leurs structures. Spécifiquement, pour la complexation hyaluronan-AuNPs, nous avons observé la diffraction (DXPA) de métacristaux mixtes de nanoparticules inattendus.

Résumé en Anglais

Electrostatic complexation process involving polyelectrolyte and nanoparticles of opposite charge are receiving an increasing interest in view of their implications in numerous domains. In this thesis, we are particularly interested in the role of ratio L_p/R on the formation of complexes. To realize the variation of this parameter, we have chosen five model systems by the combination of four polyelectrolytes of different rigidity and three oppositely charged nanoparticles of different sizes, including the positively charged AuNPs synthesized by ourselves. For each system, we have in the first place studied the macroscopic behaviors of complexes formed at different concentration ratio of PEL and NPs, which were recorded in the phase diagrams. Then, the structures of so formed complexes were studied by a combination of cryo-TEM, small-angle neutron, X-ray, and light scattering (size, fractal dimension D_f). We have in particular revealed for $L_p/R \approx 1$ the formation of well-defined single-strand nanorods and also of randomly branched complexes (D_f between 1.5 and 3) respectively in the two monophasic domains (excess of nanoparticles or of PEL chains). Besides the ratio L_p/R , the salt effect was also studied by comparing salt-free system with the one in presence of additional salt, and we proved that the addition of salt can screen the repulsive charges of complexes which results in rapid phase separation and more compact complex structure. Moreover, we have observed unexpectedly the formation of AuNPs nanoparticles- Hyaluronan chains metacrystals.